ABSTRACT

Title of Thesis: HIGH PRECISION PLASMA ETCH FOR PATTERN TRANSFER: TOWARDS FLUOROCARBON BASED ATOMIC LAYER ETCHING

Dominik Metzler, Doctor of Philosophy, 2016

Directed By: Professor Gottlieb S. Oehrlein, Department of Material Science and Engineering

A basic requirement of a plasma etching process is fidelity of the patterned organic materials. In photolithography, a He plasma pretreatment (PPT) based on high ultraviolet and vacuum ultraviolet (UV/VUV) exposure was shown to be successful for roughness reduction of 193nm photoresist (PR). Typical multilayer masks consist of many other organic masking materials in addition to 193nm PR. These materials vary significantly in UV/VUV sensitivity and show, therefore, a different response to the He PPT. A delamination of the nanometer-thin, ion-induced dense amorphous carbon (DAC) layer was observed. Extensive He PPT exposure produces volatile species through UV/VUV induced scissioning. These species are trapped underneath the DAC layer in a subsequent plasma etch (PE), causing a loss of adhesion.

Next to stabilizing organic materials, the major goals of this work included to establish and evaluate a cyclic fluorocarbon (FC) based approach for atomic layer etching (ALE) of SiO_2 and Si; to characterize the mechanisms involved; and to evaluate the impact of processing parameters.

Periodic, short precursor injections allow precise deposition of thin FC films. These films limit the amount of available chemical etchant during subsequent low energy, plasma-based Ar^+ ion bombardment, resulting in strongly time-dependent etch rates. *In situ* ellipsometry showcased the self-limited etching. X-ray photoelectron spectroscopy (XPS) confirms FC film deposition and mixing with the substrate. The cyclic ALE approach is also able to precisely etch Si substrates. A reduced time-dependent etching is seen for Si, likely based on a lower physical sputtering energy threshold. A fluorinated, oxidized surface layer is present during ALE of Si and greatly influences the etch behavior. A reaction of the precursor with the fluorinated substrate upon precursor injection was observed and characterized. The cyclic ALE approach is transferred to a manufacturing scale reactor at IBM Research. Ensuring the transferability to industrial device patterning is crucial for the application of ALE. In addition to device patterning, the cyclic ALE process is employed for oxide removal from Si and SiGe surfaces with the goal of minimal substrate damage and surface residues. The ALE process developed for SiO_2 and Si etching did not remove native oxide at the level required. Optimizing the process enabled strong O removal from the surface. Subsequent 90% H_2/Ar plasma allow for removal of C and F residues.

HIGH PRECISION PLASMA ETCH FOR PATTERN TRANSFER: TOWARDS FLUOROCARBON BASED ATOMIC LAYER ETCHING

By

Dominik Metzler

Dissertation submitted to the Faculty of the Graduate School of the
University of Maryland, College Park, in partial fulfillment
of the requirements for the degree of
Doctor of Philosophy
2016

Advisory Committee:
Prof. Gottlieb S. Oehrlein, Department of Materials Science and Engineering, Chair
Prof. Robert M. Briber, Department of Materials Science and Engineering
Prof. Raymond Phaneuf, Department of Materials Science and Engineering
Prof. Martin Peckerar, Department of Electrical and Computer Engineering
Dr. Eric Joseph, Thomas J. Watson Research Center, IBM

© Copyright by

Dominik Metzler

2016

Acknowledgements:

A lot of people have helped me on my path during my 5 years of PhD studies. First, I want to thank my advisor, Prof. Gottlieb S. Oehrlein. We have had many interesting and stimulating discussions during my time at the University of Maryland. You have taught me to think critically, how to approach problems scientifically, and how best to face the challenges present.

I want to thank all of my dissertation committee members for the interest and time invested in my work. I sincerely hope you find it worthwhile. Thank you, Prof. Briber, Prof. Phaneuf, Prof. Peckerar, and Dr. Joseph.

Thank you very much to Dr. Sebastian Engelmann, Dr. Robert Bruce, and Dr. Eric Joseph at the IBM T.J. Watson Research Center for a long-standing collaboration. Your input, feedback, and comments were always very stimulating and helpful.

I also want to thank other collaborators at Lam Research, Texas Instruments, and within the University of Maryland. The projects and work performed together were always intriguing and challenging.

I am grateful for the financial support by the U.S. National Science Foundation, the U.S. Department of Energy, and the Semiconductor Research Corporation over the years

Thank you to all my lab colleagues with whom I had the pleasure to work in the Laboratory for Plasma Processing of Materials group. First, thanks to my mentor, Dr. Florian Weilnboeck, who taught me everything I needed to know to start my career, and more. Additional thanks to, Dr. Nick Fox-Lyon, Dr. Elliot Bartis, Andrew Knoll, Chen Li, Pingshan Luan, and Adam Pranda for all the good times in and outside the lab.

Thank you to all of the undergraduate students and interns that have helped me along the way. Thank you, Mario Vollmer, Thomas Pitzel, David Kaplan, Gabriel Anfinrud, Joshua Park, Priscilla Tang, and Felix Hilpert.

I am grateful for the very generous support of the Institute for Research in Electronics and Applied Physics staff, including but not limited to Nolan Ballew, Jay Pyle, William Schuster, and Ed Condon. Thank you for all the help in and outside the laboratory.

I want to thank my parents, Edwin and Petra Metzler, who have always encouraged me in all my endeavors, near or far. I could not have asked for better support.

Last, but certainly not least, I thank all of my supportive friends - those I have had for a long time and those I have made along the way.

Table of Contents:

Acknowledgements i

Table of Contents iii

List of Tables vi

List of Figures vii

Chapter 1: Introduction 1

1.1. Advanced Semiconductor Device Processing 1

1.2 Collaborative Research 3

1.3 Plasma Processing 4

1.4 Material Description 5

1.4.1 Polymeric Masking Materials 6

1.4.2 Si-Based Materials 8

1.5 Characterization Techniques 8

1.6 Thesis Outline 10

Chapter 2: He Plasma Pretreatment of Organic Masking Materials for Performance Improvement During Pattern Transfer by Plasma Etching 12

2.1. Introduction 14

2.2. Experimental Details and Procedures 17

2.2.1 Plasma Processing and Measurements 17

2.3.2 Ellipsometric Modeling, Extinction, and Refractive Index for a-C:H Like Materials 20

2.3. Results 22

2.3.1. 193nm Photoresist 22

2.3.2. Anti-Reflection Coating 29

2.3.3 Hard Mask 30

2.3.4 Near Frictionless Carbon 33

2.3.5 Extreme Ultraviolet Resist 37

2.3.6 Comparison of all Materials 40

2.4. Conclusion 43

Chapter 3: Formation of Nanometer-Thick Delaminated Amorphous Carbon Layer by Two-Step Plasma Processing of Methacrylate-Based Polymer 45

3.1. Introduction 48

3.2. Experimental Procedures 50
3.3. Results and Discussion 53
3.3.1 Formation of Ultrathin, Dense, Amorphous Carbon Layer by Two-Step Plasma Processing 53
3.3.2 Material Characterization 54
3.3.3 Critical Parameters for Delamination 59
3.4 Discussion 62
3.4.1 Formation Mechanism 62
3.4.2 Material Properties 63
3.5 Summary 64
Chapter 4: Fluorocarbon Assisted Atomic Layer Etching of SiO_2 Using Cyclic Ar/C_4F_8 Plasma 66
4.1 Introduction 68
4.2 Experiment 69
4.3 Results and Discussion 70
4.4 Summary 76
Chapter 5: Fluorocarbon Assisted Atomic Layer Etching of SiO_2 and Si Using Cyclic Ar/C_4F_8 and Ar/CHF_3 Plamsa 78
5.1. Introduction 80
5.2. Experimental Methods 81
5.3 Results 82
5.3.1 C_4F_8 Based ALE 85
5.3.2 CHF_3 Based ALE 89
5.3.3 Etched Material per Cycle 93
5.3.4 Atomic Force Microscopy and Langmuir Probe Characterization 95
5.4 Discussion 97
5.4.1 Precursor comparions 97
5.4.2 Etch Mechanism 100
5.5 Summary and Conclusions 102
Chapter 6: Characterizing Fluorocarbon Assisted Atomic Layer Etching of Si Using Cyclic Ar/C_4F_8 and Ar/CHF_3 Plasma 104
6.1 Introduction 107
6.2 Experimental 108
6.3 Results and Discussion 110
6.3.1 Cyclic Processing 110

6.3.2 Fluorocarbon Film Deposition ... 112
6.3.3 Optical Modeling ... 114
6.3.4 Characterizing C_4F_8 Based Etching ... 115
6.3.4.1 Process Parameters ... 115
6.3.4.2 Material Etching Selectivity ... 120
6.3.4.3 Silicon Surface Chemistry ... 124
6.3.5 Characterizing CHF_3 Based Etching ... 136
6.3.6 Si Reaction During Deposition ... 138
6.4 Discussion ... 143
6.5 Summary and Conclusion ... 146
Chapter 7: Application of Cyclic Fluorocarbon/Argon Discharges to Device Patterning ... 148
7.1 Introduction ... 150
7.2 Experimental Methods ... 151
7.3 Results and Discussion ... 153
7.3.1 Substrate Temperature ... 155
7.3.2 Etch Step Length ... 157
7.3.3 Uniformity ... 159
7.3.4 Surface Chemistry ... 161
7.4 Summary and Conclusions ... 166
Chapter 8: Plasma-Based Removal of Oxide on Si and SiGe Substrates While Minimizing Surface Residues ... 168
8.1 Introduction ... 171
8.2 Experimental Procedures ... 172
8.3 Results and Discussion ... 174
8.3.1 Ar Sputtering ... 174
8.3.2 Removal of Thin, Native SiO_2 from Silicon Surfaces ... 177
8.3.2.1 Cyclic ALE Process ... 177
8.3.2.2 Continuous Bias Process ... 178
8.3.2.3 Post Cleaning H_2/Ar Treatment ... 181
8.3.3 Removal of Thin, Native Oxide from SiGe Surfaces ... 186
8.4 Conclusions and Summary ... 191
Chapter 9: Conclusions and Future Work ... 193
References ... 201

List of Tables:

Chapter 2:

Table 2.1: Thickness loss for all materials and processes.

Table 2.2: Surface roughness and average wavelength of the power spectral density distribution for all materials and processes.

Table 2.3: Summary of FTIR absorbance for all materials and processes.

List of Figures:

Chapter 1:

Figure 1.1: Schematic of the inductively coupled plasma system used.

Figure 1.2: Basic polymer structure of the organic masking materials investigated.

Chapter 2:

Figure 2.1: Schematic of rough surface morphologies for stressed bi-layer systems for (a) PE and (b) PPT with subsequent PE. The given plane strain moduli and densities are for 193nm PR.

Figure 2.2: Basic Polymer Structures of each material investigated.

Figure 2.3: The optical model used for real-time in-situ ellipsometry. A dense amorphous carbon (DAC) layer is simulated on top of a UV modified layer. The UV modified layer thickness is assumed to be only 50 nm, compared to 100 nm, for NFC due to a higher radiation absorption.

Figure 2.4: Extinction coefficient dependent on refractive index for various a-C:H like materials. The type of deposition is indicated by color, the publishing author by symbol. Also shown is the correlation established by Schwarz-Selinger[13] as well as upper and lower boundaries for the extinction coefficient for a given refractive index.

Figure 2.5: AFM of 193nm PR (DE) (a) after PE and (b) after PPT + PE. PPT reduces surface roughness and increase typical feature size. The inlet in (a) shows the basic poly(methyl methacrylate) structure of 193nm PR.

Figure 2.6: Real-time *in-situ* ellipsometry for 193nm PR (DE) (a) during PE, PPT, and PPT + PE with a pristine reference line, (b) of DAC layer formation during PE, and (c) of DAC layer formation during PE following PPT.

Figure 2.7: (a) RMS surface roughness, material removal and (b) FTIR absorbance of three characteristic bands for 193nm PR (DE) for pristine material and after each process.

Figure 2.8: AFM of AR (a) after PE and (b) after PPT + PE. The inlet in (a) shows the basic poly(methyl methacrylate) structure of AR. The PPT slightly enhance surface roughness and changes the morphology.

Figure 2.9: Real-time *in-situ* ellipsometry for AR (a) during PE, PPT, and PPT + PE with a pristine reference line, (b) of DAC layer formation during PE, and (c) of DAC layer formation during PE following PPT.

Figure 2.10: (a) RMS surface roughness, material removal and (b) FTIR absorbance of three characteristic bands for AR for pristine material and after each process.

Figure 2.11: AFM of HM (a) after PE and (b) after PPT + PE. The inlet in (a) shows the basic naphthalene structure of HM. Plasma processing shows minimal impact on HM.

Figure 2.12: Real-time *in-situ* ellipsometry for HM (a) during PE, PPT, and PPT + PE with a pristine reference line, (b) of DAC layer formation during PE, and (c) of DAC layer formation during PE following PPT.

Figure 2.13: RMS surface roughness and material removal for HM after each process.

Figure 2.14: AFM of NFC (a) after PE and (b) after PPT + PE. The inlet in (a) shows the basic polystyrene structure of NFC. The surface roughness is overall very low but slightly enhance with PPT.

Figure 2.15: Real-time *in-situ* ellipsometry for NFC (a) during PE, PPT, and PPT + PE with a pristine reference line, (b) of DAC layer formation during PE, and (c) of DAC layer formation during PE following PPT.

Figure 2.16: (a) RMS surface roughness, material removal and (b) FTIR absorbance of three characteristic bands for NFC for pristine material and after each process.

Figure 2.17: AFM of EUV (a) after PE and (b) after PPT + PE. The inlet in (a) shows the basic poly(methacrylate) structure of EUV with butyrolactone and ethyl-adamantyl sidegroups. PPT enhances the surface roughness and changes surface morphology.

Figure 2.18: Real-time *in-situ* ellipsometry for EUV (a) during PE, PPT, and PPT + PE with a pristine reference line, (b) of DAC layer formation during PE, and (c) of DAC layer formation during PE following PPT.

Figure 2.19: (a) RMS surface roughness, material removal and (b) FTIR absorbance of three characteristic bands for EUV for pristine material and after each process.

Chapter 3:

Figure 3.1: Cross-sectional SEM image of blisters formed by the delaminated DAC layer. (b) A close up of the marked area in (a). It can be seen that, especially in (c), the delaminated layer is only a few nanometer thick.

Figure 3.2: (a) Real time Ψ-Δ trajectory of in situ ellipsometry during a 60 s (squares) and 120 s (circles) PPT, each with subsequent PE. The solid lines mark a constant index of refraction. The formation of the DAC layer leads to a strong increase in Δ. The loss of adhesion leads to very rapid changes in Ψ and Δ. (b) Schematic of the optical model used to interpret the Ψ-Δ trajectory.

Figure 3.3: Cross-sectional SEM image of the delaminated DAC layer for (a) 193nm PR (DE), provided by Dow Electronics, and (b) 193nm PR (JSR), provided by Japan Synthetic Rubber Corp.

Figure 3.4: TEM images of the DAC films. (a) The diffraction pattern, characteristic of amorphous carbon with weak rings, (b) a single, thin layer, and (c) several layers.

Figure 3.5: (a) Electron energy loss spectra of the delamination film. (b) and (c) show the carbon characteristic energy range at two different locations on the sample.

Figure 3.6: The (a) Zero loss peak (ZLP) image and (b) C-K edge map show a uniform region with high C content.

Figure 3.7: Raman spectra of the blistered delaminated material after it was transferred to an SiO_2/Si substrate. The black curve was measured at the apex of a blister, while the blue curve was measured at the base of the blister.

Figure 3.8: Samples with a graded 193nm PR thickness after exposure to a two-step plasma process (120 s PPT and 60 s PE). Only films thicker than ≈150 nm (shaded area) show blister formation (c and d). Films with an initial thickness of less than ≈150 nm do not show a loss of adhesion and thus, no blister formation (b). Arrows mark examples of visible blisters.

Figure 3.9: Optical microscope images of blister formation on the surface of methacrylate-based 193nm photoresist material after 2-step plasma processes. Blister free areas are (a) randomly distributed across the surface and also around (b and c) scratches.

Figure 3.10: (a) Schematic of plasma interactions with the sample. UV/VUV radiation can cause modification, in this case specifically chain scission deep into the polymer (up to ≈200 nm, exponentially decaying). The ion penetrations depth is on the order of ≈2 nm, thus forming a thin and very dense amorphous carbon (DAC) layer at the very surface, capable of trapping photolysis products. (b) There are several possible photolysis products, with the main one being the adamantyl sidegroup. Possible bond scissioning is marked with red circles.

Chapter 4:

Figure 4.1: Example of the thickness evolution during eight cycles of an SiO_2 ALE process. The process parameters have also been specified. The cycle marked is magnified in Fig. 4.2 (a).

Figure 4.2: Thickness changes of SiO_2 during a single cycle for two thicknesses of deposited FC layer achieved by changing the C_4F_8 pulse time from (a) 1.5 s to (b) 3 s. The FC pulse is injected at the beginning of the deposition

step. Eight seconds after the pulse ends, the bias potential is applied and the etch step begins.

Figure 4.3: XPS spectra comparing SiO_2 with (a) thick (15 Å) and (b) thin (5 Å) deposited FC films after various steps of the 10th ALE cycle.

Figure 4.4: Temporal variation of etch rates of FC layer and SiO_2 layer (top row and middle row, respectively) during a cycle as a function of deposited FC film thickness and maximum ion energy. The bottom row shows SiO_2 etched for various deposited FC layer thickness and maximum ion energy.

Chapter 5:

Figure 5.1: Schematic of the cyclic ALE approach employed consisting of a repeating deposition step and etch step.

Figure 5.2: *In situ* ellipsometry of one example cycle of Si ALE for C_4F_8. The start of the etch step is marked as ‘0 s’. 5 s, 15 s, and 40 s of 25 eV ion bombardment are marked. 5 Å of FC film are deposited and ≈3 Å of Si are removed during each cycle.

Figure 5.3: *In situ* ellipsometry of a continuous Ar/C_4F_8 etch and a cyclic ALE approach etch through a SiO_2-Si-SiO_2 stack. The areas of silicon oxide and silicon etching are marked with shaded backgrounds.

Figure 5.4: XPS spectra comparing Si ALE using C_4F_8 after the deposition step, during the etch step, and at the end of the etch step.

Figure 5.5: *In situ* ellipsometry of one example cycle of Si ALE for CHF_3. The start of the etch step is marked as ‘0 s’. 5 s, 15 s, and 40 s of 25 eV ion bombardment are marked. ≈11 Å of FC film are deposited and ≈6 Å of Si are removed during each cycle.

Figure 5.6: XPS spectra comparing Si ALE using CHF_3 after the deposition step, during the etch step, and at the end of the etch step.

Figure 5.7: Thickness removal during the cycle as determined by ellipsometry for ALE of Si and SiO_2 using C_4F_8 and CHF_3 at 25 eV ion energy and 40 s etch step length.

Figure 5.8: FC film deposition, silicon removal, and silicon oxide removal during the cycle as determined by ellipsometry for ALE using CHF_3 at 25 eV ion energy and 20 s etch step length. The first 13 cycles are etching through a silicon oxide layer on top of the silicon substrate.

Figure 5.9: Surface roughness as measured by AFM (1 x 1 μm^2) after 10 cycles of SiO_2 ALE with 5 Å FC deposition per cycle, 25 eV ion energy, and 40 s etch step length.

Figure 5.10: Response in plasma parameters (a) Plasma potential V_p, (b) electron density N_e, and (c) electron temperature T_e upon brief C_4F_8 injection.

Figure 5.11: Deposition behavior of C_4F_8 (closed symbols) and CHF_3 (open symbols) on SiO_2 and Si substrates. (a) The C 1s spectrum shows a higher intensity for CHF_3 when depositing on Si (black squares) with the same precursor injection as on SiO_2 (red circles). (b) F/C ratios of the polymer films deposited in a cyclic fashion by C_4F_8 and CHF_3.

Chapter 6:

Figure 6.1: Schematic of the cyclic ALE approach employed consisting of a repeating deposition step and etch step. The process parameters varied are the FC film deposition per cycle, the ion energy during the etch step, and the etch step length.

Figure 6.2: (a) Deposited FC film thickness per cycle dependent on the amount of precursor injected per pulse, depicted by the number of molecules $N_{precursor}$. CHF_3 shows an overall lower deposition yield than C_4F_8. (b) FC film deposition per cycle on Si compared to deposition on SiO_2. The FC deposition is seen to increase during the process when transitioning from a SiO_2 to Si substrate. C_4F_8 does not show a change in deposition based on substrate material.

Figure 6.3: FC film deposition (black squares), and amount of Si etched (red circles) during each cycle. Processing conditions are CHF_3 precursor injection with a 40 s etch step at 25 eV ion energy. A schematic of the sample stack is shown as an inset. The initial 15 cycles are etching SiO_2 on top of the Si. Once the Si layer is reached, the Si etching starts and the FC deposition increases. Around cycle 30 the Si layer is completely etched away.

Figure 6.4: Example changes in thicknesses over time for one individual cycle of Si ALE using 30 eV and CHF_3. A fast and strong removal of the deposited FC film can be seen. The Si etch rate decreases throughout the cycle as F is removed during the ion bombardment. Grey shadowing marks the etch step. The optical model used is shown schematically.

Figure 6.5: Etch depth per cycle for SiO_2 (black squares) and Si (red circles) dependent on FC film thickness deposited per cycle using C_4F_8 at (a) 20 eV, (b) 25 eV, and (c) 30 eV. The etch step length is kept at 40 s.

Figure 6.6: Etch depth per cycle for SiO_2 (black squares) and Si (red circles) using C_4F_8 dependent on etch step length for 25 eV (closed symbols) and 30 eV (open symbols) ion energy. The FC deposition is 5 Å per cycle.

Figure 6.7: Si instantaneous etch rates during the initial part of the etch step (solid symbols) and during the final part of the etch step (open symbols) dependent on etch step length for 25 eV (black squares) and 30 eV (red circles). The difference in etch rates shows the removal of F during the etch step, leading to less chemically enhanced etching.

Figure 6.8: Etch depth per cycle for SiO_2 (black squares) and Si (red circles) using C_4F_8 (closed symbols) and CHF_3 (open symbols) dependent on ion energy during the etch step at 40 s etch step length. The FC deposition is 5 Å per cycle.

Figure 6.9: Cycle averaged etch yield, i.e. material removed per cycle per number of incident ions per cycle, dependent on F/Ar^+, i.e. F in the deposited FC film

per number of incident ions during one cycle. (a) The FC thickness deposited per cycle ranges from 3 to 11 Å. (b) The etch step length ranges from 20 to 60 s.

Figure 6.10: Si 2p XPS spectra comparing surface chemistry for Si ALE (a) at the end of a deposition step and (b) at the end of an etch step. ≈11 Å of FC film per cycle are deposited using C_4F_8. The etch step is 40 s long at 25 eV ion energy. Spectra are measured during quasi-steady-state conditions. A typical decomposition for each spectra is shown with the resolving fit to the measured data.

Figure 6.11: C 1s XPS spectra comparing surface chemistry for Si ALE (a) at the end of a deposition step and (b) at the end of an etch step. ≈11 Å of FC film per cycle are deposited using C_4F_8. The etch step is 40 s long at 25 eV ion energy. Spectra are measured during quasi-steady-state conditions. A typical decomposition for each spectra is shown with the resolving fit to the measured data.

Figure 6.12: O 1s XPS spectra comparing surface chemistry for Si ALE (a) at the end of a deposition step and (b) at the end of an etch step. ≈11 Å of FC film per cycle are deposited using C_4F_8. The etch step is 40 s long at 25 eV ion energy. Spectra are measured during quasi-steady-state conditions. A typical decomposition for each spectra is shown with the resolving fit to the measured data.

Figure 6.13: F 1s XPS spectra comparing surface chemistry for Si ALE (a) at the end of a deposition step and (b) at the end of an etch step. ≈11 Å of FC film per cycle are deposited using C_4F_8. The etch step is 40 s long at 25 eV ion energy. Spectra are measured during quasi-steady-state conditions. A typical decomposition for each spectra is shown with the resolving fit to the measured data.

Figure 6.14: (a) F/C ratio of the FC film (black squares) and ΔF/C (red circles) as measured per XPS during one cycle of Si ALE. ΔF/C is the difference in

F/C ratio determined by the C 1s spectra and the F 1s/C 1s ratio and is indicating the amount of F in the substrate. (b) Intensities during one cycle for CF_x species measured in the C 1s spectra (black squares) and the F 1s spectra (red circles). The process parameters are C_4F_8 with a FC film deposition per cycle of 5 Å. The etch step is kept at 40 s with 25 eV ion energy. The etch step starts at 0 s.

Figure 6.15: (a) F/C ratio of the FC film (black squares) and ΔF/C (red circles) as measured per XPS during one cycle of Si ALE. ΔF/C is the difference in F/C ratio determined by the C 1s spectra and the F 1s/C 1s ratio and is indicating the amount of F in the substrate. (b) Intensities during one cycle for CF_x species measured in the C 1s spectra (black squares) and the F 1s spectra (red circles). The process parameters are C_4F_8 with a FC film deposition per cycle of 11 Å. The etch step is kept at 40 s with 25 eV ion energy. The etch step starts at 0 s.

Figure 6.16: Etch depth per cycle for SiO_2 (black squares) and Si (red circles) dependent on FC film thickness deposited per cycle using CHF_3 at (a) 20 eV, (b) 25 eV, and (c) 30 eV. The etch step is kept at 40 s.

Figure 6.17: F/C ratio of the FC film (black squares) and ΔF/C (red circles) as measured per XPS during one cycle of Si ALE. ΔF/C is the difference in F/C ratio determined by the C 1s spectra and the F 1s/C 1s ratio and is indicating the amount of F in the substrate. The process parameters are CHF_3 with a FC film deposition per cycle of (a) 5 Å and (b) 11 Å. The etch step is kept at 40 s with 25 eV ion energy.

Figure 6.18: Example changes in thickness over time for one individual cycle of Si ALE at 25 eV ion energy using CHF_3. A 10 s delay after turning off the bias potential and before the next precursor injection is introduced. The time of precursor injection is marked with a dashed line. The Si reaction and thickness change is only observed once CHF_3 is injected. Grey shadowing marks the etch step.

Figure 6.19: FC film deposition (black squares, left scale) and amount of Si etched (red circles, left scale) during each cycle as seen in Figure 6.3. The amount of Si reacted during the deposition step (green triangles, right scale) is added. Processing conditions are CHF_3 precursor injection with a 40 s etch step at 25 eV ion energy. The initial 15 cycles are etching SiO_2 on top of the Si. Once the Si layer is reached the Si etching starts, the FC deposition increases, and a reaction of Si is seen during the deposition step. Around cycle 30 the Si layer is completely etched away.

Figure 6.20: Amount of Si reacted during the deposition step depending on (a) film thickness for 20, 25, and 30 eV ion energy for 40 s during the etch step, and (b) etch step length at 25 eV ion energy. This reaction is observed during the deposition step, but does show an impact of the etch step due to changes in the surface chemistry. It cannot clearly be determined if the Si is actually lost or reacted or a combination of both occurs.

Figure 6.21: Schematic of FC based ALE for (a) thin FC film depositions on the order of 5 Å and (b) thicker FC film depositions on the order of 11 Å. The reacted Si layer is a mix of oxidization and fluorination. The process can be controlled via the FC film deposition, e.g. film thickness and precursor, and via the low energy ion bombardment, e.g. via length and ion energy. This schematic is not to scale.

Chapter 7:

Figure 7.1: Gas and bias pulsing sequence used in this work. Typical process conditions and times are stated.

Figure 7.2: Schematic layout of (a) experimental chamber and (b) sample stack used in this work.

Figure 7.3: Etched silicon oxide thickness per cycle vs. etch step length for examined conditions.

Figure 7.4: (a) X-SEM example with measurement annotations and (b) measured dimensions (b) for examined deposition conditions. The FC top of feature, FC bottom of feature, and FC side of feature refer to the left scale, the FC penetration on side refers to the right scale.

Figure 7.5: (a) Observed etch rates and (b) silicon oxide over silicon nitride selectivity for examined substrate temperature conditions.

Figure 7.6: X-SEM images of evaluated silicon oxide features with varying substrate temperature and etch step lengths.

Figure 7.7: HR-TEM images of samples processed at (a) -20° C, (b) 10° C, and (c) 50° C substrate temperature.

Figure 7.8: Wafer scale uniformity of (a) conventional plasma process and (b) ALE process.

Figure 7.9: HR-TEM image of 200-mm wafer (a) center and (b) edge profile with atomic layer etch process.

Figure 7.10: XPS spectra of silicon oxide surface throughout one atomic layer etch cycle. 0 s etch (light blue curve) refers to the surface chemistry after the FC deposition, i.e. without ion bombardment.

Figure 7.11: Schematic illustration of the ALE window with 4 example results of non-ideal behavior.

Figure 7.12: 40nm pitch features (a) after lithography and (b) after etching in conventional plasma and (c) atomic layer etch approach at 200 W_s, 10 W_b, 10 °C, and 75 s etch time.

Figure 7.13: X-SEM of patterned 44 nm pitch feature by atomic layer etch approach.

Chapter 8:

Figure 8.1: Relative thickness change of Si native oxides exposed to Ar plasma with 15 eV (black) and 30 eV (red) ion energy.

Figure 8.2: Schematic of the cyclic ALE process used for SiO_2 etching. A FC film deposition step is followed by a subsequent etch step with low energy Ar^+ ion bombardment.

Figure 8.3: Relative oxide thickness compared to pristine thickness of ~20 Å for each cycle at various (a) FC thicknesses deposited per cycle and (b) ion energies using the cyclic ALE process on Si with native oxide.

Figure 8.4: Schematic of the continuously biased cleaning process. This process utilizes precise, periodic CF_4 injections into a continuously biased Ar plasma.

Figure 8.5: Relative changes in oxide layer thickness as measured by *in situ* ellipsometry for a continuously biased cleaning process with a 4 s CF_4 injection.

Figure 8.6: Relative changes in top layer thicknesses for post cleaning H_2/Ar plasma with 0, 10, 90, and 100 % H_2 admixture after a continuously biased clean.

Figure 8.7: XPS spectra of the (a) Si 2p, (b) C 1s, (c) O 1s, and (d) F 1s measured for a pristine Si sample (black squares), after continuous bias cleaning (red circles), after a post cleaning 10% H_2/Ar plasma (green triangles), and after a post cleaning 90% H_2/Ar plasma (cyan diamonds).

Figure 8.8: Summary of elemental intensities of (a) elemental and (b) reacted Si, (c) oxygen, and (d) carbon for cleaning processes of Si substrates relative to a Si substrate as received. (e) The fluorine intensity is taken relative to the continuously biased process. The treatments shown are Ar plasma sputtering at 15 eV, a continuously biased cleaning process, and a continuously biased cleaning process with a subsequent 90% H_2/Ar post treatment.

Figure 8.9: Relative thickness change of SiGe native oxides exposed to Ar plasma with 15 eV (black) and 30 eV (red) ion energy.

Figure 8.10: Surface chemistry of pristine SiGe with a native oxide layer (black squares), after Ar plasma exposure (red circles), after continuous bias

cleaning (green triangles), and after continuous bias cleaning with a 90% H_2/Ar post clean treatment (blue diamonds).

Figure 8.11: Summary of elemental intensities of (a) elemental and (b) reacted Ge, (c) elemental and (d) reacted Si, (e) oxygen, and (f) carbon for cleaning processes of SiGe substrates relative to a SiGe substrate as received. (g) The fluorine intensity is taken relative to the continuously biased process. The treatments shown are Ar plasma sputtering at 15 eV, a continuously biased cleaning process, and a continuously biased cleaning process with a subsequent 90% H_2/Ar post treatment.

Chapter 1: Introduction

1.1 Advanced Semiconductor Device Processing

Advanced semiconductor manufacturing requires precise control during plasma-based pattern transfer in order to further shrink critical dimensions. 193nm photoresist (PR) materials exhibit inherently high surface roughness, line-edge roughness development, and low etch-resistance during plasma-based pattern transfer. Previous work showed that a helium plasma based pretreatment (PPT) prior to the pattern transfer etch step (PE) is beneficial for the etch performance of 193nm PR by preventing synergistic roughness introduction.[1] This beneficial effect is based on 193nm PR's UV sensitivity, which is absent in other materials commonly employed in multi-layer masks. Therefore, the question remains what impact this PPT has on other commonly employed materials in multi-layer masks.

In addition to pattern transfer fidelity in photolithography, advanced semiconductor device fabrication increasingly demands atomistic surface engineering.[2-4] Moore's Law in combination with Dennard scaling has been upheld for years and set the pace for semiconductor processing.[5, 6] The continued scaling of feature sizes enabled tremendous progress in computing power. Further development of devices at the nanometer scale depends on the ability to produce features reliably, approaching dimensions comparable to just several molecules. The ability to achieve atomic precision in etching of different materials when transferring lithographically defined templates is a requirement of increasing importance for nanoscale structure fabrication in the semiconductor and related industries. High demands for etch precision and material selectivity are set for modern processes.[7, 8] As critical dimensions approach and go

beyond the 10 nm technology node, the need for an etching method analogous to atomic layer deposition, i.e. atomic layer etching (ALE), becomes essential. ALE is considered a "tipping point technology", intimately tied to enabling broad advances in the semiconductor manufacturing industry and the magnetic information storage device industry.[9] The field of ALE has seen a lot of interest in recent years leading to substantial progress.[10, 11] The idea of ALE itself, however, is more than 25 years old. In the 1990s the ability to control etch processes down to atomistic levels for III-V materials was already recognized.[12, 13] Despite this, many in industry did not have a great interest in establishing ALE of several substrate materials until recently.[14] Additionally, defects and substrate damage introduced during plasma-based etching or pattern transfer can greatly impact device performance.[15, 16] It is, therefore, essential for the success of any modern process to minimize substrate damage. Reducing ion energies helps in this regard. By temporally separating the FC deposition and etching during cyclic ALE, required ion energies can be substantially lower compared to continuous etching methods.

There is currently a lack of scientific understanding that would enable ALE process and equipment design for the production of nanoscale structures in state-of-the-art devices. This work focuses on establishing fluorocarbon (FC) based ALE of SiO_2 and Si substrates. Theoretical studies suggested the possibility of achieving self-limited SiO_2 removal by controlling the reactant flux several years ago.[4, 17] This process employs a flux control in order to limit the amount of chemical etchant available at the surface. High material selectivity is essential for nanoscale device fabrication. Especially of interest is the selective etch of SiO_2 over Si. For continuous precursor addition, material etching selectivity is based on the steady-state FC film thickness.[18] Si shows a significantly

thicker steady-state FC film thickness than SiO_2, which inhibits the substrate etch rate and therefore allows for selective etching. In ALE, however, the FC film thickness is primarily controlled by cyclic precursor injection. FC films are expected to be of similar thickness on Si and SiO_2 for cyclic injections. The lack of a thick FC film can potentially lead to little etching selectivity.

I believe that this work promises wide-ranging impacts in diverse areas of nanoscience and technology. The materials explored are commonly employed and of great interest. A cyclic ALE approach shows several key differences to established continuous etching approaches and challenges what is known about plasma-based etching of semiconductors. Our insights are expected to also be vital to emerging industries, e.g. plastic electronics or graphene-based devices. I believe that the insights offered by our work will inspire the search for new strategies in the quest to realize ALE methods.

1.2 Collaborative Research

This work was performed in a collaborative effort with world-class, interdisciplinary experts in academia and industry.

There were several key benefits of having IBM as a collaborator. IBM provided excellent experience for identifying the most crucial applications for ALE. Dr. Sebastian Engelmann, Dr. Robert Bruce, and Dr. Eric Joseph of IBM Research worked closely with the researchers at UMD to optimize the research strategy and quality to maximize the impact of this work. Monthly phone conferences ensured expert feedback and input on the work. IBM Research provided unique samples that featured sub-nanometer stacks of materials. The approaches developed at UMD were, in turn, transferred to industrial scale reactors available at IBM Research. This was critical in order to ensure that the

approaches developed at UMD are transferrable to industrial device fabrication. Additionally, sophisticated characterization tools are available at IBM Research, e.g. angle resolved spectroscopic ellipsometry and high-resolution transmission electron microscopy. Applying these to the study of ALE processes and structures complemented the characterization performed at UMD.

Lam Research and Texas Instruments provided valuable feedback and discussion on several topics pertaining to this work. Both companies are leaders in semiconductor processing research and provided high-level expertise.

The Semiconductor Research Corporation has been guiding and setting up a roadmap for research in semiconductor processing, helping to clearly define the goals of this work.

The Langmuir Probe studies were conducted in collaboration with Prof. Valery Godyak from the University of Michigan, Ann Arbor. Prof. Valery Godyak is a leading expert on Langmuir probe measurements with high skill and expertise.

1.3 Plasma Processing

Plasma processing was mostly performed in the Laboratory for Plasma Processing of Materials at the University of Maryland. The main plasma reactor used is a custom-built inductively coupled plasma system, schematically shown in Fig. 1.1. A planar, water-cooled brass coil above a quartz window was powered by a 13.56 MHz power supply with an L-type matching network. The plasma was confined within a 195 mm diameter anodized Al confinement ring. A 125 mm diameter silicon substrate is located 150 mm below the top electrode on an electrostatic chuck. Independently biasing the bottom electrode at 3.7 MHz allowed a RF self-bias potential in order to control

maximum ion energies. The base pressure achieved prior to processing was in the $5x10^{-7}$ Torr range. The temperature of the bottom electrode was stabilized at 10°C by substrate backside cooling during plasma processing. Processing parameters, e.g. processing pressure, source power, or bias power, can cover a wide range. Typical processes are operated between 10 mTorr and 100 mTorr processing pressure, and 200 W and 800 W source power. Typical plasma properties encountered during this processes are electron densities of the order of 10^{10} cm^{-3}, electron temperatures around 3 eV, and plasma potentials of about 14 V. The system is connected to a vacuum cluster, connecting three processing chambers and a surface analysis system. Additional details of the plasma system have been described elsewhere.[19-21]

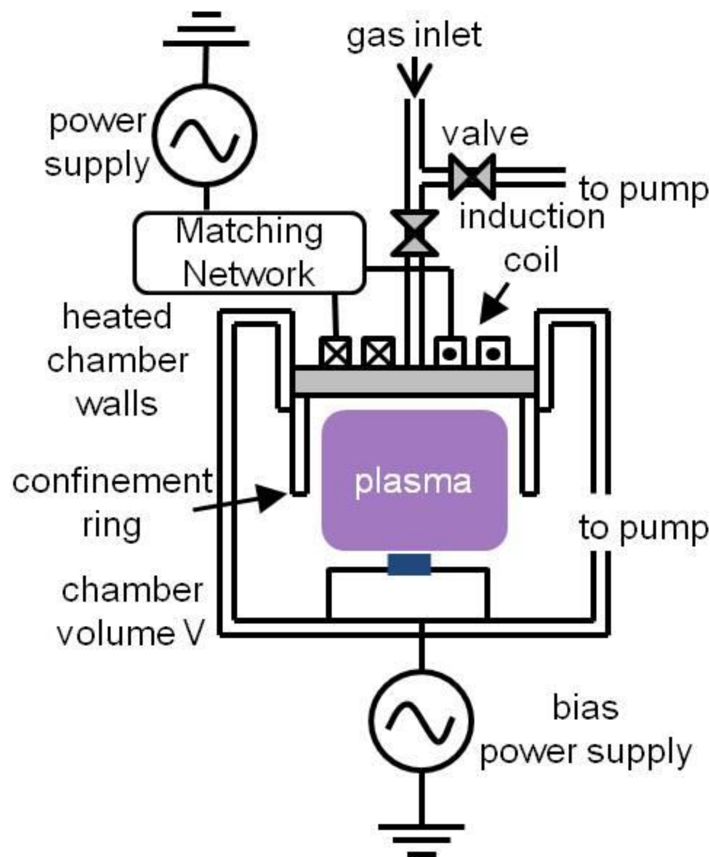

Fig. 1.1: Schematic of the inductively coupled plasma system used.

1.4 Material Description

1.4.1 Polymeric Masking Materials

All basic polymer structures of the polymeric masking materials explored are shown in Fig. 1.2. The set consists of two 193nm PRs, an anti-reflection coating (AR), a thermally activated hard mask (HM), near frictionless carbon (NFC), and an extreme ultraviolet resist (EUV). By comparing two suppliers of 193nm PR, we evaluate how generic the He PPT approach is. The AR is represented by a PMMA-based polymer that is common in multilayer masks. Also commonly used is the naphthalene-based HM. For comparison, the polystyrene-based NFC is studied as a 248nm PR type polymer. Recently, there has been a strong interest in EUV lithography as a promising successor of 193nm photolithography. Typical EUV resist materials contain a polymer-bound photoacid generator.

The first 193nm PR material studied was produced by Dow Electronics (DE) and is poly(methyl methacrylate)-based (PMMA). It was prepared in the form of blanket films (~400 nm thick), or photoresist trench patterns (120 nm width, 240 nm pitch, 140 nm height) on top of 50 nm bottom antireflection coating. This 193nm PR contained photoacid generator and base and was spin-coated onto Si. In addition to 193nm PR (DE), a 193nm PR produced by JSR Corp. (Japan Synthetic Rubber Co) was investigated. 193nm PR (JSR) is PMMA-based, like 193nm PR (DE). Although the basic polymer structure for 193nm PR (DE) is identical to 193nm PR (JSR) there are differences in the atomic composition and side groups. An anti-reflection coating (AR) is represented by a PMMA-based polymer with amidomethyl ether crosslinker. The thermally-activated hard mask (HM) is based on naphthalene. Near frictionless carbon (NFC) is used as an example for 248nm PR-type polymers with the main polymer chain being polystyrene.

The extreme ultraviolet resist (EUV) is a positive-tone chemically amplified resist based on polymer-bound photoacid generator (PAG). The basic structure is a poly(methacrylate) with butyrolactone and ethyl-adamantyl side groups next to PAG. Blanket films of these materials with an initial thickness of 200 nm, 100 nm, 100 nm, and 200 nm for 193nm PR (JSR), AR, HM, and NFC coated on Si, respectively, were employed. The EUV films were 60 nm thick and deposited on top of 75 nm of SiO_2.

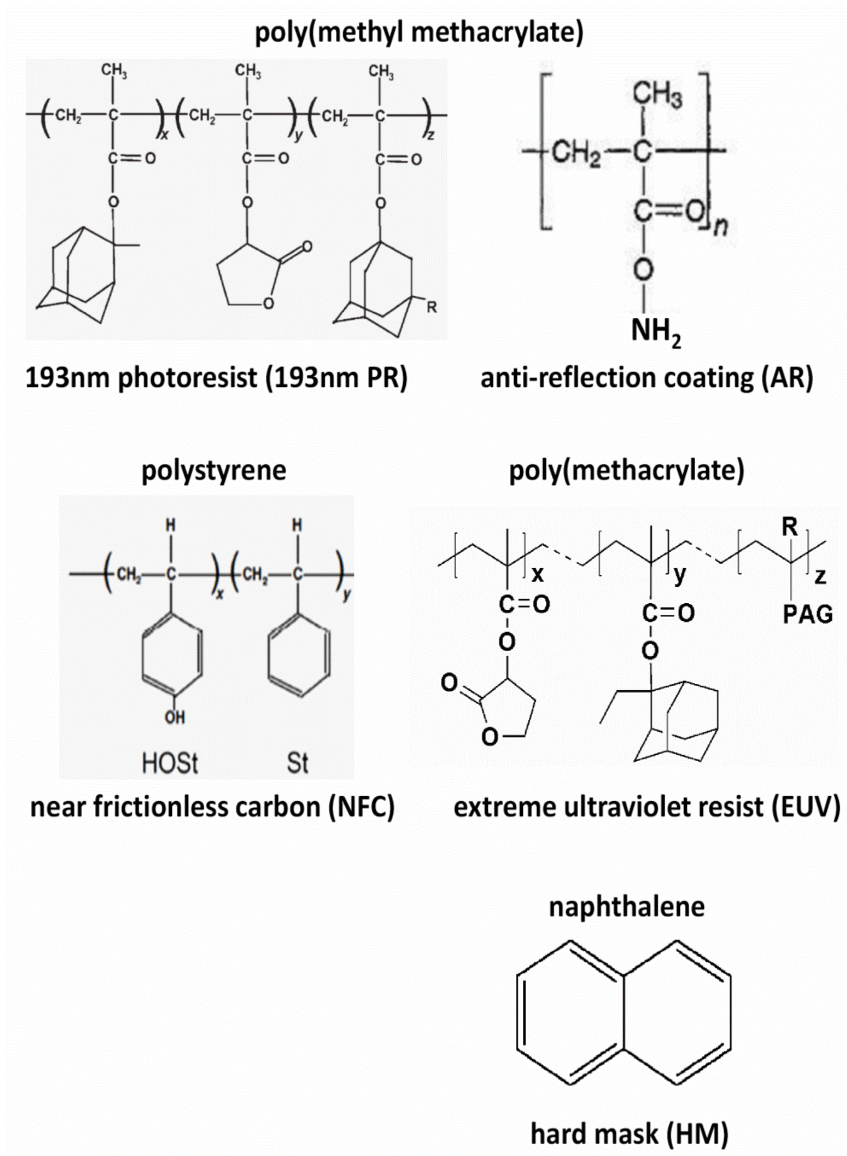

Fig. 1.2: Basic polymer structure of the organic masking materials investigated.

1.4.2 Silicon-Based Materials

Silicon-based materials studied were crystalline Si, native SiO_2 films, thermal SiO_2 films, and SiGe. Bulk Si wafers with a native SiO_2 layer were used to study the removal of a thin oxide layer from a Si surface. For SiGe cleaning, samples were ≈550 Å thick SiGe films with a native oxide. The stacks studied primarily for ALE were SiO_2-Si-SiO_2 stacks deposited on a silicon substrate by PECVD techniques with various thicknesses. Using SiO_2-Si-SiO_2 stacks allowed for precise thickness measurements as well as investigating the transition from SiO_2 to Si etching and the potential to achieve SiO_2 over Si etching selectivity.

1.5. Characterization Techniques

Materials were characterized by a variety of techniques including, but not limited to, ellipsometry, atomic force microscopy (AFM), scanning electron microscopy (SEM), X-ray photoelectron spectroscopy (XPS), and Fourier transform infrared spectroscopy (FTIR). Plasma conditions were characterized using a Langmuir Probe and Optical Emission Spectroscopy.

Ellipsometry

Film thicknesses were studied using *in-situ* ellipsometry.[22] The ellipsometer is an automated rotating compensator ellipsometer working in the polarizer-compensator-sample-analyzer (PCSA) configuration at a ≈72° angle of incidence. Measurements were performed in Ψ-Δ space, corresponding to changes in phase and relative amplitude of the polarized laser light components (He-Ne laser, λ = 632.8 nm). Optical multilayer modeling was used for interpretation of recorded data and to establish real-time thickness changes of various films. The ultra-thin films encountered in this work are at the limit of

the accuracy of the single-wavelength ellipsometer. In order to enhance measurement accuracy results are averaged over multiple cycles and experiments, each showing consistent, reproducible results. Additionally, specially prepared sample stacks of SiO_2-Si-SiO_2 are used for the ALE studies, maximizing the sensitivity. Ellipsometry is an area-averaging technique, i.e. the measurement is averaged over the area of the laser spot on the sample. Therefore, surface roughness on a smaller scale than the size of the laser spot can impact the measurement and is taken into account.

Atomic Force Microscopy (AFM)

Surface morphology and roughness was measured by a tapping mode atomic force microscopy (Veeco Dimension 3000). The scan size was fixed at 1x1 μm^2. The surface roughness values reported were calculated from the root mean square (RMS) of the surface profile.

Scanning Electron Microscope (SEM)

Surface morphology, pattern distortion, and process directionality were characterized using the Hitachi SU-70 scanning electron microscope (SEM) at the University of Maryland's Nanoscale Imaging Spectroscopy and Properties Laboratory. Additional scans were performed by collaborators at the IBM T.J. Watson Research Center. The combination of top-down and cross-sectional SEM allows full analysis of 3D structures.

X-ray Photoelectron Spectroscopy (XPS)

X-ray photoelectron spectroscopy (XPS) analysis provides information on the chemical composition of the film surface. The analysis was performed using a Vacuum

Generators ESCA Mk II surface analysis system connected to a vacuum cluster. The analysis system is employing a Mg-Kα source (1253.6 eV) at electron take-off angles of 90° (deep probing depth ≈ 8 nm) and 20° (shallow probing depth ≈ 2-3 nm) with respect to the sample surface. Narrow scan spectra of the Si 2p, C 1s, O 1s, and F 1s were obtained at 20 eV pass energy. Spectra were fitted using a least square fit after Shirley background subtraction.[23, 24] All fittings were required to show consistency across all individual spectra, i.e. the chemical information extracted from Si 2p, C 1s, O 1s, and F 1s was internally consistent.

Fourier-Transform Infrared Spectroscopy (FTIR)

Fourier-transform infrared spectroscopy (FTIR) is traditionally used to obtain information on changes in chemical composition of the material bulk. The material analysis was performed *ex situ* with the help of the IBM T.J. Watson Research Center.

Langmuir Probe

Time resolved plasma properties were characterized using a Langmuir probe from PlasmaSensors in collaboration with Dr. Valery Godyak and Dr. Ben Alexandrovich.

1.6 Thesis Outline

The main goal of this work is to establish and characterize a fluorocarbon-based cyclic process to realize atomic layer etching of SiO_2 and Si. Fundamental mechanisms behind time-dependent etch rates leading to a self-limited removal are to be identified.

In chapter 2, the He PPT, established to reduce roughness formation of 193nm PR during pattern transfer, is applied to other common organic masking materials. Chapter 3 discusses a delamination effect observed for prolonged He PPT of 193nm PR.

Theoretical studies have paved the way to establish cyclic Ar/C_4F_8 plasma capable of ALE of SiO_2. In chapter 4, self-limited removal of Ångstrom-thick layers of SiO_2 based on periodic, precise precursor injection in conjunction with synchronized low energy Ar^+ ion bombardment is demonstrated. *In situ* ellipsometry is used to measure thicknesses and etch rates in real time. Chemically enhanced etch rates are observed as long as F is present at the surface. Maximum ion energies are below the physical sputtering energy threshold, leading to a self-limited removal. Chapter 5 extends this cyclic ALE approach to Si substrates. A fluorinated, oxidized surface layer is shown to be present during ALE of Si substrates. In chapter 6, the cyclic ALE approach is characterized further, especially with regard to material etching selectivity. The three process parameters FC film thickness deposited per cycle, maximum ion energy, and etch step length are explored. A reaction of the precursor with a fluorinated Si substrate is observed and described.

In chapter 7, the ALE process developed at UMD is transferred to an industrial environment at IBM Research. The impact of various process parameters, such as substrate temperature, on device patterning is presented. Chapter 8 describes the application of ALE for surface cleaning of Si and SiGe with minimal surface residues. A cleaning procedure for removal of native oxide from Si and SiGe substrates is established and characterized.

In chapter 9, the main conclusions of this work are summarized. Additionally, future work and possible directions of the semiconductor industry are outlined and discussed.

Chapter 2: He Plasma Pretreatment of Organic Masking Materials for Performance Improvement During Pattern Transfer by Plasma Etching

Dominik Metzler [a], Florian Weilnboeck [a], [b], Sebastian Engelmann [c], Robert L. Bruce [c], and Gottlieb S. Oehrlein [a]

[a] *Department of Materials Science and Engineering*
And Institute for Research in Electronics and Applied Physics
University of Maryland, College Park, Maryland 20740

[b] *Current address: Infineon Technologies AG, Development Center Villach*

[c] *IBM T.J. Watson Research Center*
Yorktown Heights, New York 10598

Journal of Vacuum Science & Technology B, submitted

Abstract

Previous work on 193nm photoresist (PR) material has shown that a significant improvement of pattern transfer performance can be obtained by applying a helium plasma pretreatment (PPT) prior to the pattern transfer plasma etching step.[1] This work explores whether this PPT is applicable to other organic masking materials commonly employed in resist multilayer masking schemes. The materials investigated include an anti-reflection coating (AR), a thermally-activated hard mask (HM), a near frictionless carbon (NFC) similar to a 248nm PR, and an extreme ultraviolet (EUV) resist. These materials have substantially different UV/VUV sensitivity amongst each other and relative to 193 nm PR. We find that the surface roughness seen after a combination of helium PPT and Ar plasma main etching step is either the same or increased slightly relative to a single Ar main etching step, in contrast to 193 nm PR materials. The fragile adamantane group removed during PPT from 193nm PR is absent for these materials. This indicates that the He PPT efficacy and improved pattern transfer performance is specific to adamantane containing resists.

2.1 Introduction

Photoresist materials, such as methacrylate-based 193nm photoresist (PR), can exhibit high surface and line-edge roughness development in addition to low etch-resistance during plasma-based pattern transfer into other materials. Resulting limitations in pattern fidelity and etching selectivity are important problems.[25, 26] This roughening of nanoscale polymer masks during plasma etching (PE) limits critical feature dimensions in current and future lithographic technologies. Roughness formation of 193nm PR is mechanistically explained by synergy of plasma-induced changes in mechanical properties introduced simultaneously at the 193nm PR surface (≈2 nm) by ions and in the material bulk (≈200 nm) by ultraviolet and vacuum ultraviolet (UV/VUV) plasma radiation.[26, 27] A schematic is shown in Fig. 2.1. Ion bombardment leads to the formation of a dense amorphous carbon (DAC) layer at the surface. Extended, i.e. more than 45 s, helium plasma-generated UV/VUV exposure during a plasma pretreatment (PPT) of 193nm PR prevents roughness formation by saturating bulk material modifications prior to PE exposure.[1] During subsequent PE, 193nm PR patterns are stabilized and exhibit improved etch resistance and reduced surface/line-edge roughness introduction. Commonly used multilayer masks employ other polymers next to 193 nm PR. We therefore examined the question if the He PPT approach can improve the pattern transfer characteristics of these other masking materials. To this end, the impact of PPT on surface roughness, film thickness evolution, DAC layer formation and bulk material changes was studied for a set of representative organic masking materials.

All basic polymer structures are shown in Fig. 2.2. The set consists of two 193nm PRs, an anti-reflection coating (AR), a thermally activated hard mask (HM), near

frictionless carbon (NFC), and an extreme ultraviolet resist (EUV). By comparing two suppliers of 193nm PR, we evaluate how generic the He PPT approach is. The AR is represented by a PMMA-based polymer that is common in multilayer masks. Also commonly used is the naphthalene-based HM. For comparison, the polystyrene-based NFC is studied as a 248nm PR type polymer. Recently, there has been a strong interest in EUV lithography as a promising successor of 193nm photolithography. Typical EUV resist materials contain a polymer-bound photoacid generator.

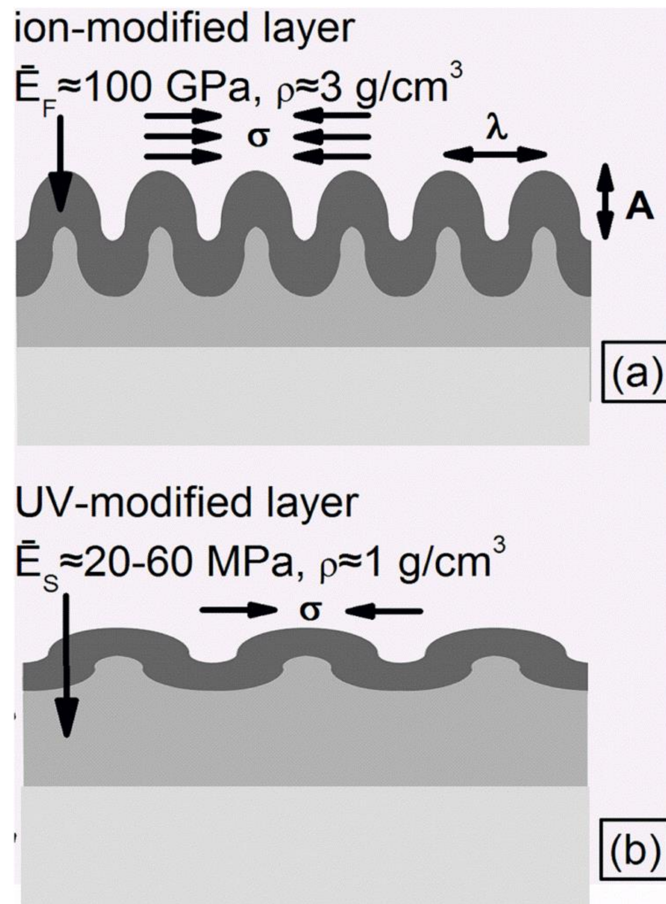

Fig. 2.1: Schematic of rough surface morphologies for stressed bi-layer systems for (a) PE and (b) PPT with subsequent PE. The given plane strain moduli and densities are for 193nm PR.

The role of the He PPT on each material individually is presented in section III A through E. Each section will first describe surface roughness and etch rates followed by material modifications introduced during processing. Section III F summarizes results and compares the investigated materials. Section IV gives an overall summary and conclusions.

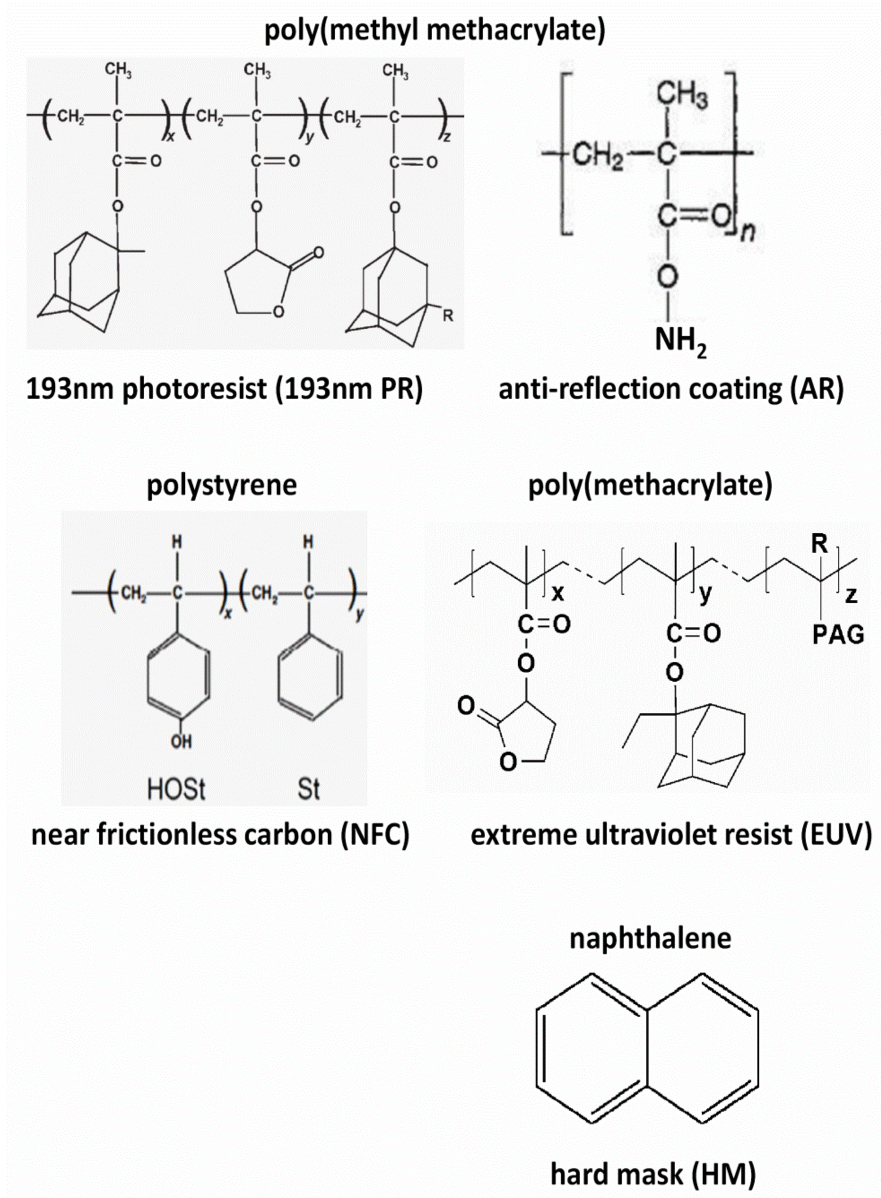

Fig. 2.2: Basic Polymer Structures of each material investigated.

2.2 Experimental Details and Procedures

2.2.1 Plasma Processing and Measurements

Details of the plasma system and 193nm PR materials have been described previously.[28, 29] Briefly, an inductively coupled plasma (ICP) system with a 125 mm diameter electrode (3.7 MHz excitation frequency) covered with a Si substrate and located 130 mm below the ICP coupling window (13.56 MHz excitation frequency) was employed for this work. The base pressure achieved before processing was below $5x10^{-6}$ Torr and the temperature of samples (25x25 mm^2) was stabilized by substrate cooling (10 ^oC) during plasma processing. The first 193nm PR material studied was produced by Dow Electronics (DE) and is poly(methyl methacrylate) (PMMA) based. It was prepared in the form of blanket films (≈400 nm thick), or photoresist trench patterns (120 nm width, 240 nm pitch, 140 nm height) on top of 50 nm bottom antireflection coating. This 193nm PR contained photoacid generator and base and was spin-coated onto Si.

In addition to 193nm PR (DE), a 193 nm PR produced by JSR Corp. (Japan Synthetic Rubber Co) was investigated. 193nm PR (JSR) is poly(methyl methacrylate) (PMMA)-based, like 193nm PR (DE). While the basic polymer structure for 193nm PR (DE) is identical to 193nm PR (JSR) there are differences in the atomic composition and side groups. An anti-reflection coating (AR) is represented by a PMMA-based polymer with amidomethyl ether crosslinker. The thermally-activated hard mask (HM) is based on naphthalene. Near frictionless carbon (NFC) is used as an example for 248nm PR-type polymers with the main polymer chain being polystyrene. The extreme ultraviolet resist (EUV) is a positive-tone chemically amplified resist based on polymer-bound photoacid generator (PAG). The basic structure is a poly(methacrylate) with butyrolactone and ethyl-adamantyl side groups next to PAG. The chemical structures of these polymer

materials are shown in Fig. 2.2 as well as the insets of Figs. 2.5(a), 2.8(a), 2.11(a), 2.14(a), and 2.17(a).

Blanket films of these materials with an initial thickness of 200 nm, 100 nm, 100 nm, and 200 nm for 193nm PR (JSR), AR, HM, and NFC coated on Si, respectively, were employed. The EUV films were 60 nm thick and deposited on top of 75 nm of SiO_2.

To reduce plasma material interactions to ions and characteristic UV/VUV emission, we used the following approach: for the PPT we exposed materials to a high pressure, high density, unbiased helium plasma (800 W source power, $E_{ion} \leq 25$ eV, 100 mTorr pressure, 60 sccm gas flow, 11.6 mA cm^{-2} ion current density) for 60 s. These parameters were chosen because helium plasma has strong photon emission at a low wavelength (58.4 nm)[30] with minimal ion-induced surface densification due to low mass, low ion energy, and enhanced ion-collision processes in the plasma sheath for the higher pressure conditions chosen here. For PE, materials were exposed for 60 s to biased argon plasma (200 W source power, $E_{ion} \leq 125$ eV, 20 mTorr pressure, 55 sccm gas flow, 3.7 mA cm^{-2} ion current density). This condition was chosen because Ar^+ ion bombardment of the 193nm PR surface introduces changes in roughness similar to typical fluorocarbon/Ar plasma etching processes without the complexity introduced by fluorocarbon surface deposition.[25] Photon fluxes have not been characterized, but are estimated to be comparable to similar systems and on the order of 10^{16} cm^{-2} s^{-1} for PE and higher for PPT.[31] Our assumptions are that radiation modification, e.g. pendant group removal, dominates during PPT since absorption is strongly increased for reduced photon wavelengths.[25, 32, 33] During PE, ion bombardment dominates changes in material

properties and etching, where ion energies substantially exceed sputter threshold energies.[25]

Roughness formation was quantified by tapping mode atomic force microscopy (AFM, Veeco Dimension 3000 Atomic Force Microscope) at a fixed scan size of 1 x 1 μm^2. All pristine materials show a root-mean-square (RMS) surface roughness of ≈0.3 nm. We also performed *in-situ* ellipsometry (λ = 632.8 nm) operating in the polarizer-rotating compensator-sample-analyzer configuration to monitor changes in film thickness and index of refraction in real-time.[22] The optical model used to interpret measured Ψ-Δ values is based on ion and UV/VUV induced modifications is schematically shown in Fig. 2.3.[27, 34, 35] Superimposed grid lines in each figure, namely Figs. 2.6, 2.9, 2.12, 2.15, and 2.18, represent the optical model used. A 2 nm thick dense amorphous carbon (DAC) layer has been simulated on top of a 100 nm UV modified layer on top of pristine bulk material with variable thickness. Horizontal and vertical lines mark index changes of 0.1 of the DAC layer (n_{DAC}), including the corresponding change in extinction, and thickness intervals of the pristine bulk of 2 nm, respectively. In order to study bulk material modifications introduced by plasma processing, for example densification, pendant group removal, chain-scissioning, and cross-linking, the various polymer films were studied by Fourier-transform infrared spectroscopy (FTIR). FTIR was performed *ex-situ* after plasma treatments. Three characteristic absorbance bands were monitored by FTIR, i.e. the CH_x band (2800 to 3100 cm^{-1}) showing CH_2 and CH_3 groups, the C=O band (1600 to 1900 cm^{-1}), and the C-O-C band (1050 to 1350 cm^{-1}). The reported absorbance is measured by the area of each band after background subtraction. No additional normalization is made, since all measurements are taken in one series.

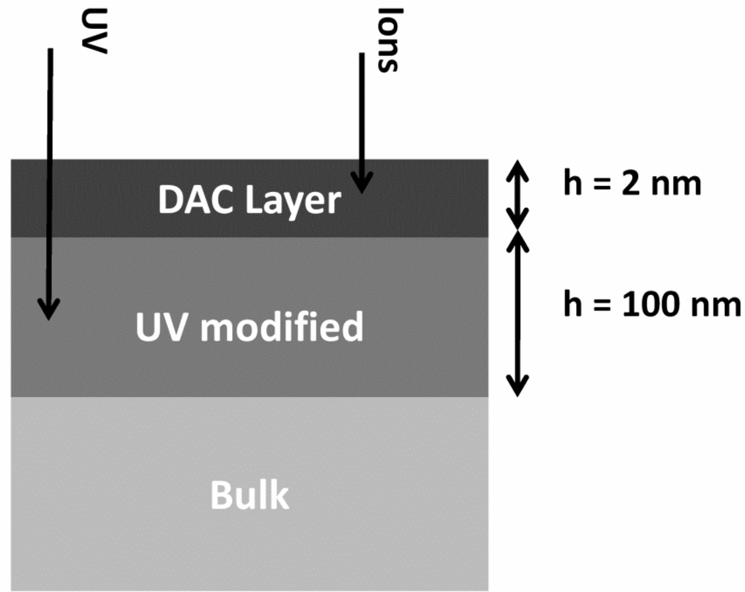

Fig. 2.3: The optical model used for real-time in-situ ellipsometry. A dense amorphous carbon (DAC) layer is simulated on top of a UV modified layer. The UV modified layer thickness is assumed to be only 50 nm, compared to 100 nm, for NFC due to a higher radiation absorption.

2.2.2 Ellipsometric Modeling, Extinction, and Refractive Index for a-C:H Like Materials

In order to model the *in-situ* ellipsometry trajectories for each material, a relationship between the imaginary and real part of the complex refractive index is necessary. To this end, we show in Fig. 2.4 the dependence of the extinction coefficient on the refractive index for a-C:H-like materials, e.g. the ion-modified layer formed during high energy Ar^+ ion bombardment. A literature survey was performed to collect this information[36-40], and a great deal of data was taken from an extensive study by Dowling *et al.*.[41] Since this study was conducted over 15 years ago, the original data set is not currently available in digital form (personal communication with the author), and the data were obtained from the published plot.

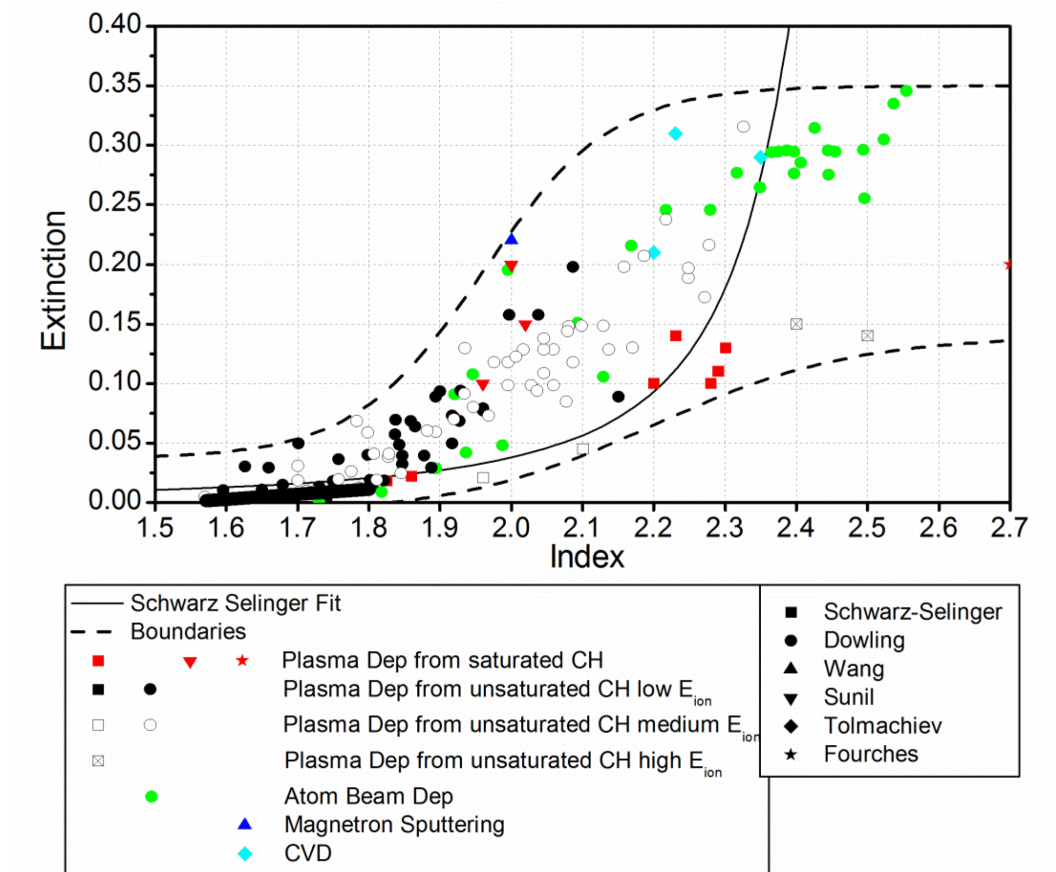

Fig. 2.4: Extinction coefficient dependent on refractive index for various a-C:H like materials. The type of deposition is indicated by color, the publishing author by symbol. Also shown is the correlation established by Schwarz-Selinger[13] as well as upper and lower boundaries for the extinction coefficient for a given refractive index.

Figure 2.4 shows that the amorphous hydrogen-containing carbon extinction coefficient increases as the real part of the index increases. Due to a variety of effects, especially variations in sp^2/sp^3 bond ratio, the extinction coefficient can change significantly for a given real part of the refractive index.[39] Minimum and maximum values of extinction coefficient depending on the real part, *n*, of the refractive index are included in Fig. 2.4 and employed for the optical multi-layer simulations performed in this work as described above in Section II A.

2.3 Results

For each material, surface roughness and etch rates will be discussed for each of the plasma processes, i.e. PE, PPT, and PPT + PE. Subsequently bulk material modifications introduced during processing are presented. Finally, we will compare the response of each material to each other.

2.3.1 193nm Photoresist

The He PPT successfully breaks the synergy-based roughness formation for 193nm PR (DE) and reduces surface roughness, line width roughness and line edge roughness in addition to stabilizing critical dimensions and increasing etch resistivity.[1] To examine the question if this behavior is generic for PMMA-based 193nm PRs, 193nm PR (JSR) produced by JSR, was investigated. 193nm PR (JSR) shows qualitatively the same behavior as 193nm PR (DE) in terms of surface roughness reduction and etch resistance improvement as a result of PPT. Figure 2.5 shows that the RMS surface roughness is reduced from 6.6 nm to 5.3 nm when applying the PPT. The surface morphology seen after PE and PPT + PE is similar for 193nm PR (DE) and 193nm (JSR). Therefore, the PPT approach appears generic for the PMMA and other characteristic side-groups found in 193nm PR materials. In the following, we will only show 193nm PR (DE) results since trends with process conditions were the same for 193nm (JSR).

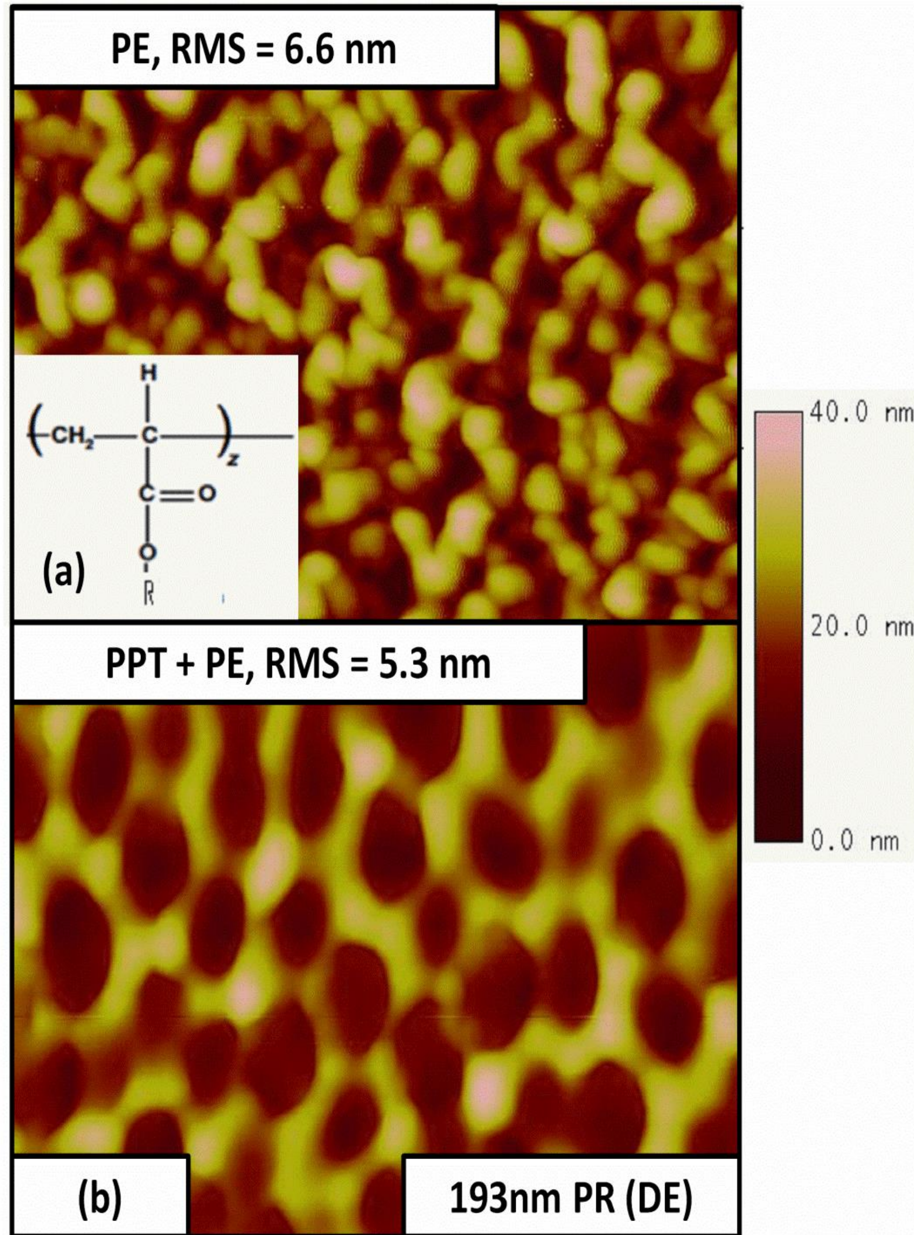

Fig. 2.5: AFM of 193nm PR (DE) (a) after PE and (b) after PPT + PE. PPT reduces surface roughness and increase typical feature size. The inlet in (a) shows the basic poly(methyl methacrylate) structure of 193nm PR.

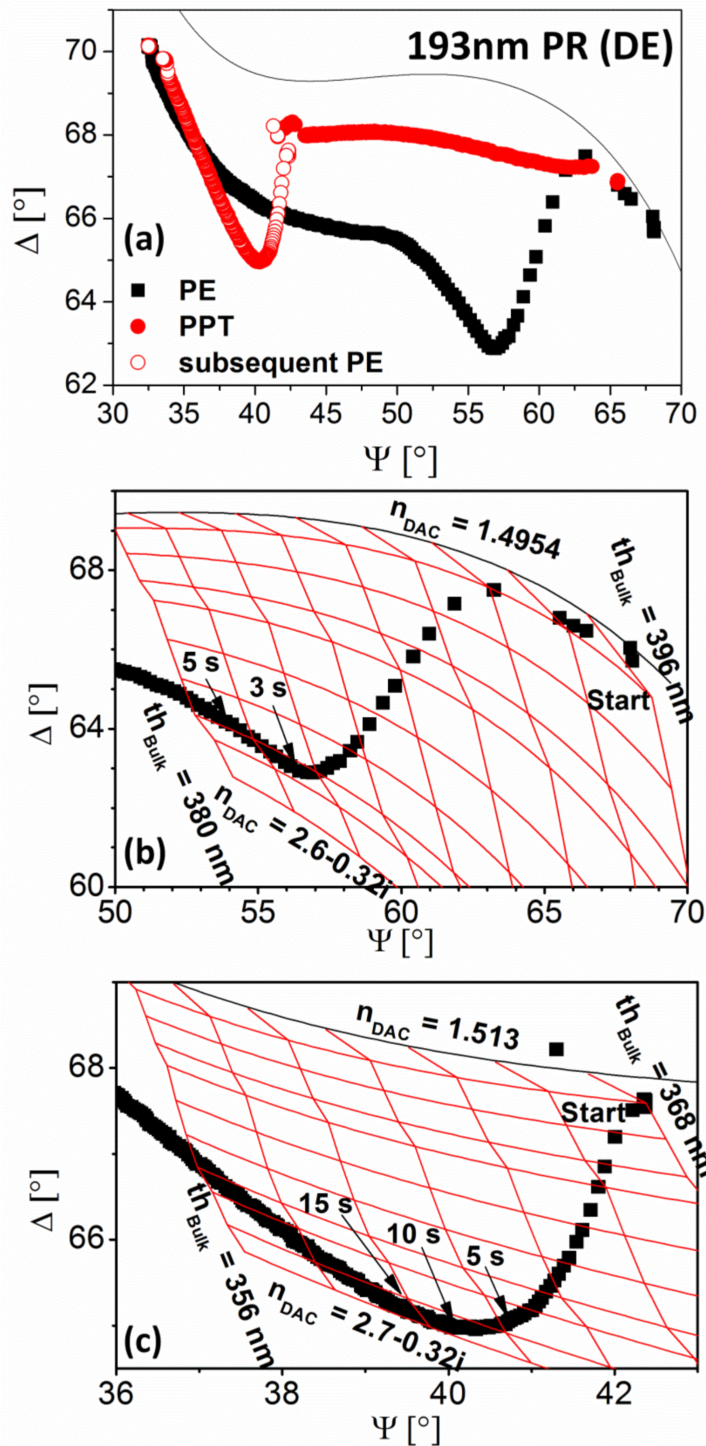

Fig. 2.6: : Real-time *in-situ* ellipsometry for 193nm PR (DE) (a) during PE, PPT, and PPT + PE with a pristine reference line, (b) of DAC layer formation during PE, and (c) of DAC layer formation during PE following PPT.

For PE alone, 53 nm of material are removed while a RMS surface roughness of 6.6 nm is introduced. As PPT does not subject materials to significant ion bombardment, no dense amorphous carbon (DAC) layer is formed during PPT (see trajectory in Fig. 2.6 (a)). However, a film thickness loss of 28 nm and slight densification is observed and can be explained by the effect of UV/VUV radiation on the materials studied.[1] The total material removal after PPT and subsequent PE is 50 nm. This shows that the etch rate during PE is significantly reduced from 53 nm/min to 22 nm/min upon application of He PPT. Fig. 2.6 (a) shows that Ψ-Δ trajectories end at nearly the same location after PE with or without prior PPT. This shows that the total thickness loss and modification are comparable for both processes. To highlight DAC layer formation during the initial seconds of each PE, with and without prior PPT, Ψ-Δ trajectories are shown in part (b) and (c) of Fig. 2.6. 193nm PR shows a clear densification by ion bombardment as the DAC layer is formed, reflected as a rapid Ψ-Δ shift towards lower values of Δ in Fig. 2.6 (b) and (c). Since the ellipsometry measurement averages over a comparably large area, and the characteristic surface roughness feature size is much smaller than the optical wavelength used here, roughening of the surface region manifests itself as a decrease in density in the Ψ-Δ trajectory. This explains the apparent decrease in density (increase of Δ) observed after the initial densification. The thickness loss and surface roughness results are summarized in Fig. 2.7 (a).

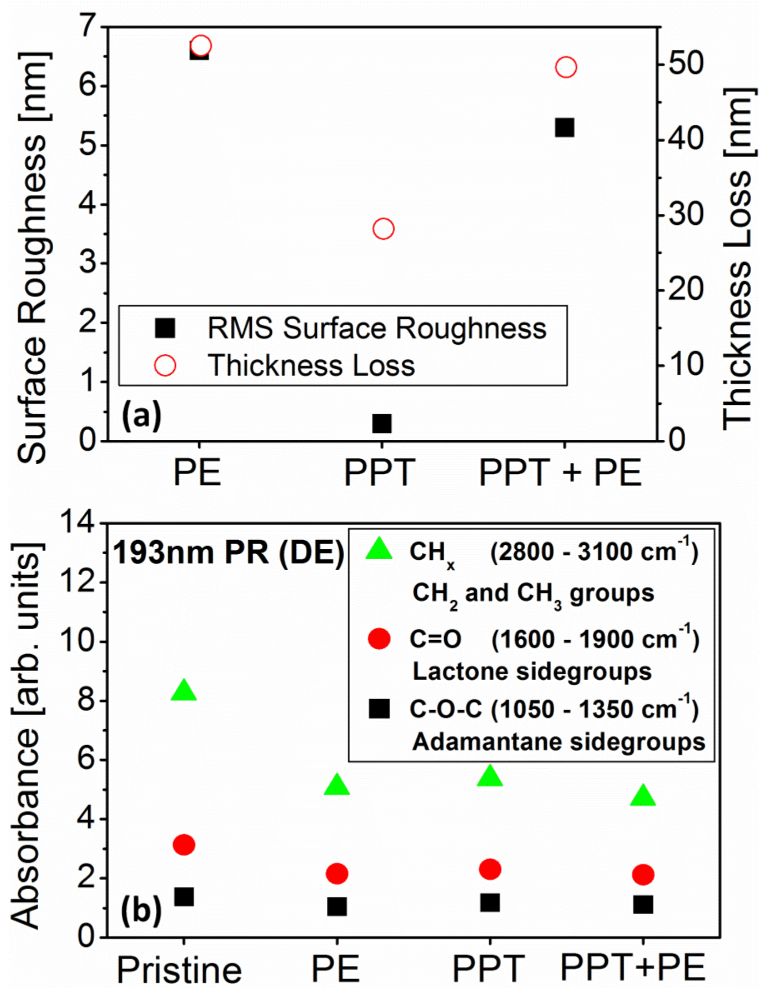

Fig. 2.7: (a) RMS surface roughness, material removal and (b) FTIR absorbance of three characteristic bands for 193nm PR (DE) for pristine material and after each process.

The PPT temporally separates material modifications due to UV/VUV radiation from ion bombardment, thus breaking the synergistic interaction and reducing surface roughness introduction.[1, 26, 27] This observation is in agreement with FTIR results presented previously.[1] Figure 2.7 (b) shows the absorbance of the CH_x band (2800 to 3100 cm^{-1}), C=O band (1600 to 1900 cm^{-1}), and C-O-C band (1050 to 1350 cm^{-1}) for each process. The main attribution to the C=O band is a peak at ≈1796 cm^{-1} corresponding to lactone.[42] A clear composition change with processing can be seen for 193nm PR (see Fig. 2.7 (b)). Previous work has shown that modifications of 193nm PR

increase with PPT exposure time and saturate at similar levels to modifications after PE, which are independent of prior PPT exposure time.[1] The C=O band was reduced for 193nm PR as a result of PPT, and has been explained by the UV/VUV radiation sensitivity of the lactone group, since UV/VUV radiation leads to strong pendant group removal, especially lactone (C=O band reduction), adamantane (C-O-C band reduction), and severe oxygen loss.[32] The overall bulk softening due to chain scissioning during PPT is the reason for its beneficial effects.[1, 32, 43]

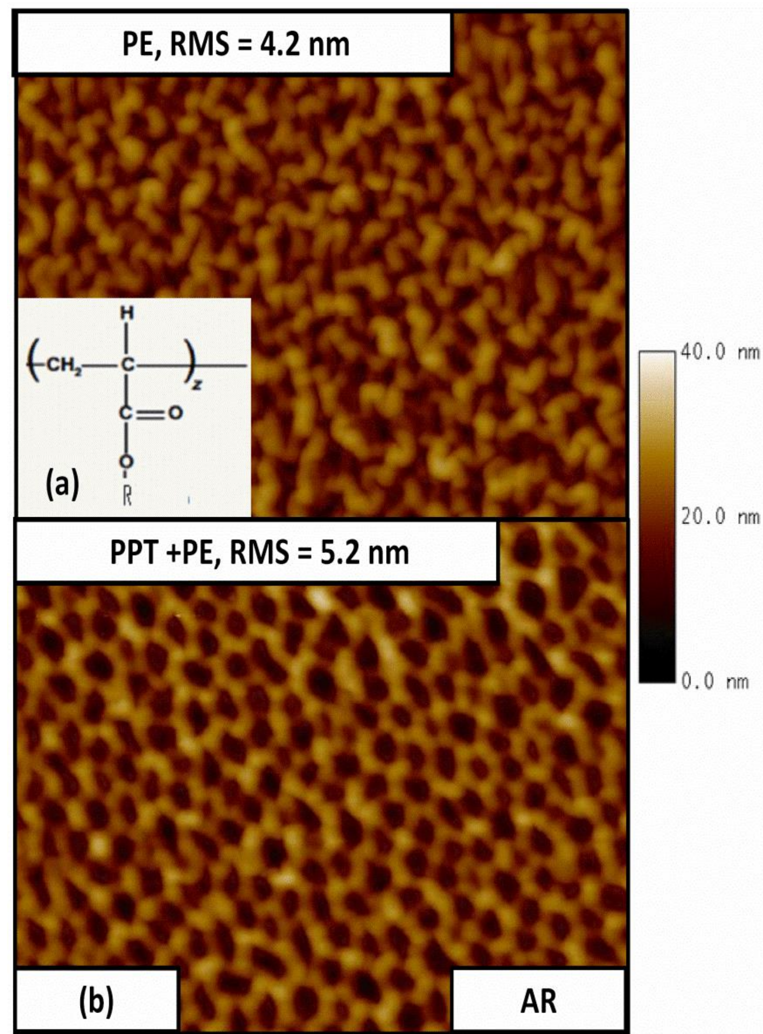

Fig. 2.8: AFM of AR (a) after PE and (b) after PPT + PE. The inlet in (a) shows the basic poly(methyl methacrylate) structure of AR. The PPT slightly enhance surface roughness and changes the morphology.

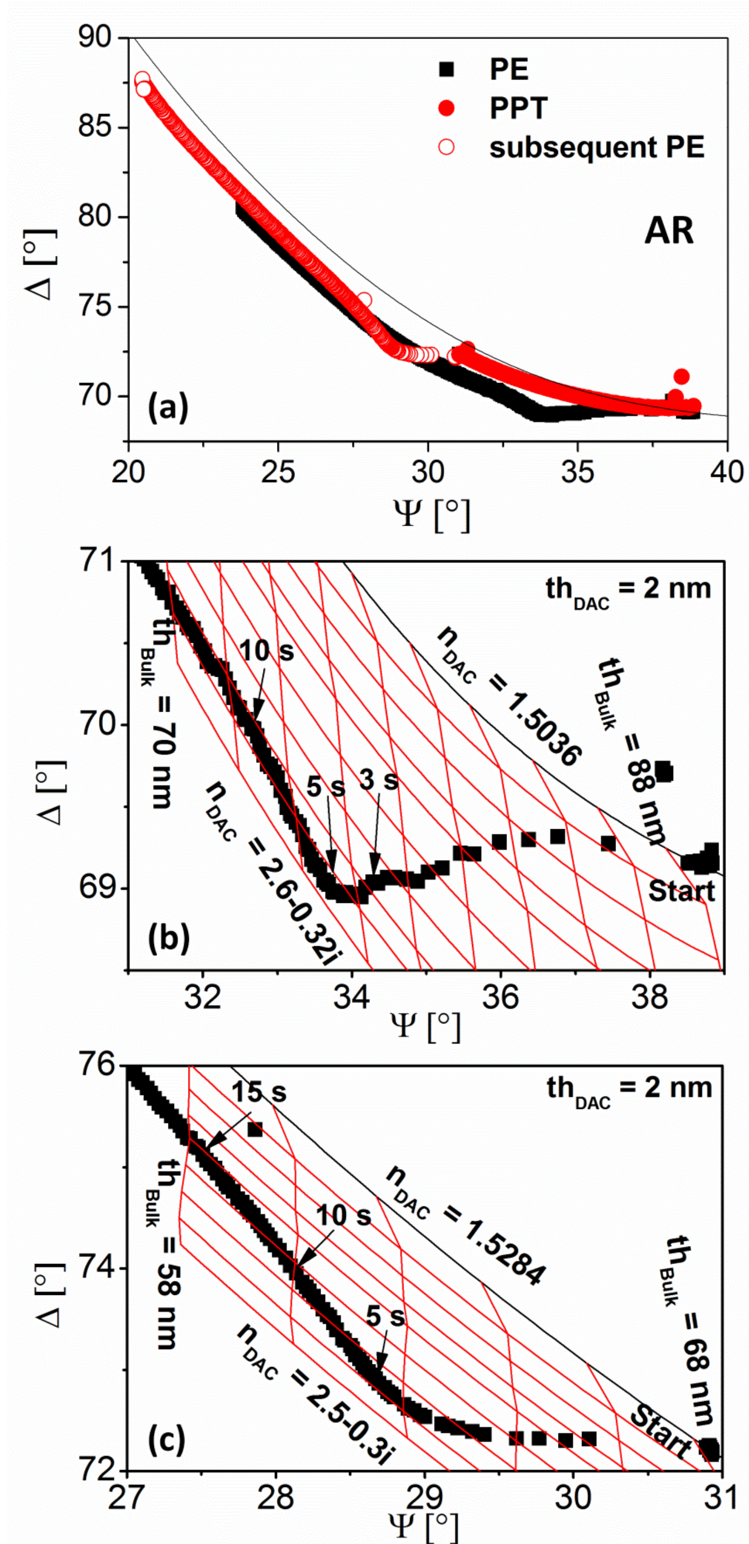

Fig. 2.9: Real-time *in-situ* ellipsometry for AR (a) during PE, PPT, and PPT + PE with a pristine reference line, (b) of DAC layer formation during PE, and (c) of DAC layer formation during PE following PPT.

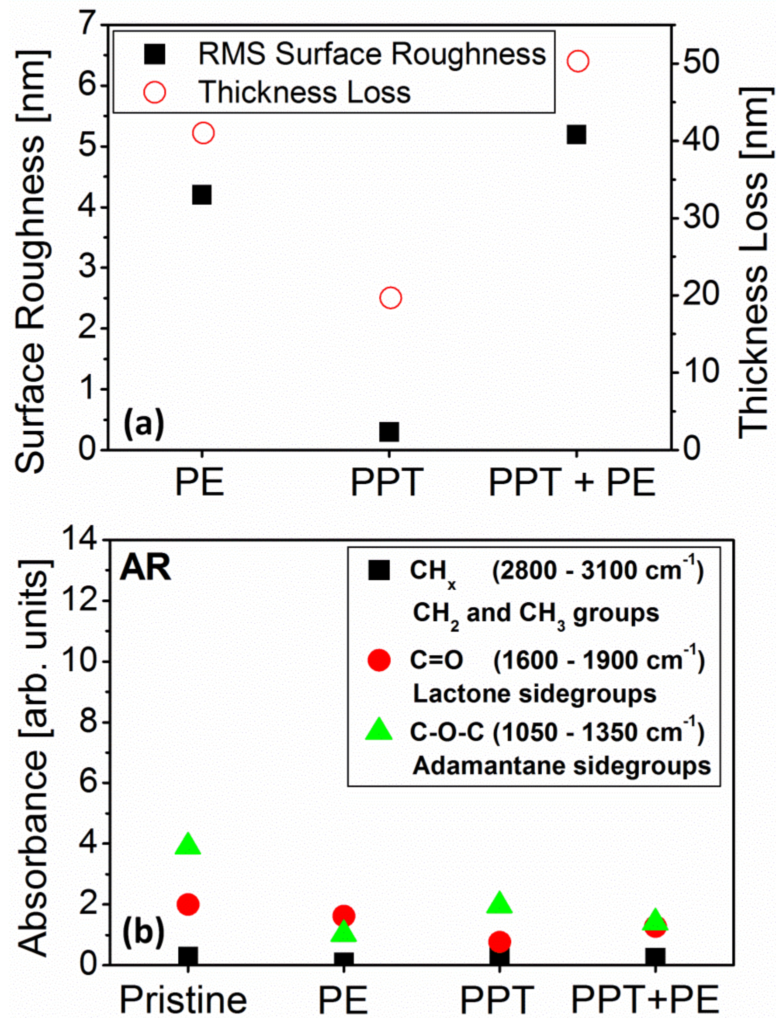

Fig. 2.10: (a) RMS surface roughness, material removal and (b) FTIR absorbance of three characteristic bands for AR for pristine material and after each process.

2.3.2 Anti-Reflection Coating

The impact of the He PPT approach on a PMMA-based anti-reflection coating (AR), an essential part of multilayer resist stacks, was explored. PE shows clear roughness introduction (RMS of 4.2 nm) as displayed in Fig. 2.8 (a). Ψ-Δ trajectories measured during PE or PPT + PE composite processes are shown in Fig. 2.9 (a). During PE, 40 nm of material are removed. During the PPT step 20 nm are etched and no surface roughness is introduced. The surface roughness after PPT + PE increases to a RMS value

of 5.2 nm with a total material removal of 50 nm. The etch rate during PE after PPT is reduced, 30 nm/min compared to 40 nm/min, and a clear change of the surface morphology can be seen. The trajectories are similarly displaced compared to a pristine reference line, see Fig. 2.9 (a), showing that the densification after PE is similar to after PPT + PE. UV/VUV radiation during PPT causes thickness reduction and slight densification. These changes are summarized in Fig. 2.10 (a). During the initial 5 s of PE exposure rapid densification forms the DAC layer, as seen by a strong decrease in Δ in Fig. 2.9 (b). Similarly to 193nm PR, a slight decrease in density is seen after the DAC layer forms, likely due to surface roughness formation. This decrease is stronger for PPT + PE, agreeing with the higher surface roughness seen in that case.

FTIR measurements of AR do not show the same clear bulk material changes as seen for 193nm PR. This is shown in Fig. 2.10 (b), and suggests a lower UV/VUV sensitivity of this material. There is no lactone peak ($\approx$1796 cm^{-1})[42] observed in the C=O band for AR in contrast to 193nm PR (DE). A strong reduction in the C-O-C band is seen as a result of each process.

2.3.3 Hard Mask

Naphthalene is the main polymer type of the hard mask (HM) used in this work. Figure 2.11 and 2.12 show AFM images and *in-situ* ellipsometry trajectories for all processes, respectively. The RMS surface roughness for HM was always less than 0.5 nm without any significant surface morphology change for PE, PPT, and PPT + PE, see Fig. 2.11 (a) and (b). For comparison, pristine samples show a RMS surface roughness of 0.3 nm. The PE did not introduce any significant surface roughness while 26 nm of material were removed. During the PPT slightly less material (20 nm) is removed. The total

material removed after PPT + PE is 48 nm. The etch rate during subsequent PE after PPT is similar to PE without a PPT application. The combined, total material modification after PE and after PPT + PE is similar as can be seen by a similar displacement of the Ψ-Δ trajectory in Fig. 2.12 (a). PE leads to a significant DAC layer formation within 5 s of exposure, see Fig. 2.12 (b). Despite having no significant impact on surface roughness, applying the He PPT clearly changes the DAC layer formation as the resulting DAC layer is less dense. The surface roughness and material removal are summarized in Fig. 2.13.

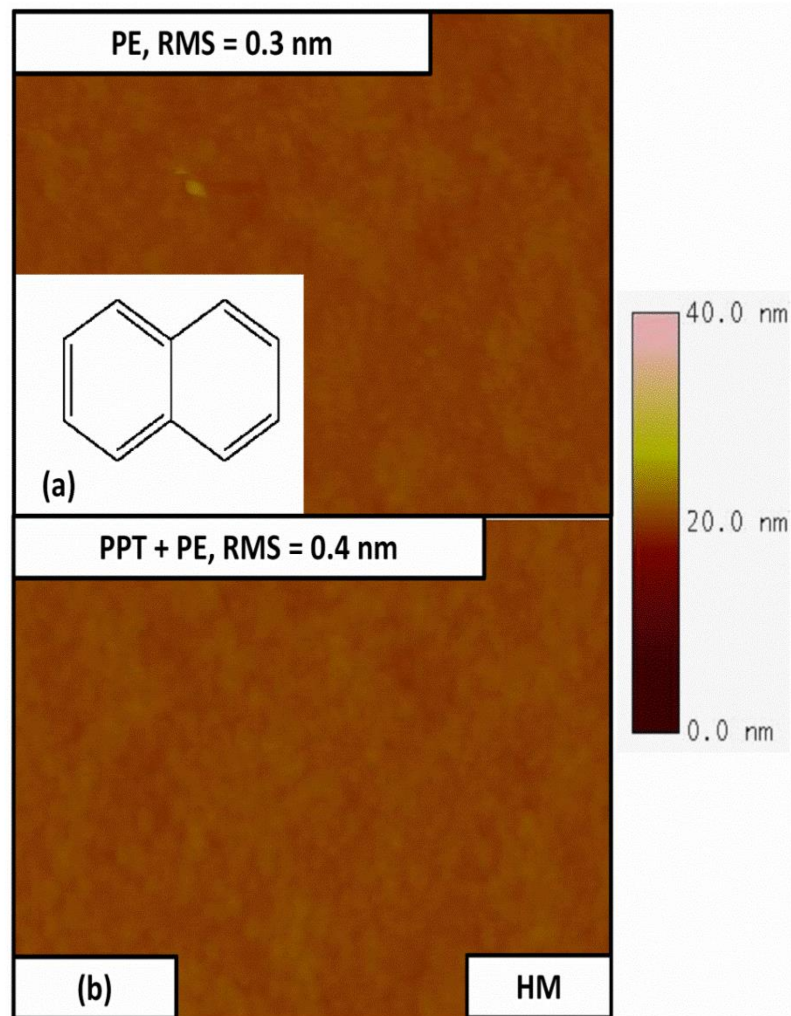

Fig. 2.11: AFM of HM (a) after PE and (b) after PPT + PE. The inlet in (a) shows the basic naphthalene structure of HM. Plasma processing shows minimal impact on HM.

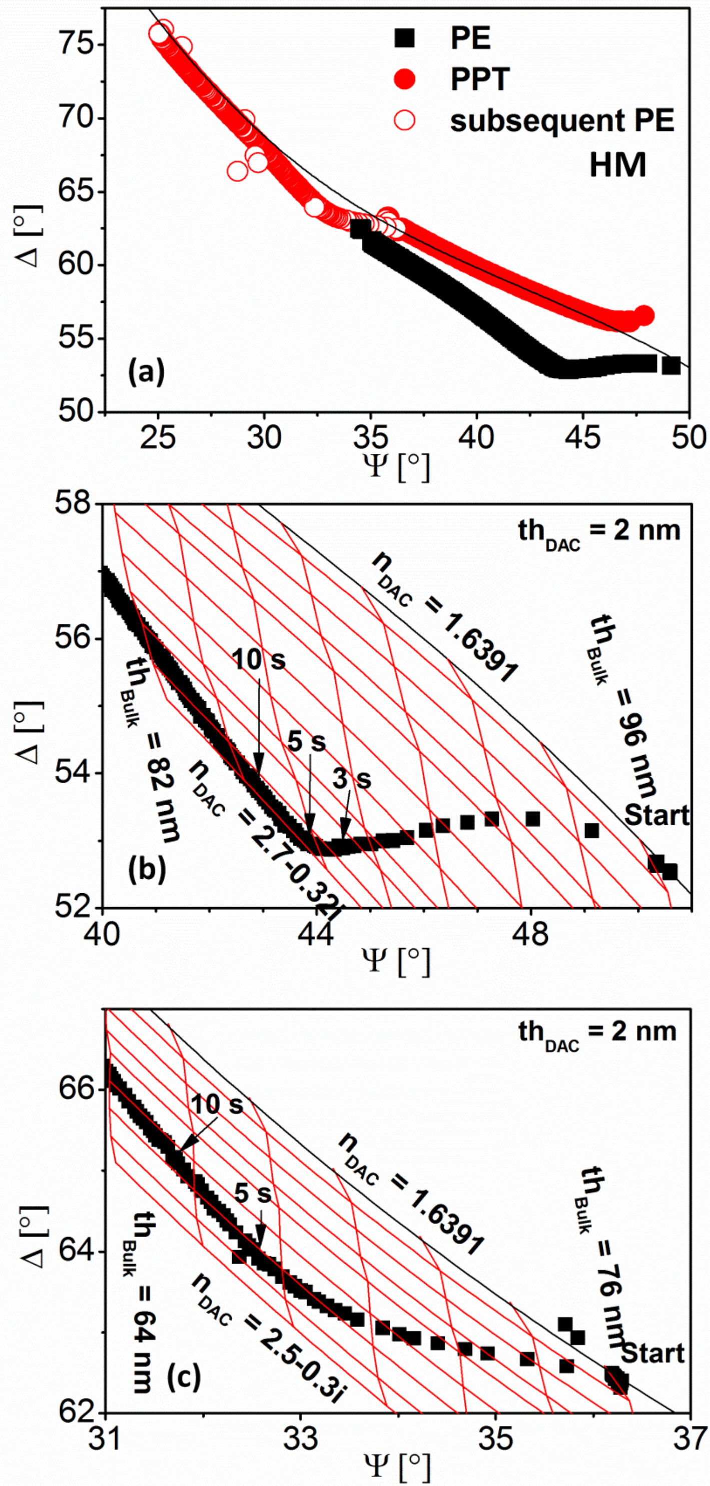

Fig. 2.12: Real-time *in-situ* ellipsometry for HM (a) during PE, PPT, and PPT + PE with a pristine reference line, (b) of DAC layer formation during PE, and (c) of DAC layer formation during PE following PPT.

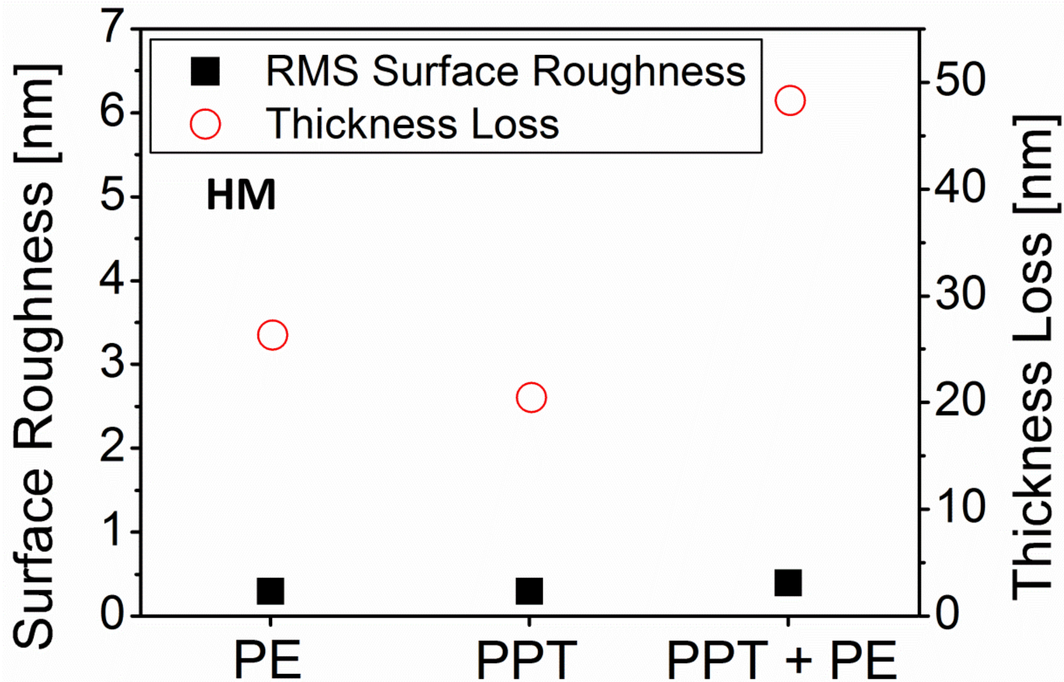

Fig. 2.13: RMS surface roughness and material removal for HM after each process.

2.3.4 Near Frictionless Carbon

248nm photoresists are typically composed of aromatic ring structures, such as polystyrene, and show low roughness introduction upon plasma processing.[34] Polystyrene-based near frictionless carbon (NFC) is employed in this work as a 248nm photoresist-like material to examine the impact of the He PPT approach. Please note that the radiation penetration depth is less for NFC than for other materials considered due to a higher absorption.[33] To represent this in the optical model, the thickness of the UV modified layer is assumed to be only 50 nm for NFC, [33] compared to 100 nm for all other materials. A RMS surface roughness of 0.7 nm is introduced during PE while 23 nm of material are removed. The PPT itself does not introduce surface roughness and etches only 1 nm. Figure 2.14 (b) shows that applying a PPT prior to PE slightly enhances the RMS surface roughness to 1.1 nm while also increasing the etch resistivity leading to a total material removal of 12 nm after PPT + PE. These changes are summarized in Fig.

2.16 (a). The overall high etch resistivity can be explained by an inherently lower oxygen content of NFC.[34] Figure 2.15 (b) shows that the DAC layer is established within 5 s of ion bombardment. After this rapid densification, there appears to be ongoing further densification throughout the PE treatment. PPT significantly alters the Ψ-Δ trajectory of NFC. A substantial DAC layer is still formed during the initial PE after PPT application. However, an apparent thickness increase in the form of an S-like trajectory is seen in Fig. 2.15 (c).

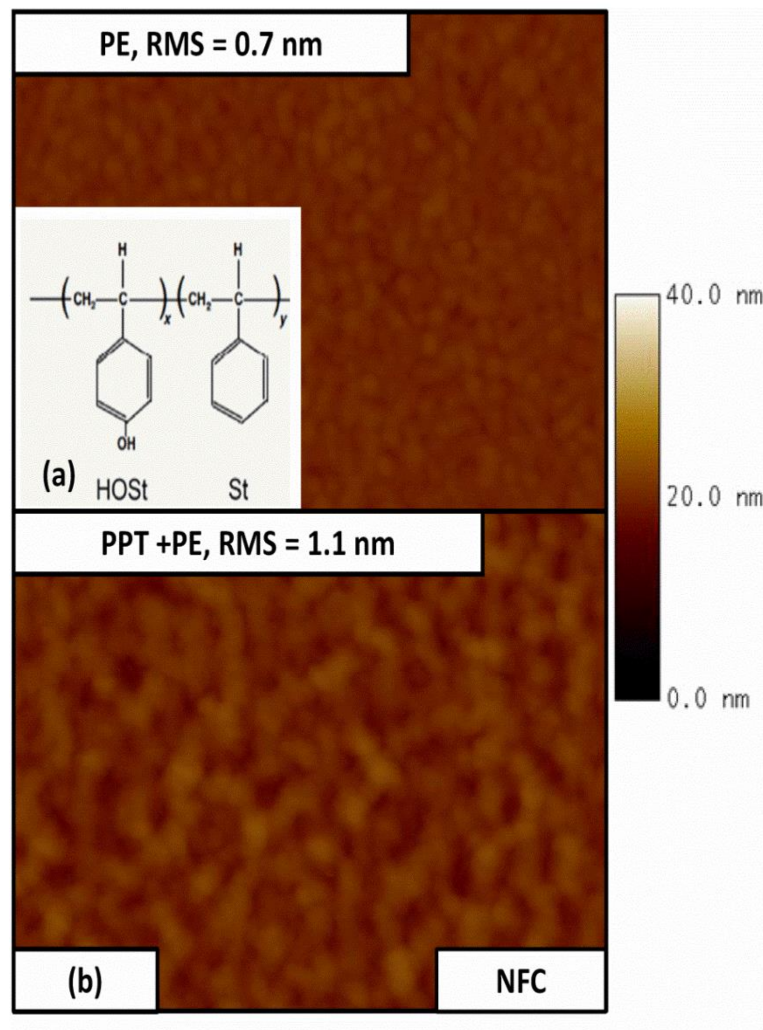

Fig. 2.14: AFM of NFC (a) after PE and (b) after PPT + PE. The inlet in (a) shows the basic polystyrene structure of NFC. The surface roughness is overall very low but slightly enhance with PPT.

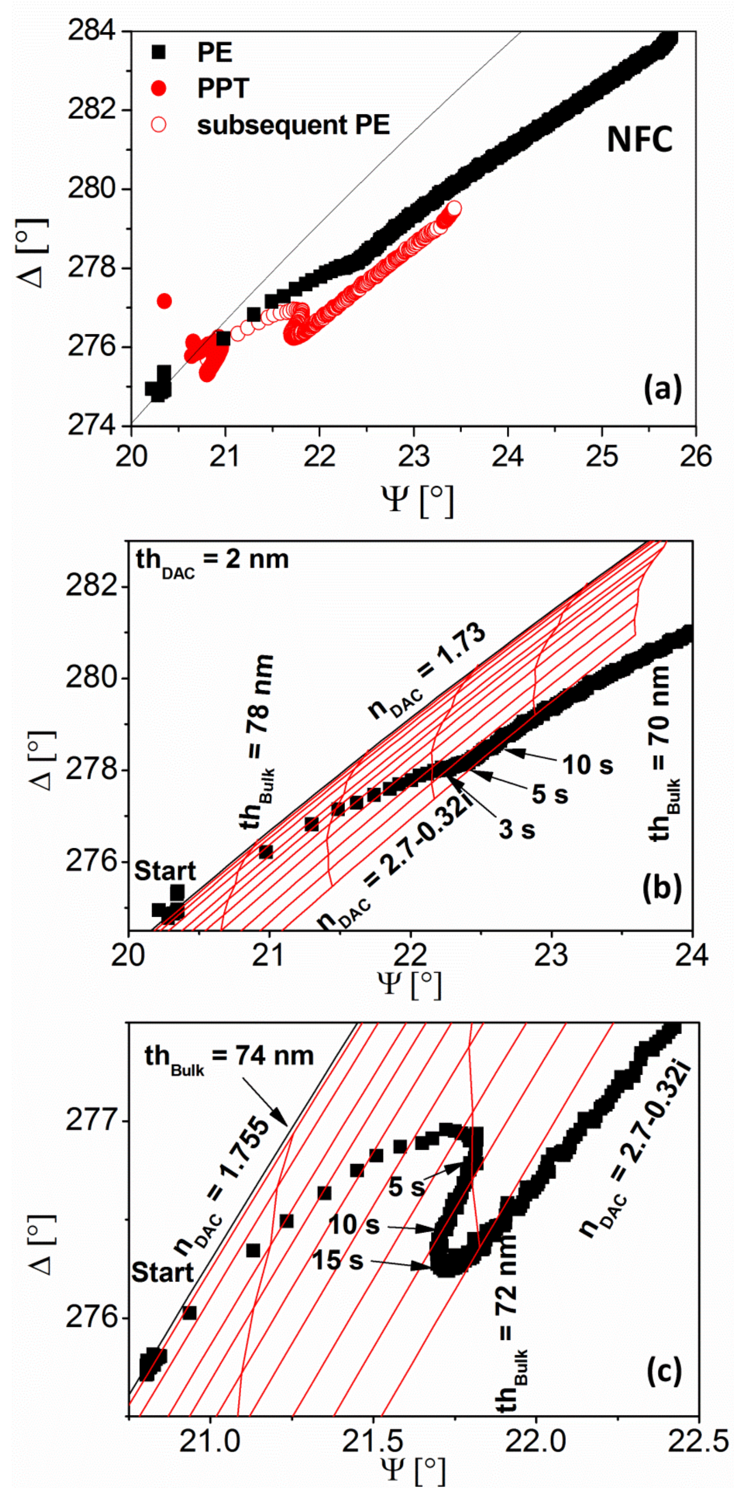

Fig. 2.15: Real-time *in-situ* ellipsometry for NFC (a) during PE, PPT, and PPT + PE with a pristine reference line, (b) of DAC layer formation during PE, and (c) of DAC layer formation during PE following PPT.

The relative amount of C-O-C bonds is increased during PE, as has been reported before for 248nm PRs with a similar polystyrene structure.[32] NFC has a low oxygen content and does not show a significant C=O band, i.e. no lactone structure. This leads to a high radiation stability and therefore only a small response to the PPT, as can be seen in Fig. 2.16 (b). There is however a clear impact of the PPT on the PE. The C-O-C band signal is significantly lower after PPT + PE compared to after PE. The high radiation stability also explains the overall low surface roughness.[32, 34]

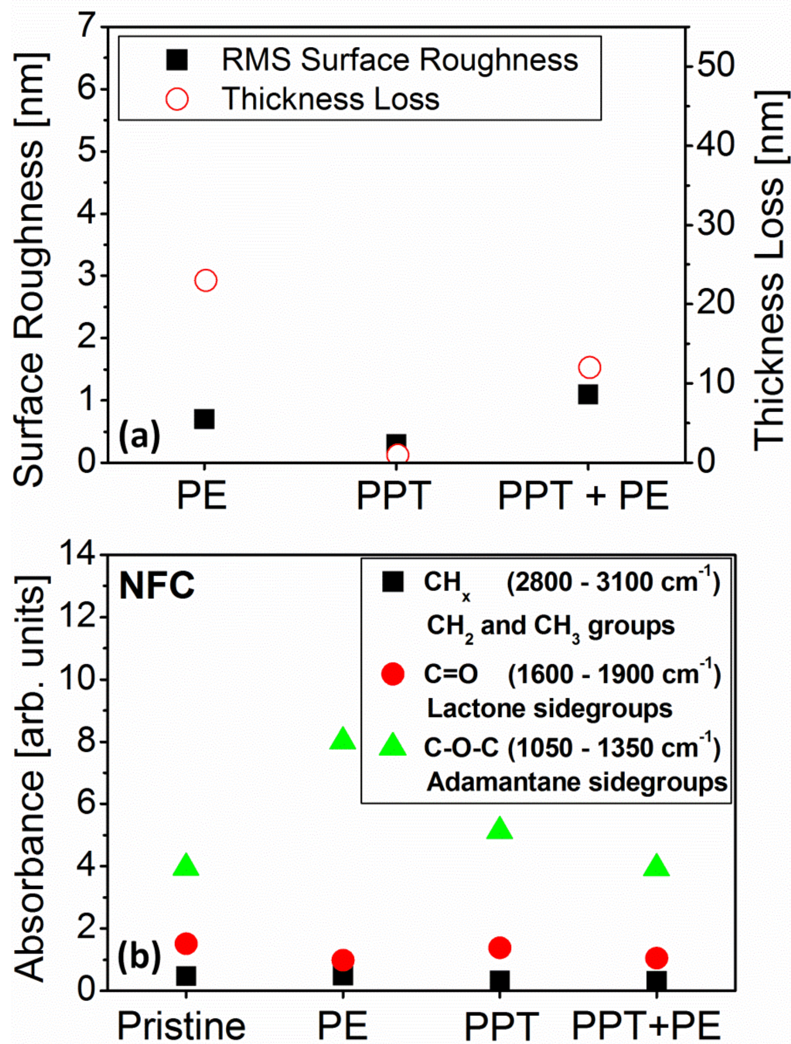

Fig. 2.16: (a) RMS surface roughness, material removal and (b) FTIR absorbance of three characteristic bands for NFC for pristine material and after each process.

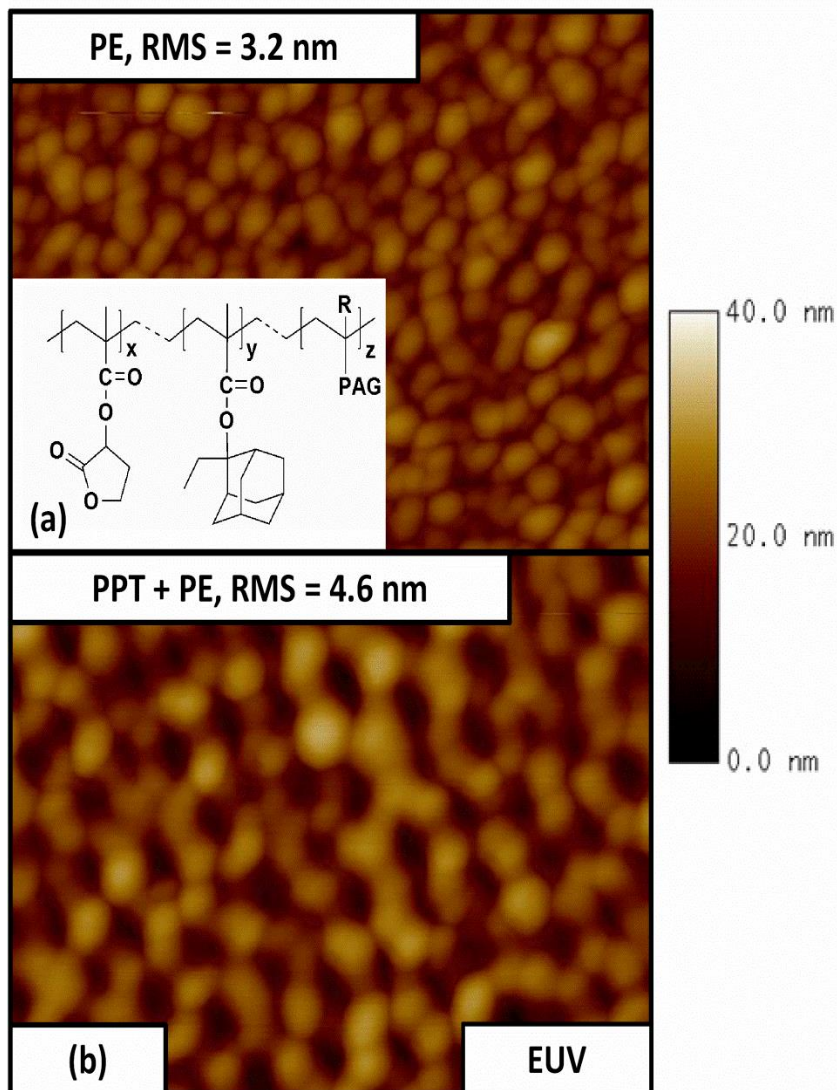

Fig. 2.17: AFM of EUV (a) after PE and (b) after PPT + PE. The inlet in (a) shows the basic poly(methacrylate) structure of EUV with butyrolactone and ethyl-adamantyl sidegroups. PPT enhances the surface roughness and changes surface morphology.

2.3.5 Extreme Ultraviolet Resist

An extreme ultraviolet (EUV) resist[44] was examined to evaluate if the application of the PPT approach to the EUV material is beneficial in terms of surface roughness introduction. The material used in this work is based on polymer bound-PAG (PBP) which can improve line width roughness (LWR).[45] In order to reduce transmittance,

fluorine is incorporated into the alycyclic polymer. AFM and i*n-situ* ellipsometry for plasma-processed EUV are shown in Figs. 2.17 and 2.18, respectively. The RMS surface roughness introduction during PE is moderate at 3.2 nm, see Fig. 2.17 (a), while 41 nm of material are etched. The morphology is similar to 193nm PR. Applying the He PPT does not introduce surface roughness and removes 10 nm of material. The RMS surface roughness after PPT + PE is increased to 4.6 nm with a larger average feature size. The total material removed after PPT + PE is 30 nm, less than during PE only. Figure 2.18 (b) and (c) show a clear DAC layer formation during PE and PE after PPT, with a fast, strong densification. The DAC layer is established within 4 s before a slight decrease in density is observed. The PPT results in a significantly denser DAC layer during subsequent PE, as is apparent from Fig. 2.15. The denser DAC layer is a likely explanation for the enhanced surface roughness. This behavior is summarized in Fig. 2.19 (a)

No significant C=O band, but a comparably high C-O-C signal is observed for EUV, see Fig. 2.19 (b). PE of EUV results in minor bulk material modifications. PPT slightly increases the already high C-O-C band signal and decreases the C=O band. The total bulk material modifications after PPT + PE are a combination of the individual processes, with the C-O-C as well as the C=O band signal increased.

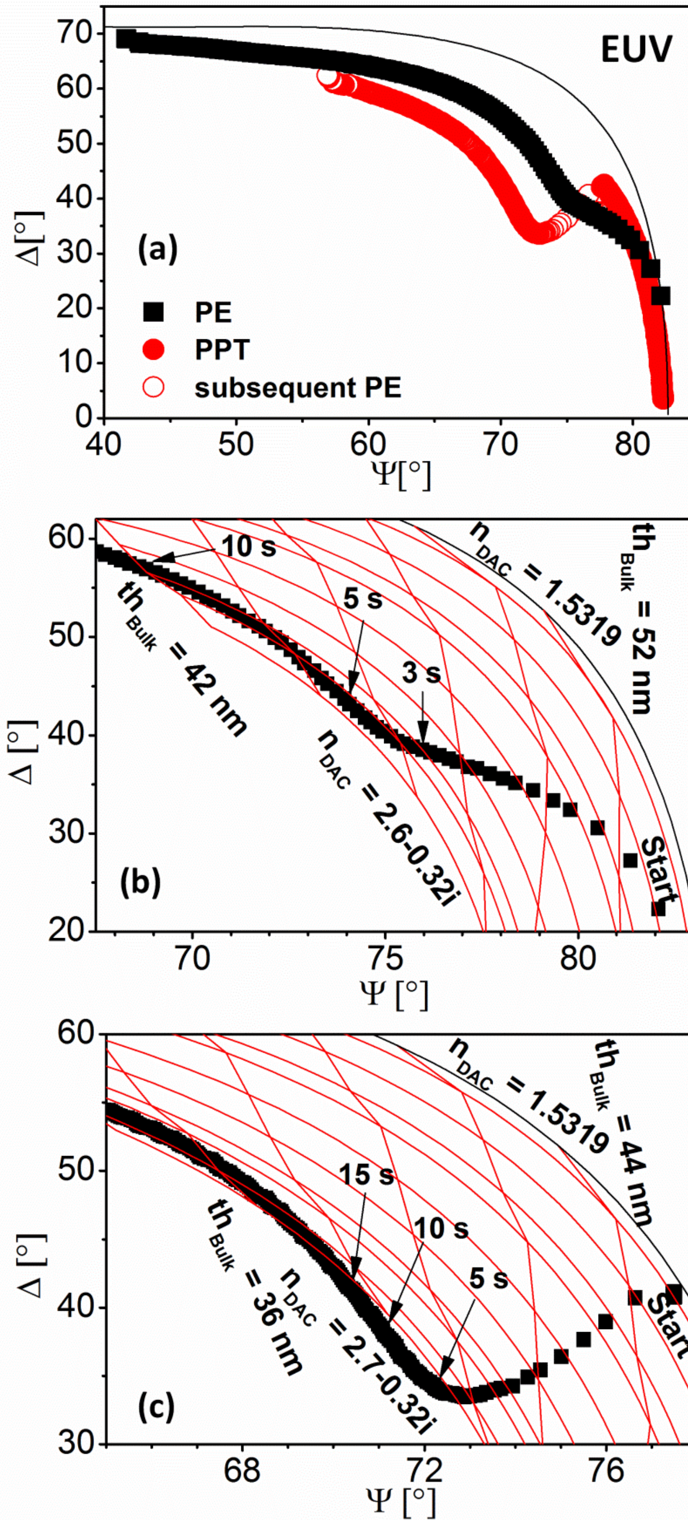

Fig. 2.18: Real-time *in-situ* ellipsometry for EUV (a) during PE, PPT, and PPT + PE with a pristine reference line, (b) of DAC layer formation during PE, and (c) of DAC layer formation during PE following PPT.

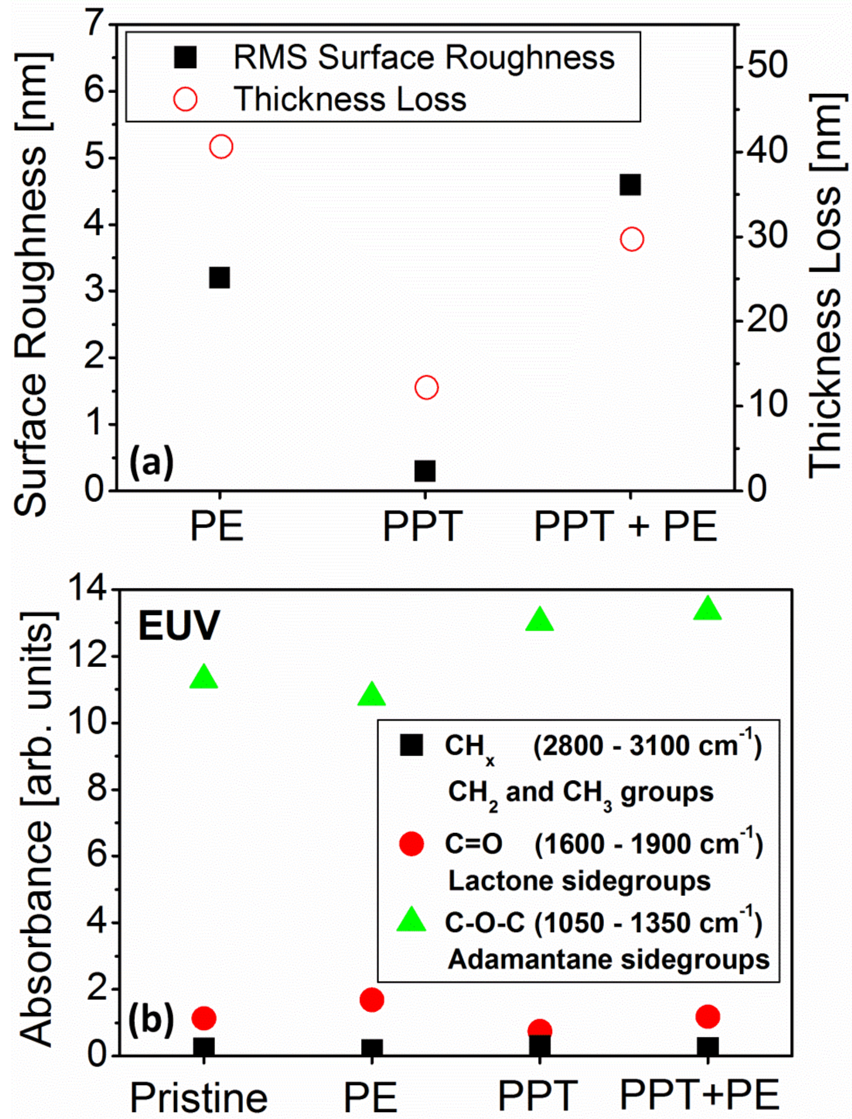

Fig. 2.19: (a) RMS surface roughness, material removal and (b) FTIR absorbance of three characteristic bands for EUV for pristine material and after each process.

2.3.6 Comparison of all materials

Table 2.1 and 2.2 summarize the material loss, surface roughness, and average wavelength from the power spectral density distribution for all materials studied in this work. All multilayer stack materials studied in this work show generally less surface roughness than 193 nm PR, especially HM and NFC. In contrast to 193nm PR (DE), surface roughness of AR, NFC, and EUV is slightly increased by PPT while 193nm

(JSR) exhibits a similar roughness improvement. There is, in addition to the change in surface roughness, also a clear impact on the surface morphology when applying PPT prior to PE. Applying only the PPT does not introduce surface roughness on any material.

Material	Thickness		PE	PPT	PPT + PE
	Start [nm]	DAC Layer [nm]	Thickness loss [nm]	Thickness loss [nm]	Thickness loss [nm]
193nm PR (DE)	400	2	49	29	51
193nm PR (JSR)	200	2	53	28	50
AR	100	2	41	20	50
HM	100	2	26	48	48
NFC	200	2	23	1	12
EUV	60	2	41	30	30

Table 2.1: Thickness loss for all materials and processes.

Material	PE		PPT		PPT + PE	
	RMS Surface Roughness [nm]	Average Wavelength [nm]	RMS Surface Roughness [nm]	Average Wavelength [nm]	RMS Surface Roughness [nm]	Average Wavelength [nm]
193nm PR (DE)	7.8	95	0.3	334	4.4	120
193nm PR (JSR)	6.6		0.3	334	5.3	
AR	4.2	63	0.3	334	5.2	59
HM	0.3	505	0.3	334	0.4	168
NFC	0.7	250	0.3	505	1.1	100
EUV	3.2	78	0.3	334	4.6	100

Table 2.2: Surface roughness and average wavelength of the power spectral density distribution for all materials and processes.

Along with the lowest surface roughness, HM and NFC also show the lowest etch rates during PE. Film thickness loss and slight densification during PPT is observed for all materials and can be explained by the effect of UV/VUV radiation on the materials studied.[1] NFC and EUV exhibit a lower etch rate during PPT than 193nm PR, AR, and HM, as seen in Table 2.1, which can be explained by the lower oxygen content of these two materials.[34] Similarly, for NFC and EUV less material has been removed after PPT + PE than 193nm PR, AR, and HM. All materials except HM showed a decrease in etch rate during PE upon PPT application. The difference in index of refraction of the DAC layer after PE relative to the pristine material is comparable for all materials considered. In contrast, the difference in index of refraction of the DAC layer in comparison to pristine material varies significantly after PPT + PE. HM shows a greatly reduced DAC

layer index of refraction, while 193nm PR and EUV on the other hand exhibit a higher DAC layer index of refraction after PPT and PE. After the DAC layer is established, each material shows a trend towards higher values of Δ, indicating a less dense material, opposite to the initial DAC layer formation. Formation of surface roughness is the most likely explanation, although there may be other possible explanations, especially for HM. PPT leads to an increase in etch resistivity during PE for 193nm PR,[1] AR, NFC, and EUV. HM does not show a significant impact of PPT on the etch rate during subsequent PE.

Material	Band	Absorbance [arb. units]			
		Pristine	PE	PPT	PE + PPT
193nm PR (JSR)	CH_x	1.4	1.1	1.2	1.1
	C=O	3.1	2.2	2.3	2.1
	C-O-C	8.3	5.1	5.4	4.7
AR	CH_x	0.3	0.1	0.3	0.2
	C=O	2.0	1.6	0.8	1.3
	C-O-C	3.9	1.0	2.0	1.4
NFC	CH_x	0.5	0.5	0.3	0.3
	C=O	1.5	1.0	1.4	1.0
	C-O-C	3.9	8.0	5.1	3.9
EUV	CH_x	0.2	0.2	0.3	0.2
	C=O	1.1	1.7	0.7	1.2
	C-O-C	11.3	10.8	13.0	13.4

Table 2.3: Summary of FTIR absorbance for all materials and processes.

The absorbance as measured by FTIR is summarized for all materials and processes explored in table 2.3. Comparing the absorbance of the three characteristic bands for 193nm PR (DE), AR, NFC, and EUV demonstrates that the PPT has a much smaller impact for the other materials than for 193nm PR. NFC and EUV show overall a small impact of plasma processing on the FTIR signature. EUV shows the highest C-O-C band signal as well as a largest increase in index of refraction during PPT across all materials examined. In contrast to 193nm PR, none of the other materials show a UV/VUV sensitive lactone peak and an overall lower C=O band signal, leading to a higher radiation stability. Since the strong UV/VUV modifications are absent for the investigated materials besides 193nm PR, there is a lack of synergistic interaction with the introduction of the densified surface layer. This synergy is the root cause of the pronounced surface roughness introduction for 193nm PR.[26, 27] The lack of this moiety makes it plausible therefore, that the PPT does not provide the same improvements for other organic masking materials as it does for PMMA-based photoresists, especially with regard to surface roughness introduction. The absence of dramatic changes in plasma etch characteristics of AR, NFC, and EUV after prior He PPT is consistent with a lower UV/VUV sensitivity of these materials compared to 193nm PR.

2.4 Conclusion

The beneficial helium plasma-based pretreatment (PPT) established for 193nm PR[1] cannot easily be extended to other organic masking materials. While the approach is generic for PMMA-based 193nm PR polymers, other materials show significant differences in UV/VUV sensitivity based on their polymer structure. This leads to substantially different results in terms of plasma-induced surface/line edge roughness

introduction during the main PE step. UV/VUV radiation leads to pendant group removal and severe oxygen loss for 193nm PR[32] in contrast to AR, HM, NFC, and EUV due to a lack of the radiation sensitive lactone side group, as seen in the C=O band. The PPT has an overall smaller impact on all other materials studied compared to 193nm PR. For 193nm PR, PPT reduces surface roughness, line edge roughness, and side wall roughness. It also stabilizes the critical dimensions and enhances etch resistivity.[1] No impact on surface roughness was seen for HM while AR, NFC, and EUV showed a small increase in surface roughness. This increase is likely related to a denser DAC layer as seen using *in-situ* ellipsometry.

Acknowledgements

We thank Andrew Knoll, Priscilla Tang, Dr. Nick Fox-Lyon, and Dr. Elliot Bartis for collaboration and helpful insights and discussion on this project. We gratefully acknowledge financial support of this work by Semiconductor Research Corporation under Task No. 2071.004. This work was supported in part by US Department of Energy Office of Fusion Energy Science Contract DE-SC0001939.

Chapter 3: Formation of nanometer-thick delaminated amorphous carbon layer by two-step plasma processing of methacrylate-based polymer

Dominik Metzler [a], Florian Weilnboeck [b], Sandra C. Hernández [c], Scott G. Walton [c], Robert L. Bruce [d], Sebastian Engelmann [d] Lourdes Salamanca-Riba [a], and Gottlieb S. Oehrlein [a]

[a] *Department of Materials Science and Engineering*
And Institute for Research in Electronics and Applied Physics
University of Maryland, College Park, Maryland 20740

[b] *Current address: Infineon Technologies AG, Development Center Villach, Austria*

[c] *Plasma Physics Division, Naval Research Laboratory*
4555 Overlook Ave. SW, Washington, District of Columbia 20375

[(d] *IBM T.J. Watson Research Center*
Yorktown Heights, New York 10598

Journal of Vacuum Science & Technology B 33, 051601 (2015)

doi: 10.1116/1.4928493

Abstract:

We show that extended He plasma pretreatment (PPT) of methacrylate-based 193nm photoresist (PR) material in conjunction with a subsequent biased Ar plasma treatment can lead to blister formation at the polymer surface due to delamination of an ultra-thin, ion-induced, dense, amorphous carbon (DAC) layer formed by low energy ion bombardment. For our experimental conditions, the delaminated layer is 1-2 nanometers thick and primarily composed of sp^2-hybrized amorphous carbon. A He or Ar plasma process alone will not lead to this phenomenon, and so far we have only observed it for a methacrylate polymer. A possible mechanism of the formation of the ultra-thin layer that is consistent with all observations is as follows: During He plasma pretreatment, volatile species are produced by UV-VUV radiation-induced photolysis of the polymer pendant groups, e.g. adamantyl, and chain-scissioning of the polymer backbone to a depth of greater than 100 nm. While volatile products formed close to the polymer surface can diffuse out during He PPT, those formed deep within the polymer bulk cannot and their concentration will become significant for extended He PPT. During the biased Ar plasma treatment step, a dense amorphous carbon (DAC) surface layer is generated by Ar^+ ion bombardment within the first seconds of plasma exposure. The thickness is dependent on ion energy and in the range of 1 to several nanometers. This layer appears to be impermeable to gaseous products formed in the PR material. Thus, volatile species diffusing to the surface can accumulate underneath the DAC layer, causing a loss of adhesion and subsequent delamination of this layer from the PR bulk film. We also report surface and electrical characterizations of the ultra-thin DAC layer using optical

microscopy, transmission electron microscopy, Raman and x-ray photoemission spectroscopy, and two-point probe techniques.

3.1 Introduction

Photoresist materials, such as methacrylate-based 193nm photoresist (PR), can exhibit high surface and line-edge roughness formation during plasma-based pattern transfer (see for example[25, 46, 47]). Roughness formation in 193nm PR has been linked to plasma-induced changes in mechanical properties driven by the simultaneous flux of energetic ions at the 193nm PR surface and ultraviolet/ vacuum ultraviolet (UV/VUV) plasma radiation penetrating deep into the material bulk.[26, 27, 48-50] Energetic ion bombardment leads to rapid (≈3 s for our conditions) removal of H and O, strong densification (density increase from 1 to ≈2-3 g/cm^3), and a substantially increased plane strain modulus in a thin (≈2 nm or less), stiff amorphous carbon layer at the surface.[27, 35, 43, 51-55] UV/VUV radiation introduces, at longer timescales (≈30 s), chain scission to a depth of up to 200 nm, resulting in a decrease in the bulk material plane strain modulus.[32, 43] The compressive stress in the top layer of this bilayer structure causes it to undergo a buckling instability, resulting in surface wrinkling.[27, 49] We have previously reported a possible approach to overcome this synergistic roughening by introducing an extended helium plasma pretreatment (PPT) of 193nm PR prior to the plasma etching (PE).[1] Plasma-generated UV/VUV exposure during a He plasma pretreatment saturates bulk material modifications and prevents roughness formation during the subsequent etch step. As a result, the 193nm PR patterns are stabilized and exhibit improved etch resistance and reduced surface/line-edge roughness formation.

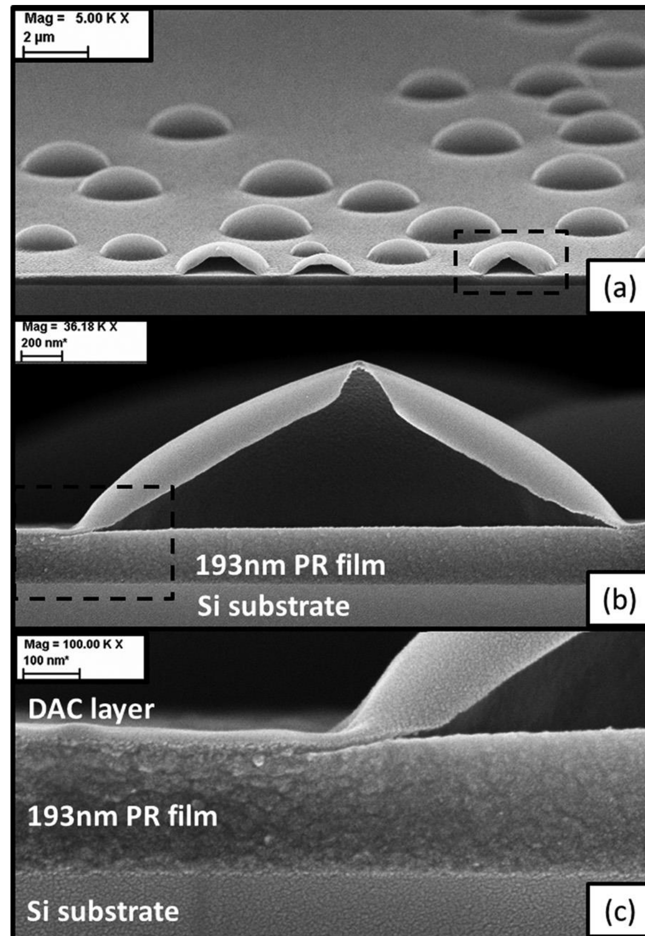

Fig. 3.1: Cross-sectional SEM image of blisters formed by the delaminated DAC layer. (b) A close up of the marked area in (a). It can be seen that, especially in (c), the delaminated layer is only a few nanometer thick.

While investigating the dependence of surface roughness evolution on the parameters of the He PPT, we observed an unexpected phenomenon which we describe here. For PMMA-based polymers, we observed the formation of ultra-thin blisters at the surface due to delamination of the dense, amorphous carbon (DAC) layer formed by low energy Ar^+ ion bombardment during the Ar plasma treatment simulating a plasma etch (PE) step. This is seen only after a prior, extended He PPT (see Fig. 3.1). The thickness of the delaminated film is on the order of the ion penetration depth (less than 2 nm for our conditions)[27, 56, 57] and shows an amorphous carbon structure. This phenomenon provides

the potential for large scale production of ultra-thin, amorphous carbon material. This graphene-like material is of potential interest for example for energy, fuel cell, 3D electronics, and photovoltaic applications. In this article, we describe characterization results of the formation conditions of the delaminated, ultra-thin DAC layers as well as their properties.

3.2 Experimental Procedures

Details of the 193nm PR materials used and the plasma system have been described previously.[19, 28] The most important experimental details are briefly summarized here. The 193nm PR materials studied are blanket films provided by Dow Electronics (DE), with a thickness of ≈400 nm and the Japan Synthetic Rubber Corp. (JSR), with an initial thickness of ≈200 nm. Both 193nm PRs are poly(methyl methacrylate) (PMMA)-based with functionalized sidegroups. In particular, the labile adamantyl group that is photolyzed by UV/VUV irradiation[1, 19, 26] is thought to be important for blister formation.

This work was performed using an inductively coupled plasma system. The top spiral antenna drives plasma production (13.56 MHz excitation frequency) and is located 130 mm above a 125 mm diameter Si electrode which can be RF biased (3.7 MHz excitation frequency) to control ion energies at the substrate. For the He PPT we exposed materials to a high pressure, high density, unbiased helium plasma (800 W source power, $E_{ion} \leq 25$ eV, 100 mTorr pressure, 60 sccm gas flow, 11.6 mA cm^{-2} ion current density). For the subsequent PE step, materials were exposed for 60 s to a biased argon plasma (200 W source power, $E_{ion} \leq 125$ eV, 20 mTorr pressure, 55 sccm gas flow, 3.7 mA cm^{-2} ion current density). PPT conditions have been chosen so that radiation modification, e.g.

pendant group removal, dominates.[1, 25, 32, 33] During PE, where ion energies substantially exceed sputter threshold energies,[1, 25, 33] ion bombardment dominates changes in material properties. The temperature of the samples was stabilized by substrate cooling (10 ^{o}C) during plasma processing by circulating water on the substrate backside.

We performed *in-situ* ellipsometry (λ = 632.8 nm) operating in the polarizer-rotating compensator-sample-analyzer configuration to monitor changes in film thickness and index of refraction in real-time. The optical model used to interpret the measured Ψ-Δ values is based on ion and UV/VUV induced modifications and is shown in Fig. 3.2 (b). Optical microscopy, scanning electron microscopy (SEM), and cross-section SEM were used to analyze surface morphologies of delaminated samples. Additionally, transmission electron microscopy (TEM) characterization of the ultra-thin delaminated material was performed.

The samples in this work were subjected to conditions that would preferentially dissolve a non-cross-linked photoresist polymer versus one that is cross-linked or, at the very least, one containing stronger bonds than the other. The intrinsic nature of the ultra-thin delaminated material makes it amenable to a simple wet transfer process. The transfer was performed by submerging the DAC/193nm PR/Si complex in warm acetone (40 °C) under light stirring for less than 30 seconds to preferentially dissolve the bulk 193nm PR and release the DAC film. The suspended ultra-thin film was then ladled from the acetone using a SiO_2/Si (200 nm SiO_2 thickness) receiving substrate. Afterwards, the film and SiO_2/Si substrate was spun at 2000 rpm to remove excess acetone, and then air dried.

Micro-Raman spectroscopy was performed on a Thermo Scientific DXR system using a 9 mW, 532 nm laser with a 0.7 mm spot size. Raman spectroscopy was used to interrogate the sp^2 nature of the DAC films, and was performed before and after 193 nm PR transfer to the SiO_2/Si substrate.

Electrical characterization was performed by metal evaporation of Au/Ti contact pads (100nm/5nm) using a physical mask, in a two point probe configuration using a Cascade Microtech probe station in combination with a Keithley 2400 measurement system. Current-voltage characteristics were obtained by sweeping the source-drain voltage from -5V to 5 V at a zero gate voltage.

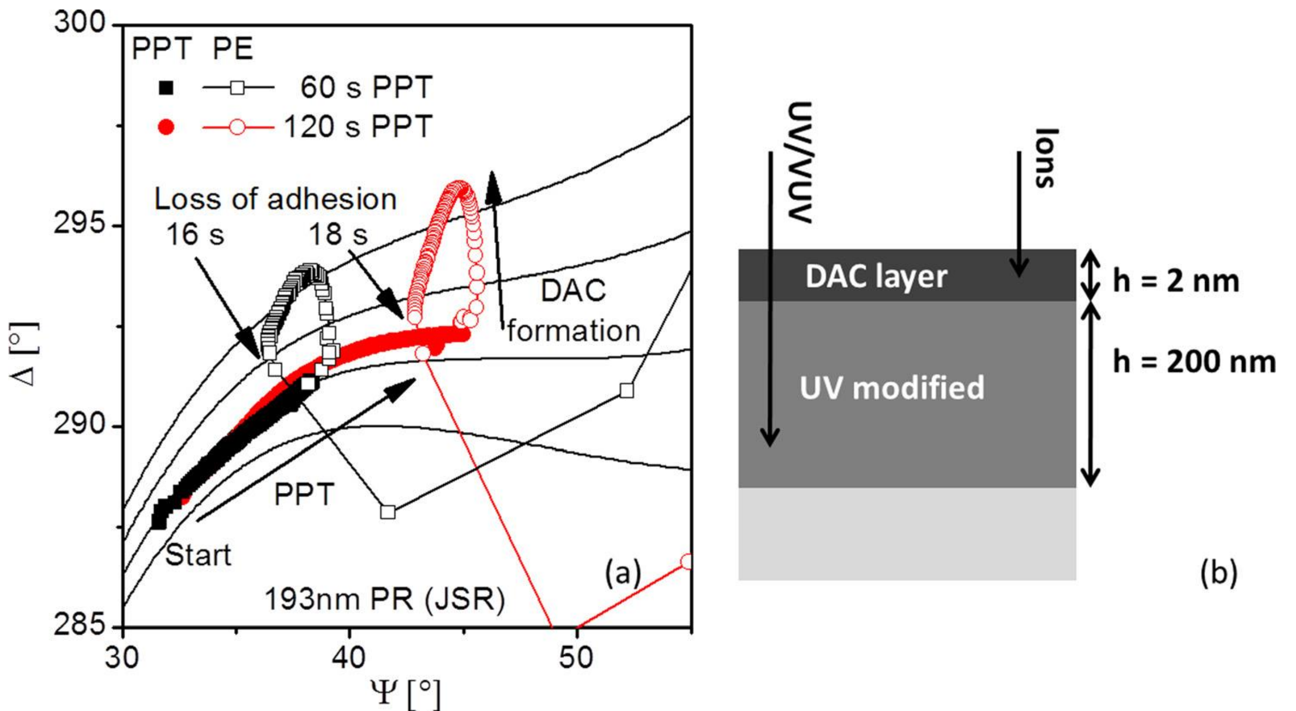

Fig. 3.2: (a) Real time Ψ-Δ trajectory of in situ ellipsometry during a 60 s (squares) and 120 s (circles) PPT, each with subsequent PE. The solid lines mark a constant index of refraction. The formation of the DAC layer leads to a strong increase in Δ. The loss of adhesion leads to very rapid changes in Ψ and Δ. (b) Schematic of the optical model used to interpret the Ψ-Δ trajectory.

3.3 Results and Discussion

3.3.1 Formation of ultrathin, dense, amorphous carbon layer by 2-step plasma processing

Blister formation has only been observed when the He PPT is applied for exposure times exceeding about 40 s for 193nm PR (JSR) and the phenomenon only takes place during the subsequent Ar PE. This indicates that polymer modifications caused by extended He PPT in conjunction with biased Ar plasma-induced polymer modifications cause delamination of the ultra-thin DAC layer during the Ar PE step.

A typical Ψ-Δ trajectory of 193nm PR (JSR) for the PPT and the subsequent PE measured by *in situ* ellipsometry is shown in Fig. 3.2 (a). The interpretation of the measurement is as follows: A gradual thickness loss during He PPT leads to an increase in Ψ. A strong increase in Δ during the first seconds of the subsequent PE indicates DAC layer formation.[27, 43, 52-55] Sudden large changes in Ψ and Δ, i.e. the optical constants of the polymer, on the order of several degrees, mark the macroscopic changes associated with blister formation on the 193nm PR surface. The very rapid change in the Ψ-Δ trajectory occurs after ≈17 s of PE exposure for 193nm PR (JSR), as can be seen in Fig. 3.2 (a). It is noteworthy that the DAC layer is already fully established after ≈3 s of PE exposure time.[27] In summary, blister formation only occurs if the 193nm PR is first treated for more than 40 s with a He PPT and then for at least ≈17 s with a Ar PE. Therefore, the compressive stress formed by the bi-layer system responsible for the surface roughness[26, 27, 48-50] cannot be the only driving factor for blister formation.

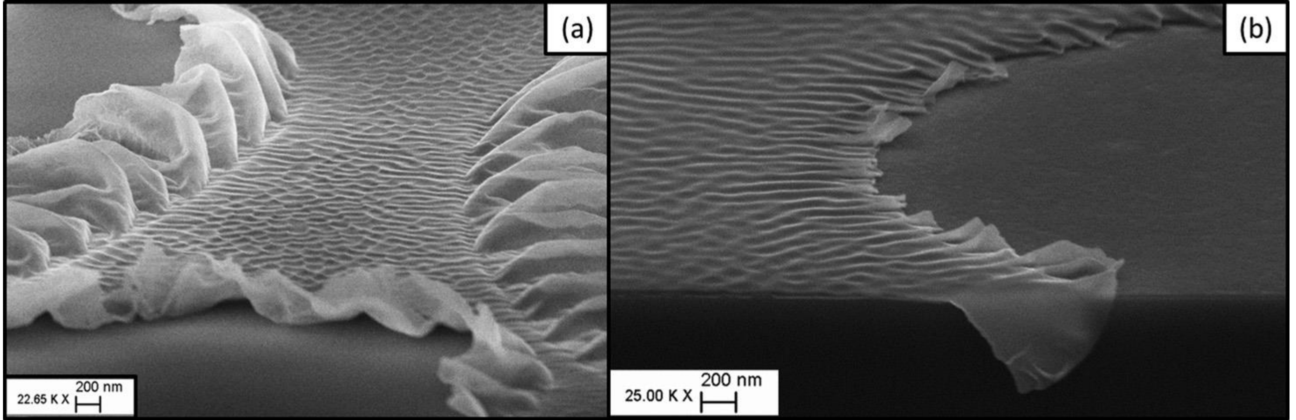

Fig. 3.3: Cross-sectional SEM image of the delaminated DAC layer for (a) 193nm PR (DE), provided by Dow Electronics, and (b) 193nm PR (JSR), provided by Japan Synthetic Rubber Corp.

3.3.2 Material Characterization

Polymer surfaces with blisters were examined by scanning electron microscopy. Cross-sectional SEM micrographs, shown in Fig. 3.1 and Fig. 3.3, show the blister formation on the surface and delamination. The close ups in Fig. 3.1 (b) and (c) reveal that only the ion-induced DAC layer is delaminated from the underlying polymer film rather than the whole film delaminating from the Si substrate. This DAC layer is only a few nm thick[27] and can be seen clearly in Fig. 3.1 (c). The surface morphology between the blisters is rough and similar to non-delaminated samples,[1, 27] as seen in Fig. 3.3. According to Moon *et al.*,[58] surface defects can lead to blister formation of diamond-like carbon films, suggesting a possible connection between the surface roughness formed during PE and blister formation.

The delaminated thin film was further characterized using TEM. The diffraction patterns observed are shown in Fig. 3.4 (a) and are characteristic of amorphous carbon. Electron energy loss spectra (EELS), shown in Fig. 3.5, of the delaminated film show a pre-peak at 284 eV in the C-K edge. This pre-peak indicates some degree of sp^2 bonding,

which was also confirmed by Raman spectroscopy. The peak intensity varies depending on sample location, indicating a non-uniform sp^2 bonding throughout the film. However, Figure 3.6 shows a zero loss peak (ZLP) image and C-K edge map of a uniform region with high carbon content.[59, 60]

Raman spectra of the transferred, delaminated blistered film (Fig. 3.7) reveal pronounced peaks in the ~1590 cm^{-1} and 2949 cm^{-1} regions, associated with sp^2 and sp^3 carbon hybridization. In particular, the spectrum of the top surface of a blister shows an additional peak at ~1338 cm^{-1}, which, in combination with the other two peaks described earlier is indicative of disordered sp^2 carbon.

Electrical characterization of the transferred, blistered delaminated film showed negligible conductivity, even at high biasing potentials (± 5 V), with a measured resistivity well in excess of 10^5 Ω. This is not surprising since both TEM and Raman show a degree of sp^2 nature and contribution of sp^3 hybridization, indicating that the resulting film had enough disorder in the carbon-carbon bonding matrix to inhibit conductivity. The results agree with previous studies,[27] which found the ion-induced layer to be amorphous carbon.

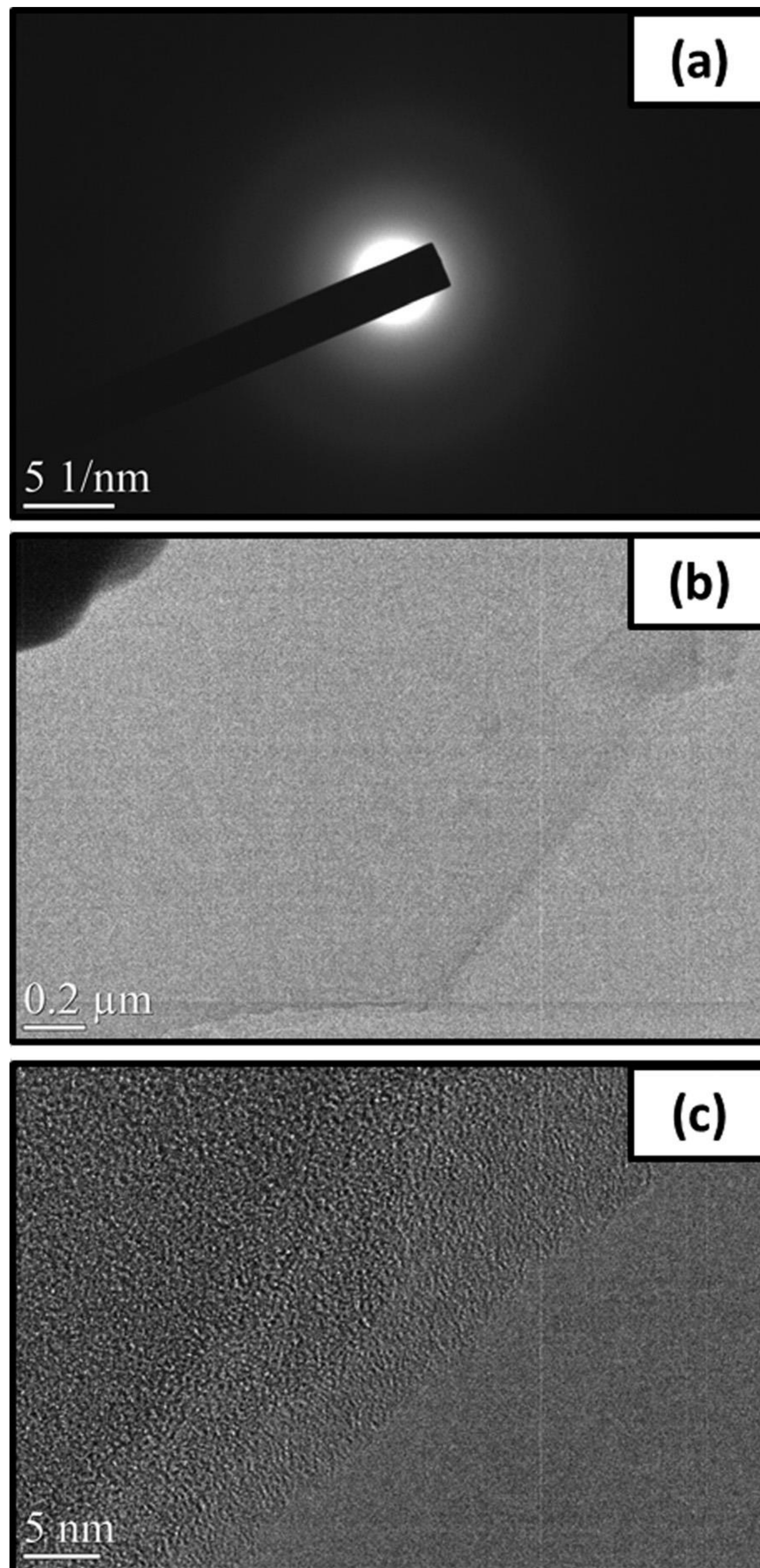

Fig. 3.4: TEM images of the DAC films. (a) The diffraction pattern, characteristic of amorphous carbon with weak rings, (b) a single, thin layer, and (c) several layers.

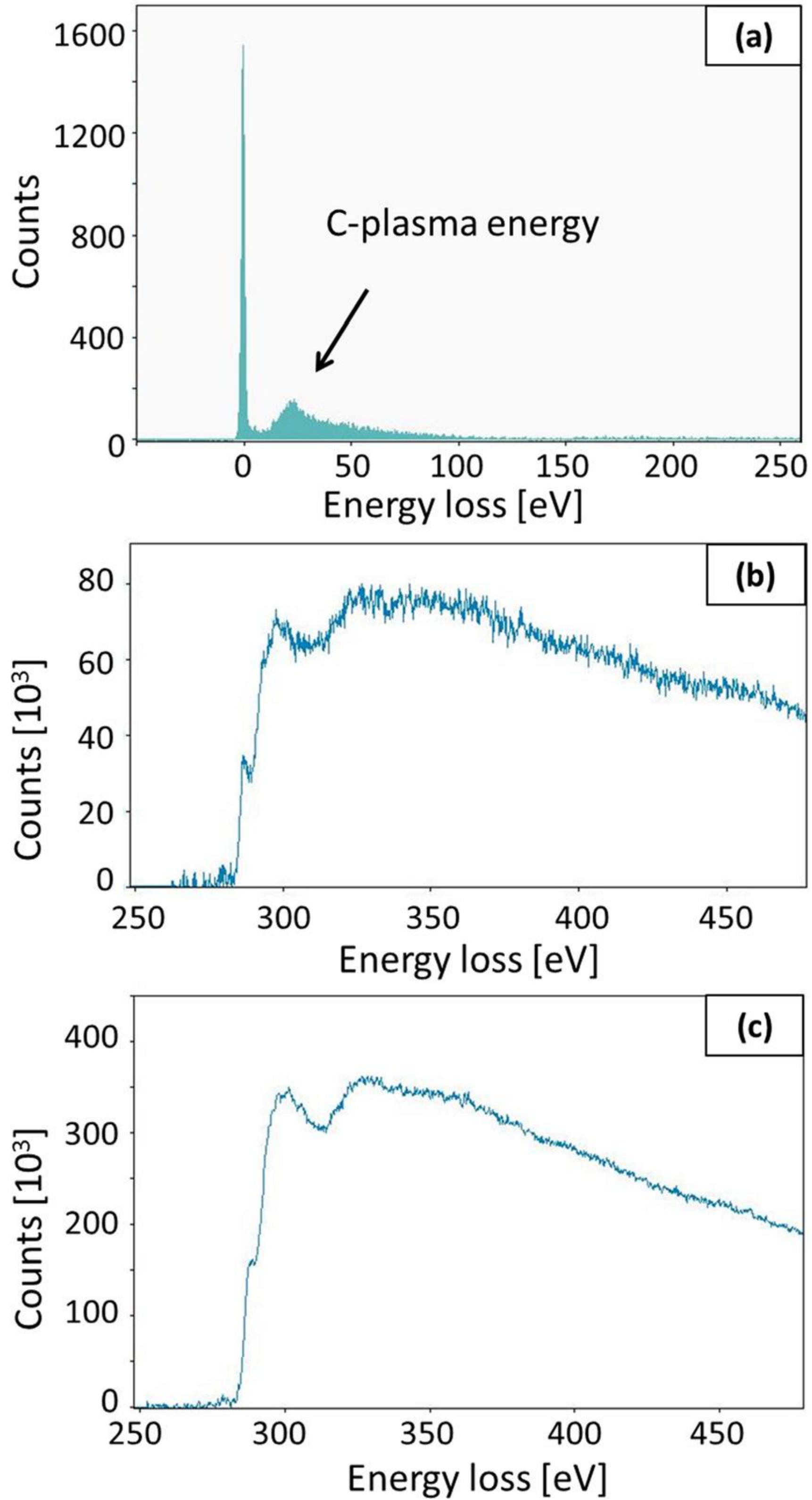

Fig. 3.5: (a) Electron energy loss spectra of the delamination film. (b) and (c) show the carbon characteristic energy range at two different locations on the sample.

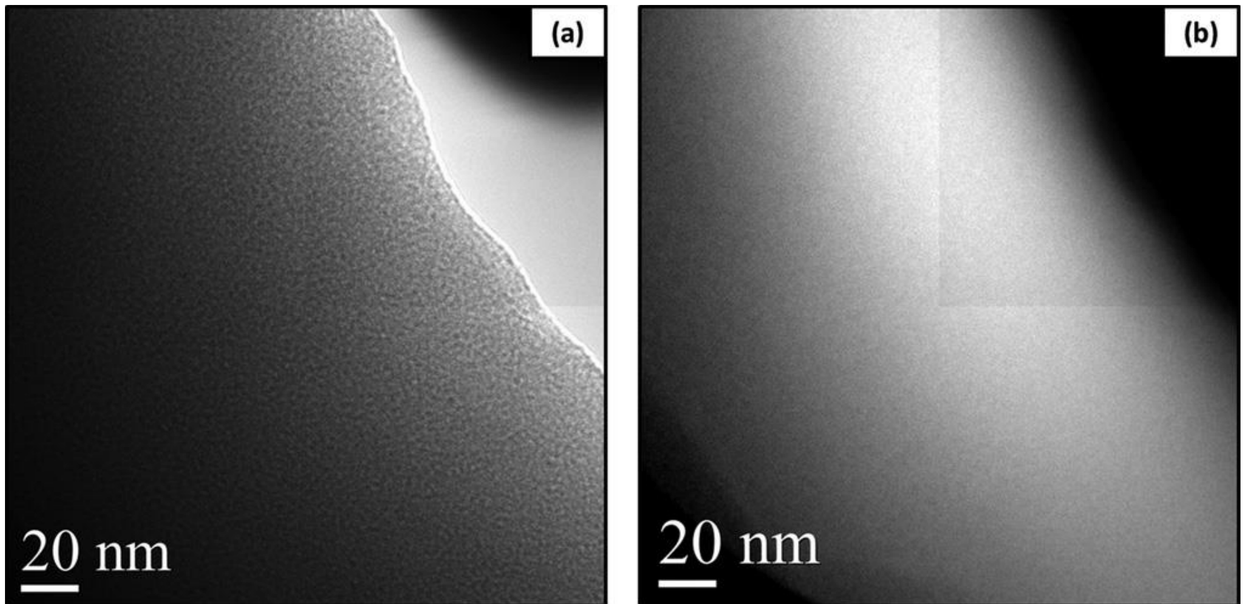

Fig. 3.6: The (a) Zero loss peak (ZLP) image and (b) C-K edge map show a uniform region with high C content.

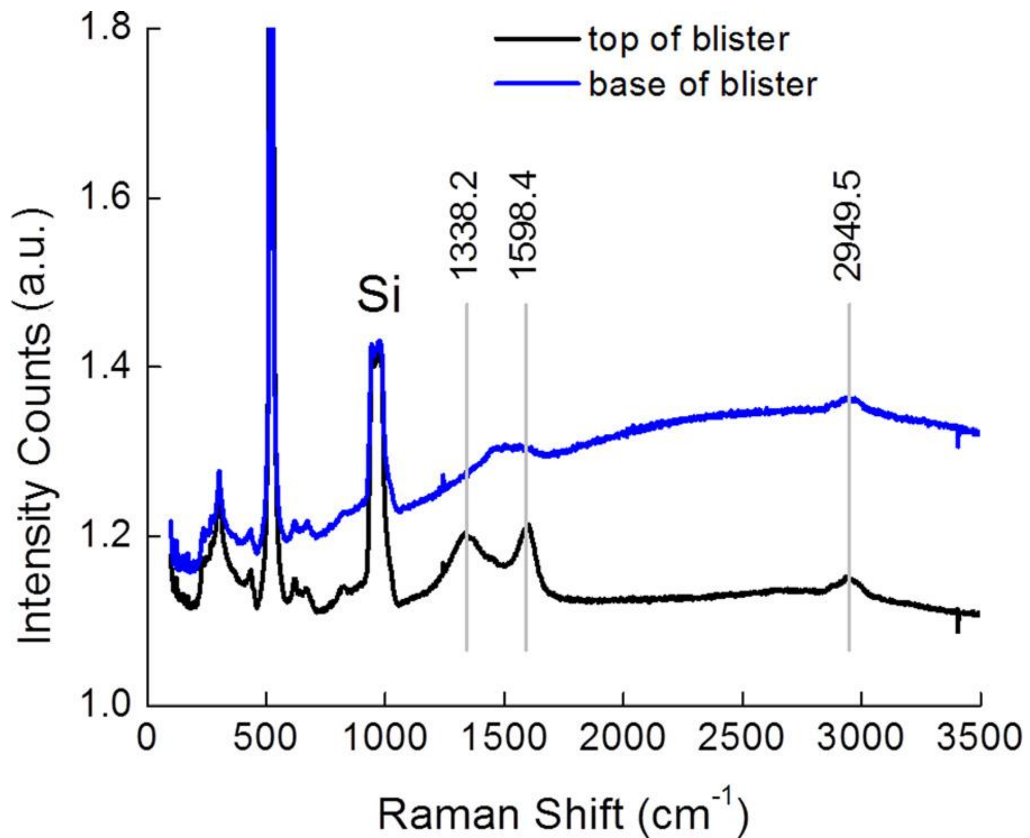

Fig. 3.7: Raman spectra of the blistered delaminated material after it was transferred to an SiO_2/Si substrate. The black curve was measured at the apex of a blister, while the blue curve was measured at the base of the blister.

3.3.3 Critical parameters for Delamination

The role of initial film thickness has been investigated using thickness graded samples. An oxygen plasma etch was employed to prepare 193nm PR (JSR) samples with a graded film thickness ranging from 185 nm to 130 nm, see Fig. 3.8 (a). The density of blisters across the surface gradually decreases with decreasing film thickness before completely vanishing; no blister formation is observed in areas of the sample that have an initial film thickness less than ≈150 nm (see Fig. 3.8).

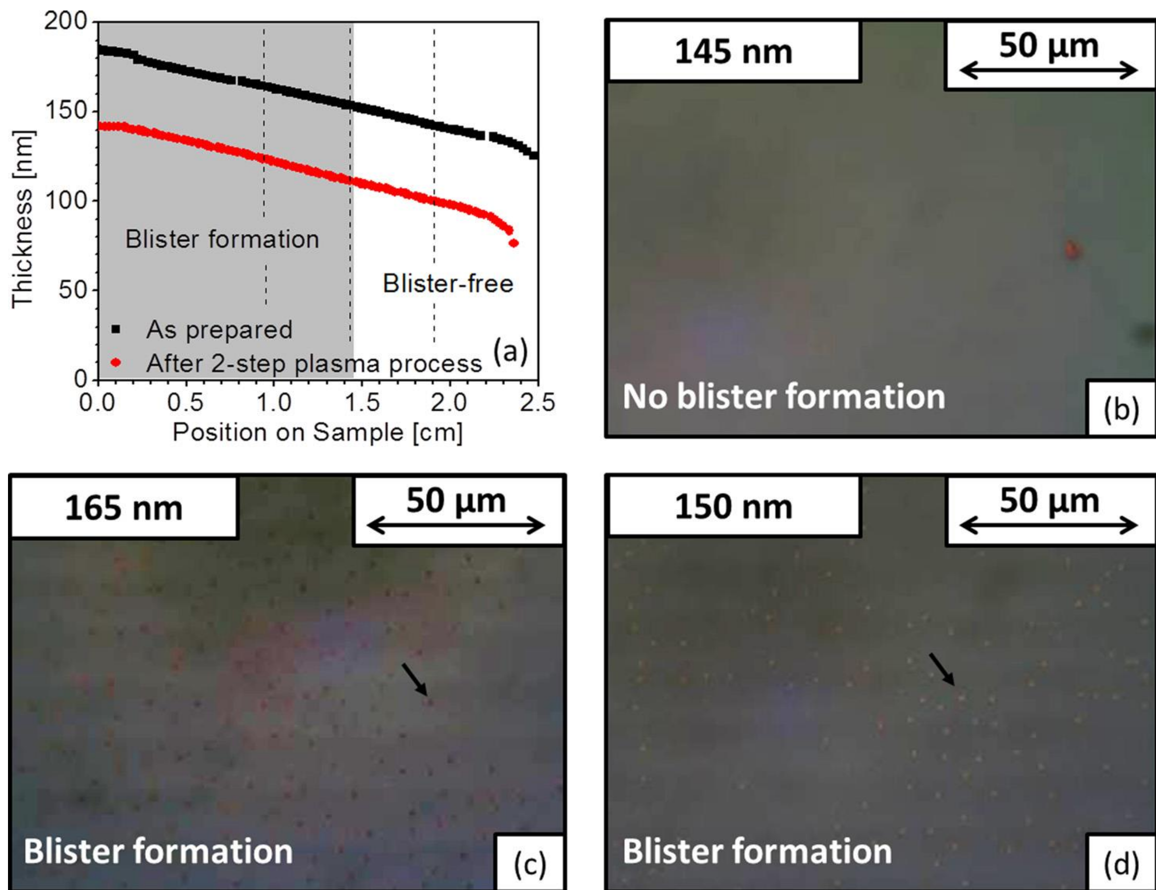

Fig. 3.8: Samples with a graded 193nm PR thickness after exposure to a two-step plasma process (120 s PPT and 60 s PE). Only films thicker than ≈150 nm (shaded area) show blister formation (c and d). Films with an initial thickness of less than ≈150 nm do not show a loss of adhesion and thus, no blister formation (b). Arrows mark examples of visible blisters.

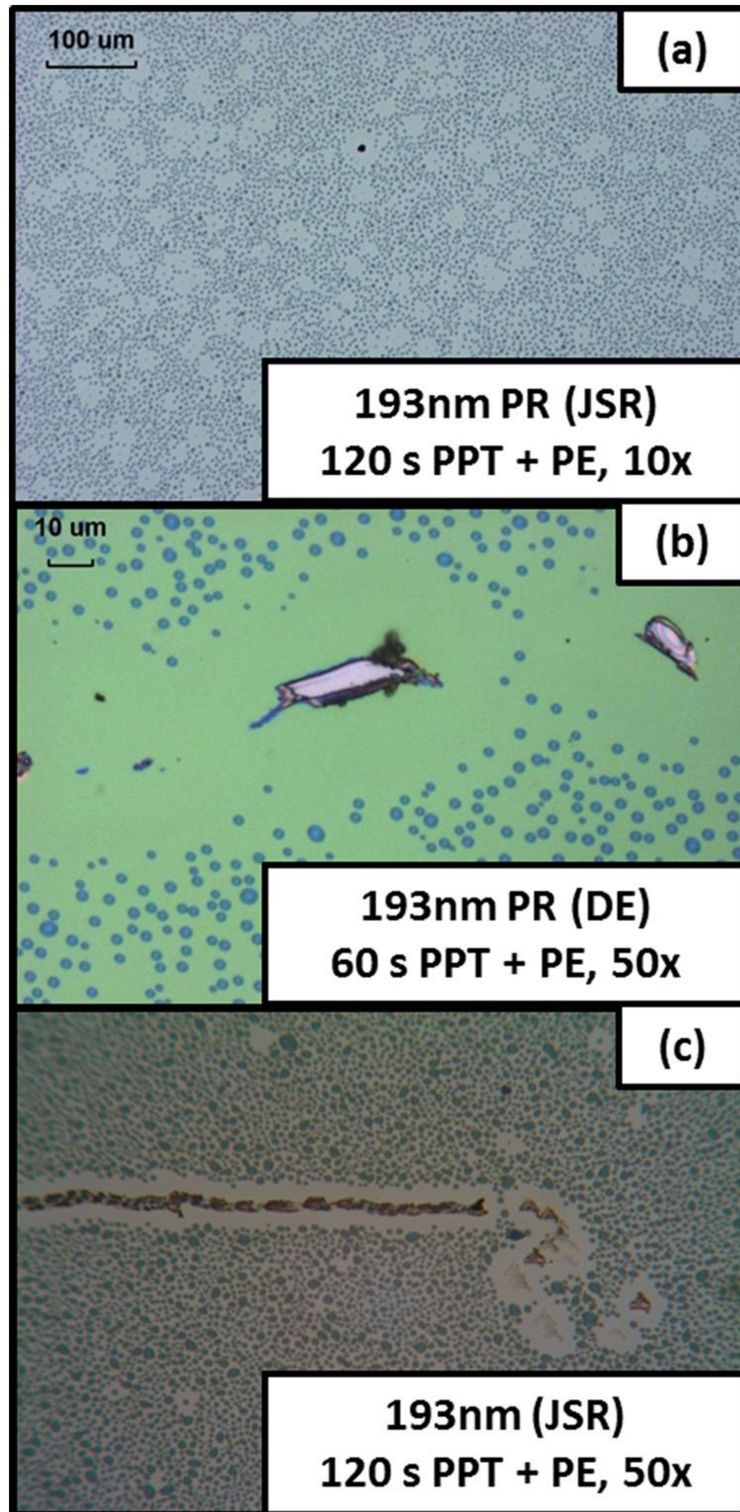

Fig. 3.9: Optical microscope images of blister formation on the surface of methacrylate-based 193nm photoresist material after 2-step plasma processes. Blister free areas are (a) randomly distributed across the surface and also around (b and c) scratches.

Blister density and distribution was studied using an optical microscope. Figure 3.9 shows typical images of the 193nm PR films after plasma processing at conditions that facilitate blister formation. From the optical images, it is evident that blisters are randomly distributed across the 193nm PR surface with areas of high and low (or zero) density – the latter appears as lighter colored regions in Fig. 3.9 (a). Areas around scratches are void of blisters, as seen in Fig. 3.9 (b) and (c).

Other organic masking materials were also investigated for blister formation. The materials studied include a 100 nm thick PMMA based anti-reflection coating, a naphthalene polymer-based hard mask, and a polystyrene based 248nm photoresist-like film. None of these materials showed blister formation and are therefore not shown here. A likely explanation is that these materials do not show the formation of volatile products by photolysis due to a different UV/VUV irradiation response and therefore do not provide significant outgassing driving the delamination. The PMMA based anti-reflection coating was only available with a film thickness of 100 nm, which can likely be another reason for the lack of blister formation.

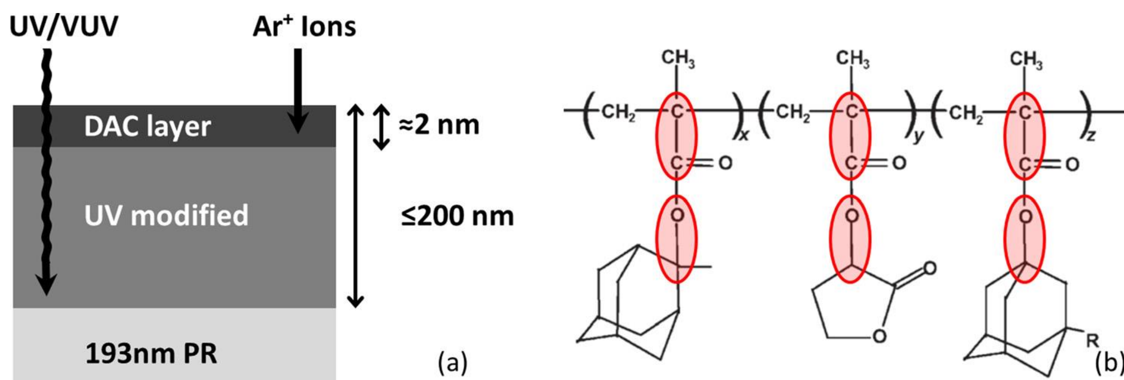

Fig. 3.10: (a) Schematic of plasma interactions with the sample. UV/VUV radiation can cause modification, in this case specifically chain scission deep into the polymer (up to ≈200 nm, exponentially decaying). The ion penetrations depth is on the order of ≈2 nm, thus forming a thin and very dense amorphous carbon (DAC) layer at the very surface, capable of trapping photolysis products. (b) There are several possible photolysis products, with the main one being the adamantyl sidegroup. Possible bond scissioning is marked with red circles.

3.4 Discussion

3.4.1 Formation Mechanism

For the mechanism that leads to delamination of the DAC layer and appearance of blisters after long PPT exposure times, we suggest the following model based on the schematic shown in Fig. 3.10. Several sources[61-63] suggest outgassing as a factor driving the delamination. It has been shown that UV/VUV treatment of mask materials leads to chain scissioning with strong pendant group removal.[26, 32] The He PPT treatment provides a large UV/VUV photon flux (on the order of more than 10^{16} $cm^{-2}s^{-1}$)[64] that causes scissioning of the 193 nm polymer materials, and produces volatile adamantyl and other fragments.[26, 65] While the fluence of the UV/VUV radiation exponentially decays with depth into the polymer material according to Beer's law, photon-induced modifications can extend into the bulk of the acrylate polymer film to a depth of ≈200 nm. With the substrate held at 10 ^{o}C during the He PPT, volatile products are expected to escape if they

are produced close to the surface, but not if produced at greater depths. The concentration of volatile species produced at greater depths will become significant when applying the He PPT for extended times. During the subsequent biased Ar plasma step, an impermeable ion-induced DAC layer forms within the first few seconds at the polymer surface. The volatile species produced deep in the polymer during He PPT are trapped during etching and can produce a buckling instability, leading to blister formation. Conventional one-step plasma processes provide an insufficient UV/VUV to ion flux ratio and do not show a sufficient buildup of volatile species in the film to observe this phenomenon. We also speculate that prolonged PPT exposure additionally reduces the adhesion between the polymer bulk and DAC layer due to bulk softening by chain scissioning, further supporting the appearance of blisters only with long PPT exposure times. The blister-free areas observed (Fig 3.9) are likely due to alternative pathways of stress relaxation through scratches, imperfections, and other mechanical defects.

Buckling instability and blister formation have been observed in other systems. Moon *et al.*[58, 66] shows delamination of diamond-like carbon films based on surface imperfections. Unai *et al.*[62] reports blister formation on PMMA resist caused by ion beam lithography. They showed that the ion beam induces chain scissioning which drives outgassing and leads to delamination.

3.4.2 Material Properties

The blistered thin film showed the potential to be removed from its bulk and transferred to other surfaces, allowing further *ex situ* characterization and potential use for device fabrication. It is evident from the Raman spectra that a completely amorphous material was generated via this plasma processing sequence technique, exhibiting

graphitic properties and sp^2 hybridization. While the blistered thin film showed no conductivity, the ability to produce large area amorphous carbon films that can be transferred to other surfaces (allowing further *ex situ* characterization in this work) suggests potential uses in other applications that can benefit from large area, atomically thin films, e.g. for protective or diffusion barriers.

3.5 Summary

We have found that extended He plasma pretreatment (PPT) exposures can lead to ultra-thin blister formation during subsequent plasma etching (PE), based on an ion-induced dense, amorphous carbon (DAC) layer delamination phenomenon for PMMA-based polymers with adamantyl side groups. This two-step process is essential for the blister formation as neither process alone causes delamination. The blisters formed are hollow with the delaminated film being the only a few nanometer thick DAC layer. This DAC layer is composed of amorphous carbon with some degree of sp^2-hybridization. The pendant group removal previously discussed for 193nm PR materials[1] appears to cause the phenomenon discovered in this work.

The blister formation phenomenon appears to be related to the fundamental PMMA polymer structure since we have not observed this for other polymers. The PPT treatment provides a large photon flux that causes scissioning deep in the 193 nm polymer. The scission products, i.e. volatile adamantyl fragments, produced at large depths during the PPT cannot diffuse out for a substrate at 10^oC. During the subsequent Ar^+ ion dominated PE step, the impermeable ion-induced DAC layer forms and traps these photolyzed products. The gaseous fragments accumulate under the DAC layer and ultimately lead to delamination and blister formation.

Two types of blister-free areas are observed, around scratches and randomly distributed across the sample. The scratches provide another mechanism for stress relaxation and outgassing, thus preventing blister formation. This work demonstrates careful investigation of the blister formation process, and the ability to produce large area carbon based films that can be transferred to other surfaces for potential applications in protective or diffusion barriers.

Acknowledgements

We thank Andrew Knoll, Dr. Nick Fox-Lyon, Adam Pranda and Dr. Elliot Bartis for collaboration and helpful insights and discussion on this project. We gratefully acknowledge financial support of this work by Semiconductor Research Corporation under Task No. 2071.004. This work was also supported in part by US Department of Energy Office of Fusion Energy Science Contract DE-SC0001939 and the Naval Research Laboratory base program.

Chapter 4: Fluorocarbon Assisted Atomic Layer Etching of SiO_2 Using Cyclic Ar/C_4F_8 Plasma

D. Metzler [a], R.L. Bruce [b], S. Engelmann [b], E.A. Joseph [b], and G.S. Oehrlein [a]

[a] *Department of Material Science and Engineering, Institute for Research in Electronics and Applied Physics, University of Maryland, College Park, Maryland 20742, USA*

[b] *IBM T.J. Watson Research Center, Yorktown Heights, New York 10598, USA*

Journal of Vacuum Science & Technology A 32, 020603 (2014)

doi: 10.1116/1.4843575

Abstract:

We demonstrate atomic layer etching of SiO_2 using a steady-state Ar plasma, periodic injection of a defined number of C_4F_8 molecules and synchronized plasma-based Ar^+ ion bombardment. C_4F_8 injection enables control of the deposited fluorocarbon (FC) layer thickness in the 1 to several Ångstrom range and chemical modification of the SiO_2 surface. For low energy Ar^+ ion bombardment conditions, the physical sputter rate of SiO_2 vanishes, whereas SiO_2 can be etched when FC reactants are present at the surface. We have measured for the first time the temporal variation of the chemically enhanced etch rate of SiO_2 for Ar^+ ion energies below 30 eV as a function of fluorocarbon surface coverage. This approach enables controlled removal of Ångstrom-thick SiO_2 layers. Our results demonstrate that development of atomic layer etching processes even for complex materials is feasible.

4.1 Introduction

The ability to precisely add and/or remove Ångstrom thick layers from a surface is required for advanced semiconductor manufacturing and related technologies that increasingly demand atomistic surface engineering.[2-4] Past efforts have shown that a key obstacle toward realizing ALE is achieving self-limited etching, in particular for situations when ion bombardment to remove the reacted material and precise control of surface coverage by the chemical precursor is required. Self-limited etching requires both negligible spontaneous chemical etching by the precursor used to passivate the surface and insignificant physical sputtering of the unmodified material after etch product removal.[4] Minimizing physical sputtering has been difficult to realize consistently, and additional factors, e.g. photon-induced etching for plasma environments,[67] have also been invoked to explain persistent etching for certain conditions. On the other hand, recent computational studies have demonstrated the feasibility of ALE for certain systems. For instance, Agarwal and Kushner described a computational investigation of ALE of silicon and SiO_2 using conventional plasma etching tools.[4] They showed that self-limited etching can be achieved by careful control of chemistry and ion energies during the passivation and etching step, respectively. Rauf *et al.* applied molecular dynamics (MD) simulations to examine the possibility of realizing ALE using nanometer-scale fluorocarbon passivation of SiO_2 and silicon followed by argon ion etching.[17] They observed self-limited etching of SiO_2 and Si for Ar^+ energies smaller than 40 eV. No experimental validation of these computational studies has been reported to the best of our knowledge.

It is the goal of the present study to evaluate these ideas using cyclic Ar/C_4F_8 plasma interacting with SiO_2 and to explore for what conditions controlled removal of

SiO_2 layers approaching one atomic layer thickness per cycle can be achieved. We use time-resolved surface characterization to confirm ALE. In our approach, we deposit Ångstrom thick fluorocarbon (FC) layers to form a modified SiO_2 surface layer. Subsequently, low energy Ar^+ ion bombardment is used to remove both the FC layer and a thin reacted SiO_2 layer. Material etching stops once the reacted SiO_2 surface layer has been removed,[17] resulting in a self-limited process. To realize FC layer deposition on the order of Ångstrom, we use pulsed C_4F_8 injection into a low power Ar plasma. For an unbiased substrate, precise FC film thickness control in the 1 to several Å range is possible by adjusting the total number N_{C4F8} of C_4F_8 molecules entering the reactor by varying pulse duration and C_4F_8 gas flow rate appropriately. For these conditions, FC film thickness increases linearly with N_{C4F8}. Following FC deposition, a small RF self-bias voltage (-5, -10 and -15 V) is applied for 35 s in the cases described here, creating average ion energies of 20, 25 and 30 eV, respectively. For the lower ion energies, Ar^+ ion induced physical sputtering of unmodified SiO_2 is negligible.[68] This was confirmed in this work. At the end of a cycle, the process sequence is repeated to achieve precise control over the total etched thickness.

4.2 Experiment

We used an inductively coupled plasma system excited at 13.56 MHz. The plasma was confined within a 195 mm diameter anodized Al confinement ring. A 125 mm diameter Si substrate is located 150 mm below the top electrode on an electrostatic chuck and can be biased at 3.7 MHz. The base pressure achieved before processing was in the $1x10^{-6}$ Torr range and the temperature of the samples (25 x 25 mm^2) was stabilized by substrate cooling (10 °C) during plasma processing. Details of the plasma system have

been described previously.[19, 20] The materials studied were SiO_2-Si-SiO_2 stacks deposited on a Si substrate by PECVD techniques and studied by *in-situ* ellipsometry[22] in real time.

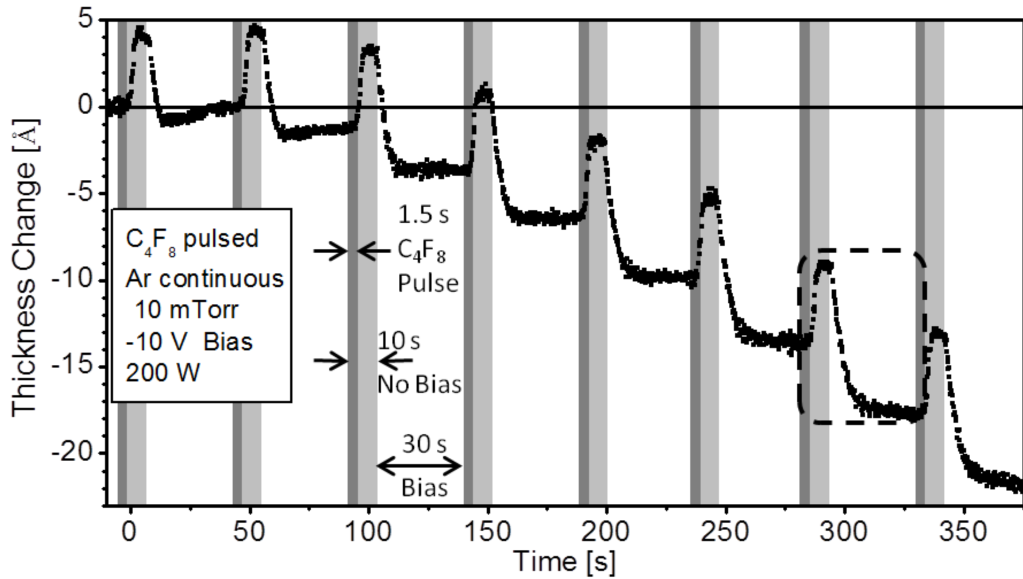

Figure 4.1: Example of the thickness evolution during eight cycles of an SiO_2 ALE process. The process parameters have also been specified. The cycle marked is magnified in Fig. 4.2 (a).

4.3 Results and Discussion

In Fig. 4.1, a typical thickness evolution for an SiO_2 layer is shown for multiple cycles, along with the process parameters of one cycle. At the beginning of each cycle a pulse of C_4F_8 is injected for 1.5 s into a continuous argon plasma, and deposits about 5 Ångstrom of FC film. A synchronized RF bias potential is applied to the substrate 8 s after the C_4F_8 pulse to increase Ar^+ ion bombardment energies. This initiates FC film etching, followed by strongly time-dependent SiO_2 etching. Fig. 4.1 shows that the initially high SiO_2 etch rate continuously decreases and finally ceases. The ion-induced reaction of deposited FC with SiO_2 enables transient etching and controlled removal of an ultra-thin SiO_2 layer. Each cycle shows a similar behavior, although there are small

systematic differences which will be discussed below. Figure 4.1 shows that the present approach permits a high degree of control over total etched SiO_2 thickness. The observed behavior is consistent with both the MD simulations of Rauf et al.[17] and computational simulations of Agarwal and Kushner.[4] For instance, the MD work showed that for Ar^+ ion energies of 20 eV ion-induced removal of chemical reaction products dominates etching and unmodified SiO_2 etches at a negligible rate.

Etching of SiO_2 for the low energy ion conditions is completely dominated by the fluorocarbon reactants and results in an etch rate decrease with time until the initially deposited FC layer is depleted and etching ceases. This effect can be clearly seen in the expanded views of single etching cycles for two conditions in Fig. 4.2. In Fig. 4.2 (a), after deposition of 5 Å FC, a bias potential of -10 V is applied. The low energy ions induce etching of the FC layer and additionally reaction of carbon and fluorine with the underlying SiO_2.[17, 69] The resulting modified SiO_2 surface layer is etched by low energy Ar^+ ion bombardment until the modified layer has been removed, when SiO_2 etching ceases. A similar change in etch rate over time can be observed upon deposition of a thicker FC layer (15 Å) on SiO_2 (see Fig. 4.2 (b)). The use of a longer C_4F_8 pulse produces a thicker FC layer on the SiO_2 surface, but also increases FC on the chamber walls. Overall, there is a larger amount of FC in the system, and the additional FC increases the etch rate during the second half of the cycle. A steady-state is not reached within the period the RF bias was applied for in this case. Therefore, even at the end of the etching cycle, FC material is still present at the SiO_2 surface and enables a finite etch rate. This can be reduced by using shorter C_4F_8 pulses.

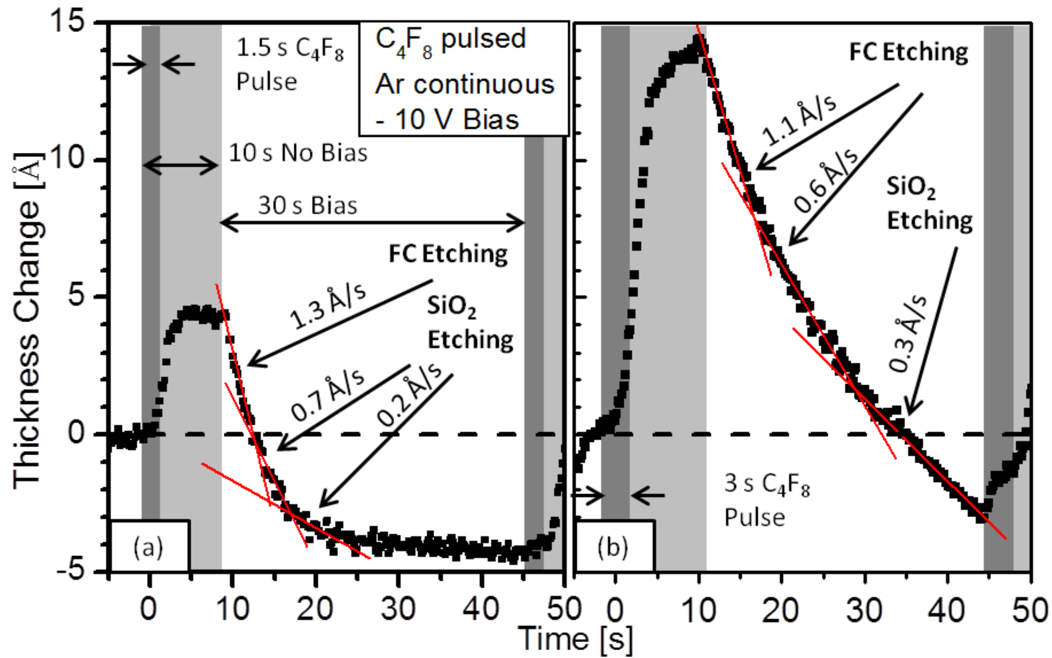

Figure 4.2: Thickness changes of SiO_2 during a single cycle for two thicknesses of deposited FC layer achieved by changing the C_4F_8 pulse time from (a) 1.5 s to (b) 3 s. The FC pulse is injected at the beginning of the deposition step. Eight seconds after the pulse ends, the bias potential is applied and the etch step begins.

Since one crucial factor of this approach is precise admission of chemical reactants to the system, we expect that residual FC deposited on the chamber walls will interfere with the management of chemical reactant supply at the substrate surface and reduce control over the etching process. Figure 4.1 shows that the time-dependent etch rate during the second half of each cycle increases slightly from cycle to cycle. Residual FC entering the gas phase from the chamber walls between C_4F_8 pulses can redeposit on the exposed, unmodified SiO_2 and increase SiO_2 etching for FC reactant-starved process conditions in the later part of a cycle. One key requirement for achieving ALE processes in a plasma reactor is to maintain well-defined clean process chamber conditions to control supply of chemical reactants.

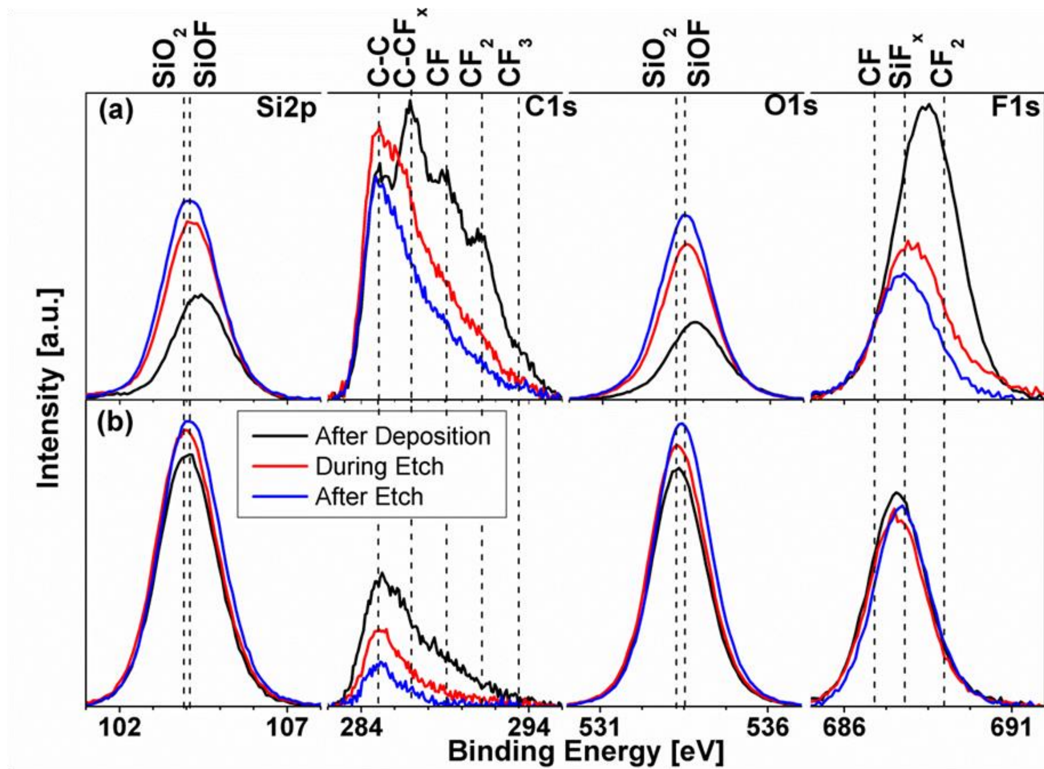

Figure 4.3: XPS spectra comparing SiO_2 with (a) thick (15 Å) and (b) thin (5 Å) deposited FC films after various steps of the 10th ALE cycle.

To obtain insights on changes in surface chemistry throughout one cycle, x-ray photoelectron spectroscopy (XPS) has been performed after the FC deposition step, during the SiO_2 etch step, and after completion of a cycle. To study steady-state conditions, these experiments were performed for the 10th cycle of a sequence. The results are displayed in Fig. 4.3, which summarizes the different binding energy regions of interest (Si 2p, C 1s, O 1s and F 1s). Data are shown for 15 Å and 5 Å thick FC films in Figs. 4.3 (a) and (b), respectively. Si 2p and O 1s spectra were fit using SiO_2 and SiOF at 103.9 eV and 104.1 eV and 533.2 eV and 533.4 eV, respectively. C 1s spectra were fit using C-C/H, C-CF_x, CF, CF_2, and CF_3 peaks at 285 eV, 287 eV, 289.1 eV, 291.2 eV, and 293.4 eV, respectively. F 1s spectra were fit using SiF_x, CF, and CF_2 at 687.8 eV, 686.9 eV and 689 eV, respectively.[70] A more detailed description of this analysis has

been given in previous publications.[32, 71, 72] A clear reduction in F content is seen throughout the etch step for a deposited film of 15 Å as seen in Fig. 4.3 (a). The C 1s spectra show a reduction in carbon-bonded fluorine. The Si 2p and O 1s signals increase correspondingly since they originate from the SiO_2 underneath the FC film. An SiO_2 surface covered with a thin FC film (5 Å, Fig. 4.3 (b)) shows little of the characteristic fluorocarbon bonding signature in the C 1s spectrum and only a slight F 1s signal reduction after etching in contrast to samples covered with a thick FC film. Since the C 1s spectrum shows the same reduction of carbon bonded to fluorine as the thicker films, the remaining fluorine must be associated with SiO_2. Bonding of fluorine with SiO_2 is shown by a slight shift of the Si 2p and O 1s spectra towards higher binding energy, consistent with the more electronegative environment. The MD simulations of Rauf *et al.* also show residual fluorine on the SiO_2 surface after the etch rate ceases for low energy ion bombardment conditions.[17]

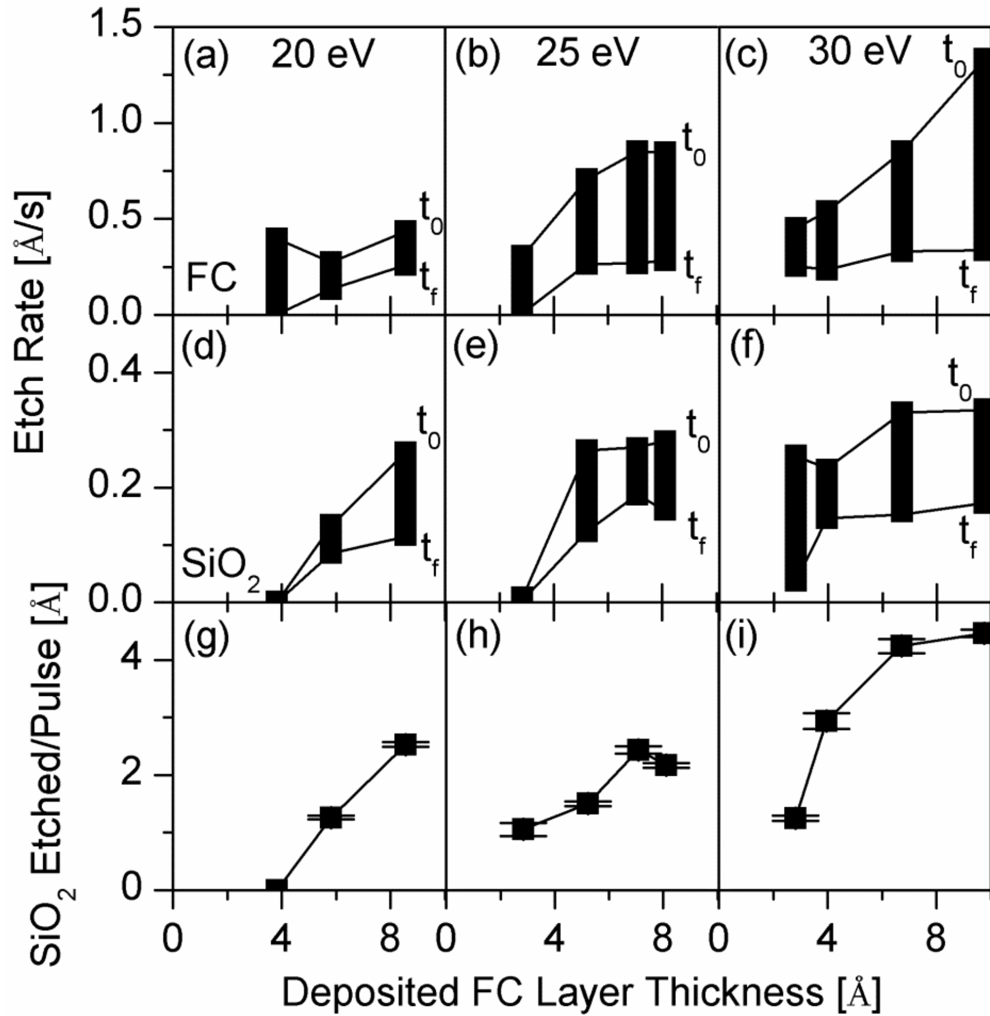

Figure 4.4: Temporal variation of etch rates of FC layer and SiO_2 layer (top row and middle row, respectively) during a cycle as a function of deposited FC film thickness and maximum ion energy. The bottom row shows SiO_2 etched for various deposited FC layer thickness and maximum ion energy.

The FC layer plays a critical role in enabling SiO_2 etching for the low energy ion bombardment conditions used here. Figure 4.4 summarizes the variation of FC etching rate ((a) - (c)), SiO_2 etching rate ((d) - (f)), and SiO_2 thickness removal ((g) - (i)), respectively, with FC layer thickness and maximum ion energy. The time dependent etch rate within one cycle increases with FC film thickness and maximum Ar^+ ion energy. We expect that once a critical FC layer thickness on SiO_2 is reached, the FC reaction with

SiO_2 will no longer increase with FC film thickness, and SiO_2 etched per cycle will saturate.[69] If the FC layer thickness exceeds this critical thickness, on the order of the projected range of Ar^+ ions in the FC material, the additional FC deposited will be etched by Ar^+ bombardment with little interaction with the SiO_2 underneath. The impact of FC film thickness on SiO_2 etch rate is clearly seen in Figs. 4.4 (d), (e) and (f), which shows an increase with both FC layer thickness and maximum ion energy. The maximum SiO_2 etch rate is not a strong function of total FC film thickness above 5 Å, but the minimum SiO_2 etch rate (achieved at the end of the cycle), depends strongly on FC film thickness. A deposited FC film thickness of 4 Å or less is required to achieve minimal SiO_2 etching at the end of the cycle at the low ion energies used in this study. Figure 4.4 shows that the SiO_2 etch rate and SiO_2 thickness removed per etching cycle increase with maximum Ar^+ ion energy for a given FC layer thickness.

4.4 Summary

In summary, we have shown that using a steady-state Ar plasma, periodic injection of a defined number of C_4F_8 molecules and synchronized plasma-based Ar^+ ion bombardment, atomic layer etching of SiO_2 is possible. The thickness of a deposited fluorocarbon (FC) layer in the range of 1 to several Ångstrom and Ar^+ ion bombardment are used to control the chemical modification of SiO_2, thus enabling etching of SiO_2 for low energy ion bombardment conditions for which the physical sputter rate of SiO_2 is negligible. We have measured for the first time the enhancement of the SiO_2 etch rate relative to the physical sputter rate at Ar^+ ion energies below 30 eV as a function of fluorocarbon surface coverage. Our results are consistent with computational simulations that first suggested the feasibility to achieve ALE for the fluorocarbon/Ar^+/SiO_2 system.

Acknowledgements

The authors gratefully acknowledge the financial support of this work by the National Science Foundation (CBET-1134273) and US Department of Energy (DE-SC0001939). The authors thank N. Fox-Lyon, E. Bartis, A. Knoll, M. Vollmer, and P. Tang for collaboration and assistance during phases of this project.

Chapter 5: Fluorocarbon assisted atomic layer etching of SiO2 and Si using cyclic Ar/C_4F_8 and Ar/CHF_3 plasma

D. Metzler [a], C. Li [b], S. Engelmann [c], R.L. Bruce [c], E.A. Joseph [c], and G.S. Oehrlein [a]

[a] *Department of Materials Science and Engineering*
And Institute for Research in Electronics and Applied Physics
University of Maryland, College Park, Maryland 20740

[b] *Department of Physics*
And Institute for Research in Electronics and Applied Physics
University of Maryland, College Park, Maryland 20740

[c] *IBM T.J. Watson Research Center*
Yorktown Heights, New York 10598

Journal of Vacuum Science & Technology A 34, 01B101 (2016)

doi: 10.1116/1.4935462

Abstract:

The need for atomic layer etching (ALE) is steadily increasing as smaller critical dimensions and pitches are required in device patterning. A flux-control based cyclic Ar/C_4F_8 ALE based on steady-state Ar plasma in conjunction with periodic, precise C_4F_8 injection and synchronized plasma-based low energy Ar^+ ion bombardment has been established for SiO_2.[73] In this work, the cyclic process is further characterized and extended to ALE of silicon under similar process conditions. The use of CHF_3 as a precursor is examined and compared to C_4F_8. CHF_3 is shown to enable selective SiO_2/Si etching using a fluorocarbon (FC) film build up. Other critical process parameters investigated are the FC film thickness deposited per cycle, the ion energy, and the etch step length. Etching behavior and mechanisms are studied using *in situ* real time ellipsometry and X-ray photoelectron spectroscopy. Silicon ALE shows less self-limitation than silicon oxide due to higher physical sputtering rates for the maximum ion energies used in this work, ranged from 20 to 30 eV. The surface chemistry is found to contain fluorinated silicon oxide during the etching of silicon. Plasma parameters during ALE are studied using a Langmuir probe and establish the impact of precursor addition on plasma properties.

5.1 Introduction:

Advanced semiconductor manufacturing is increasingly demanding atomic-scale process controllability to further decrease critical dimensions and pitches in order to uphold Moore's Law.[5] High etching precision and material selectivity are essential.[7, 8] Furthermore, device structures become more complex, adding to the challenge of shrinking dimensions.[74-76] Atomic layer deposition (ALD) was developed as early as 1977 by Suntola,[77] and has been established as a common tool in device patterning.[3, 78-80] Its counterpart, atomic layer etching (ALE), however, is currently still mostly in development.[11] One of the key challenges for ALE is the long processing time that many approaches in use require, leading to an overall low wafer throughput.[4] ALE has seen several recent advances, however.[9, 10]

A number of theoretical studies paved the way for the development of ALE. For instance, Agarwal and Kushner described a computational investigation of ALE of silicon and silicon oxide using conventional plasma etching tools.[4] Simulations showed that a careful control of chemistry and ion energies enables a self-limited etching behavior. Rauf *et al.* applied molecular dynamics simulations to examine the possibility of realizing ALE using nanometer-scale fluorocarbon (FC) passivation of silicon and silicon oxide followed by low energy Ar^+ ion bombardment.[17] This approach has been realized experimentally using a steady-state Ar plasma in conjunction with periodic, precise C_4F_8 injection and synchronized plasma-based low energy Ar^+ ion bombardment.[73]

In this article, the authors extended the application of this cyclic approach to silicon. Etching characteristics, surface chemistry mechanisms, and the potential for SiO_2/Si etching selectivity are studied and discussed for C_4F_8 and CHF_3 as a precursor.

Additionally, advances made in the characterization of the flux-control based ALE of silicon oxide by Langmuir probe and atomic force microscopy (AFM) measurements are reported.

5.2 Experimental Methods

Processing conditions are identical to previous work,[73] with the exception of the use of a load lock for all work, and are briefly described here. This work was performed using an inductively coupled plasma system. A planar, water cooled brass coil above a quartz window is powered by a 13.56 MHz power supply with an L-type matching network. All plasma processes presented here are at a source power of 200 W and processing pressure of 10 mTorr with an Ar flow of 50 sccm. The plasma was confined within a 195 mm diameter anodized Al confinement ring. A 125 mm diameter silicon substrate is located 150 mm below the top electrode on an electrostatic chuck and can be independently biased at 3.7 MHz. A RF self-bias potential of -5 to -15 V creates maximum ion energies of about 20 to 30 eV. The base pressure achieved prior to processing was in the $5x10^{-7}$ Torr range and the temperature of the samples (25 x 25 mm^2) was stabilized by substrate cooling (10 °C) during plasma processing. In order to minimize impacts of atmospheric exposure of both the sample and processing chamber, a load lock was used for all experiments. The load lock allows for sample loading and transfer of etched samples to a surface analysis station under vacuum without having to expose the processing chamber to atmosphere. A standard oxygen plasma-based cleaning process and an Ar plasma-based conditioning process between each experiment allows for processing conditions to be as comparable as possible at the start of each experiment. Details of the plasma system have been described previously.[19-21]

Material modification and etching was studied by *in-situ* ellipsometry.[22] The ellipsometer is an automated rotating compensator ellipsometer working in the polarizer-compensator-sample-analyzer (PCSA) configuration at a ≈72° angle of incidence. Measurements were performed in Ψ-Δ-space, corresponding to changes in phase and relative amplitude of the polarized laser light components (He-Ne laser, λ = 632.8 nm). The recorded data was interpreted in terms of changes in film thickness of different materials based on ellipsometric multilayer modeling. The materials studied were SiO_2-Si-SiO_2 stacks deposited on a silicon substrate by PECVD techniques with various thicknesses. Using SiO_2-Si-SiO_2 stacks allows for precise thickness measurements as well as investigating the transition from silicon oxide to silicon etching and the potential to achieve SiO_2/Si etching selectivity using this etching approach.

To obtain insights on changes in surface chemistry, X-ray photoelectron spectroscopy (XPS) has been performed at various characteristic points throughout the ALE process. To study periodic, quasi steady-state conditions, all measurements were performed when the etch behavior was nearly identical from cycle to cycle. Measurements were performed by a Vacuum Generators ESCALAB MK II surface analysis system after vacuum transfer to avoid exposure to air. Narrow scan spectra of the Si 2p, C 1s, O 1s, and F 1s were obtained at 20 eV pass energy at an electron take-off angle of 20° (shallow probing depth ≈20 to 30 Å) and 90° (deep probing depth ≈80 Å) with respect to the sample surface. Spectra were charge compensated by calibrating the binding energy position of the Si-Si peak to 99.3 eV, and fitted using a least square fit after Shirley background subtraction.[23, 24] Si 2p spectra were fit with peaks corresponding to Si-Si, SiF, SiF_2, SiF_3, SiC, SiO_2, and fluorinated silicon oxide. C 1s spectra were fit

with peaks corresponding to C-C, SiC, C-CF_x (x = 1, 2, and 3), CF, CF_2, and CF_3. O 1s spectra were fit with peaks corresponding to SiO_2 and fluorinated silicon oxide. F 1s spectra were fit with peaks corresponding to SiF_x (x = 1, 2, and 3), fluorinated silicon oxide, and CF. Additional information about this analysis can be found in previous publications[24, 32, 69-72, 81] and also will be subject of a future publication.[82]

5.3 Results

A cyclic process is employed to realize atomic layer etching (ALE) of silicon oxide and silicon on the order of several Ångstrom per cycle. One cycle consists of a deposition step and an etch step, as schematically shown in Fig. 5.1. Precise precursor injection at the beginning of each deposition step allows controlled FC film deposition at a thickness in the Ångstrom range. After allowing the precursor to deplete for 12 s, a small bias potential in the range of -5 to -15 V is applied, creating maximum ion energies of 20 to 30 eV. This low energy Ar^+ ion bombardment induces FC film etching, mixing with the underlying substrate and etching of the mixed, reacted material.[83-85] Etch rates decrease once the FC and reacted substrate layer have been removed, and are followed by physical sputtering. These two steps can be repeated and enable control over the total etched thickness. The ion energies are below the physical sputtering threshold for silicon oxide (≈50 eV),[9] leading to a strongly time-dependent etching based on chemical etchant control, i.e. fluorine, for this material.

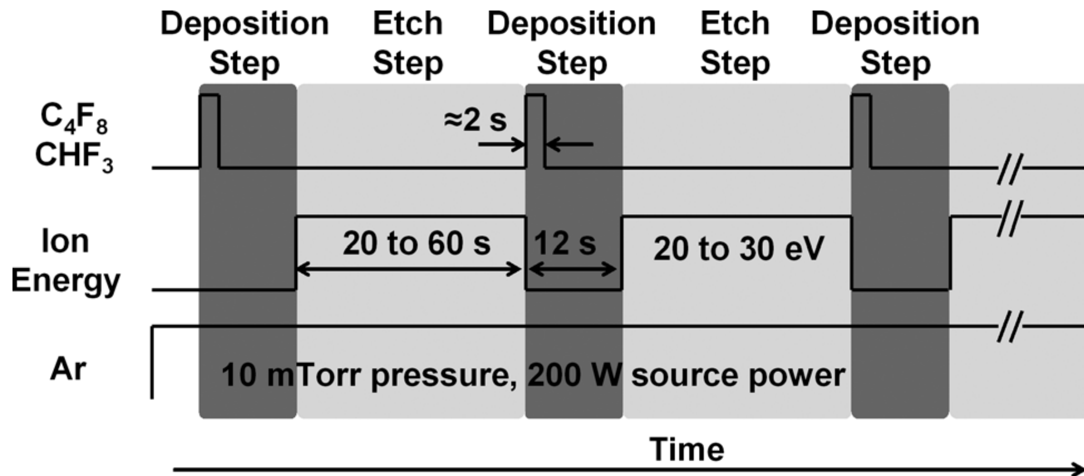

Fig. 5.1: Schematic of the cyclic ALE approach employed consisting of a repeating deposition step and etch step.

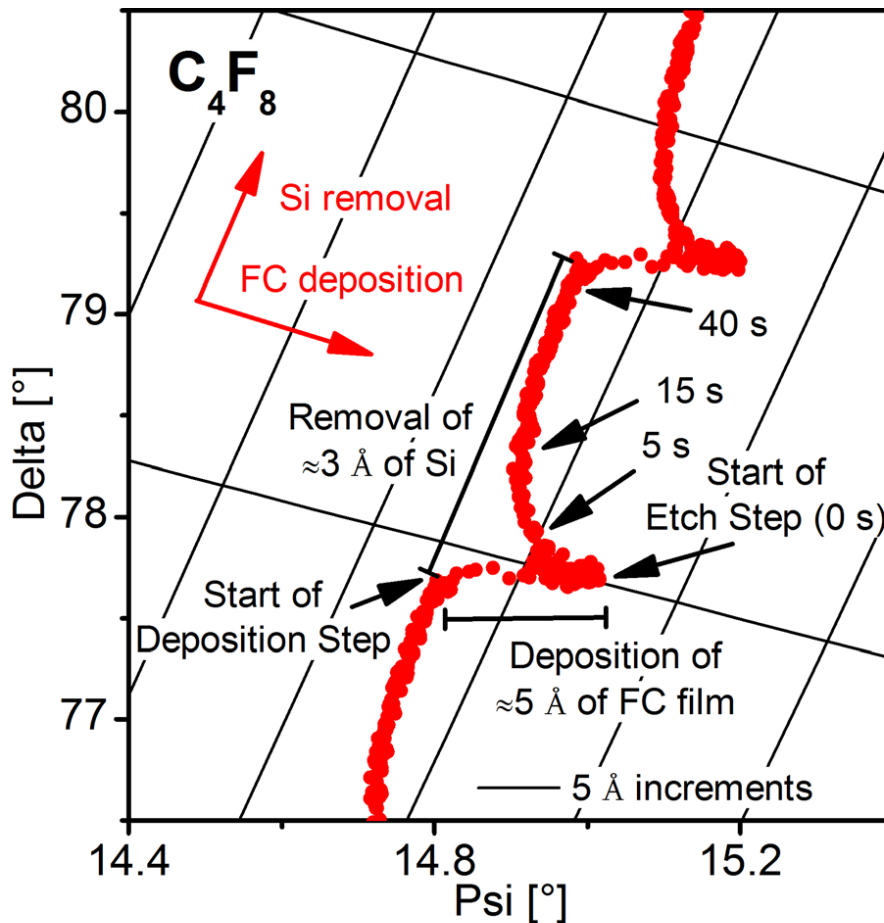

Fig. 5.2: ***In situ*** **ellipsometry of one example cycle of Si ALE for C_4F_8. The start of the etch step is marked as '0 s'. 5 s, 15 s, and 40 s of 25 eV ion bombardment are marked. 5 Å of FC film are deposited and ≈3 Å of Si are removed during each cycle.**

5.3.1 C_4F_8 based ALE

Interpretation of single wavelength ellipsometry data relies on differences in the optical properties of the materials investigated.[22] Since the FC film, fluorinated silicon, and fluorinated silicon oxide have similar refractive indices, it is difficult to distinguish the presence of these films on the substrate via single wavelength ellipsometry alone. The refractive index of elemental silicon, however, is very different, which allows to clearly separate the unreacted silicon from FC, fluorinated silicon, and fluorinated silicon oxide. Therefore, *in situ* ellipsometry allows visualization of the various phases within a single cycle of ALE of silicon. This is shown in Fig. 5.2 using C_4F_8 as a fluorocarbon film precursor. The conditions shown are for processes employing 25 eV ion energy with an etch step length of 40 s. The precursor injection conditions had been chosen to deposit 5 Å FC material on a silicon oxide substrate, and a similar amount of FC material is deposited on the Si surface. FC deposition can clearly be seen as an increase in Ψ with little change in Δ. The trajectory during initial etching does not follow the trajectory of the FC deposition, indicating fluorination and loss of silicon, driven by low energy ion bombardment. The subsequent decrease in Ψ and increase in Δ can be interpreted by the removal of FC material, fluorinated silicon and silicon oxide, and elemental silicon. Depending on processing conditions, a physical sputtering phase can be seen during a reactant-starved phase at the end of the etch step. The total Si removal per cycle is ≈3 Å for the conditions shown in Fig. 5.2 for C_4F_8. Using the same process conditions for silicon oxide ALE results in a FC film deposition of 5 Å per cycle and a material removal of ≈2 Å.

For comparison, *in situ* ellipsometry monitoring of a continuous plasma etch approach is shown in Fig. 5.3, along with data obtained for cyclic a ALE approach using 5 Å of FC film deposition per cycle and 30 eV ion energy. The continuous etch was performed at 4% C_4F_8/Ar, 200 W source power, 10 mTorr processing pressure, and 70 eV ion energy. Figure 5.3 shows clearly the formation of a thicker steady-state FC layer on the Si surface during continuous plasma etching as compared to reactant-limited ALE. The periodic injection of a precursor, in contrast to continuous addition, allows for flux-controlled etching and produces significantly thinner FC films and reacted Si layers on the Si surface, along with overall much less FC material in the system.

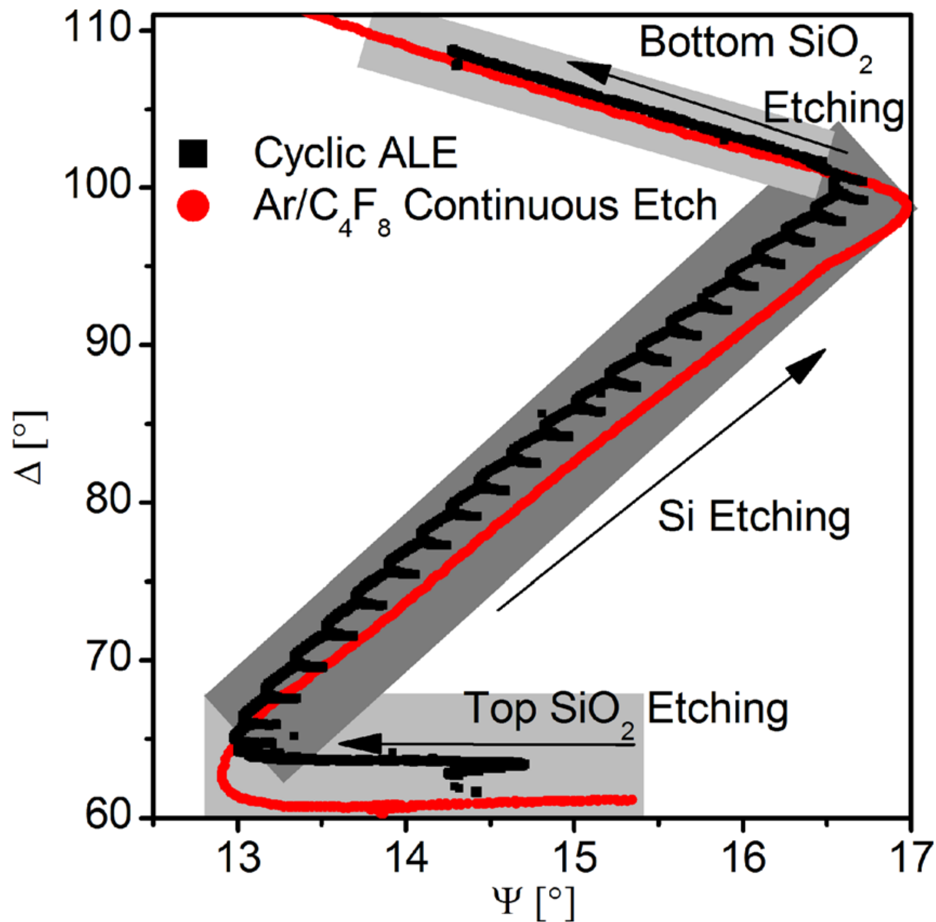

Fig. 5.3: ***In situ*** **ellipsometry of a continuous Ar/C_4F_8 etch and a cyclic ALE approach etch through a SiO_2-Si-SiO_2 stack. The areas of silicon oxide and silicon etching are marked with shaded backgrounds.**

As discussed above, the interpretation of single wavelength ellipsometry data involving materials with similar optical properties, e.g. FC films and fluorinated silicon oxide, is difficult. Combining real time ellipsometry kinetic data with X-ray photoelectron spectroscopy (XPS) surface analysis data that provide elemental analysis allowed the authors to explain the evolution during one ALE cycle in detail. The surface chemistry was measured via XPS after reaching four characteristic points throughout one cycle: 1) after completion of FC deposition, 2) after initiation of etching, 3) once the middle of the etch step was reached, and 4) at the end of the etch step.

The corresponding spectra for silicon ALE using C_4F_8 are shown in Fig. 5.4. The times shown correspond to times within one cycle, e.g. 0 s corresponds to the end of FC deposition, right after which the bias potential is applied and the etch step starts. Other spectra were taken after 5 s, 15 s, and 40 s of low energy Ar^+ ion bombardment. In this article we present the raw data, whereas detailed analysis of these spectra is in progress, and will be described in a future publication. The following statements are based on this more thorough analysis.

A strong FC film removal takes place upon ion bombardment, predominately in the form of C-F_x species (x = 1, 2, and 3) removal. The F/C ratio of the film, based on decomposition of the C 1s spectra,[69] decreases from ≈0.45 after deposition to ≈0.2. This strong decrease is already seen after only 5 s of ion bombardment. Most of this removal takes place within the first 15 s of ion bombardment as the C 1s signal after 15 s and 40 s of ion bombardment is comparable. The real time ellipsometry, shown in Fig. 5.2, confirms this observation and shows only little change in the FC film thickness after 15 s

of ion bombardment. Furthermore, a residual carbon film is seen in XPS at the end of the etch step, i.e. after 40 s of ion bombardment.

The Si 2p spectra show two main signal peaks located at 99.5 eV and 104.2 eV. The peak at the lower binding energy originates from silicon related species while the one at higher binding energies originates from silicon oxide related species. The overall amount of fluorinated silicon, located at binding energies from 100 to 103 eV, is relatively low. It has to be noted that the asymmetry of the elemental silicon peak is due to spin-orbit splitting of the signal,[70] rather than chemical shifts. Thus, the majority of the lower binding energy signal originates from elemental silicon.

The scans at each time point show a significant O 1s signal. Additional studies performed with bulk, crystalline silicon substrates with a native oxide show that the oxide layer is fluorinated but never fully removed, even after more than 30 cycles of ALE. The silicon removal is therefore taking place with a fluorinated silicon oxide layer on top of the silicon substrate. An increase in the O 1s signal is seen as the etch moves to a reactant-starved condition, i.e. the later part of the etch step, showing a formation of a fluorinated oxide layer on top of the silicon. One possible oxygen source is the interaction of the steady-state Ar plasma with the quartz coupling window.[18, 86, 87]

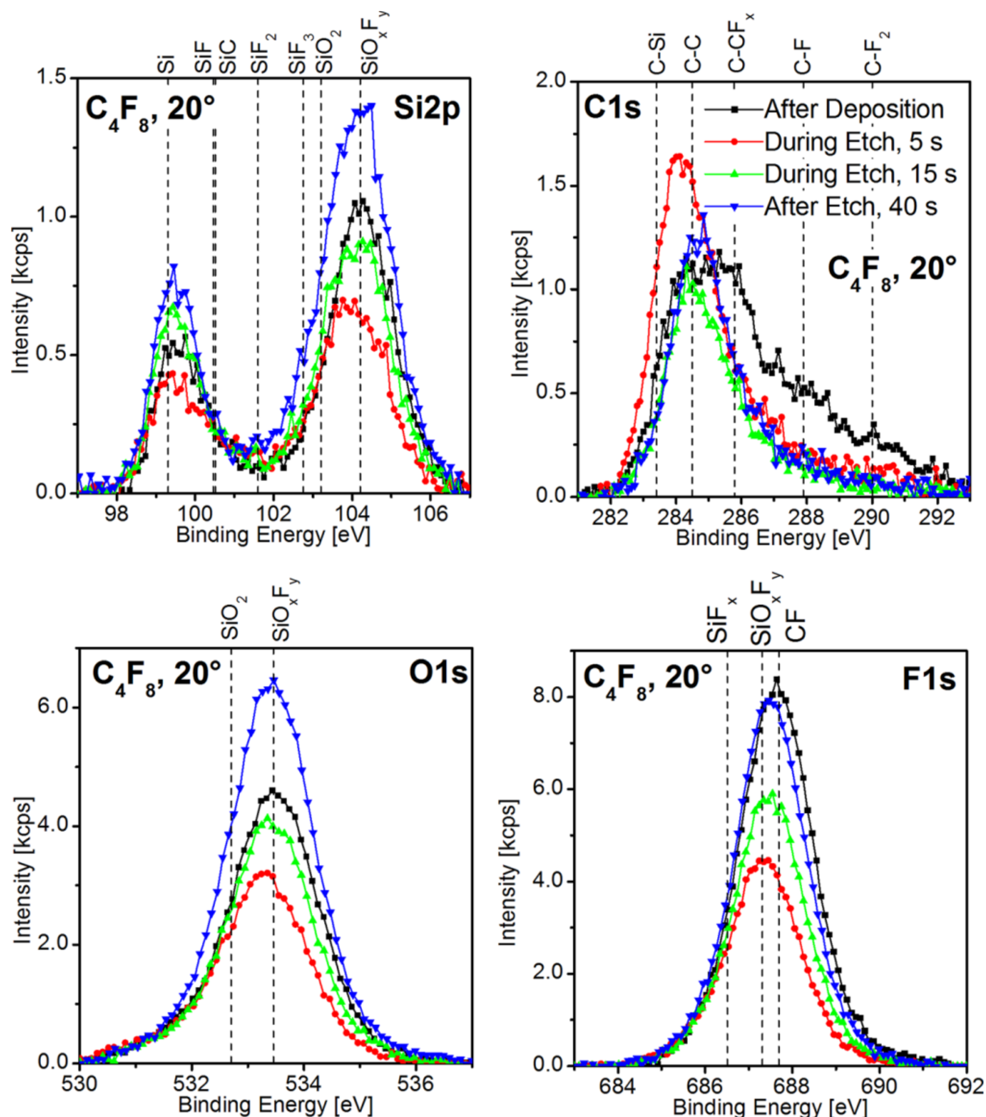

Fig. 5.4: XPS spectra comparing Si ALE using C_4F_8 after the deposition step, during the etch step, and at the end of the etch step.

5.3.2 CHF_3 based ALE

The choice of precursor has a significant impact on the etching behavior. Using CHF_3 as a precursor instead of C_4F_8 has been explored. Figure 5.5 shows the *in situ* ellipsometry trajectory of silicon ALE using CHF_3 as a precursor. The deposition step and etch step can clearly be distinguished in the trajectory. A strong increase in Ψ is seen upon precursor injection, corresponding to a FC film deposition of ≈11 Å. Detailed

optical modeling and examination suggests an apparent silicon loss during the deposition step. This loss could be based on formation of fluorinated silicon, silicon carbide, spontaneous etching due to hydrogen or fluorine interaction, or a combination of these. The FC film deposition can lead to a fluorination of the substrate, which would show as an apparent silicon loss in ellipsometry. However, XPS spectra do not suggest a significant increase in fluorinated silicon upon deposition. Similarly, formation of silicon carbide, due to film deposition, would also show an apparent silicon loss in ellipsometry. Additionally, the hydrogen from the CHF_3 precursor as well as the fluorine can react with the fluorinated silicon substrate, forming volatile species.[88] The total silicon removed per cycle is ≈6 Å for the conditions shown in Fig. 5.5. The same process conditions result in a FC film deposition of 5 Å per cycle and a material removal of ≈4 Å per cycle for silicon oxide ALE.

The surface chemistry during the ALE cycle using CHF_3 as a precursor is shown in Fig. 5.6. A strong decrease in the F 1s can be seen during the etch step. A small O 1s signal is seen during all stages of the ALE cycle. The signal does not change strongly during the cycle compared to other spectra, e.g. the F 1s and C 1s. Since ellipsometry shows a decrease in silicon thickness, the etching is taking place while a fluorinated silicon oxide layer is present. The Si 2p spectra show a significant intensity around 104 eV, corresponding to this fluorinated silicon oxide. A relatively small fluorinated silicon signal is observed. The majority of the signal around 99.5 eV is due to elemental silicon. The asymmetry of this peak is based on spin-orbit splitting,[70] rather than chemical shifts. Strong FC film removal is observed during the etch step. The high binding energy shoulder in the C 1s spectra, related to $C\text{-}F_x$ species ($x = 1, 2$, and 3), is significantly

reduced after only 5 s of ion bombardment. A strong FC film defluorination takes place as the F/C ratio drops from ≈0.6 after deposition to ≈0.2 after 40 s of ion bombardment at the end of the etch step. This defluorination and FC film removal takes place more gradually than for C_4F_8 and is seen to occur over the whole etch step length. This is evident from the continuous decrease of the C 1s signal and is consistent with the real time ellipsometry data.

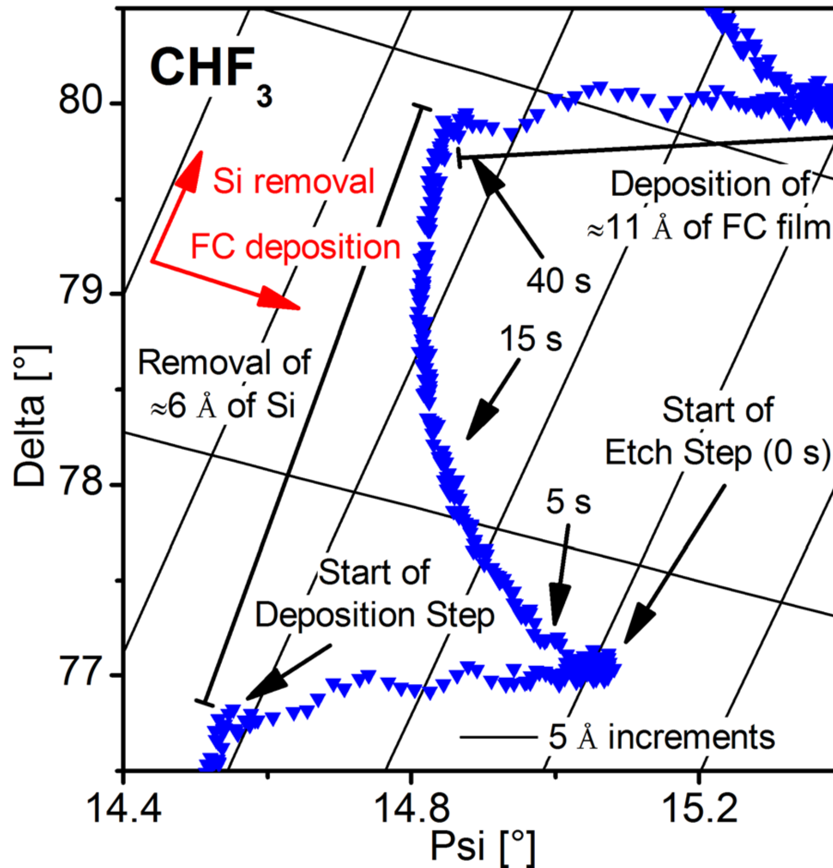

Fig. 5.5: ***In situ*** **ellipsometry of one example cycle of Si ALE for CHF_3. The start of the etch step is marked as '0 s'. 5 s, 15 s, and 40 s of 25 eV ion bombardment are marked. ≈11 Å of FC film are deposited and ≈6 Å of Si are removed during each cycle.**

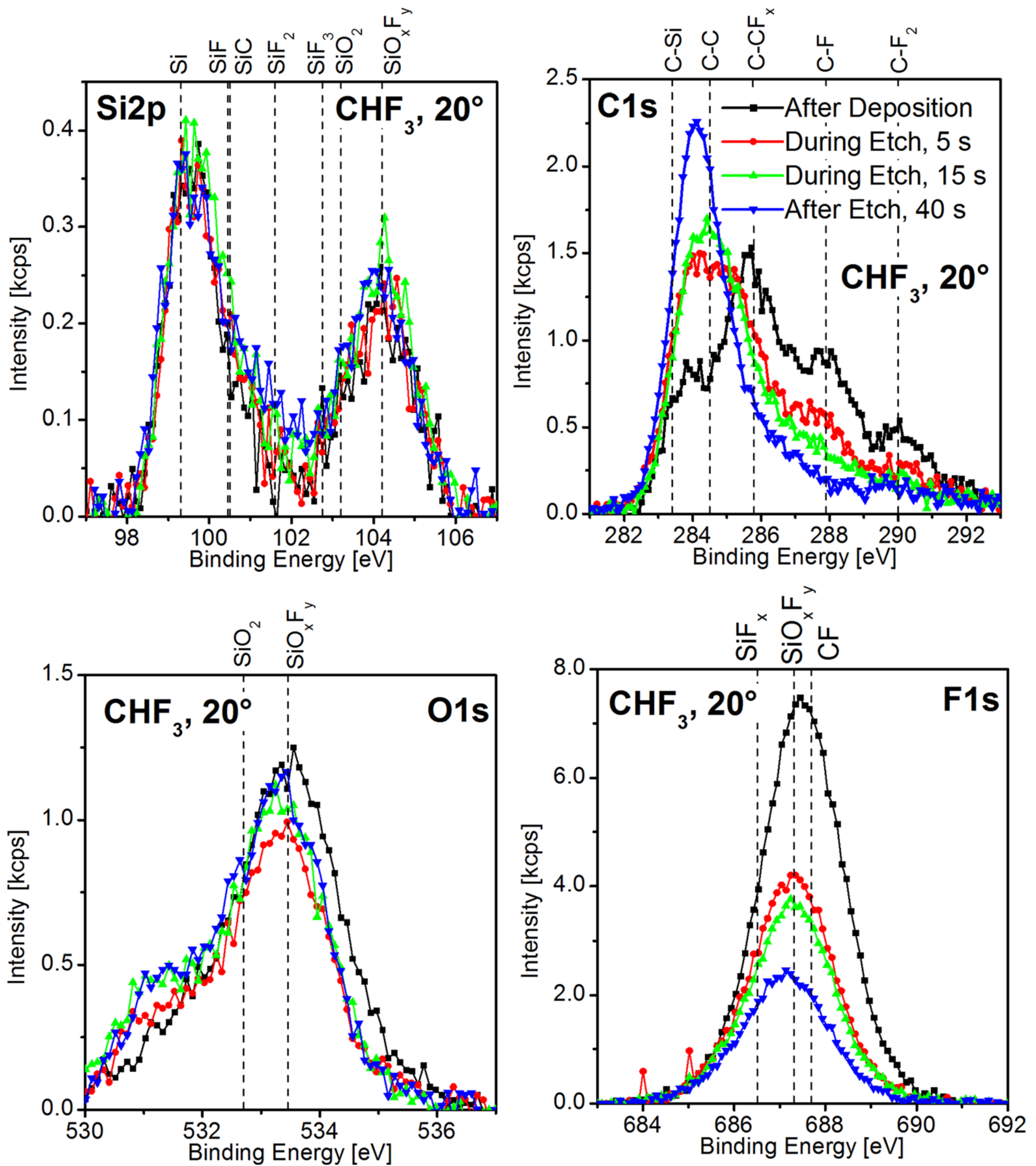

Fig. 5.6: XPS spectra comparing Si ALE using CHF_3 after the deposition step, during the etch step, and at the end of the etch step.

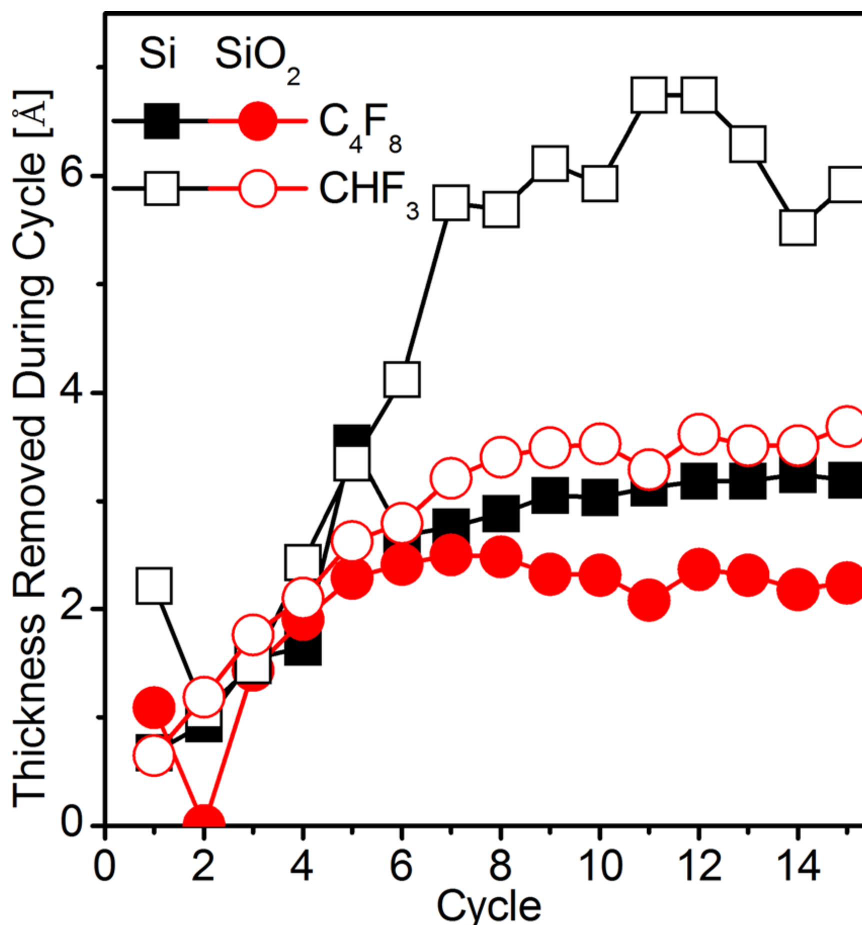

Fig. 5.7: Thickness removal during the cycle as determined by ellipsometry for ALE of Si and SiO_2 using C_4F_8 and CHF_3 at 25 eV ion energy and 40 s etch step length.

5.3.3 Etched Material per Cycle

Figure 5.7 shows the amount of material etched during each cycle for ALE of silicon and silicon oxide using C_4F_8 and CHF_3 at 25 eV ion energy and 40 s etch step length. The precursor injection has been set for a deposition of 5 Å of FC film per cycle on a silicon oxide substrate. These conditions are identical to the ones discussed in section III A. and B. The average removal per cycle is higher for CHF_3 compared to C_4F_8. This can be explained for silicon oxide by the higher F/C ratio of the FC film deposited. A film of similar thickness, 5 Å in this case, will provide more reactive fluorine for the chemically assisted etching and hence cause a higher material removal.

For silicon ALE, the FC film thickness deposited per cyle does additionally increase for CHF_3 based ALE, as will be described in detail in section IV A. Similar to silicon oxide, more reactive fluorine is available compared to C_4F_8 based silicon ALE leading to significantly more material removed per cycle for CHF_3. The initial increase in amount of material removal during the first 6 cycles is based on increased substrate fluorination and increased availability of reactive fluorine.[17, 73]

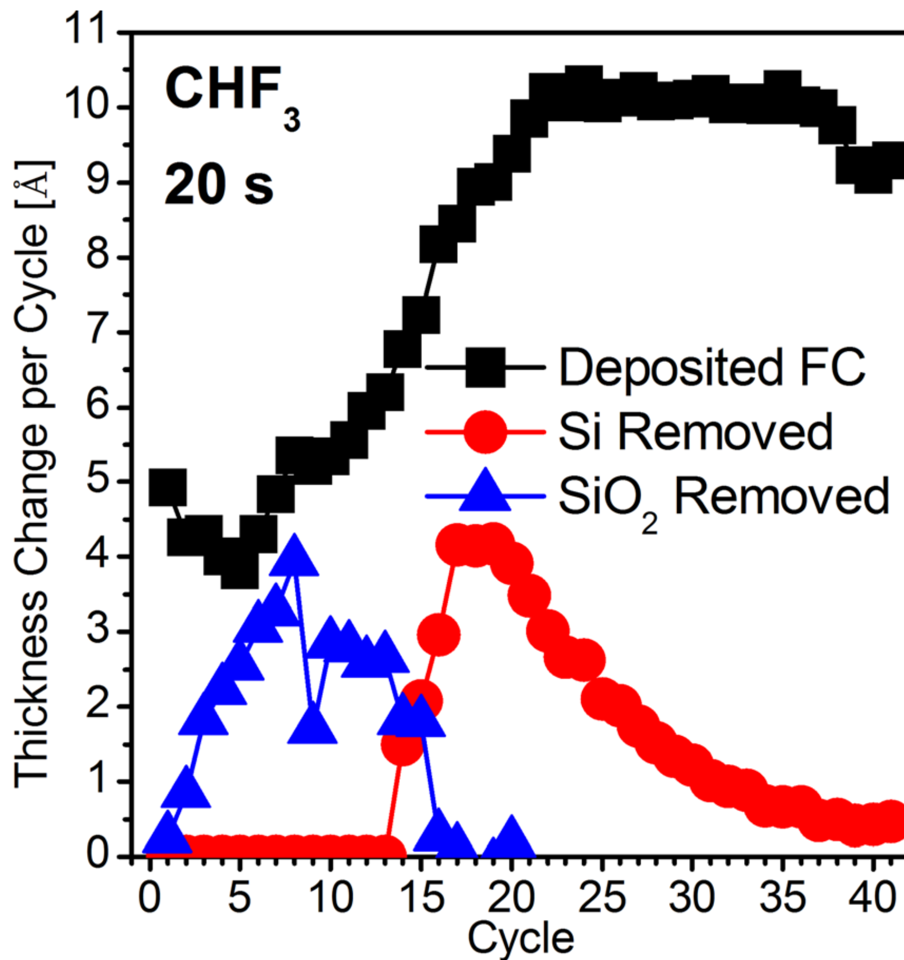

Fig. 5.8: FC film deposition, silicon removal, and silicon oxide removal during the cycle as determined by ellipsometry for ALE using CHF_3 at 25 eV ion energy and 20 s etch step length. The first 13 cycles are etching through a silicon oxide layer on top of the silicon substrate.

Reducing the etch step length from 40 s to 20 s leads to insufficient FC film removal in the case of silicon ALE using CHF_3. The relatively thick depositions of ≈11 Å of FC film per cycle cannot be fully etched within 20 s of ion bombardment. This leads to a residual film at the end of each cycle, and therefore to an overall FC film build-up from cycle to cycle. The FC film inhibits silicon etching, thus reducing the silicon removal per cycle, see Fig. 5.8. During the first 13 cycles a silicon oxide on top of the silicon substrate is etched. In cycle 14 the silicon substrate is reached. Initially clean surfaces show an increasing silicon removal of up to 4 Å per cycle. Subsequently, the silicon removal per cycle drops to less than 1 Å per cycle within 18 cycles of silicon ALE, i.e. cycle 14 to 32, as a FC film builds up on the surface. About 45 Å of silicon are etched during these 18 cycles, before the removal per cycle drops below 1 Å.

5.3.4 Atomic Force Microscopy and Langmuir Probe Characterization

The surface roughness of blanket silicon oxide surfaces was measured by atomic force microscopy (AFM) and is shown in Fig. 5.9. The processing conditions used are 10 cycles of ALE with 5 Å of FC deposition per cycle using C_4F_8 and 25 eV ion energy, identical to conditions presented and discussed in Section III A. It can be seen that SiO_2 surfaces remain smooth after the ALE, i.e. root-mean-square surface roughness values were below 0.4 nm at all points measured compared to a pristine value of 0.3 nm. This suggests a good uniformity of the process, which is essential for industrial applications.[89, 90]

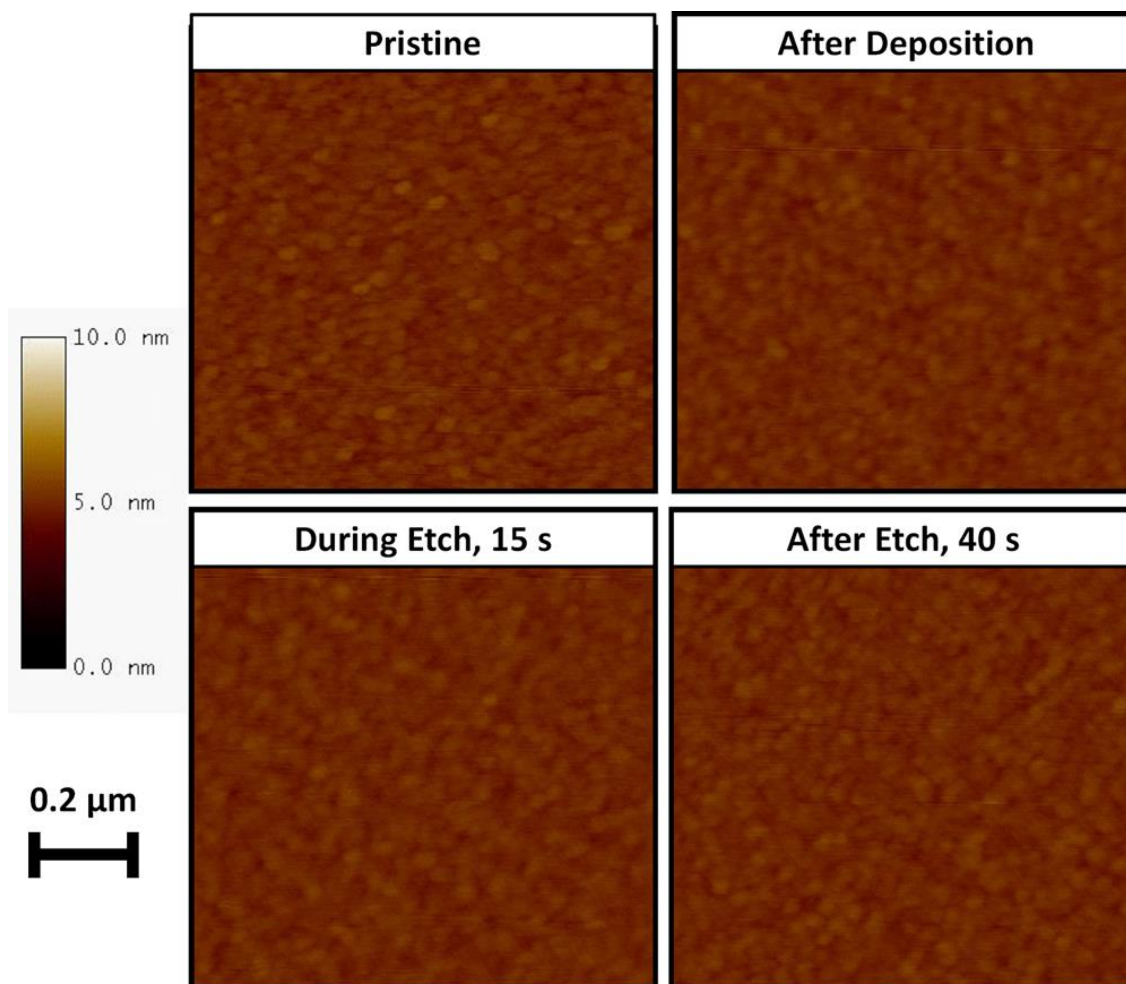

Fig. 5.9: Surface roughness as measured by AFM (1 x 1 µm^2) after 10 cycles of SiO_2 ALE with 5 Å FC deposition per cycle, 25 eV ion energy, and 40 s etch step length.

Time resolved plasma properties were measured using a Langmuir probe. In a first step, it was shown that applying a bias potential of up to 15 V does not have any significant impact on the plasma properties. Therefore, all changes observed during the cyclic Ar/C_4F_8 approach are due to precursor injection and not the application of a bias potential. Short precursor injection results in a clear change in plasma properties during each cycle and is shown in Fig. 5.10. While the plasma potential V_p and the electron temperature T_e spike, the plasma density N_e drops significantly. These changes upon C_4F_8 injection are in agreement with the impact of a continuous precursor addition.[57] A

recovery of all three plasma properties to initial values before the pulse injection is seen within ≈20 s. There is, however, a small change in plasma properties from cycle to cycle due to FC wall coverage. In agreement with continuous precursor addition, FC wall coverage leads to a decrease in V_P and N_e, and a small increase in T_e. These effects are more pronounced for longer precursor pulses. The recovery time of the plasma parameters after precursor injection is significantly longer, especially for V_p, and exceeds gas residence times. Additionally, the use of CHF_3 as a precursor instead of C_4F_8 has been explored. Overall, CHF_3 shows the same trends as C_4F_8, i.e. a brief increase in V_p and T_e and a drop in N_e, but on a smaller scale.

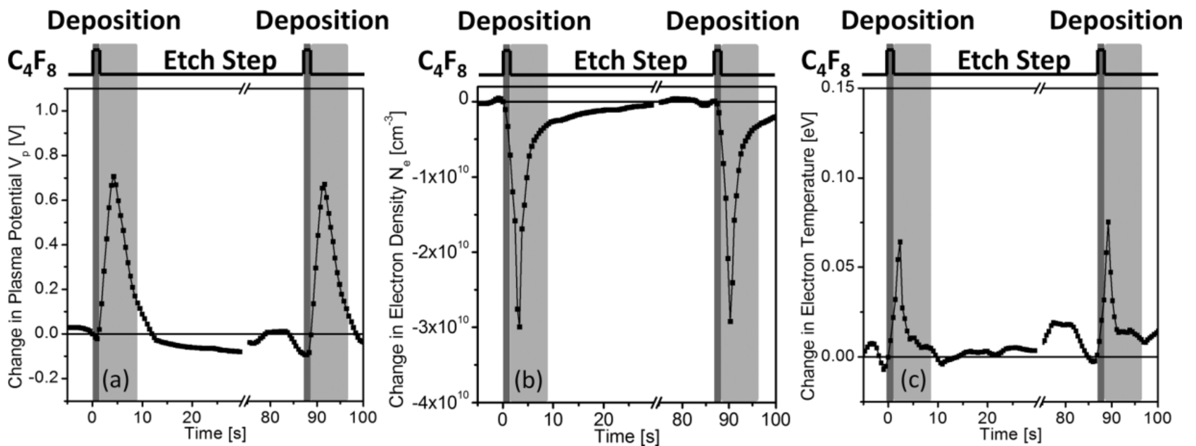

Fig. 5.10: Response in plasma parameters (a) Plasma potential V_p, (b) electron density N_e, and (c) electron temperature T_e upon brief C_4F_8 injection.

5.4 Discussion:

5.4.1 Precursor Comparison

The C_4F_8 and CHF_3 fluorocarbon gases employed here show several significant differences. The deposition yield, i.e. the amount of FC film deposited divided by the amount of precursor injected, of CHF_3 is lower than for C_4F_8. This is in agreement with the smaller impact of CHF_3 injection on the plasma properties, as described in section III D. To achieve comparable deposited FC film thicknesses as for C_4F_8, more CHF_3 needs

to be injected during the deposition step. Using C_4F_8 as a precursor shows generally only little change in the deposition behavior on silicon compared to silicon oxide. On the other hand, CHF_3 shows a strong change when transitioning from silicon oxide to silicon, see Fig. 5.8 and 5.11. The thickness increase, during the deposition step, as measured by ellipsometry, is significantly higher on silicon than on silicon oxide with the same precursor injection. A higher C 1s signal intensity is observed on silicon for CHF_3, compared to C_4F_8 for Si, and to a FC deposition on SiO_2 using CHF_3, confirming the thicker FC layer.

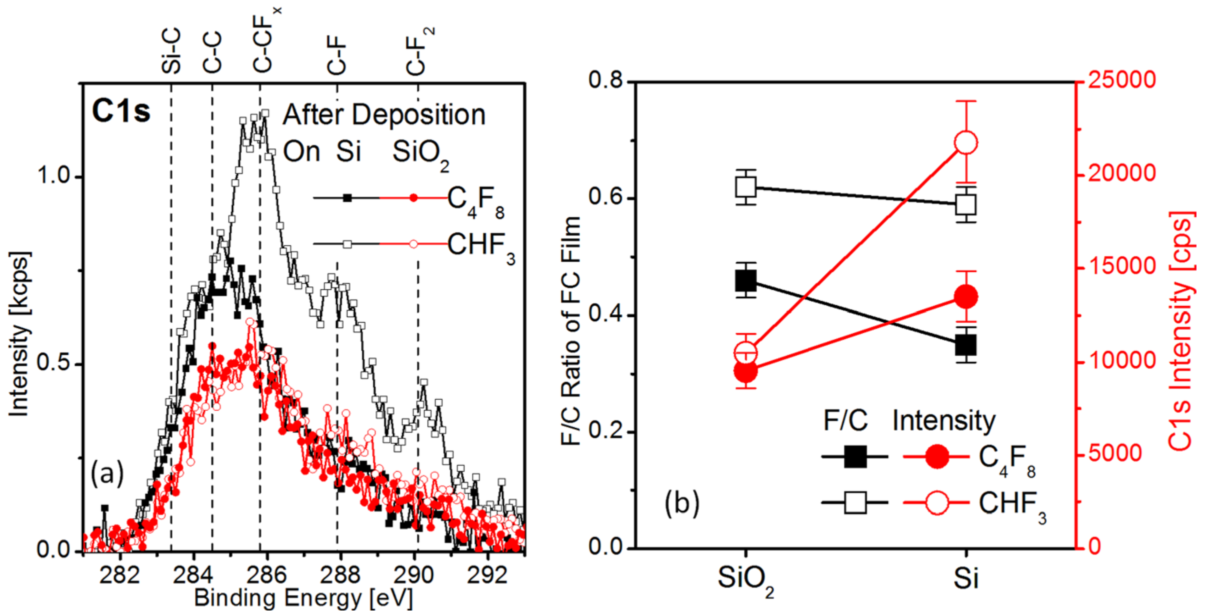

Fig. 5.11: Deposition behavior of C_4F_8 (closed symbols) and CHF_3 (open symbols) on SiO_2 and Si substrates. (a) The C 1s spectrum shows a higher intensity for CHF_3 when depositing on Si (black squares) with the same precursor injection as on SiO_2 (red circles). (b) F/C ratios of the polymer films deposited in a cyclic fashion by C_4F_8 and CHF_3.

The increase in FC deposition per cycle seen for CHF_3 can be used to achieve selective SiO_2/Si etching. Using an etch step length of 20 s shows insufficient etching of the relatively thick FC film on silicon, while etching silicon oxide under the same process conditions. As discussed in section III C. and shown in Fig. 5.8, a FC film build up

inhibits silicon etching and reduces the silicon removal per cycle. The current, non-optimized, process conditions show a relatively high total silicon removal during the FC film build up, but highlight the possibility of using this approach to achieve selective SiO_2/Si etching.

The F/C ratio of the deposited film depends on the choice of precursor and thickness of the deposited film.[9] Surface chemistry analysis after deposition of 5 Å thick FC films on the silicon oxide substrate using this cyclic process shows a higher F/C ratio for the FC film deposited by CHF_3 than C_4F_8. This is in contrast to typical continuous etch approaches, for which CHF_3 leads to a significantly fluorine-poorer steady-state film due to the impact of hydrogen.[69, 83] This demonstrates just one of many differences between ALE and continuous plasma etch approaches. Etch mechanisms and known phenomena can be very different when moving to ultra-thin layers and reactant-starved conditions. For example, Hua *et al.* also demonstrated the importance and difference of initial, short-term plasma exposure in comparison to longer, steady-state plasma etching.[91] Comparing the C 1s spectra of films deposited by C_4F_8 and CHF_3 on silicon under comparable conditions shows a similar difference in the F/C ratio of the FC films. Similar to films deposited on silicon oxide, FC films deposited on silicon by CHF_3 show a higher F/C ratio compared to films deposited by C_4F_8 for the thin films investigated here (less than 10 Å).

We observed that a fluorinated oxide layer persists during ALE of silicon using this cyclic flux-controlled process. Surface chemistry results presented above show significant intensities of the O 1s during each step of the cycle. The fluorinated oxide will interact with and is involved in the etching mechanism of the silicon substrate. For

example, for certain process conditions oxidation of the Si substrate can take place.[23] A possible source of oxygen is erosion of the quartz coupling window as described in previous publications.[18, 86, 87] This surface chemistry potentially constrains possible selective etching of silicon oxide over silicon, which can remain oxidized at the surface during etching, thus reducing substrate chemistry effects on the etching behavior. The fluorinated oxide signal is significantly stronger for C_4F_8 based etching as compared to CHF_3 based etching. Additionally, the total O 1s signal is fairly constant throughout the ALE cycle for CHF_3, while the O 1s signal increases towards the end of a cycle for C_4F_8 based ALE. It is important to note that the FC film thickness deposited per cycle is significantly higher for CHF_3, as explained above. This thicker FC film coverage can lead to stronger etching and potentially prevent surface oxidation, therefore reducing the importance of fluorinated oxide.[23, 69, 73]

5.4.2 Etch Mechanism

One challenge for control of silicon ALE is the high reactivity of a silicon surface under continuous ion bombardment. This is in contrast to silicon oxide, which exhibits a fairly inert surface, allowing controlled FC deposition and SiO_2 etching. The silicon surface is very reactive and easily undergoes oxidation by trace amounts of oxygen, and fluorination, e.g. due to plasma-chamber wall interactions.

Another challenge lies in the lower threshold for physical sputtering of silicon compared to silicon oxide.[9] The sputtering threshold for silicon oxide is ≈50 eV, while the sputtering threshold for silicon is ≈20 eV. This threshold energy is below the ion energies used for the present ALE approach, and imply that the physical sputtering rate of

silicon is still finite at the end of the ALE cycle and true self-limited etching is not achieved.

Additionally, silicon etching using the current ALE approach depends very sensitively on process conditions. While the changes in process parameters for this study were small, e.g. the FC deposition thickness per cycle was varied only over a range of a few Ångstroms, and the ion energy range was varied from 20 to 30 eV, a significant impact on Si etching behavior was observed. Our work has shown that rigorous control of process parameters and chamber conditions are essential to maintain high precision etch control for ALE. For instance, FC material on the chamber walls is a source of additional chemical etchant and can prevent self-limited etching.[92]

The etch step length, i.e. time of ion bombardment during each cycle, is a very important process parameter. This etch step length is a "new process parameter" as there is no equivalent in conventional continuous plasma etching, and highlights the increased flexibility of cyclic ALE processes. The etch step length impacts the FC depletion from the surface. Short etch steps do not remove sufficient amounts of FC, leading to an overall fluorine-rich situation, and prevent reactant controlled etching. Longer etch steps remove more FC from the surface and fluorine from the substrate. However, avoiding extended ion bombardment of the substrate minimizes silicon damage and potential oxidation. Additionally, long etch steps exhibit extended physical sputtering of silicon.

The goal of this work is to characterize the etch mechanism involved in Si ALE rather than achieving high SiO_2/Si selectivity. Therefore, results presented here show limited selectivity of silicon oxide over silicon etching for the conditions examined. The authors are currently investigating the impact of etch step length, FC film thickness, ion

bombardment energies and FC precursor chemistry on silicon etch behavior and silicon oxide over silicon etching selectivity. It is expected that a carefully chosen combination of shorter etch step lengths, thicker FC film deposition per cycle, and the use of CHF_3 is beneficial for achieving high selectivity and will be discussed in detail in a future publication.[82] Using CHF_3 compared to C_4F_8 for cyclic ALE is shown to have a higher potential for high SiO_2/Si selectivity. This is in contrast to continuous plasma etch approaches, for which C_4F_8 shows higher SiO_2/Si selectivity.[23, 81] Hudson *et al.* reported achieving highly selective silicon oxide over silicon nitride etching using a similar cyclic approach of alternating FC deposition and low energy ion bombardment.[93, 94] The approach utilizes a film build-up based on a difference in FC film etch rate on top of a silicon oxide substrate compared to a silicon nitride substrate. Each cycle leaves a residual film, adding up from cycle to cycle and eventually prohibiting further substrate etching.

5.5 Summary and Conclusions:

The cyclic Ar/C_4F_8 ALE approach established for silicon oxide has been extended to silicon ALE. The FC film thickness deposited per cycle determines the amount of fluorine available and strongly controls material removal. The ion energy has a high impact on observed Si etch rates. As compared to silicon oxide, less variation of the silicon etch rate during a cycle is seen. This can be explained by the fact that the physical sputtering energy threshold of about 20 eV for silicon is significantly lower than that of SiO_2 and prevents true self-limited etching for the conditions employed. The etch step length is expected to play a major role in achieving ultra-high etching selectivity of silicon oxide over silicon etching. CHF_3 is shown to exhibit a significantly thicker FC

film deposition on silicon than on silicon oxide for comparable injection parameters than when C_4F_8 is used as a film precursor. For the latter, little substrate dependence on FC film deposition is seen. The change in FC film deposition observed for CHF_3 is shown to enable selective SiO_2/Si etching. The F/C ratio of thin films deposited by CHF_3 is higher than for FC films deposited by C_4F_8. A significant fluorinated silicon oxide layer is observed on the surface during silicon ALE when C_4F_8 is used as a precursor, and involved in the etching mechanism of silicon. The surface chemistry changes throughout a cycle depend on process conditions, e.g. FC film thickness deposited per cycle. Precursor injection has been shown to have a strong, but brief impact on measured plasma parameters. Consistent with continuous precursor injection, the plasma potential and electron temperature increase, while the electron density drops.

The authors are currently investigating the impact of FC film thickness deposited per cycle, ion energy, etch step length and precursor chemistry on the etch mechanism in detail. The surface chemistry is being analyzed in detail to establish a more complete picture of the surface chemical processes underlying the ALE process. This employs the correlation of *in situ* ellipsometry data with more detailed analysis of XPS data.

Acknowledgments

We thank Andrew Knoll, Dr. Nick Fox-Lyon, Adam Pranda, Pingshan Luan, and Dr. Elliot Bartis for collaboration and helpful insights and discussion on this project. We thank Drs. Eric Hudson, Steven Lai, Michal Danek, and Alexander Dulking from Lam Research for helpful discussions. We gratefully acknowledge financial support of this work by the National Science Foundation under award No. CBET-1134273 and US Department of Energy (DE-SC0001939).

Chapter 6: Characterizing Fluorocarbon Assisted Atomic Layer Etching of Si Using Cyclic Ar/C_4F_8 and Ar/CHF_3 Plasma

D. Metzler [a)], C. Li [b)], S. Engelmann [c)], R. L. Bruce [c)], E. A. Joseph [c)], G. S. Oehrlein [a)]

[a)]Department of Materials Science and Engineering
And Institute for Research in Electronics and Applied Physics
University of Maryland, College Park, Maryland 20740

[b)]Department of Physics
And Institute for Research in Electronics and Applied Physics
University of Maryland, College Park, Maryland 20740

[c)]IBM T.J. Watson Research Center
Yorktown Heights, New York 10598

Journal of Vacuum Science & Technology A, in preparation

Abstract:

With the increasing interest in establishing directional etching methods capable of atomic scale resolution for fabricating highly scaled electronic devices, the need for development and characterization of atomic layer etching (ALE) processes is growing. In this work, a flux-controlled cyclic plasma process is used for etching of SiO_2 and Si at the Angstrom-level. This is based on steady-state Ar plasma, periodic, with precise injection of a fluorocarbon (FC) precursor (C_4F_8 and CHF_3), and synchronized, plasma-based Ar^+ ion bombardment [D. Metzler *et al.*, J Vac Sci Technol A **32**, 020603 (2014), and D. Metzler *et al.*, J Vac Sci Technol A **34**, 01B101 (2016)]. For low energy Ar^+ ion bombardment conditions, physical sputter rates are minimized, whereas material can be etched when FC reactants are present at the surface. This cyclic approach offers a large parameter space for process optimization. Etch depth per cycle, removal rates, and self-limitation of removal, along with material dependence of these aspects, were examined as a function of FC surface coverage, ion energy, and etch step length using *in situ* real time ellipsometry. The deposited FC thickness per cycle is found to have a strong impact on etch depth per cycle of SiO_2 and Si, but is limited with regard to control over material etching selectivity. Ion energy over the 20 to 30 eV range strongly impacts material selectivity. The choice of precursor can have a significant impact on the surface chemistry and chemically enhanced etching. CHF_3 has a lower FC deposition yield for both SiO_2 and Si, and also exhibits a strong substrate dependence of FC deposition yield, in contrast to C_4F_8. The thickness of deposited FC layers using CHF_3 is found to be greater for Si than for SiO_2. X-ray photoelectron spectroscopy was used to study surface chemistry. When thicker FC films of 11 Å are employed, strong changes of FC film

chemistry during a cycle are seen whereas the chemical state of the substrate varies much less. On the other hand, for FC film deposition of 5 Å for each cycle, strong substrate surface chemical changes are seen during an etching cycle. The nature of this cyclic etching with periodical deposition of thin FC films differs significantly from conventional etching with steady-state FC layers since surface conditions change strongly throughout each cycle.

6.1 Introduction

Advanced semiconductor manufacturing sets high demands for etch precision and material selectivity.[7, 8] Consequently, the field of atomic layer etching (ALE) has seen a great increase in interest during recent years.[9-11, 14] Many different types of processes aiming to achieve atomic resolution are being investigated.[95] Atomic layer deposition (ALD) is an established and widely employed process for device fabrication.[3, 78-80] Several advances made and insights gained in the field of ALD are being exploited to drive forward the development of ALE methods.[96] For example, spatially resolved ALE, based on existing processing methods for ALD, is being investigated to negate low wafer throughput, one of the obstacles of ALE processing.[97]

Many ALE processes offer a larger parameter space and more process adaptability than continuous etching processes. It is therefore important to characterize the influence of process parameters and surface chemistry on ALE mechanisms. One attractive approach is a flux controlled etching process. This process offers high flexibility because of the possibility to balance reactive surface chemistry and low energy ion bombardment. Controlled, precise etching of SiO_2 and Si based on such a flux controlled, cyclic Ar plasma has been described previously.[73, 98] Additionally, the process has shown promise for device patterning on a manufacturing scale.[89] In this article we further characterize this process, especially with regard to process parameter impact on etch behavior, material etching selectivity, and surface chemistry. Additionally, several interesting phenomena have been observed and will be presented here.

6.2 Experimental

Processing conditions employed closely match our previous work[73, 98] and are briefly described here. This work was performed using an inductively coupled plasma system. A planar, water-cooled brass coil above a quartz window was powered by a 13.56 MHz power supply with an L-type matching network. The source power, processing pressure, and Ar flow were kept constant at 200 W, 10 mTorr, and 50 sccm, respectively. The plasma was confined within a 195 mm diameter anodized Al confinement ring. A 125 mm diameter silicon substrate is located 150 mm below the top electrode on an electrostatic chuck. Independently biasing the bottom electrode at 3.7 MHz allowed a RF self-bias potential of -5 to -15 V, creating maximum ion energies of about 20 to 30 eV. The base pressure achieved prior to processing was in the $5x10^{-7}$ Torr range. The temperature of the samples (25 x 25 mm^2) was stabilized at 10°C by substrate backside cooling during plasma processing. In order to minimize impacts of atmospheric exposure of both the sample and processing chamber, a load lock and vacuum transfer were used for all experiments. A standard O_2 plasma-based cleaning process and an Ar plasma-based conditioning process between each experiment ensured processing conditions were as comparable as possible for each experiment. Additional details of the plasma system have been described previously.[19-21]

Material removal was studied by *in-situ* ellipsometry.[22] The ellipsometer was an automated rotating compensator ellipsometer working in the polarizer-compensator-sample-analyzer (PCSA) configuration at a ≈72° angle of incidence. Measurements were performed in Ψ-Δ-space, corresponding to changes in phase and relative amplitude of the polarized laser light components (He-Ne laser, λ = 632.8 nm). Optical multilayer

modeling was used for interpretation of recorded data and to establish real-time thickness changes of various films. The materials studied were SiO_2-Si-SiO_2 stacks deposited on a silicon substrate by PECVD techniques with various thicknesses. Using SiO_2-Si-SiO_2 stacks allowed for precise thickness measurements as well as investigating the transition from SiO_2 to Si etching and the potential to achieve SiO_2 over Si etching selectivity.

To obtain insights on surface chemistries, X-ray photoelectron spectroscopy (XPS) has been performed at various characteristic points after the ALE process after vacuum transfer of the sample. All measurements were performed when the etch behavior was nearly identical from cycle to cycle in order to study quasi-steady-state conditions. Measurements were performed by a Vacuum Generators ESCALAB MK II surface analysis system after vacuum transfer to avoid exposure to air. Narrow scan spectra of the Si 2p, C 1s, O 1s, and F 1s binding energy regions were obtained at 20 eV pass energy at an electron take-off angle of 20° (shallow probing depth ≈20 to 30 Å) and 90° (deep probing depth ≈80 Å) with respect to the sample surface. Results presented and discussed here typically focus on shallow probing depths to emphasize the very surface. Spectra were surface charge compensated by calibrating the binding energy position of the Si-Si peak to 99.3 eV, and fitted using a least square fit after Shirley background subtraction.[23, 24] Si 2p spectra were fit with peaks corresponding to Si-Si, SiF, SiF_2, SiF_3, SiC, SiO_2, and fluorinated silicon oxide (SiO_xF_y). C 1s spectra were fit with peaks corresponding to C-C, SiC, C-CF_x ($x = 1, 2$, and 3), CF, CF_2, and CF_3. O 1s spectra were fit with peaks corresponding to SiO_2 and fluorinated silicon oxide. F 1s spectra were fit with peaks corresponding to SiF_x ($x = 1, 2$, and 3), fluorinated silicon oxide, and CF. All fittings were required to show consistency across all individual spectra, i.e. the chemical

information extracted from Si 2p, C 1s, O 1s and F 1s was internally consistent. Additional information about this analysis method can be found in previous publications.[24, 32, 69-72, 81, 98]

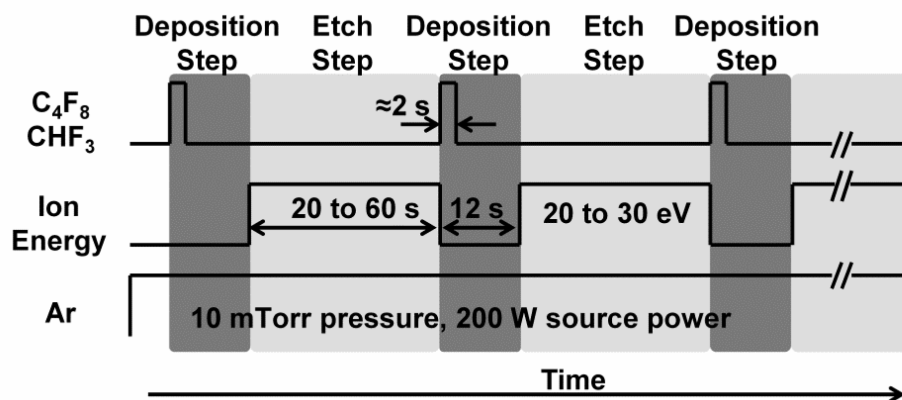

Fig. 6.1: Schematic of the cyclic ALE approach employed consisting of a repeating deposition step and etch step. The process parameters varied are the FC film deposition per cycle, the ion energy during the etch step, and the etch step length.

6.3 Results and Discussion

6.3.1 Cyclic Processing

The cyclic process used for the fluorocarbon (FC) based atomic layer etching (ALE) discussed here has been described in detail previously and is schematically shown in Fig. 6.1.[73, 98] Each cycle consists of two steps, the reactant deposition step and the etch step. During the reactant deposition step a short, precise precursor injection allows for controlled, thin FC film deposition. Sufficient time is given to allow for the deposition to saturate and any precursor in the gas phase to be pumped out. Subsequently, a bias potential is applied to induce low energy Ar^+ ion bombardment during the etch step. The two steps are repeated in a cyclic fashion enabling precise control over material removal. Etch rates are chemically enhanced as long as a chemical etchant, F in this case, is present on the surface, but will decrease once it is depleted.[83-85] This leads to time-

dependent etch rates, i.e. material etch rates change throughout each cycle. The instantaneous etch rate, i.e. etch rate at a given point in time, has an impact on the etch depth per cycle, i.e. amount of substrate material removal per cycle. If instantaneous etch rates are overall lower during a given cycle, the total removal per cycle will be lower. However, the etch depth per cycle is also dependent on the etch step length.

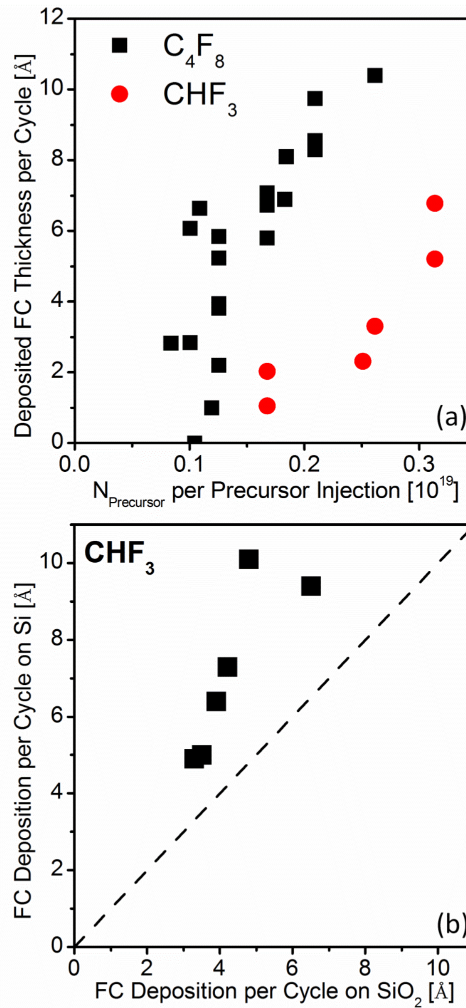

Fig. 6.2: (a) Deposited FC film thickness per cycle dependent on the amount of precursor injected per pulse, depicted by the number of molecules $N_{precursor}$. CHF_3 shows an overall lower deposition yield than C_4F_8. (b) FC film deposition per cycle on Si compared to deposition on SiO_2. The FC deposition is seen to increase during the process when transitioning from a SiO_2 to Si substrate. C_4F_8 does not show a change in deposition based on substrate material.

6.3.2 Fluorocarbon Film Deposition

The FC film composition and thickness deposited during each cycle plays an essential role in the etching of SiO_2 and Si. The film provides a limited amount of F as a chemical etchant to the surface during each cycle, and it is important to characterize the FC film deposition. The deposited film thickness per cycle based on the precursor injection, i.e. the number of precursor molecules in each pulse, is shown in Fig. 6.2 (a). C_4F_8 has a higher deposition yield than CHF_3, leading to an easier control of very thin FC deposition by CHF_3. Lower deposition yields make resulting film thickness less dependent on small fluctuations in the number of precursor molecules injected. A shift in deposition behavior was observed when comparing deposition on the substrate and on an already existing FC film. Previous work has shown a change in FC film composition based on its thickness.[73] Figure 6.2 (a) additionally shows an initial onset for FC film deposition. A linear increase in film thickness can be observed when injecting at least $0.15*10^{19}$ molecules per pulse. A relatively sharp drop off in deposited thickness is seen for small precursor injections.

CHF_3 showed a deposition behavior not observed for C_4F_8. For CHF_3, the deposition yield showed a dependence on whether a SiO_2 or Si substrate was used for the FC film deposition. Figure 6.2 (b) shows the deposited FC film thickness on Si as compared to deposited thickness on SiO_2 for several process conditions. Each data point was taken as an average over several cycles within the same experiment. The deposited thickness increases significantly for CHF_3 when depositing on Si instead of SiO_2. This increase in deposition has also been confirmed via XPS surface analysis.[98] An example of the evolution of FC deposition from cycle to cycle can be seen in Fig. 6.3. A SiO_2-Si-

SiO_2 stack was etched using CHF_3 and an ion energy of 25 eV. The first 15 cycles etched through the top SiO_2 layer, depositing about 4 Å of FC film each cycle. The SiO_2-Si interface was reached around cycle 15. The etching of the silicon interlayer is also shown, and provides information on the etching depth in the SiO_2/Si/SiO_2 stack. The FC deposition can be seen to rapidly increase to ≈7.5 Å per cycle within 5 cycles. It is noteworthy that the external processing parameters, such as the precursor injection, have been kept constant throughout the whole experiment.

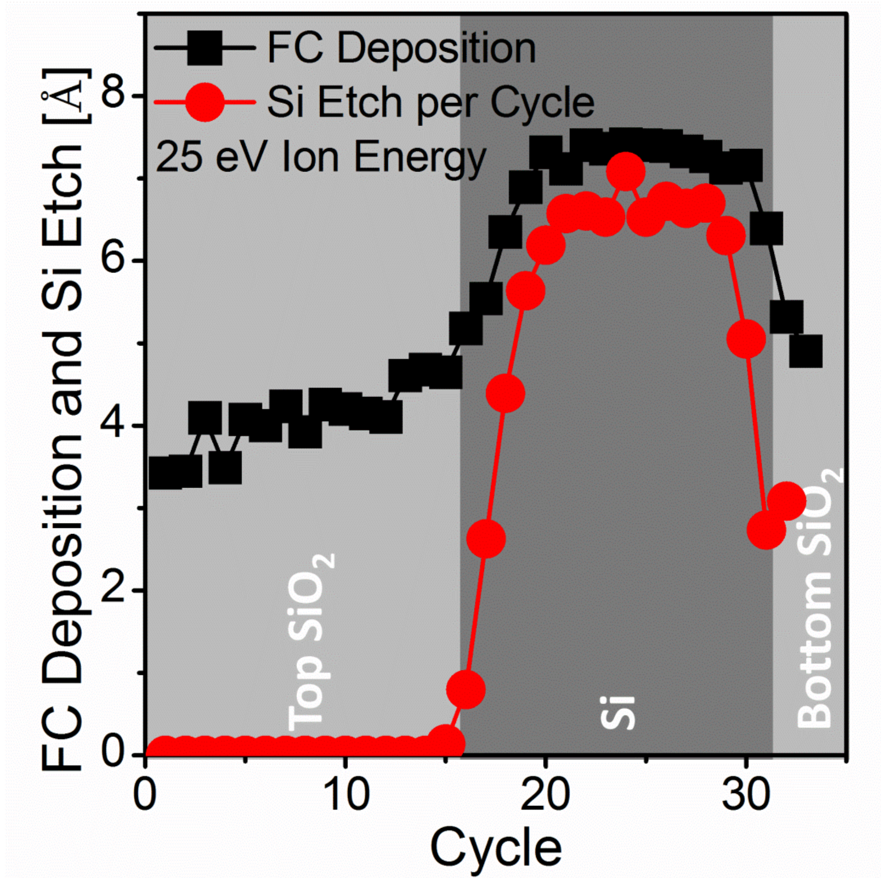

Fig. 6.3: FC film deposition (black squares), and amount of Si etched (red circles) during each cycle. Processing conditions are CHF_3 precursor injection with a 40 s etch step at 25 eV ion energy. A schematic of the sample stack is shown as an inset. The initial 15 cycles are etching SiO_2 on top of the Si. Once the Si layer is reached, the Si etching starts and the FC deposition increases. Around cycle 30 the Si layer is completely etched away.

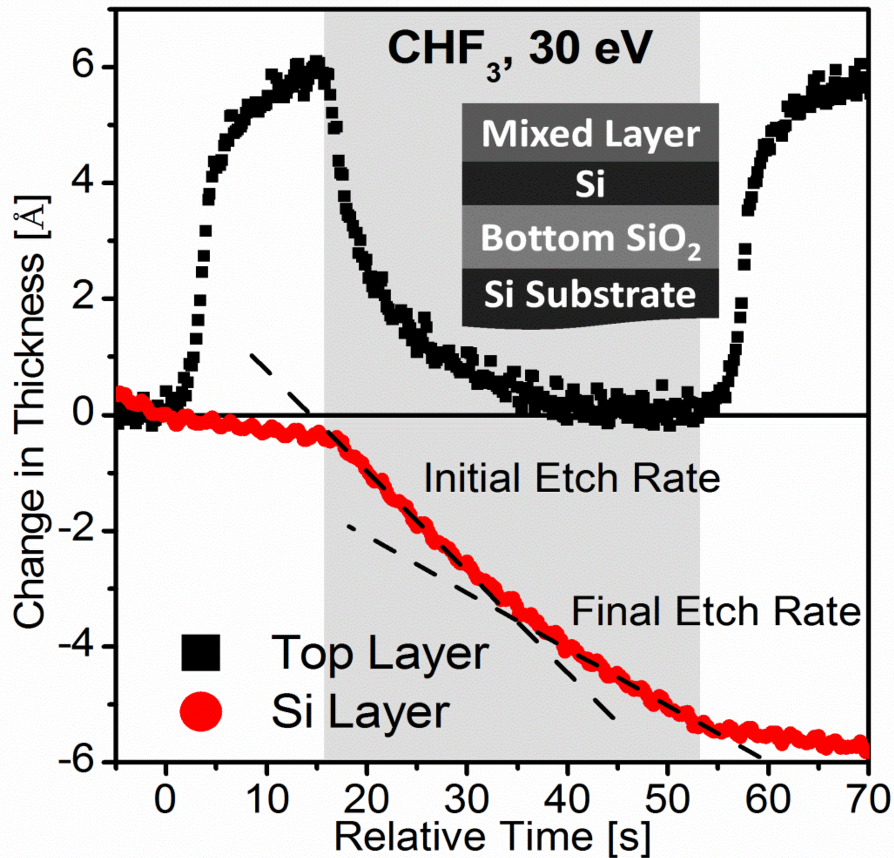

Fig. 6.4: Example changes in thicknesses over time for one individual cycle of Si ALE using 30 eV and CHF_3. A fast and strong removal of the deposited FC film can be seen. The Si etch rate decreases throughout the cycle as F is removed during the ion bombardment. Grey shadowing marks the etch step. The optical model used is shown schematically.

6.3.3 Optical Modeling

In situ ellipsometry allows for real-time measurement of the thickness evolution during ALE. An optical model has been established for this work to interpret measured values of Ψ and Δ in terms of changes in layer thicknesses. The model has been chosen based on a thorough consideration of various parameters and stringent testing and confirmation. Single wavelength ellipsometry is not capable of distinguishing between materials of similar optical properties.[22] The optical model employed therefore combines FC, SiO_2, and fluorinated substrate material in a mixed layer on top of elemental Si and is

shown schematically as an inset in Figure 6.4. Figure 6.4 shows an example thickness trajectory of a single cycle of ALE of Si obtained with the methods explained above. While ALE of SiO_2 showed strongly time-dependent instantaneous etch rates, leading to a truly self-limited process, ALE of Si using the same process conditions showed a significantly reduced variation of instantaneous etch rate during a single cycle.[98] One possible explanation is the lower physical sputtering threshold for Si, leading to comparable amounts of physical sputtering and thus preventing strongly time-dependent instantaneous etch rates.[9] Additionally, it has been suggested that Si shows a significantly larger, chemically reacted, near-surface region than SiO_2.[69] Since etching primarily takes place in the reacted, mixed top layer, the presence of a relatively thick reacted layer can reduce the time-dependence of instantaneous Si etch rates for the etch step lengths explored here.

6.3.4 Characterizing C_4F_8-Based Etching

6.3.4.1 Process Parameters

The impact of several processing parameters on the etching behavior is discussed here. The process parameters explored are the FC film deposition thickness per cycle, the ion energy during the etch step, and etch step length, i.e. the duration of the ion bombardment step during each cycle. The range of FC film thicknesses investigated has been limited to thicknesses of up to 12 Å. The lower part of this range enables processing under F-starved surface conditions and time-dependent instantaneous etch rates based on chemical reactant depletion. Similarly, ion energies were kept at or below 30 eV to prevent significant physical sputtering. The resulting etch step lengths leading to FC depletion are on the order of 20 to 60 s.

Precise FC film deposition is the source of chemical etchant during the etch step. Similar to continuous etch approaches, the FC film is actively involved in the etching mechanism of the substrate material.[23, 83, 99] Thicker FC film depositions provide more F reactant, but also inhibit energy deposition into the substrate. It can be seen in Fig. 6.5 that thicker FC film depositions led to more substrate removal for SiO_2 and Si at all ion energies. The etch step length has been kept constant at 40 s for this consideration. A saturation in etch depth at thicker FC films can be observed. If the FC film deposition per cycle becomes relatively large, a large fraction of each etch step is required to remove the FC film deposited. Little additional interaction with the substrate occurs, leading to a saturation in etch depth per cycle.

The FC film removal during each cycle plays a significant role for these processes. The removal can be controlled via the ion energy, but also via the time of ion bombardment in each cycle, i.e. the etch step length. One would expect longer ion bombardment times per cycle to lead to more removal. This is seen for SiO_2, whereas the opposite behavior was observed for Si. Figure 6.6 summarizes the etch depth per cycle for SiO_2 and Si at 25 and 30 eV for a 5 Å FC deposition per cycle. An ion energy of 30 eV leads to a faster FC removal, but is still below the physical sputtering threshold of SiO_2. A saturation in etch depth per cycle with etch step length for ALE of SiO_2 at 30 eV can therefore be seen, and the substrate removal is limited by the amount of FC admitted during the deposition step. This can be generally referred to as a reactant-limited regime. Ion energies of 25 eV did not show this saturation yet, due to a slower FC removal compared to 30 eV. It is expected, however, that extending the etch step length beyond the 60 s explored in this work will lead to a similar saturation.

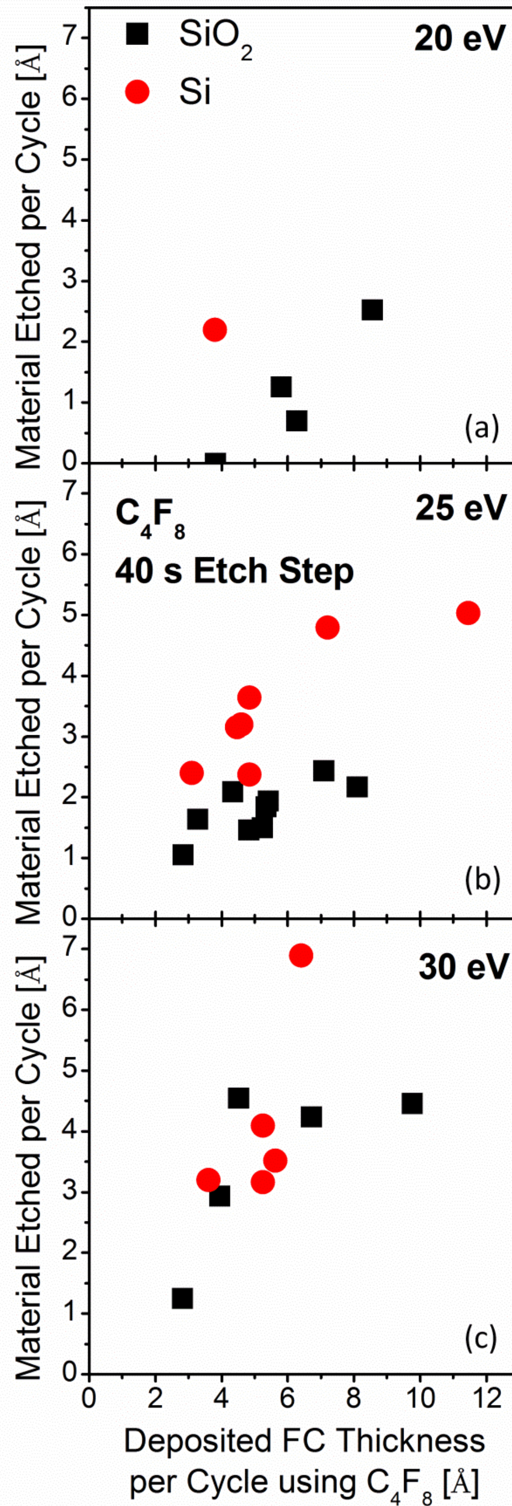

Fig. 6.5: Etch depth per cycle for SiO_2 (black squares) and Si (red circles) dependent on FC film thickness deposited per cycle using C_4F_8 at (a) 20 eV, (b) 25 eV, and (c) 30 eV. The etch step length is kept at 40 s.

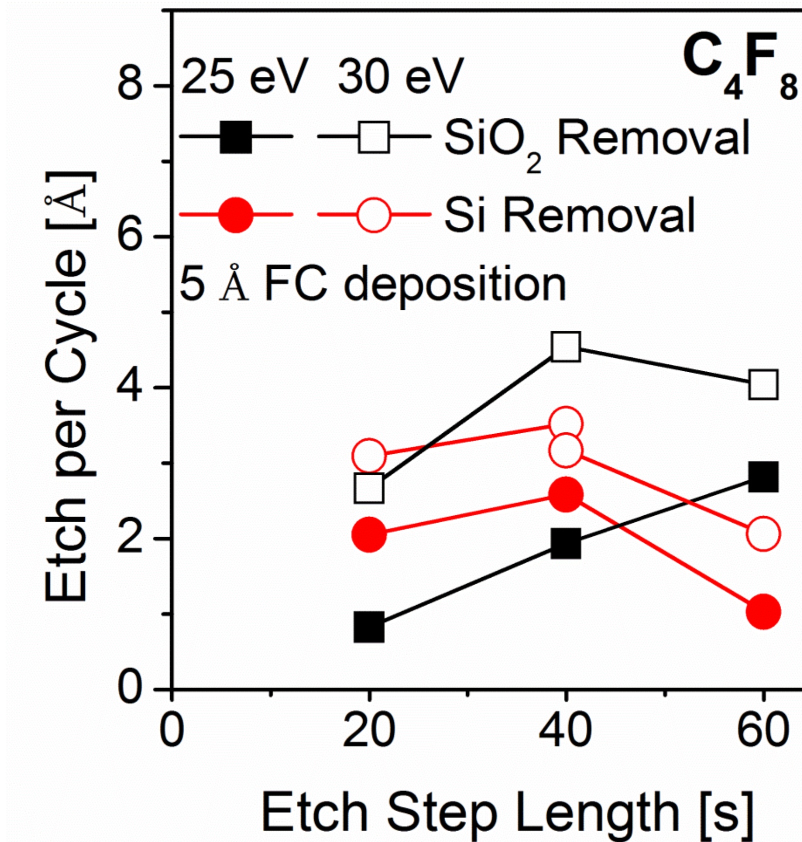

Fig. 6.6: Etch depth per cycle for SiO_2 (black squares) and Si (red circles) using C_4F_8 dependent on etch step length for 25 eV (closed symbols) and 30 eV (open symbols) ion energy. The FC deposition is 5 Å per cycle.

The Si removal per cycle showed a slight decrease with increasing etch step length. In order to explain this, the instantaneous Si etch rate during the etch step has to be considered. Figure 6.7 shows that longer etch step lengths led to a significantly reduced instantaneous etch rate for Si. The strong reduction in instantaneous etch rate can be explained by an overall F poorer environment combined with a thicker reacted Si layer on the surface. Surface chemistry analysis showed a higher signal intensity at 104 eV in the Si 2p spectra, related to the fluorinated oxide layer, for longer etch step lengths. The additional ion bombardment during each cycle can cause ion enhanced oxidation of the Si surface by very low levels of oxygen present in the ICP chamber, e.g. due to erosion of

the quartz coupling window.[18, 23, 86, 87] This oxide layer inhibits the etching of the underlying Si substrate, thus reducing the instantaneous etch rate.[100] The reduction in instantaneous etch rate offsets the longer ion bombardment time, leading to an overall comparable or even slightly decreased removal per cycle. Additionally, the change in instantaneous etch rate within one cycle, i.e. the variation from the initial to the final instantaneous Si etch rate, was increasing with increasing etch step length. This shows a strong depletion of F species, leading to time-dependent etch rates similar to those seen for SiO_2 etching. In addition, the stronger change in instantaneous etch rate within one cycle shows the overall F poorer environment, offering less chemical etchant for enhance substrate etching.

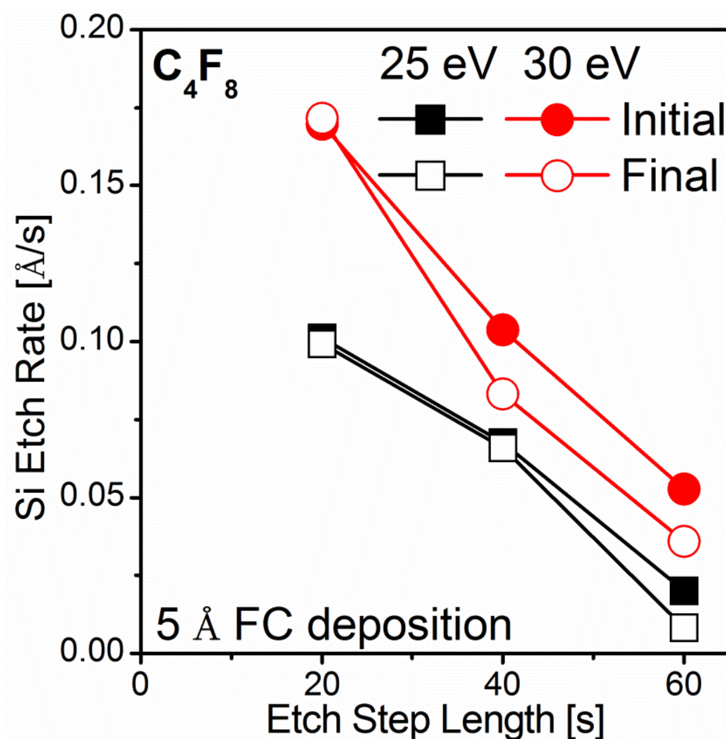

Fig. 6.7: Si instantaneous etch rates during the initial part of the etch step (solid symbols) and during the final part of the etch step (open symbols) dependent on etch step length for 25 eV (black squares) and 30 eV (red circles). The difference in etch rates shows the removal of F during the etch step, leading to less chemically enhanced etching.

6.3.4.2 Material Etching Selectivity

For many applications, the material etching selectivity, i.e. etching one material selectively to another, is essential. The following describes how each process parameter can control material etching selectivity for SiO_2 and Si.

It has been shown previously that choosing appropriate process conditions allows for selective etching of SiO_2 over Si.[98] Etching selectivity was achieved using a FC film build-up condition, meaning process conditions were chosen so as not to entirely remove the deposited FC film from Si during each cycle, while still etching a SiO_2 substrate. Due to an increase in FC film deposition on Si, the chosen etch step conditions are not sufficient to remove the deposited FC film from Si substrates, leading to a growing FC film from cycle to cycle. Eventually, the FC is thick enough to inhibit etching of the underlying Si substrate. While this method yields technically infinite selectivity of SiO_2 over Si, there is a significant Si loss during the FC build-up phase, about 45 Å for conditions examined, and a thick FC film is left on the surface after processing. Etching selectivity can in principle also be achieved through different approaches. ALE of Si has shown an oxidized layer at the surface which can also inhibit substrate etching, somewhat similar to a thick FC film.[98, 100] Additionally, intrinsic etch properties, e.g. bond breaking energies, can lead to differences in etch depth per cycle, enabling material etching selectivity.

The FC film thickness deposited per cycle has a great impact on etch depth per cycle. Since the dependence of etch depth per cycle on FC film thickness is quite similar for SiO_2 and Si, the FC film thickness deposited per cycle is not an ideal parameter to tune etching selectivity. FC film thickness deposited per cycle is instead useful to control

the overall amount of substrate material removed per cycle. Strong changes in the deposited film thickness can additionally shift the process into different parameter regimes, such as F-rich versus F-starved conditions.

The etch step length (ESL) is a crucial parameter of flux controlled ALE processes. It has a great impact on instantaneous etch rates and material removal per cycle. Short etch step lengths can lead to insufficient FC film removal. Prolonged etch step lengths can cause potential surface oxidation and physical sputtering, especially for Si substrates, by extended ion bombardment. Significant differences between SiO_2 and Si are seen and described above. SiO_2 etch depth per cycle is increasing, whereas the Si etch depth per cycle is fairly constant or even slightly decreasing with increasing etch step length. This opposite behavior allows for material etching selectivity control. On the one hand, increasing etch step lengths leads to a strongly F-starved surface chemistry regime enabling selective etching of SiO_2 over Si. On the other hand, reducing etch step lengths leads to a selective Si over SiO_2 etch.

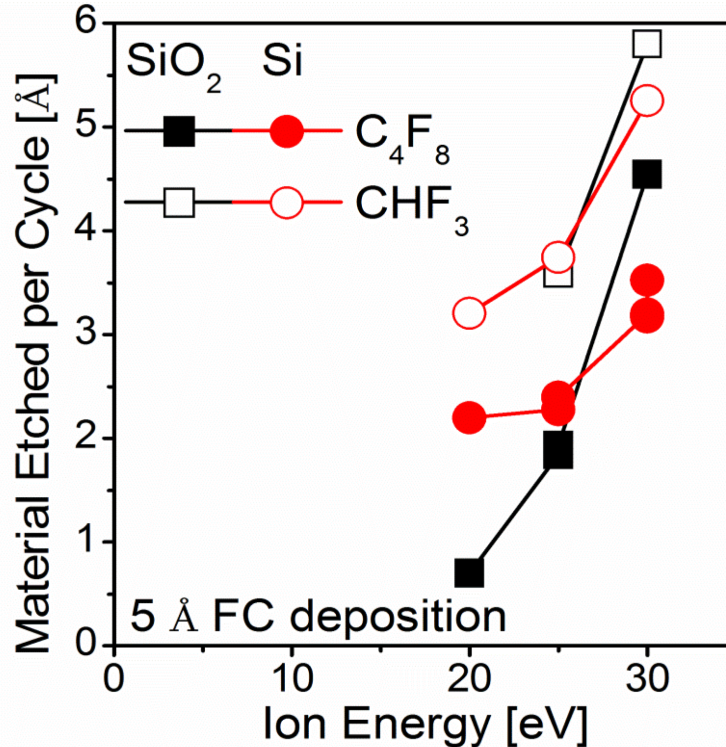

Fig. 6.8: Etch depth per cycle for SiO_2 (black squares) and Si (red circles) using C_4F_8 (closed symbols) and CHF_3 (open symbols) dependent on ion energy during the etch step at 40 s etch step length. The FC deposition is 5 Å per cycle.

In addition to etch step length, ion bombardment energy during the etch step is useful for control of material etching selectivity. The ion bombardment energy impacts FC film defluorination and removal, energy transport to the substrate, and ion-enhanced surface oxidation.[23, 83] An overview of material removal per cycle at 5 Å FC film deposition per cycle is presented in Fig. 6.8. A strong increase in removal per cycle with ion energy can be seen for SiO_2. Si removal does also increase, but less than SiO_2. A possible explanation for this is based on ion-enhanced surface oxidation. Higher ion energies can lead to a stronger surface oxidation of Si. The oxidized surface layer then, in turn, inhibits substrate etching.[100] Therefore, higher ion energies show selective SiO_2 over Si etching, while lower ion energies show selective Si over SiO_2 etching. The same process can be tuned for selectively etching either material.

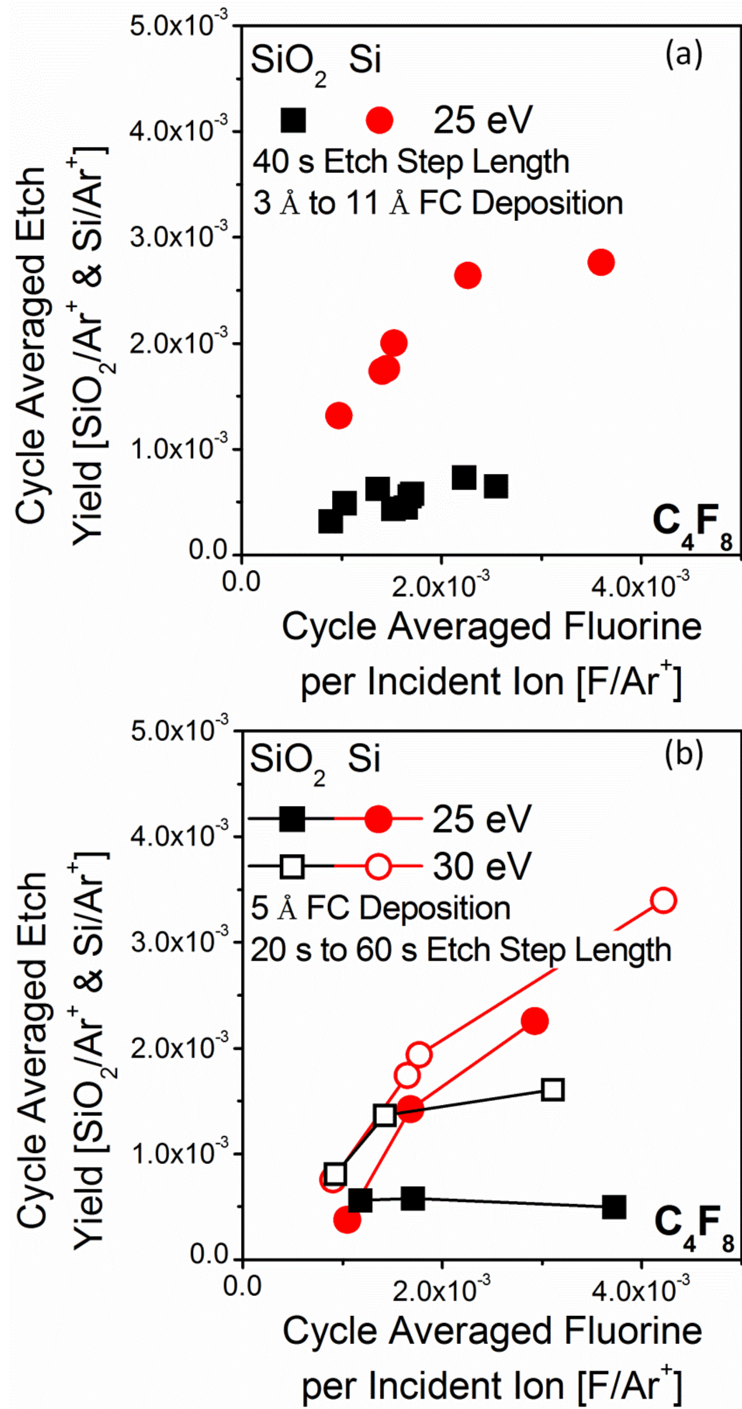

Fig. 6.9: Cycle averaged etch yield, i.e. material removed per cycle per number of incident ions per cycle, dependent on F/Ar^+, i.e. F in the deposited FC film per number of incident ions during one cycle. (a) The FC thickness deposited per cycle ranges from 3 to 11 Å. (b) The etch step length ranges from 20 to 60 s.

In continuous etch processes the etch yield is defined as the number of atoms removed per incident ion per unit time. Due to the strongly time-dependent conditions of this cyclic ALE process, the etch yield is averaged over a cycle and defined as the number of atoms removed per cycle divided by the number of incident ions per cycle. The amount of FC available per incident ion (F/Ar^+) can be calculated by the FC thickness deposited per cycle divided by the number of incident ions per cycle and provides a measure of F availability. A high F/Ar^+ ratio describe a F-rich condition, i.e. high amounts of F are available per incident ion, while a low F/Ar^+ ratio describes F-starved conditions. The etch yield dependence on the F/Ar^+ ratio for ALE of SiO_2 and Si is shown in Fig. 9 for 25 eV and 30 eV ion energy. The etch step length ranged from 20 s to 60 s and FC thickness deposited per cycle ranged from 3 Å to 11 Å. ALE of Si shows a stronger increase in etch yield than SiO_2. Additionally, the etch yield saturates at higher values for ALE of Si compared to SiO_2. This suggests that ALE of Si is depending stronger on the availability of F than SiO_2 while the limiting factor for etching of SiO_2 is the ion bombardment. The physical sputtering yield for SiO_2 is lower than for Si,[9] suggesting that more ion bombardment is required to etch SiO_2 substrates. This agrees with the observation above that ALE of SiO_2 is limited by the ion bombardment, while ALE of Si does not require the same ion bombardment and is therefore limited by the availability of chemical etchant, i.e. F.

This behavior is quite different from continuous etch approaches due to very different surface chemistries and etching conditions. Continuous FC-based etching of Si-based materials shows a decrease in etch yield with increasing steady-state FC film thickness.[18, 81, 101] Additionally, the etch yield presented here are averaged over a full

ALE cycle and significantly lower due to the comparably F-starved condition. Furthermore, a lot of previous ALE of Si work focused on a Cl/Ar chemistry. The Si-Cl-system showed a self-limited behavior with similar trends and phenomena regarding the cycle averaged etch yield dependent on the Cl/Ar^+ ratio.[102-105]

6.3.4.3 Silicon Surface Chemistry

The available chemical etchant is based on the deposited FC film, and changes in the properties of the various surface layers will strongly influence the etch behavior. X-ray photoelectron spectroscopy (XPS) was used to characterize the typical surface chemistry at crucial points of the ALE cycle for various conditions of Si etching. Surface chemistry during ALE of SiO_2 has been discussed previously and will therefore not be discussed again here.[73] High resolution spectra of the Si 2p, C 1s, O 1s, and F 1s core levels were taken and decomposed based on a thorough analysis. Owing to the complexity of these surfaces, all results were checked for agreement across all spectra for a given surface to provide an overall consistent depiction of the surface chemistry. Exemplary decompositions of each spectrum are shown in Figs. 6.10 through 6.13.

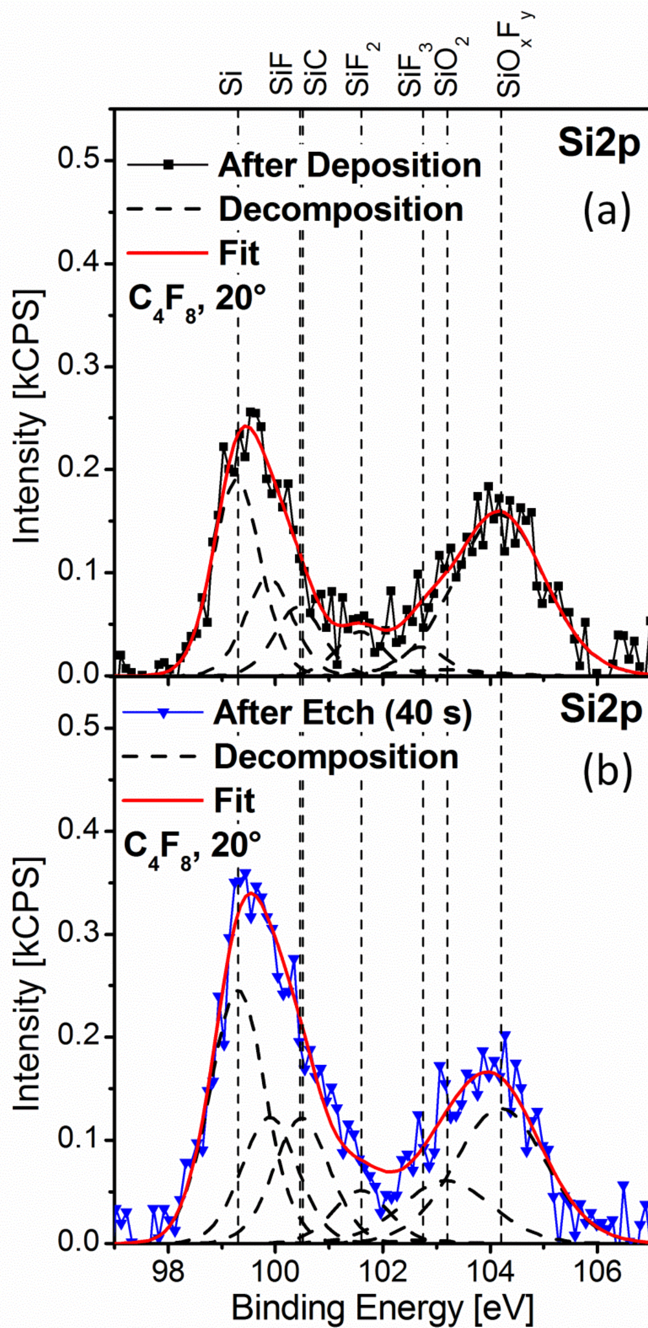

Fig. 6.10: Si 2p XPS spectra comparing surface chemistry for Si ALE (a) at the end of a deposition step and (b) at the end of an etch step. ≈11 Å of FC film per cycle are deposited using C_4F_8. The etch step is 40 s long at 25 eV ion energy. Spectra are measured during quasi-steady-state conditions. A typical decomposition for each spectra is shown with the resolving fit to the measured data.

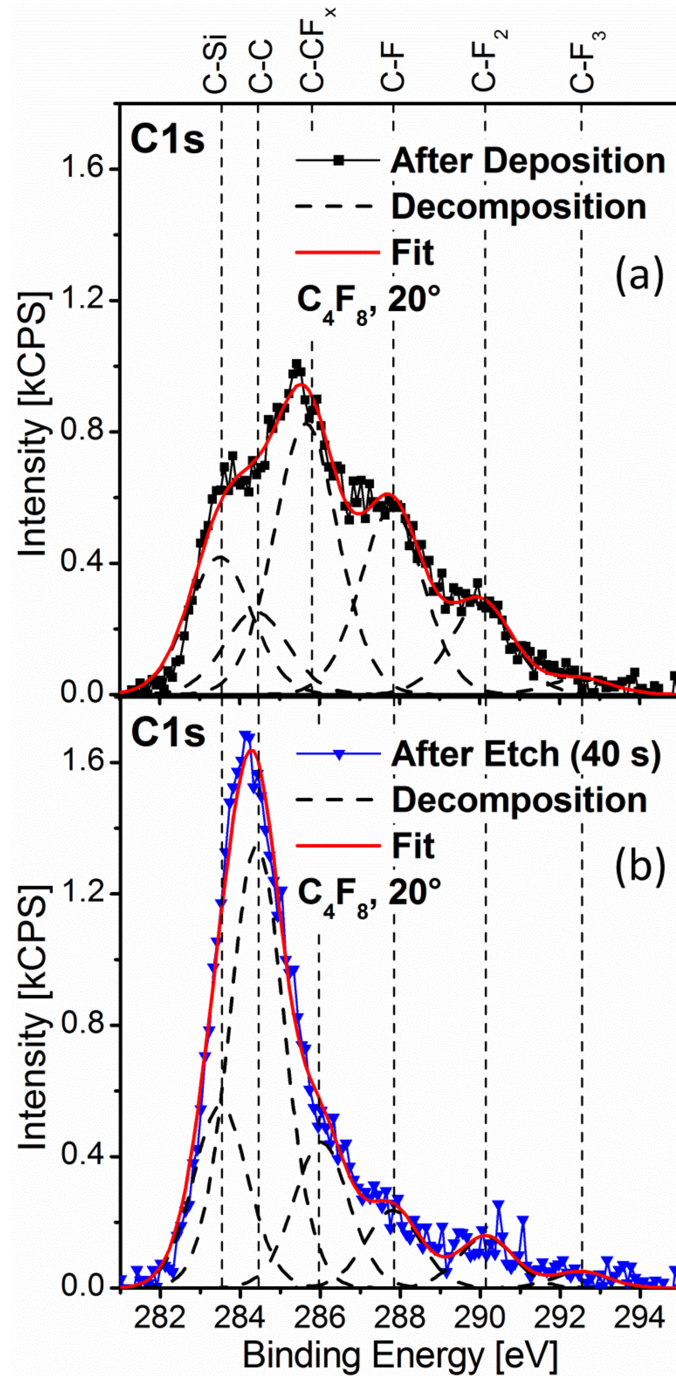

Fig. 6.11: C 1s XPS spectra comparing surface chemistry for Si ALE (a) at the end of a deposition step and (b) at the end of an etch step. ≈11 Å of FC film per cycle are deposited using C_4F_8. The etch step is 40 s long at 25 eV ion energy. Spectra are measured during quasi-steady-state conditions. A typical decomposition for each spectra is shown with the resolving fit to the measured data.

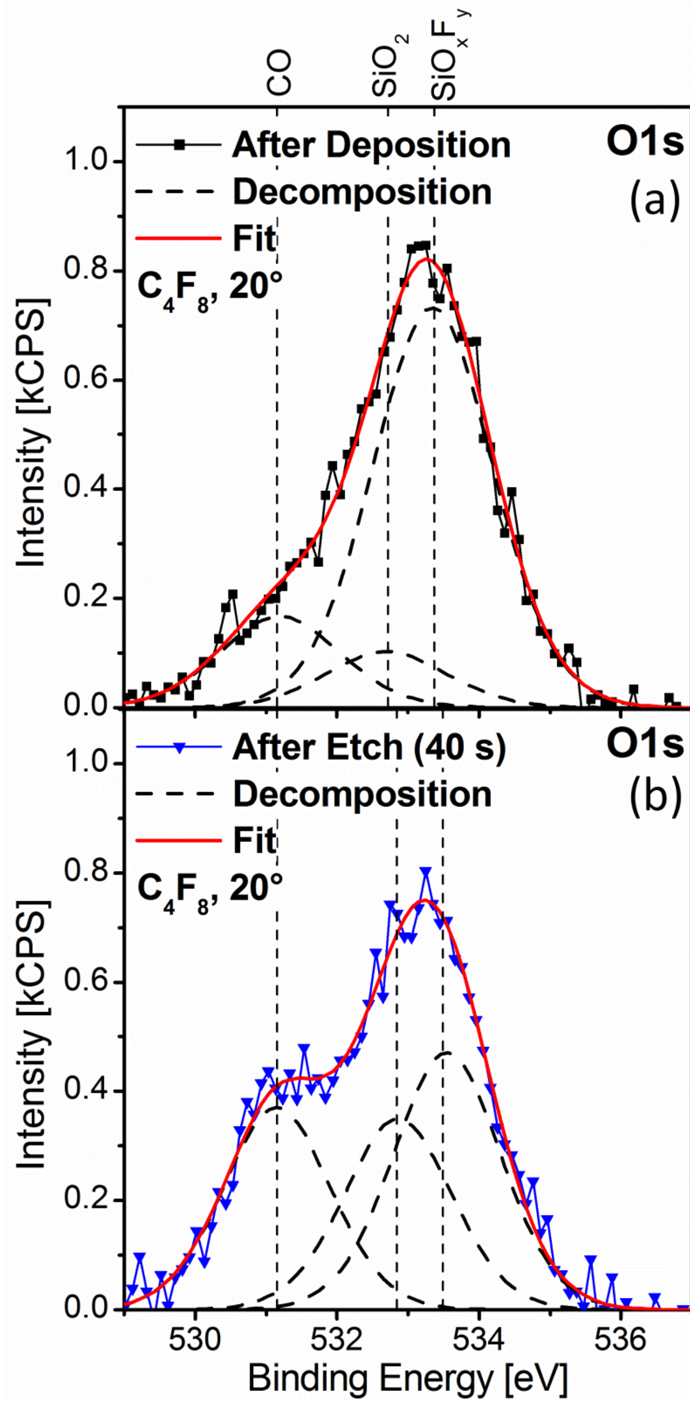

Fig. 6.12: O 1s XPS spectra comparing surface chemistry for Si ALE (a) at the end of a deposition step and (b) at the end of an etch step. ≈11 Å of FC film per cycle are deposited using C_4F_8. The etch step is 40 s long at 25 eV ion energy. Spectra are measured during quasi-steady-state conditions. A typical decomposition for each spectra is shown with the resolving fit to the measured data.

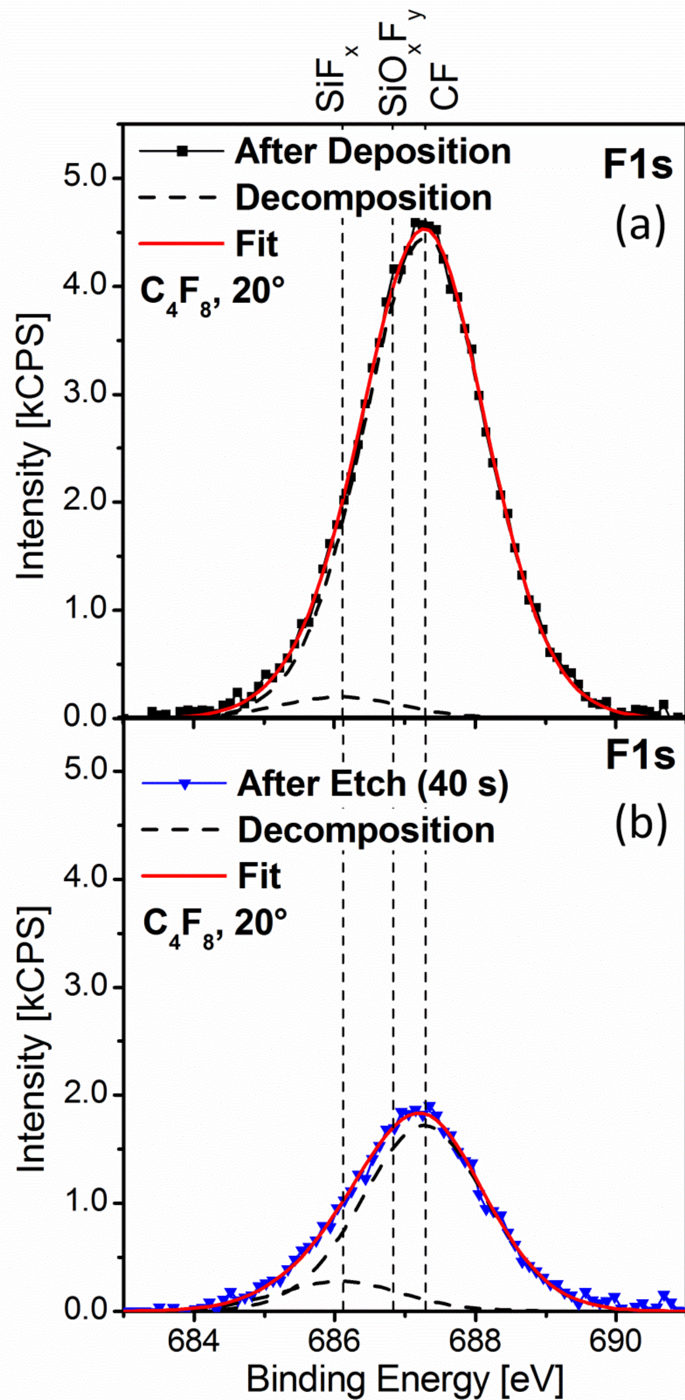

Fig. 6.13: F 1s XPS spectra comparing surface chemistry for Si ALE (a) at the end of a deposition step and (b) at the end of an etch step. ≈11 Å of FC film per cycle are deposited using C_4F_8. The etch step is 40 s long at 25 eV ion energy. Spectra are measured during quasi-steady-state conditions. A typical decomposition for each spectra is shown with the resolving fit to the measured data.

The Si 2p spectra (examples shown in Fig. 6.10) are composed of a large variety of moieties. The two main peaks observed originated from elemental Si, at 99.3 eV, and oxidized Si, around 104 eV. Fluorination of the oxide slightly shifts the binding energy to higher levels.[24] Fluorinated Si intensities are located between these two main peaks, around a binding energy of 100 to 103 eV. Generally, the signal of these fluorinated Si species was low in comparison to the two main peaks.

The deposited FC film is primarily characterized by the C 1s spectral signatures. Figure 6.11 shows an exemplary decomposition of the C 1s spectrum after deposition of a 11 Å thick FC film and after completion of the etch step. The high binding energy region in the C 1s spectrum is attributed to CF_x (x = 1, 2, and 3) species. The more F atoms a C atom is bonded to, the larger the chemical shift from the C-C binding energy.[23, 69, 81] In addition to bonding to F, bonding to O causes a very similar shift in the C binding energy. It is therefore difficult to distinguish between CF_x and C-O species solely by the C 1s spectra. As will be noted below, a cross-reference to the O 1s and F 1s spectra is established to account for C-O species. The F/C ratio is a common characteristic used for FC films and can be calculated using the decomposed C 1s spectra.[69, 81] Essentially, the CF_x species intensity is calculated relative to the total C 1s intensity. A strong removal in CF_x species and, therefore, reduction in the F/C ratio, was typically seen during ion bombardment, consistent with the ellipsometric measurements.

Typical O 1s spectra are shown in Fig. 6.12. The main signal intensity originated from O bound to Si, in the form of SiO_2 and fluorinated oxide. Additionally, a peak at lower binding energy was observed and attributed to C-O species, and related to the C-O intensities seen in the C 1s spectra, as described above. Additionally, O 1s intensities

were compared to oxide intensities in the Si 2p spectra. This relationship provides a measure of Si oxidation.

Figure 6.13 shows typical decompositions of an F 1s spectrum after FC film deposition and after completion of the etch step. The signal was a combination of F associated with either the FC film or the substrate. The C 1s spectra were used to determine the intensity of CF_x species and cross-referenced to the F 1s spectra. Furthermore, F 1s intensities were compared to fluorinated Si intensities in the Si 2p spectra, providing a measure of substrate fluorination. Comparing the amount of F relative to C with the F/C ratio of the FC films allows estimation of the amount of F located in the substrate.[81] To this end, we calculated the F/C ratio of the FC films based on the C 1s spectra and the ratio of F 1s/C 1s intensity. If both ratios are similar, the F is primarily located in the FC film. If the F 1s/C 1s ratio is significantly greater than the F/C ratio, significant amounts of F must be located in the substrate. The difference ΔF/C, i.e. F 1s/C 1s – F/C, is therefore an indication of substrate fluorination.

A strong difference in surface chemistry evolution was observed between 5 Å and 11 Å FC film depositions per cycle. Figure 6.14 (a) shows that the F/C ratio of thin FC films is decreasing rapidly upon ion bombardment, and that the film is being defluorinated. At the same time ΔF/C is increasing, i.e. relatively more of the F becomes associated with the Si substrate than the FC film. Therefore, F is preferentially removed from the FC film and mixing with the Si substrate takes place. It has been shown that F can be 'recycled' in an advancing reacted layer, i.e. the F is propagating through a reacted layer, rather than being removed from the substrate.[99] Additionally, there could be a chamber wall interaction. FC material on the chamber walls, from prior cycles, can be an

additional source of F during the etch step. At the end of the etch step, the FC film deposition introduces F in the form of a FC film, therefore reducing $\Delta F/C$. The evolution of the F 1s and CF_x species intensity confirms the behavior of the F/C ratio and $\Delta F/C$ described above, and is shown in Fig. 6.14 (b). For 5 Å FC film depositions per cycle the CF_x species, as measured in the C 1s, decrease rapidly to a stable low level, but the F 1s intensity does not follow this behavior.

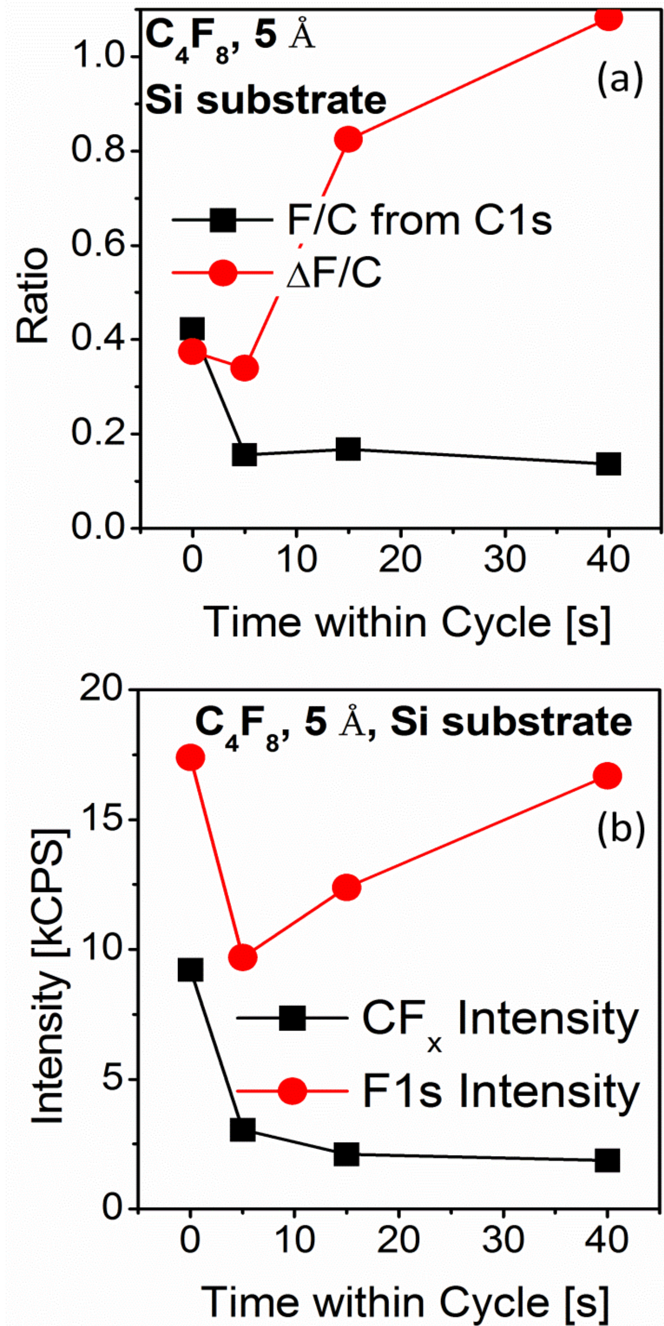

Fig. 6.14: (a) F/C ratio of the FC film (black squares) and ΔF/C (red circles) as measured per XPS during one cycle of Si ALE. ΔF/C is the difference in F/C ratio determined by the C 1s spectra and the F 1s/C 1s ratio and is indicating the amount of F in the substrate. (b) Intensities during one cycle for CF_x species measured in the C 1s spectra (black squares) and the F 1s spectra (red circles). The process parameters are C_4F_8 with a FC film deposition per cycle of 5 Å. The etch step is kept at 40 s with 25 eV ion energy. The etch step starts at 0 s.

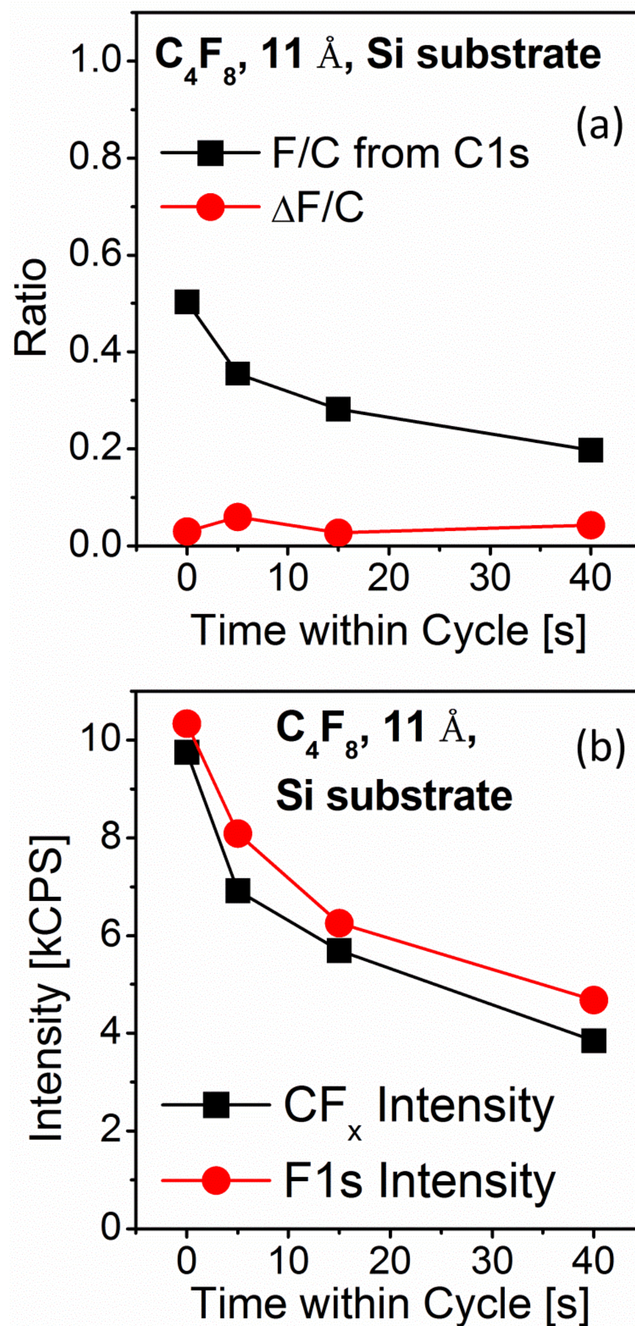

Fig. 6.15: (a) F/C ratio of the FC film (black squares) and ΔF/C (red circles) as measured per XPS during one cycle of Si ALE. ΔF/C is the difference in F/C ratio determined by the C 1s spectra and the F 1s/C 1s ratio and is indicating the amount of F in the substrate. (b) Intensities during one cycle for CF_x species measured in the C 1s spectra (black squares) and the F 1s spectra (red circles). The process parameters are C_4F_8 with a FC film deposition per cycle of 11 Å. The etch step is kept at 40 s with 25 eV ion energy. The etch step starts at 0 s.

Thicker FC film depositions of 11 Å, however, show a different behavior. The F/C ratio and ΔF/C are shown in Fig. 6.15 (a). The F/C ratio of the FC films decreases more slowly and over the entire etch step. ΔF/C is stable and close to 0 throughout the entire cycle. Additionally, the F 1s and CF_x intensities are very similar, as seen in Fig. 6.15 (b). The substrate is therefore in a fairly steady state throughout the etching. The FC film is being removed from the surface, together with substrate material, while a mixed, reacted substrate layer is propagating further down. The steady state of the substrate is additionally reflected in the observation of minimal changes in the Si 2p and O 1s spectra throughout one cycle for FC film depositions of 11 Å.

Thicker FC depositions of 11 Å show a relatively lower intensity of reacted Si in the Si 2p spectrum than thinner FC depositions of 5 Å. Thicker films inhibit the ion bombardment onto the Si surface, thus reducing ion-enhanced surface oxidation. It has been shown before that a thicker FC film during continuous etching leads to a thinner fluorinated Si reaction layer underneath.[81] The relative amount of reacted Si in the Si 2p spectra is fairly stable throughout the cycle.

In order to confirm the XPS surface analysis, SIMS measurements have been performed with samples processed for a 5 Å FC film deposition per cycle and 25 eV ion energy for 40 s condition. Good agreement between results obtained by XPS and SIMS was observed. The very surface layer is a mix of C, F, O, and Si species. This mixed layer extends up to 15 Å into the sample. F and O species are predominately located at the surface with a decreasing concentration up to 25 Å into the sample.

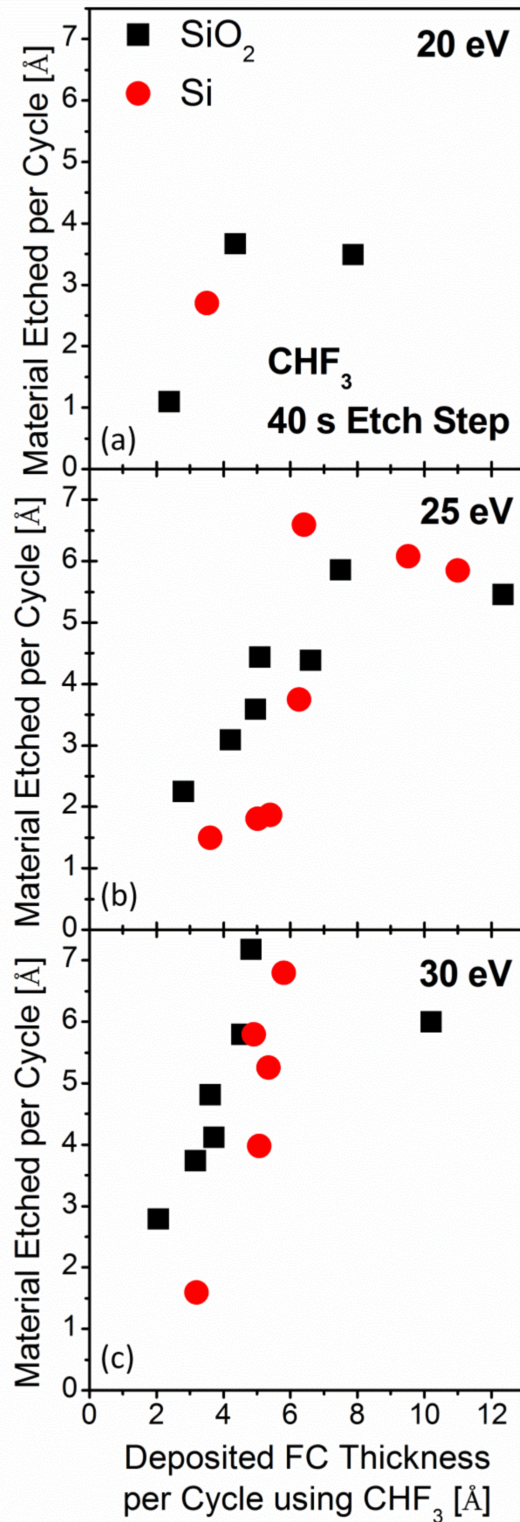

Fig. 6.16: Etch depth per cycle for SiO_2 (black squares) and Si (red circles) dependent on FC film thickness deposited per cycle using CHF_3 at (a) 20 eV, (b) 25 eV, and (c) 30 eV. The etch step is kept at 40 s.

6.3.5 Characterizing CHF_3-Based Etching

In addition to C_4F_8, CHF_3 has also been employed as a precursor. These two precursors have shown several significant differences in continuous etching and are therefore of interest to compare when used for the ALE approach.[81, 83] C_4F_8 and CHF_3 show significantly different steady-state FC films during continuous etching, based on monomer dissociation and H scavenging F from the FC film.[106] The presence of H in CHF_3 can have a strong impact on etching behavior. H species can penetrate deep into and bond to the Si substrate.[107, 108] Enhanced FC deposition has been observed for H_2 addition to FC based Si etching.[106] However, since C_4F_8 and CHF_3 show many intrinsic differences in addition to the H, further work is required to precisely determine the specific impact of H on the ALE process.

The dependence of the SiO_2 and Si thickness removed per cycle on FC film thickness deposited per cycle is shown in Fig. 6.16 for CHF_3. Similar to C_4F_8, an increase in etched thickness per cycle with increasing FC film deposition is seen, along with a saturation for thick deposited FC films. Higher ion energies of 30 eV show a very strong dependence on the FC film thickness with a rapidly increasing etch depth for thin FC films. The etch depth per cycle shows a similar dependence on ion energy for CHF_3 and C_4F_8, as described above and shown in Fig. 6.8.

When considering material selectivity for CHF_3, it is important to keep the change in deposition yield discussed above in mind. FC film deposition using CHF_3 showed an increased deposited thickness on Si compared to SiO_2 substrates. Therefore, selective etching of SiO_2 over Si can be achieved via a FC build-up regime, as described previously. If process conditions not showing a FC build-up are chosen, the etch depth

per cycle will be higher for Si compared to SiO_2 based on the thicker FC film deposition per cycle.

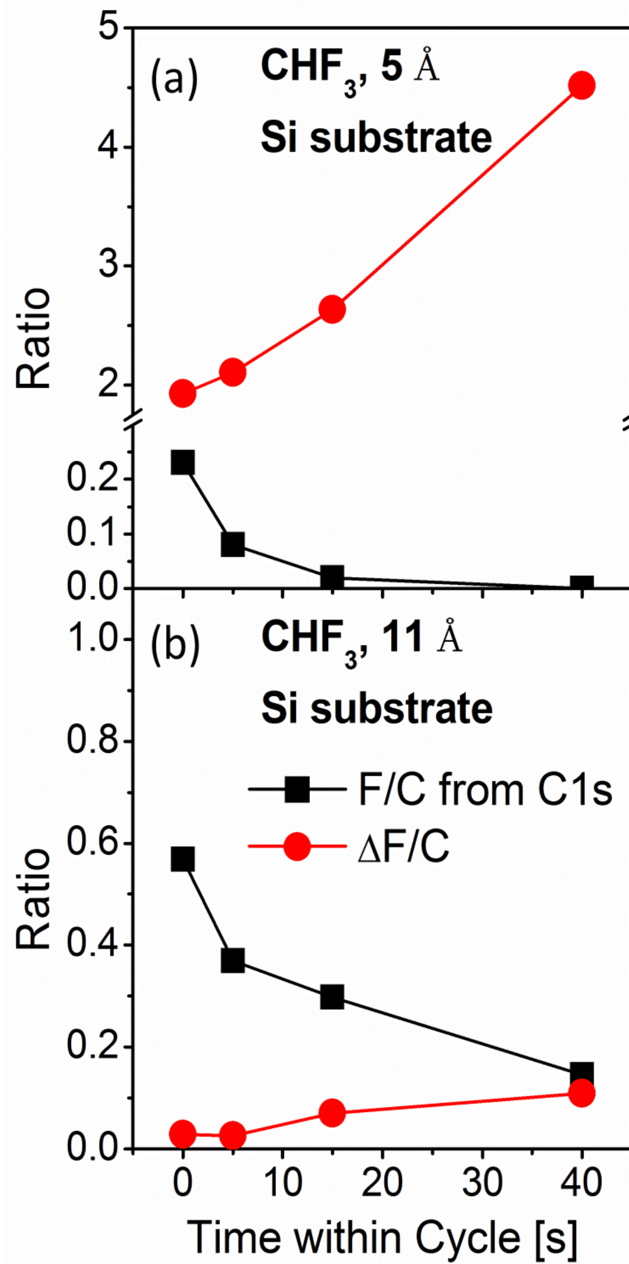

Fig. 6.17: F/C ratio of the FC film (black squares) and ΔF/C (red circles) as measured per XPS during one cycle of Si ALE. ΔF/C is the difference in F/C ratio determined by the C 1s spectra and the F 1s/C 1s ratio and is indicating the amount of F in the substrate. The process parameters are CHF_3 with a FC film deposition per cycle of (a) 5 Å and (b) 11 Å. The etch step is kept at 40 s with 25 eV ion energy.

CHF_3 behaves similarly in terms of surface chemistry, shown in Fig. 6.17, when compared with C_4F_8. Thicker films show a fairly steady state substrate condition, while thinner films show a change in substrate condition throughout the ALE cycle. The F/C ratio of films deposited by CHF_3 has been shown to be slightly higher compared to C_4F_8 during this ALE process.[98] This results in a slightly larger substrate removal per cycle for CHF_3, based on additional available F.[18] The F/C ratio is not only dependent on the precursor, but also on the thickness of the deposited films at these low thicknesses. Figure 6.17 shows that 11 Å thick FC films have a F/C ratio of 0.6 while 5 Å thick films show a F/C ratio of only 0.25. The evolution of the F/C ratio as well as ΔF/C is similar for CHF_3 and C_4F_8. However, it is noteworthy that ΔF/C is significantly larger for 5 Å FC film depositions per cycle using CHF_3 compared to using C_4F_8, potentially due to H interactions. The oxidized top layer present during ALE of Si depends more strongly on the FC film thickness than on the choice of precursor. For instance, for both C_4F_8 and CHF_3 thinner FC film depositions of 5 Å show a stronger oxidized layer than thicker FC film depositions of 11 Å.

6.3.6 Si Reaction During Deposition

In situ ellipsometry revealed a very interesting phenomenon during FC film deposition on Si substrates. A representative individual cycle of ALE of Si is shown in Fig. 6.18. To highlight this phenomenon, a 10 s delay was introduced between each cycle, i.e. after the etch step. No bias potential was applied during this time, but the Ar plasma was sustained. The thickness trajectory shows that Si removal stops once the bias potential is no longer applied and the Si thickness is constant. Once the precursor is injected into the plasma, marked with a dashed line at 10 s, a decrease in Si thickness is

observed, along with FC film deposition. The initially faster Si reaction rate is seen to decrease with time during the deposition step. This reduction in elemental Si thickness can be based on several phenomena. One possibility is spontaneous etching of Si based on an interaction with F and/or H.[88] Another possibility is the reaction of Si forming fluorinated silicon or silicon carbide. This reaction of Si causes a change in optical properties, which is detected as an apparent loss of elemental Si in ellipsometry. XPS surface analysis does not show evidence of a change in substrate fluorination upon FC film deposition, however, the magnitude of these effects is small, i.e. on the order of 1 Å or less, and it may be difficult to detect these changes after the ALE process.

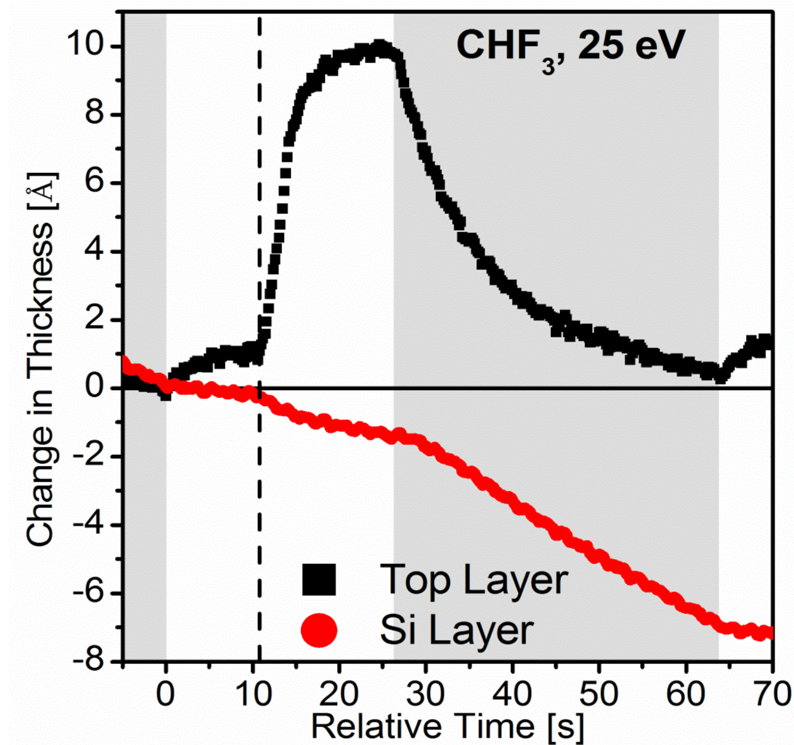

Fig. 6.18: Example changes in thickness over time for one individual cycle of Si ALE at 25 eV ion energy using CHF_3. A 10 s delay after turning off the bias potential and before the next precursor injection is introduced. The time of precursor injection is marked with a dashed line. The Si reaction and thickness change is only observed once CHF_3 is injected. Grey shadowing marks the etch step.

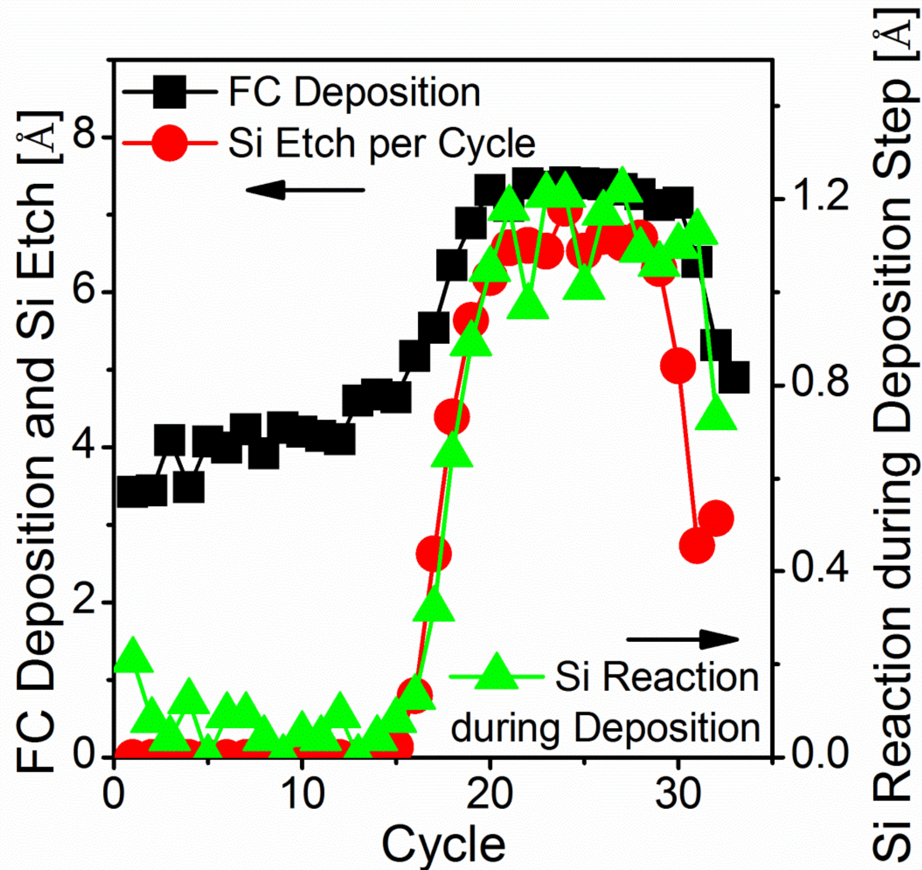

Fig. 6.19: FC film deposition (black squares, left scale) and amount of Si etched (red circles, left scale) during each cycle as seen in Figure 6.3. The amount of Si reacted during the deposition step (green triangles, right scale) is added. Processing conditions are CHF_3 precursor injection with a 40 s etch step at 25 eV ion energy. The initial 15 cycles are etching SiO_2 on top of the Si. Once the Si layer is reached the Si etching starts, the FC deposition increases, and a reaction of Si is seen during the deposition step. Around cycle 30 the Si layer is completely etched away.

Figure 6.19 shows the FC film deposition and amount of reacted Si per cycle for ALE of a SiO_2-Si-SiO_2 stack. The reaction of Si during the deposition steps appears to be connected to the change in deposited film thickness, as both are increasing during the transition from SiO_2 to Si. The amount of Si reacted, i.e. via spontaneous etch and/or formation of fluorinated silicon and silicon carbide, based on the processing conditions is

shown in Fig. 6.20. The following trends can be observed. Thicker FC film depositions, i.e. stronger precursor injections, lead to a stronger Si reaction. CHF_3 causes a stronger Si reaction than C_4F_8. Longer etch step lengths as well as higher ion energies reduce the amount of Si reacted during the deposition step. This holds true for both precursors, C_4F_8 and CHF_3, as well as thinner and thicker (5 and 10 Å) FC film depositions. Therefore, generally speaking, a F-richer processing environment leads to a stronger Si reaction, i.e. a larger change in elemental Si thickness. It is noteworthy that the etch step conditions strongly impact this Si reaction, which is occurring during the deposition step. This shows the importance of surface chemistry and a form of history effect of the substrate.

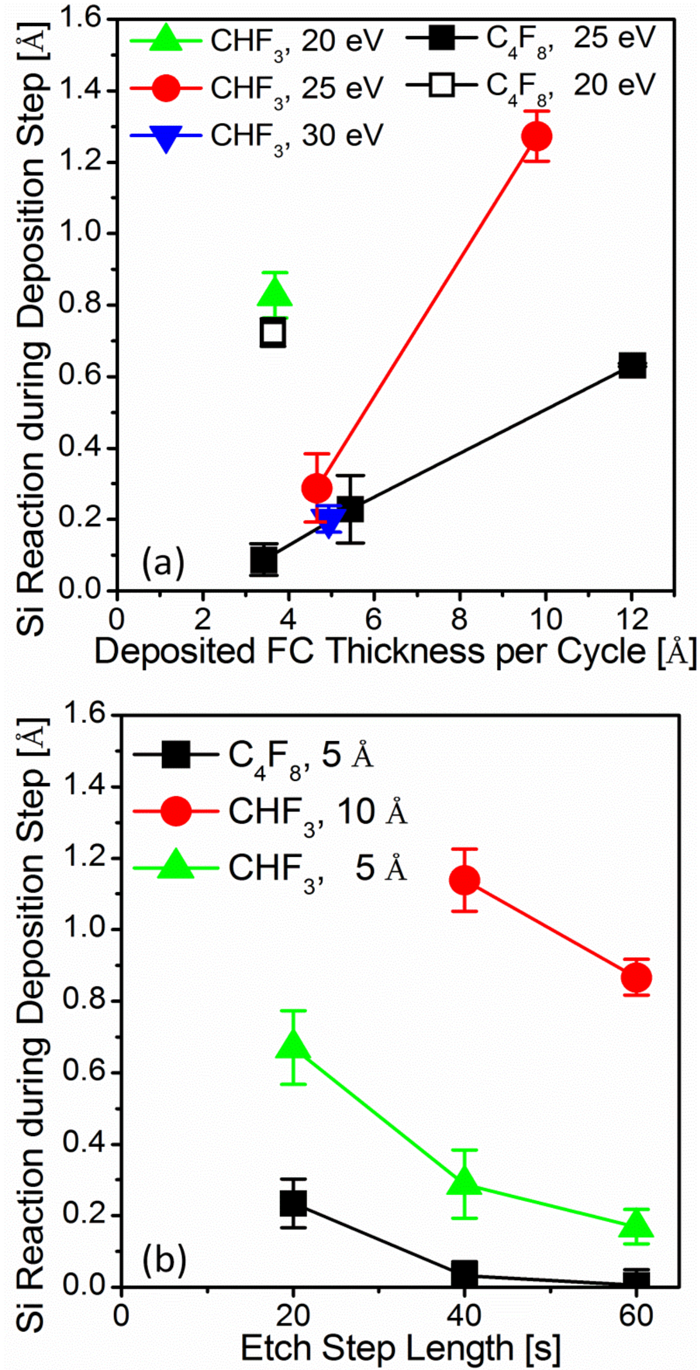

Fig. 6.20: Amount of Si reacted during the deposition step depending on (a) film thickness for 20, 25, and 30 eV ion energy for 40 s during the etch step, and (b) etch step length at 25 eV ion energy. This reaction is observed during the deposition step, but does show an impact of the etch step due to changes in the surface chemistry. It cannot clearly be determined if the Si is actually lost or reacted or a combination of both occurs.

6.4 Discussion

The FC based ALE process is schematically shown in Fig. 6.21 (a) for a thin FC deposition on the order of 5 Å and in Fig. 6.21 (b) for a thicker FC deposition on the order of 10 Å. It has to be noted that the surface is not comprised of clearly separate layers as depicted in this schematic, but, especially for thin FC films, rather a mix of several moieties. Surface analysis via XPS and SIMS has shown that the various species are intermixed. The main interactions involved during the deposition step are the FC deposition on the surface and a reaction of the Si substrate with F and/or H. Interactions during the etch step include reaction/intermixing of F with the substrate and the removal of FC film and mixed, reacted substrate material. The process was controlled via the composition and thickness of the deposited FC film, as well as the time and energy of ion bombardment during the etch step.

The etch mechanism for FC based etching of Si materials, e.g. Si, SiO_2, Si_3N_4, has been intensely investigated.[84, 109-112] During typical continuous etching approaches, a constant FC flux is given, leading to a balance of FC film deposition and etching. This results in a steady-state FC film during etching, which heavily influences the etch rate and mechanism.[23, 69, 113] A key difference between this cyclic approach and continuous etching is the limitation of FC and the temporal separation of FC film deposition and etching, in addition to lower ion energies. The FC film is never in a steady-state condition, although similar from cycle to cycle, but changing within each cycle. These continuous changes lead to several key differences in the mechanism and characteristics of cyclic ALE.

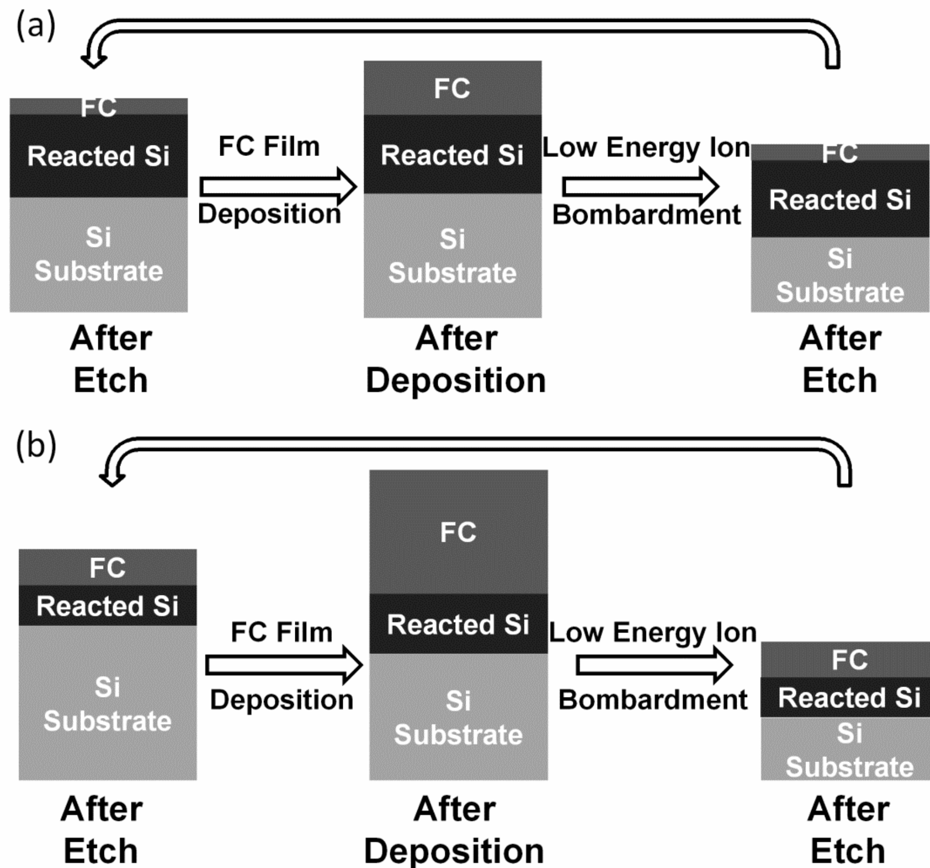

Fig. 6.21: Schematic of FC based ALE for (a) thin FC film depositions on the order of 5 Å and (b) thicker FC film depositions on the order of 11 Å. The reacted Si layer is a mix of oxidization and fluorination. The process can be controlled via the FC film deposition, e.g. film thickness and precursor, and via the low energy ion bombardment, e.g. via length and ion energy. This schematic is not to scale.

In continuous etch approaches, the steady-state FC film thickness has proven to be of great importance.[81, 114-116] Thick films can inhibit etching of the underlying substrate, similar to the material selectivity considerations described above. Interaction with the substrate, e.g. O from a SiO_2 substrate, can heavily impact the steady-state FC film thickness and therefore enhance material selectivity. Since cyclic ALE processes do not have a steady-state FC film, the mechanisms of etching are different. FC film thickness deposited per cycle yields good control over material removal per cycle for

ALE. Since the FC films are removed during each etch step, the deposited film thickness does not provide good control over selectivity, except for FC build-up conditions, which were not investigated in detail here. A saturation of etch depth per cycle with deposited FC film thickness is seen. This is reminiscent of the etch-inhibiting properties of thick steady-state FC films in continuous etch approaches. Thick films inhibit ion bombardment of and reactant transport to the underlying substrate and require a substantial energy dose to maintain a steady-state thickness, thus taking away energy otherwise delivered to the substrate.[23, 81] The surface characterization results are consistent with the overall idea that the FC film is strongly involved in the etch mechanism of the substrate material.[113] F from the FC film interacts with Si bonds as a result of ion bombardment and a mixed layer is formed, while the FC film is simultaneously defluorinated.[99, 117-119]

The process parameters were changed over a fairly small range in this work, e.g. the FC deposition thickness per cycle ranged from 3 to 11 Å, and the ion energy ranged from 20 to 30 eV. However, a significant impact on etch behavior and etch depth per cycle was observed. This suggests the high sensitivity of ALE and the potential impact of even small levels of contamination. As discussed above, even a small amount of oxygen from the quartz window can lead to surface oxidation. In addition, FC films on the chamber walls can be a source of chemical etchant and affect process stability.[57] This shows very high process and equipment reproducibility and control is essential for the success of ALE.

6.5 Summary and Conclusions

Throughout this work, ALE of SiO_2 was generally easier to control than ALE of Si. This general difference can be attributed to the high reactivity of Si surfaces, in contrast to relatively unreactive SiO_2 surfaces. Since flux-controlled ALE is heavily dependent on surface chemistry, a highly reactive surface will be significantly more sensitive to any form of process fluctuation or impurity compared to an unreactive surface. Additionally, a fluorinated, oxidized surface layer is present during ALE of Si. This layer was shown to greatly impact the etching behavior of Si substrates.

Overall, the FC film deposition per cycle provides strong control of material removal, while the etch step length and ion energy provide strong control of material selectivity. Thicker FC depositions lead to more material removal, based on a higher F availability for chemically enhanced etching. The material removal per cycle saturates with deposited FC thickness. Higher ion energies and longer etch steps provide SiO_2 over Si selectivity, while lower ion energies and shorter etch steps provide Si over SiO_2 selectivity. For Si etching, with a lower physical sputtering energy threshold than SiO_2, the additional ion bombardment seen for extended etch step lengths causes physical sputtering and potential oxidation of the surface. It should be noted that a FC build-up regime needs to be considered separately.

XPS analysis has shown that for FC depositions of 11 Å per cycle, surface chemistry changes during one cycle mostly occur in the FC film. The substrate chemistry is considerably stable throughout one cycle, resulting in a quasi-steady-state. For FC depositions of 5 Å per cycle, however, $\Delta F/C$ is increasing during one cycle, indicating that F is preferentially removed from the FC film. Defluorination of the FC film can be

seen in the strong reduction of the F/C ratio. Thinner FC depositions of 5 Å show a relatively higher intensity of reacted Si in the Si 2p spectrum than thicker FC depositions of 11 Å.

A reaction of Si is seen during the deposition step. This reaction occurs upon injection of the precursor and is believed to be based on a chemical reaction with the fluorinated substrate. Higher ion energies during the etch step and longer etch steps reduce the amount of Si reacted upon injection.

CHF_3 has an overall similar etch behavior to C_4F_8. The deposition yield for CHF_3 is lower than C_4F_8 and does depend on substrate material. The Si reaction seen during FC film deposition is stronger for CHF_3 and believed to be related to the change in deposition yield.

Acknowledgements

We thank Andrew Knoll, Dr. Nick Fox-Lyon, Adam Pranda, Pingshan Luan, and Dr. Elliot Bartis for collaboration and helpful insights and discussion on this project. We thank Drs. Eric Hudson, Steven Lai, Michal Danek, and Alexander Dulking from Lam Research for helpful discussions. We thank Michael Saccomanno and Marinus Hopstaken for help with the SIMS results. We gratefully acknowledge financial support of this work by the National Science Foundation under award No. CBET-1134273 and US Department of Energy (DE-SC0001939).

Chapter 7: Application of cyclic fluorocarbon/argon discharges to device patterning

Dominik Metzler[a)b)], Kishore Uppireddi[a)], Robert L. Bruce[a)], Hiroyuki Miyazoe[a)], Yu Zhu[a)], William Price[a)], Ed S. Sikorski[a)], Chen Li[b)], Sebastian U. Engelmann[a)], E.A. Joseph[a)] and G.S. Oehrlein[b)]

[a)]IBM T.J. Watson Research Center
Yorktown Heights, New York 10598

[b)]Department of Materials Science and Engineering
and Institute for Research in Electronics and Applied Physics
University of Maryland, College Park, Maryland 20740

Journal of Vacuum Science & Technology A 34, 01B102 (2016)

doi: 10.1116/1.4935460

Abstract:

With increasing demands on device patterning to achieve smaller critical dimensions and pitches for the 5nm node and beyond, the need for atomic layer etching (ALE) is steadily increasing. In this work, a cyclic fluorocarbon/Ar plasma is successfully used for ALE patterning in a manufacturing scale reactor. Self-limited etching of silicon oxide is observed. The impact of various process parameters on the etch performance is established. The substrate temperature has been shown to play an especially significant role, with lower temperatures leading to higher selectivity and lower etch rates, but worse pattern fidelity. The cyclic ALE approach established with this work is shown to have great potential for small scale device patterning, showing self-limited etching, improved uniformity and resist mask performance.

7.1 Introduction

Advanced semiconductor manufacturing is increasingly demanding atomic-scale process controllability. In order to uphold Moore's Law,[5] critical dimensions and required pitches steadily shrink, demanding higher and higher etching precision and selectivity.[7, 8] Additionally, increased complexity in device structure adds to the challenge.[74-76] Atomic layer deposition (ALD) has been developed as early as 1977 by Suntola[77] and has become a commonly utilized process since.[3, 78-80] Its counterpart, atomic layer etching (ALE), however, is still only beginning to enter production.[11] ALE is expected to be able to minimize substrate damage and increase pattern fidelity. Growing interest in ALE has led to several recent advances.[9, 10] There are, however, several key challenges for ALE to overcome, e.g. long process times and low throughput.[4, 11]

While enhanced energy control and reaction chemistry control schemes may show promise to attain atomic scale precision, one of the most attractive approaches currently under investigation is via employing flux control. In this technique, an inert plasma is maintained continuously throughout the process, below the energy threshold for etching. As can be seen in Fig. 7.1, a fluorocarbon chemistry is then introduced via gas pulsing, to provide the reactant adsorption. Subsequently, once the gas pulse has concluded, a time delay is applied (greater than the residence time of the adsorbent gas within the chamber) and then bias power is introduced to the inert chemistry plasma, to provide enough energy to initiate reaction of the adsorbent with the substrate surface below. The advantage of this approach is that instabilities and variability associated with pulsing the plasma source and the subsequent evacuation steps are reduced or eliminated.

Furthermore, this process offers the highest flexibility for the processing of multiple materials, since the inert chemistry and fluorocarbon chemistry can be tuned together to achieve the desired feedgas dissociation and radical generation for selective deposition, allowing the process to be adapted for etching various substrate materials.

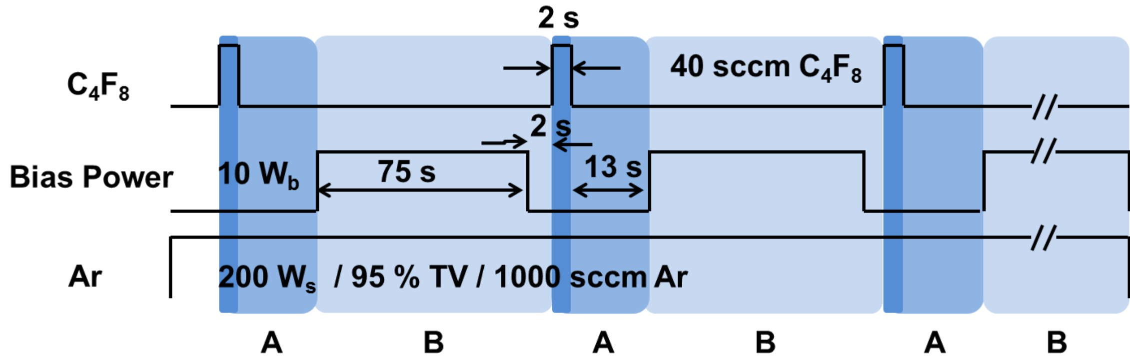

Fig. 7.1: Gas and bias pulsing sequence used in this work. Typical process conditions and times are stated.

Given these advantages, the authors evaluated this flux controlled approach, as proposed for silicon oxide ALE by Oehrlein et al.,[73] using a manufacturing scale reactor. In this article, the authors will present a baseline for device patterning using a cyclic fluorocarbon (FC)/Ar plasma etch. Substrate temperature, etch step length, source power, and bias power have been examined for their impact on etch behavior, FC deposition, uniformity, and pattern profile.

7.2 Experimental Methods

We used a conventional deep silicon etch reactor (Bosch-type) based on an inductively coupled plasma (ICP) source, schematically shown in Fig. 7.2 (a), that is able to pulse mass flow controllers with millisecond precision and is able to operate the plasma and gas injection in the desired cyclic operation. Source power W_s, bias power

W_b, substrate temperature, and processing times have all been varied to investigate a wide range of parameters. A throttle valve (TV) is used to adjust the processing pressure. The reactor used in this work is mostly identical to common manufacturing reactors. This also meant that instead of in-situ process fine tuning, process development was executed in a traditional way, i.e. based on scanning electron microscopy (SEM) analysis of etch features post process. In addition to SEM and cross-sectional SEM, transmission electron microscopy (TEM) analysis has been performed of selected conditions, allowing much greater resolution of feature structures and thin layers.

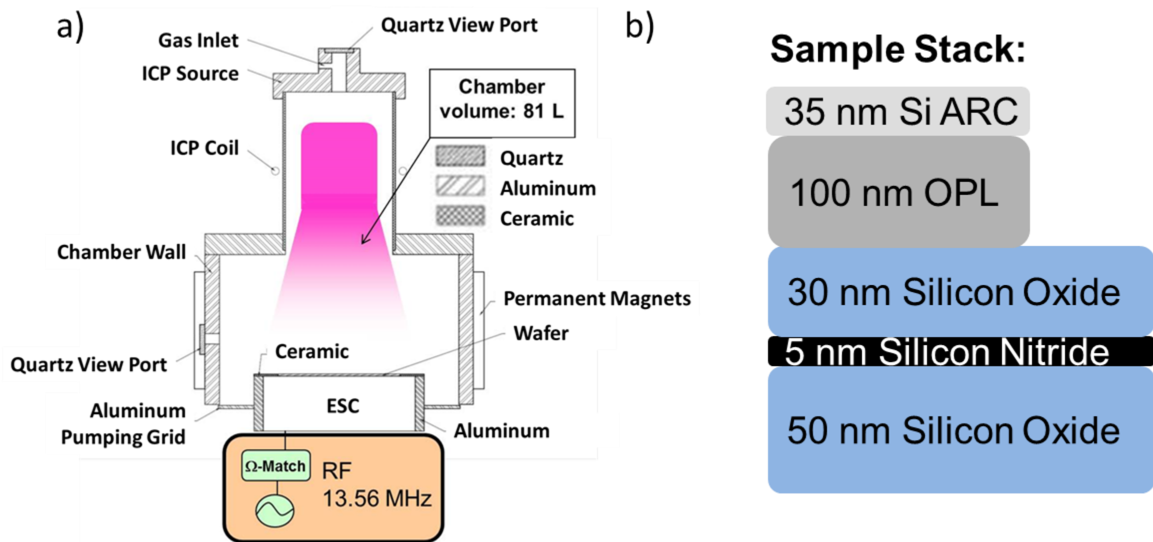

Fig. 7.2: Schematic layout of (a) experimental chamber and (b) sample stack used in this work.

The experimental structures used consisted of patterns defined by a 193nm lithography process for 200 nm and 400 nm pitch features and e-beam lithography for small pitch features (<50 nm line/space pitch). The 200 nm pitch features have an initial height of 100 nm and width of 85 nm. The resist patterns were then transferred into an organic planarizing layer (OPL) mask using a conventional N_2 based plasma etch. The OPL material used was an industry standard material, mostly consisting of C_xH_y polymer.

Typical structures are schematically shown in Fig. 7.2 (c). A 5 nm thin silicon nitride barrier layer is located between two silicon oxide layers. This layer serves as a stopping layer and to investigate the selectivity of silicon oxide over silicon nitride etching.

7.3 Results and Discussion

Initial experiments confirmed no measurable silicon oxide loss when only this inert Ar plasma was applied to the structures shown in Fig. 7.2 (b). No measurable loss was also found when the Ar plasma was biased without fluorocarbon present. A C_4F_8 chemistry is introduced via short gas pulses, to provide adsorption of chemical reactant, i.e. fluorocarbon films. Subsequently, once the gas pulse and adsorption have concluded, a small substrate bias is applied to the sample facing the inert Ar plasma, providing enough energy to the surface to initiate etching reactions of the adsorbent with the substrate surface below. The ion energy is kept low to avoid excessive physical sputtering and substrate damage. The necessary times and delays to conclude the deposition and clearly separate the steps in each cycle are based on the processing chamber volume and pump speed.

Since the adsorption step had not been well established, the authors needed to settle on a condition that more closely resembles the deposition of a thin polymer layer rather than the formation of a precise monolayer-thick film. Nevertheless, quasi-ALE behavior is observed for these conditions, as seen in Fig.7.3. Here the authors observe that during step B, the *top layer reaction step,* we are close to a saturation regime, i.e. the amount of material etched per cycle does not increase significantly if the etch step length is increased beyond 60 s. This is indicative of a self-limited process, albeit not with monolayer precision at the current processing conditions. The error bars show the range

of etch depth observed after initial analysis of these conditions at different SEM locations. 60 s etch step length showed a larger variation and uncertainty in the SEM micrographs compared to other conditions. The self-limited process was achieved without significant process optimization, showcasing the comparably straightforward implementation of cyclic flux-controlled processes. Further process optimization is expected to allow greater etch control. However, the goal of this work was to set a baseline for the application of cyclic flux-controlled etch processes in device patterning rather than to achieve maximum etch rate control. To this end, various process parameters and their impact on etch behavior have been examined and are presented here.

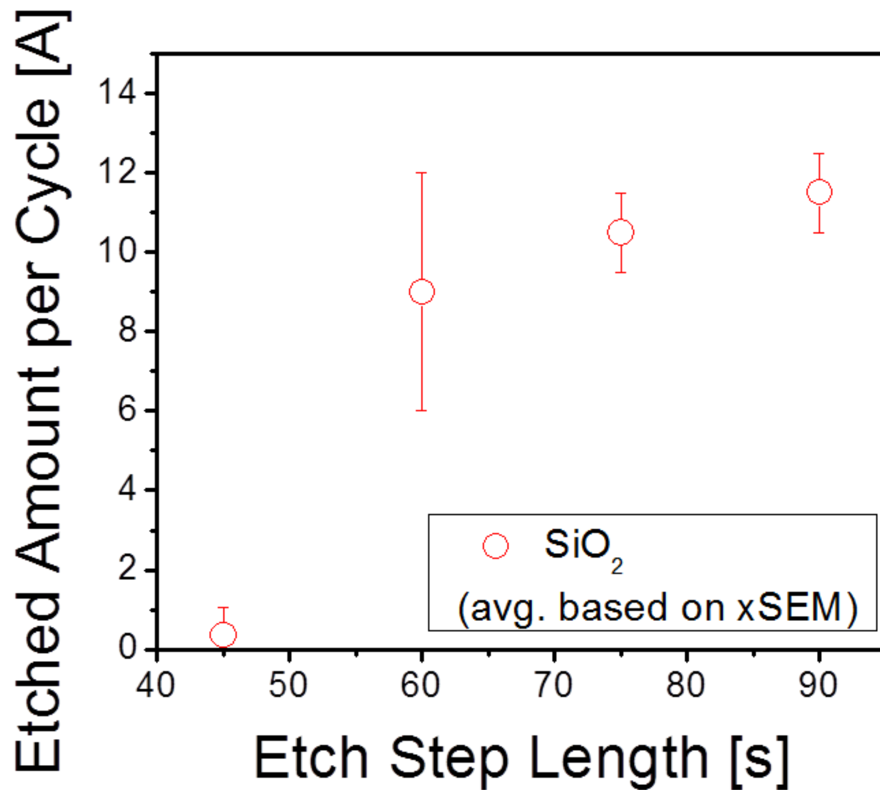

Fig. 7.3: Etched silicon oxide thickness per cycle vs. etch step length for examined conditions.

7.3.1 Substrate Temperature

The substrate temperature has a significant impact on the sticking coefficient of the FC deposit and therefore the FC film deposition and also the cyclic etch approach. Figure 7.4 shows a detailed investigation of FC deposition at various locations in a trench feature and its dependence on the substrate temperature. To enhance visibility of the FC films, they are deposited by a continuous plasma for 60 s. Nonetheless, the deposition behavior is representative of the cyclic deposition used for ALE. The sidewall deposition is crucial, especially for very small critical dimensions. Too much sidewall deposition can prevent reactive species from reaching the bottom of the feature and even lead to complete occlusion of very small features. Similarly, the penetration of the FC film into the feature is essential for high aspect ratio etching. To allow high aspect ratio etching of feature with small critical dimensions, the sidewall FC deposition needs to be small and penetrate uniformly deep into the feature. Figure 7.4 shows that sidewall deposition increases and FC penetration along the sidewall of the feature decreases with increasing substrate temperature, suggesting low temperature processing as advantageous. Deposition at the top and bottom of the feature is comparable at the critical dimensions investigated. Lower substrate temperatures lead to an increase in FC film deposition.[121, 122]

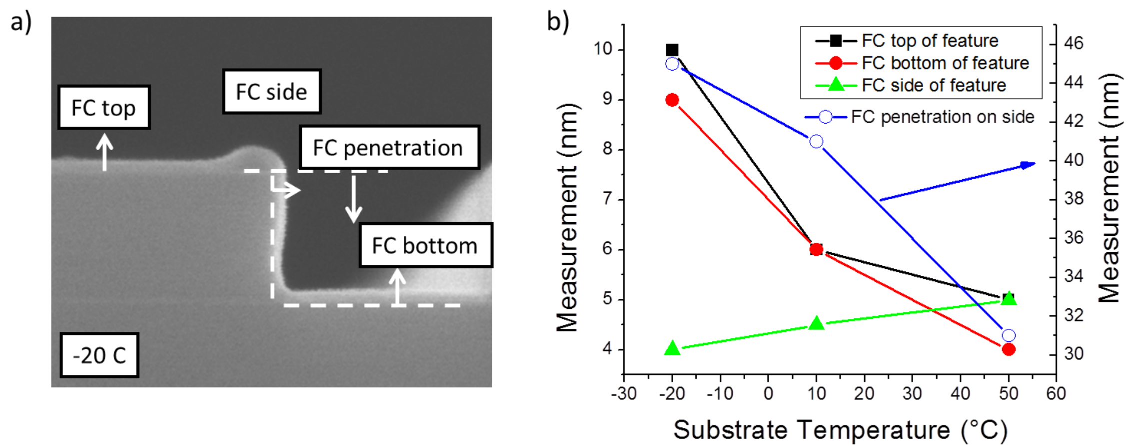

Fig. 7.4: (a) X-SEM example with measurement annotations and (b) measured dimensions (b) for examined deposition conditions. The FC top of feature, FC bottom of feature, and FC side of feature refer to the left scale, the FC penetration on side refers to the right scale.

Substrate temperature greatly affects the selectivity observed. Figure 7.5 shows that the selectivity of silicon oxide over silicon nitride increases with lower substrate temperatures, again promoting low temperature etching as beneficial. This increase in selectivity is likely related to the change in FC deposition described above. Lower temperatures lead to thicker FC films and vice versa. Therefore, very thin films are expected at higher temperature, and the necessary differences in film thickness as a function of substrate material (which is the standard mechanism to achieve high selectivity observed in continuous etching[69, 81]) is not significant enough to promote enhanced selectivity. At lower substrate temperatures, FC film thicknesses are generally thicker and can lead to inhibited etching of silicon nitride based on a thicker FC film compared to silicon oxide, similar to continuous, FC-based etching. Additionally, a decrease in etched thickness per cycle, along with increased selectivity, was observed at lower substrate temperatures, despite a higher FC deposition.[123] Similarly to the

selectivity, this decrease in etch rate is likely due to inhibited etching of the substrate based on thicker FC films.[69]

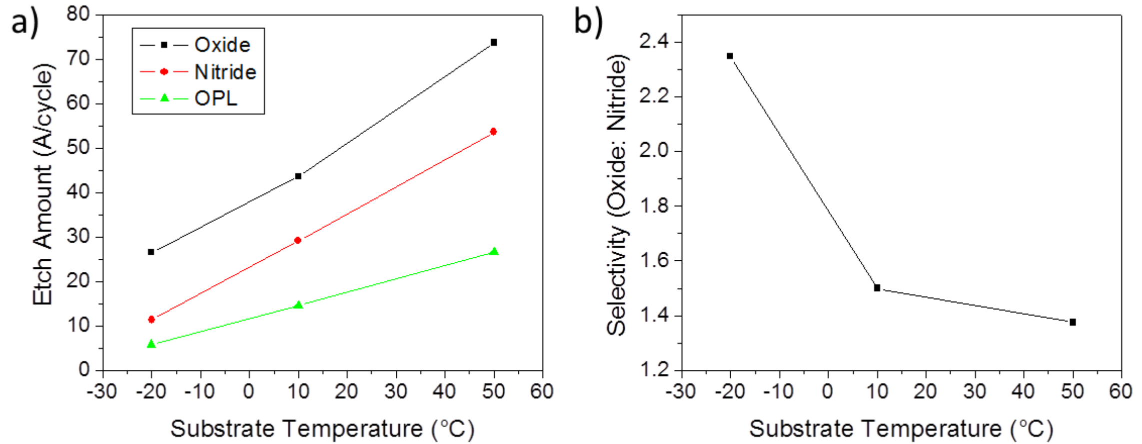

Fig. 7.5: (a) Observed etch rates and (b) silicon oxide over silicon nitride selectivity for examined substrate temperature conditions.

7.3.2 Etch Step Length

An overview of the impact of etch step length (along with substrate temperature) for patterned structures is given in Fig. 7.6. The etch step length, i.e. time of ion bombardment in each cycle, has been varied from 60 s to 90 s and substrate temperatures of -20 °C, 10 °C, and 50 °C are investigated. As discussed above, lower substrate temperatures exhibit a lower etch rate. With this in mind, insufficient etching can be seen at -20 °C substrate temperature and 60 s etch step length (Fig. 7.6 (a)). Extending the etching time per cycle leads to silicon oxide etching with a saturation effect, indicative of self-limited etching. No significant increase in etched material is observed when increasing the etch step length from 75 s to 90 s at -20 °C (Fig. 7.6 (d) and (g)). For 10 °C substrate temperature, all etch step lengths investigated show similar total material removal (Fig. 7.6 (b), (e), and (h)). A strong increase in etching is observed at 50 °C substrate temperature (Fig. 7.6 (c), (f), and (i)). As can be seen in Fig. 7.5 and Fig. 7.6,

the selectivity of silicon oxide over silicon nitride is significantly reduced at 50 °C and etch rates are enhanced. This combination leads to etching through the silicon nitride stopping layer and significant removal of the underlying silicon oxide layer.

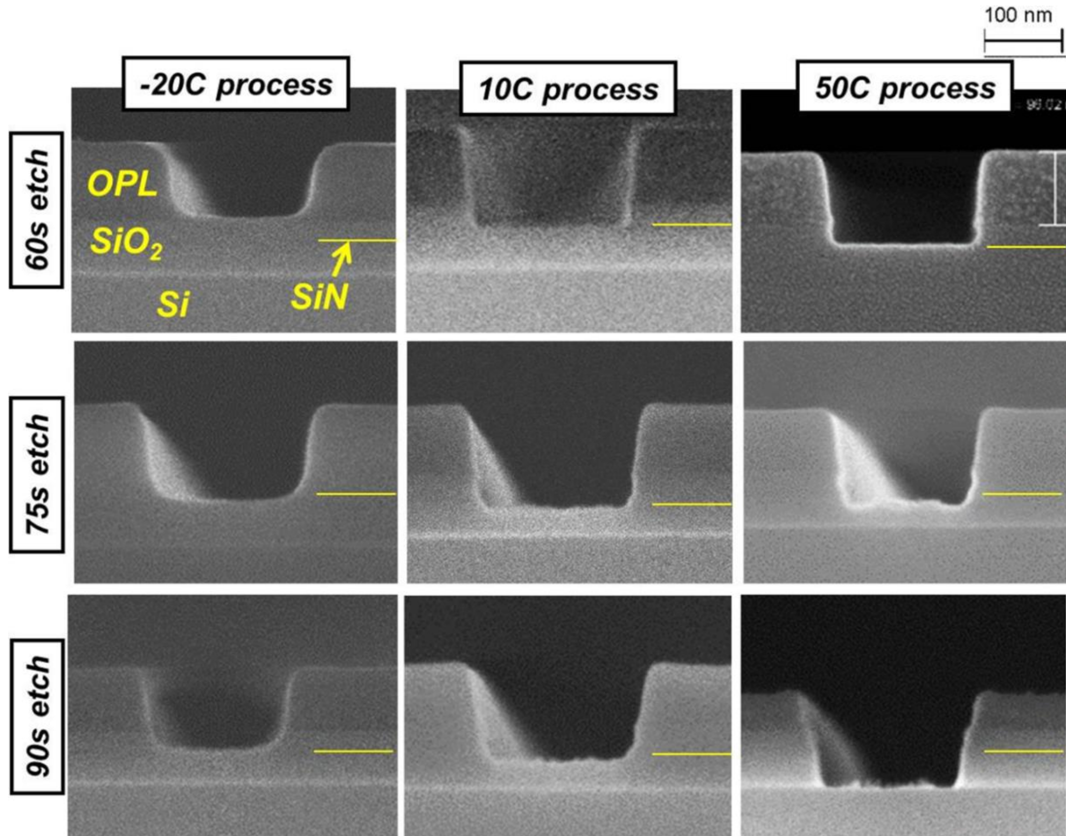

Fig. 7.6: X-SEM images of evaluated silicon oxide features with varying substrate temperature and etch step lengths.

Further examination of profile fidelity as a function of substrate temperature is highlighted in Fig. 7.7. The high magnification cross-section TEM of patterns etched at -20 °C, 10 °C, and 50 °C is shown. Lower processing temperatures show a tapered profile, while higher temperatures show a better pattern fidelity.[122] The higher FC penetration into the feature, i.e. higher sidewall deposition deeper into the feature, leads to an effective inhibition of substrate etching at the edges. This results in a tapered profile. Ohiwa *et al.*[122] observed a similar effect for continuous reactive ion etching of silicon oxide using a fluorocarbon discharge.

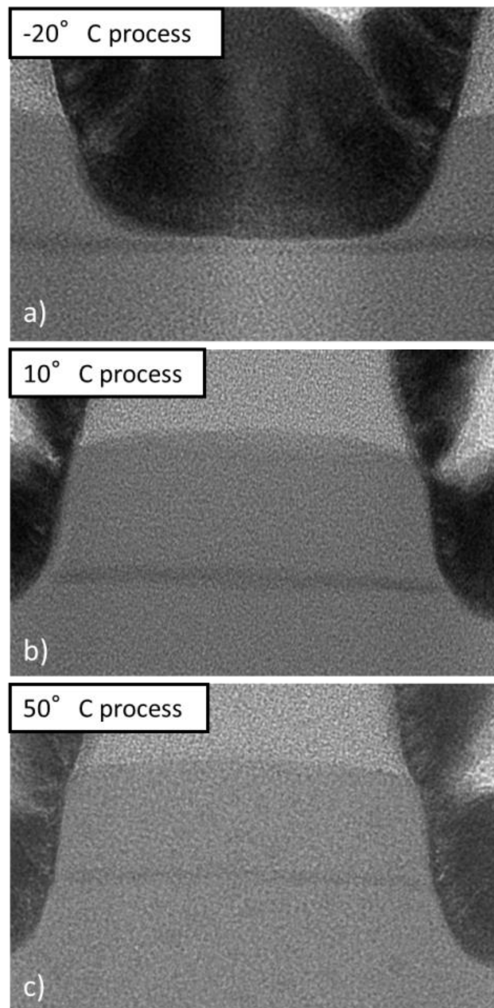

Fig. 7.7: HR-TEM images of samples processed at (a) -20° C, (b) 10° C, and (c) 50° C substrate temperature.

7.3.3 Uniformity

Wafer uniformity is essential for large scale applications. Typically edge effects and non-uniform plasma distributions, such as electron density and temperature, lead to a loss of uniformity across the wafer. The etch uniformity of a typical continuous etch at comparable conditions is compared to the cyclic FC/Ar etch in Fig. 7.8. It can be seen that the cyclic nature of the ALE process reduces edge effects and increases uniformity across the wafer, even for non-optimized conditions employed here. The ALE process is

a flux-controlled etch using a reactant starved regime. The self-limitation in each cycle allows for a small overetch, negating plasma non-uniformities and hence improving the etch uniformity across the wafer. As previously mentioned, conditions used in this work were typically not optimized to their maximum potential. This means that the advantages of the cyclic process observed are very promising and expected to be able to be further tailored and enhanced, especially given the great flexibility and parameter space of this type of cyclic flux controlled process. Figure 7.9 further highlights the uniformity improvement, showing quite comparable pattern profiles for the wafer center and edge across a 200 mm wafer.

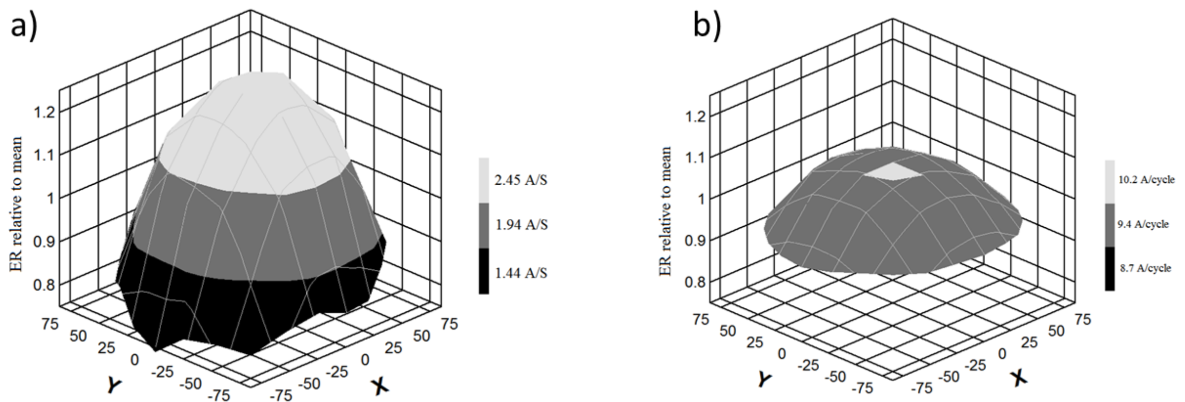

Fig. 7.8: Wafer scale uniformity of (a) conventional plasma process and (b) ALE process.

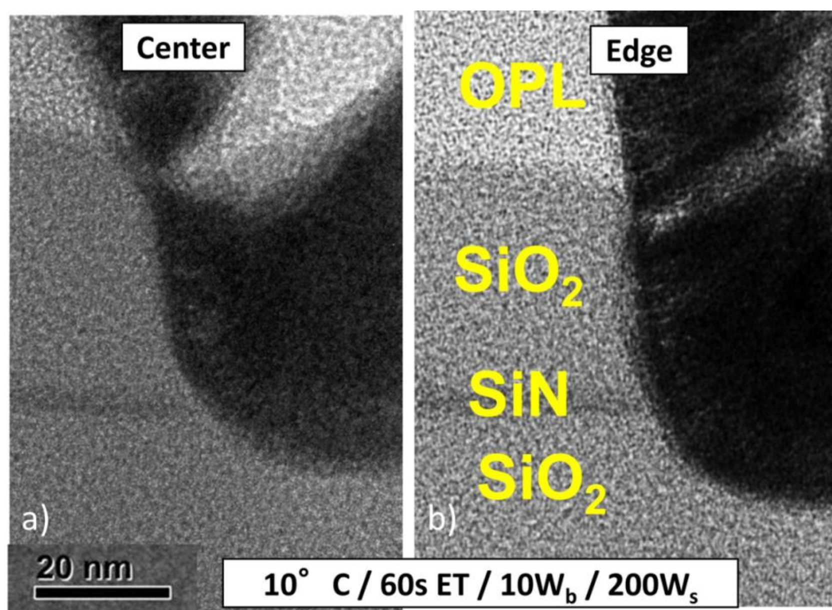

Fig. 7.9: HR-TEM image of 200-mm wafer (a) center and (b) edge profile with atomic layer etch process.

7.3.4 Surface Chemistry

The chemistry of the FC film during the cyclic etching approach is analyzed by X-ray photoelectron spectroscopy and compared to a continuous etch approach. The continuous etch leads to a CF_2 rich steady-state FC film during etching, as seen in Fig. 7.10.[23, 69] The FC film is changing significantly throughout each cycle.[73] The deposited film is of similar nature as the steady-state FC film seen during continuous etching. However, there is no real steady-state during cyclic etching. Since the precursor is only periodically injected and the bias power synchronized with the injection, the surface chemistry changes significantly within each cycle, but is quite similar from cycle to cycle. As can be seen in Fig. 7.10, the initial F rich FC film is defluorinated and etched throughout the cycle.[73] Extended ion bombardment, i.e. longer etch steps, leave little to no F in the film and therefore lead to a reactant starved etch, setting the basis for a self-limited etching behavior.[17]

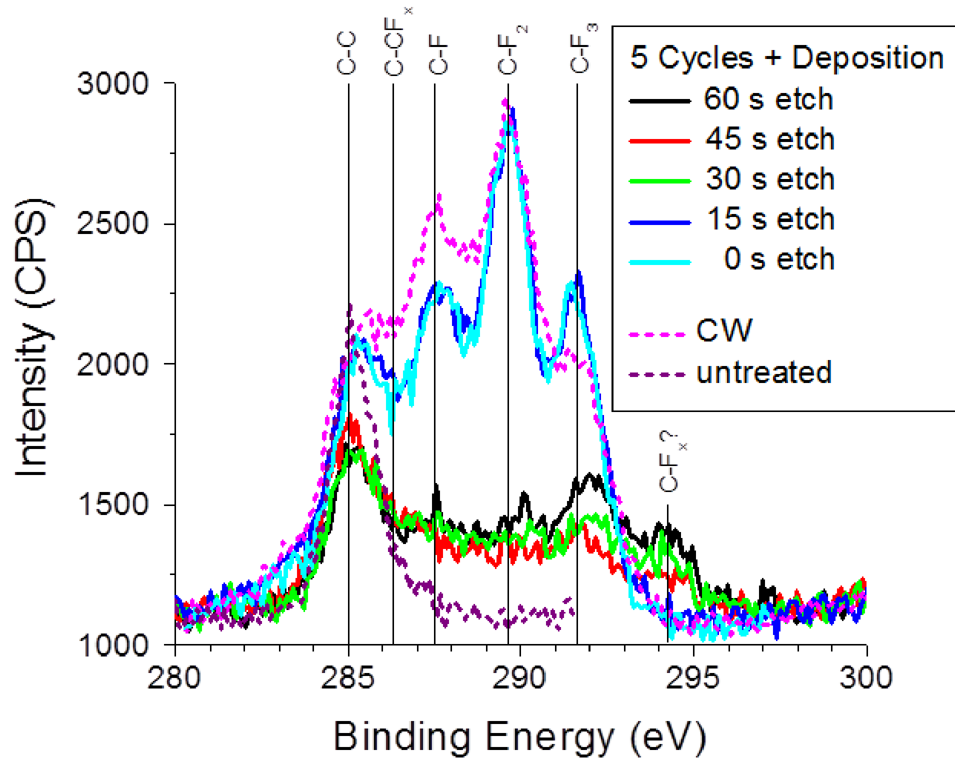

Fig. 7.10: XPS spectra of silicon oxide surface throughout one atomic layer etch cycle. 0 s etch (light blue curve) refers to the surface chemistry after the FC deposition, i.e. without ion bombardment.

The various aspects of ALE and self-limited etching can be visualized with 4 different zones, schematically shown in Fig. 7.11.[95] To achieve self-limitation, and therefore true atomic layer etching, one needs to achieve a careful balance of the energy and chemical reactant provided. This window for ALE processing may be found between the lower energy E_1 and higher energy E_2, in between which etch rates of about 1 monolayer can be achieved. Figure 7.11 also includes examples of each of the non-ideal zones. Zone 1 exhibits higher than expected etch rates, even though the ion energy is still below the sputter threshold E_s, ≈50 eV for silicon oxide.[9] The example SEM in Fig. 7.11 (a) shows a very strong increase in etch depth, while the ion energy was raised from ≈35 V to ≈60 V only, corresponding to 10 W_b and 20 W_b. In contrast, Zone 2, Fig. 7.11 (b),

shows lower than expected etch rates. In this example, altered polymer deposition leads to a decrease of the etch depth to only about 80% of the expected value. In the extreme case, one can also enter Zone 3, Fig. 7.11 (c), behavior, where a complete etch stop and net deposition are observed. In zone 4 the ion energy is sufficiently low, however, the etch rate is elevated. The example here in Fig. 7.11 (d) is the condition from Fig. 7.6 (i), where a 160% increase in etch depth was achieved by a mere 50% increase in etch step time. The authors suspect that the desired self-limitation of the etch step time may not be given due to re-release of F-rich particles from the chamber walls in this condition. With the parameter space explored in this work one can see that the ALE window is indeed rather narrow, as expected. Aiming for etch control on the Ångstrom level with ultra-high selectivity requires very careful and high control of all processing parameters, e.g. ion energy, FC coverage, and chamber wall condition.

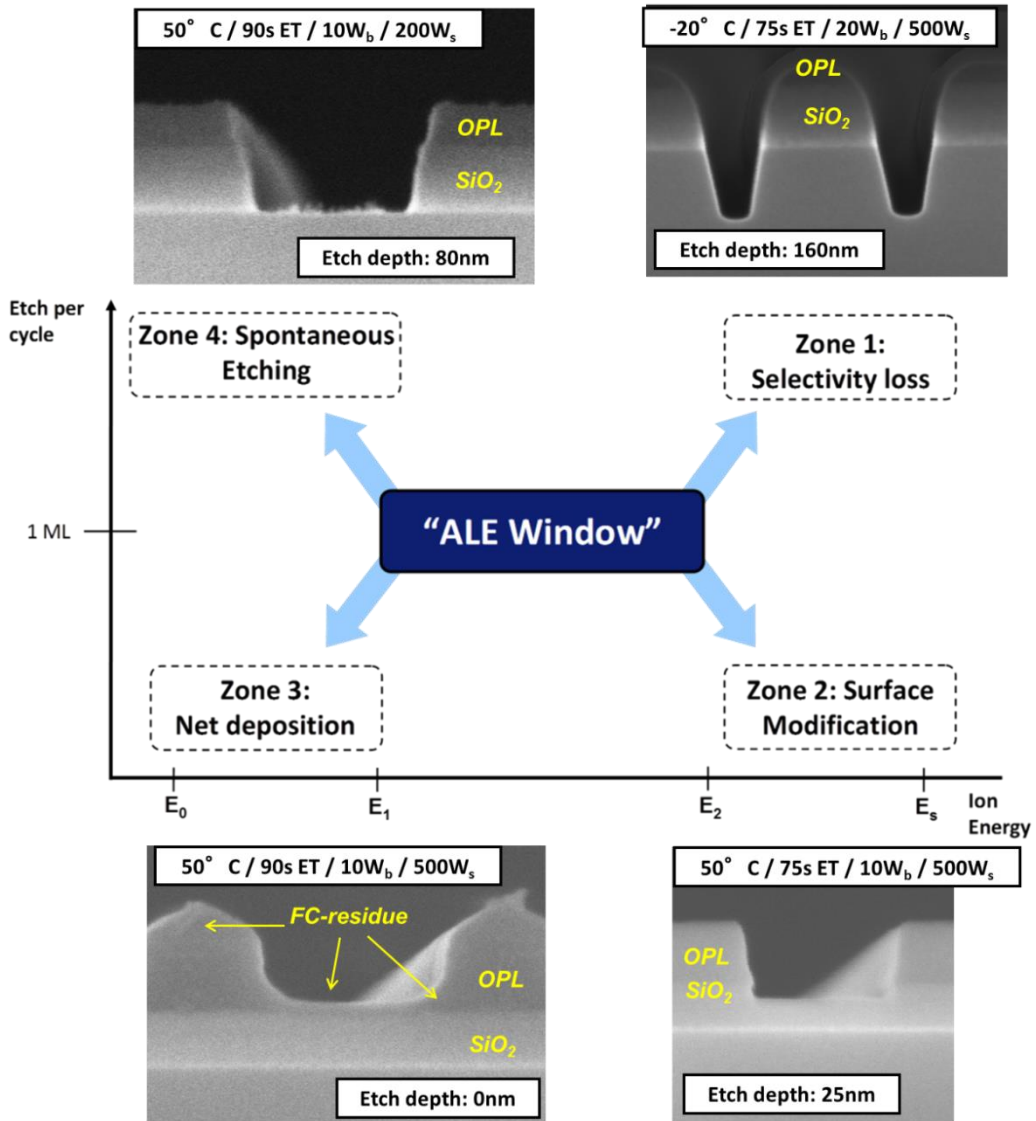

Fig. 7.11: Schematic illustration of the ALE window with 4 example results of non-ideal behavior.

To further investigate the application of cyclic FC/Ar etches to small scale device patterning, more aggressive pitch structures have been investigated. Figure 7.12 shows etching of 40 nm pitch structures with a continuous etch approach and a cyclic FC/Ar ALE approach. Continuous etch approaches typically show wiggling issues for small pitches and critical dimensions, as observed in Fig. 7.12 (b). The ALE approach,

however, is shown to yield straighter lines and pattern fidelity, promising a significant improvement over continuous etch approaches.

The pattern profile, as measured by cross-section SEM, is shown in Fig. 7.13. The pattern profile shows the successful small pitch patterning of silicon oxide and a great selectivity over OPL.

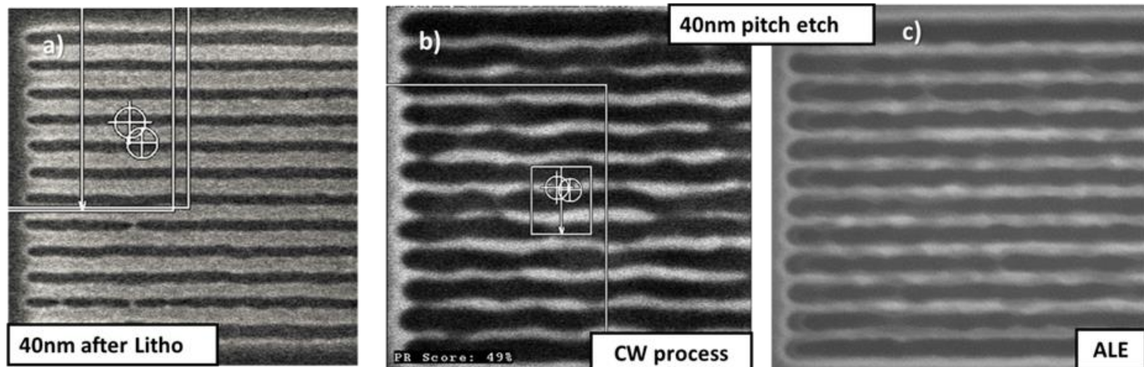

Fig. 7.12: 40nm pitch features (a) after lithography and (b) after etching in conventional plasma and (c) atomic layer etch approach at 200 W_s, 10 W_b, 10 °C, and 75 s etch time.

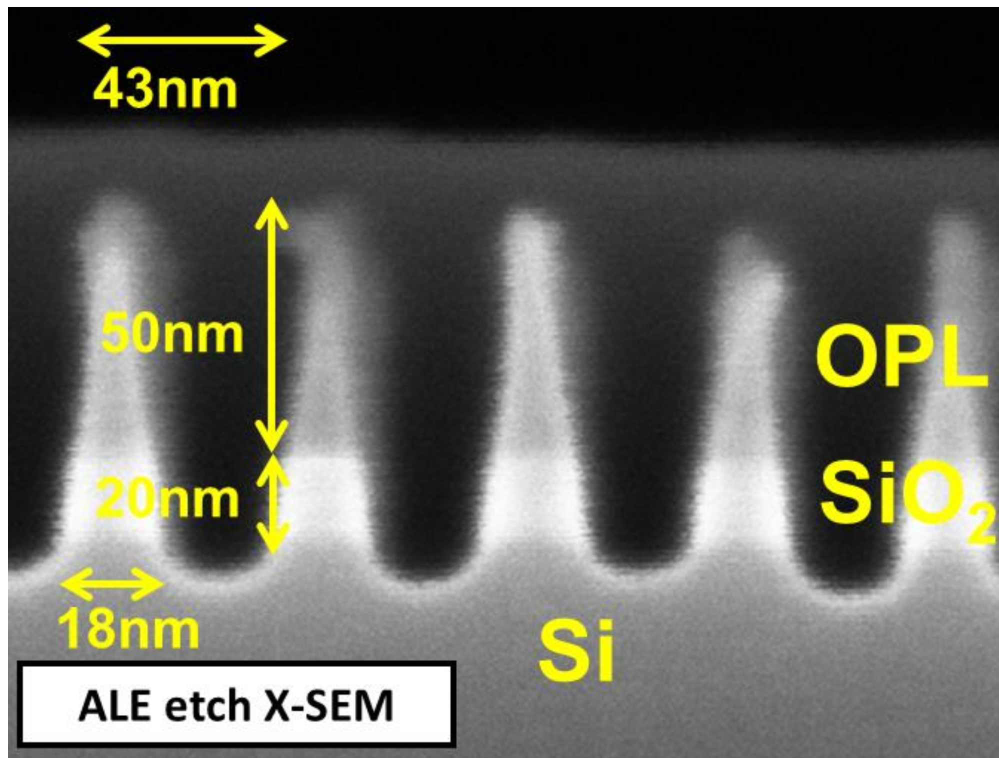

Fig. 7.13: X-SEM of patterned 44 nm pitch feature by atomic layer etch approach.

7.4 Summary and Conclusions

A cyclic fluorocarbon/Ar atomic layer etch approach has been studied. Several important process parameters, such as substrate temperature, etch step length, source power, and bias power, have been investigated. This parameter exploration allows to set a baseline for process characterization, tailoring and optimization. The intention of this work was to provide insight on the impact of the process parameters studied on the etch behavior, rather than process optimization. Therefore, the improvements over continuous etch approaches seen here are very promising as they are expected to increase further with detailed process parameter fine tuning.

A successful application of the cyclic ALE approach as proposed by Oehrlein et al.[73] to device patterning is shown. Overall, the cyclic FC/Ar etch has proven to pattern devices well, with great potential for significant improvement in overall etch performance based on process optimization. The cyclic FC/Ar ALE approach is based on chemically assisted etching. Therefore, substrate temperature has a significant impact on the FC film deposition, etch per cycle, and selectivity. A low substrate temperature has shown benefits with a lower etch rate and higher selectivity, but trading off for worse pattern fidelity. Wafer uniformity is improved in comparison to a continuous etch approach, further establishing cyclic FC/Ar ALE as a promising device patterning process.

The extendibility to small pitch patterning was shown for 44 nm pitch features. Using C_4F_8 as a precursor has, however, also shown limitations. Future work will therefore include exploration of other gas chemistries. Different precursors are expected to lead to significant impacts. The change in FC deposition based on substrate temperature shown here highlights the importance of the nature of the FC film, which is

heavily dependent on the choice of precursor. Additionally, other reactants, such as hydrogen for example, can be introduced through the precursor and polymer film for further process tailoring. The high flexibility and tuneability of the ALE approach is expected to allow significant process optimization, e.g. in terms of precursor, ion energies, FC coverage, substrate temperature, and etch time, to further decrease critical dimensions and pitches towards the 5 nm node.

Acknowledgments:

Special thanks go to J.M. Papalia, Y. Zhang and N. Fuller. The results shown have been mostly produced in the Microelectronics Research Laboratory (MRL) at the T.J. Watson Research Center, Yorktown Heights, NY. The authors would also like to thank the MRL staff & MRL management for support of this work. The authors thank Andrew Knoll, Pingshan Luan, and Dr. Elliot Bartis for helpful insights and discussion on this project. The authors gratefully acknowledge financial support of this work by the National Science Foundation under award No. CBET-1134273 and US Department of Energy (DE-SC0001939).

Chapter 8: Plasma-Based Removal of Oxide on Si and SiGe Substrates While Minimizing Surface Residues

Dominik Metzler[1], Chen Li[2], C. Steven Lai[3], Eric Hudson[3], and Gottlieb S. Oehrlein[1]

[1] Department of Materials Science and Engineering
and Institute for Research in Electronics and Applied Physics,
University of Maryland, College Park, Maryland 20740

[2] Department of Physics,
and Institute for Research in Electronics and Applied Physics,
University of Maryland, College Park, Maryland 20740

[3] Lam Research Corporation, 4400 Cushing Parkway, Fremont, CA 94538

Journal of Vacuum Science & Technology A, in preparation

Abstract:

The evaluation of a plasma-based native oxide surface cleaning process for Si and SiGe substrates is described. Objectives include removal of the native oxide while minimizing substrate damage and surface residues. This work is based on recent advances in atomic layer etching of SiO_2 [D. Metzler *et al.*, J Vac Sci Technol A **32**, 020603 (2014)]. To achieve controlled etching of SiO_2 at the Ångstrom level a cyclic approach consisting of a deposition step and etch step was initially employed. The deposition step deposits fluorocarbon (FC) films up to 10 Å thick on the surface. Subsequent low energy Ar^+ ion bombardment during the etch step induces mixing of the FC film with the substrate and removal of the FC film together with the mixed, reacted substrate material. Oxide layer thicknesses were measured using *in situ* ellipsometry and surface chemistry was analyzed by X-ray photoelectron spectroscopy. The cyclic ALE approach when used for removal of a native SiO_2 from Si did not remove native oxide from a Si substrate at the level required. A modified process was evaluated which used continuously biased Ar plasma with periodic CF_4 injection. By eliminating a dedicated FC film deposition step, optimizing process times and ion energies, significant O removal from the Si surface was achieved, while leaving residual C. An additional H_2/Ar plasma exposure performed at higher pressure and minimizing ion bombardment successfully removed residual carbon and fluorine originating from the surface cleaning process while passivating surfaces. The combined treatment reduced oxygen and carbon levels to about half compared to as received silicon surfaces but removed ≈37 Å of Si. The modified cleaning approach was then applied to SiGe substrates. Similar to Si substrates, oxide removal was seen upon applying the cleaning process, while the H_2/Ar post treatment

subsequently removed F-related species. Oxygen and carbon levels are reduced to ≈70 % after the combined treatment while ≈55 Å of SiGe are removed. In addition, the surface is Ge richer after the cleaning process compared to SiGe surfaces as received.

This feasibility study of Ar/FC based native oxide cleaning approaches for Si and SiGe substrates shows the potential to reduce oxygen levels but at the cost of introducing low levels of carbon and fluorine at the Si and SiGe surface. A key issue is the substantial Si and SiGe substrate material loss that accompanies the oxide removal.

8.1 Introduction

One challenge in atomic scale surface engineering is the minimization of substrate damage and surface residues while achieving etch control at the Ångstrom level.[15, 124] Cleaning surfaces via dry etching methods has been of great interest.[125, 126] However, device performance can be greatly reduced by defects and damage introduced during the process.[15, 16] Minimizing substrate damage is therefore crucial for the success of any surface cleaning application.[127] These considerations are of great importance, for example, for source/drain and metalized regions of materials such as Si and SiGe.[107] When continuous plasma etching of Si-based material using fluorocarbon (FC) containing Ar plasma is performed,[8] high ion energies are required to counter the FC deposition. This etching process introduces substrate damage, and leaves behind a residual FC film on the surface after etching.[10, 109-111, 124] The field of atomic layer etching (ALE) has seen several recent advances.[9, 10, 14] For example, Kim *et al.* have investigated the possibility of removing damaged layers by employing ALE.[128, 129] The possibility to remove SiO_2 with Ångstrom precision using a steady-state Ar plasma in conjunction with periodic, precise precursor injection and synchronized low energy, plasma-based Ar^+ ion bombardment has been demonstrated.[73] Cleaning surfaces requires controlling unwanted contamination and preventing formation of a reacted surface layer. Direct plasma exposure is accompanied by ion bombardment, even if ion bombardment energies are minimized, and reactive species interact with the surface, leading to a mixed layer. These mixed layers are thin when using low energies, but are not completely avoidable.[69, 118] In addition, Si surfaces are typically very reactive, especially during plasma exposure. In order to keep processed surfaces clean, they need to be passivated.

In this work we examine the possibility to remove thin oxide layers from Si and SiGe by adapting a cyclic ALE process for thin oxide removal while minimizing surface residues and substrate damage. Continuous Ar plasma exposure, described in section III.1, serves as a baseline and points out silicon surface oxidation due to low levels of oxygen during low energy Ar sputtering as a key issue of surface cleaning. The cyclic approach developed for precise ALE of SiO_2 is evaluated for removal of native oxide from crystalline Si in section III.2 a). Section III.2 b) describes the optimization of the Si cleaning process to minimize surface contamination and damage introduced by plasma exposure. This approach is also applied to native oxide removal from SiGe substrates in section III.3.

8.2 Experimental Procedures

All processes examined for surface cleaning are of a cyclic nature, utilizing periodic precursor injection to control the amount of available chemical etchant. Details of the inductively coupled plasma system excited at 13.56 MHz used for this work have been described previously.[19-21] The plasma was confined within a 195 mm diameter anodized Al confinement ring. A 125 mm diameter Si substrate was located 150 mm below the top electrode on an electrostatic chuck and can be biased at 3.7 MHz. The base pressure achieved before processing was on the order of $6x10^{-7}$ Torr and the temperature of the samples (25 x 25 mm^2) was stabilized by substrate cooling (10 °C) during plasma processing. Standard process conditions were 10 mTorr processing pressure, 200 W source power, and 30 eV maximum ion energy. Bulk Si wafers with a native SiO_2 layer were used to study the removal of a thin oxide layer from a Si surface. For SiGe cleaning, samples were ≈550 Å thick SiGe films with a native oxide. In order to achieve high

control over chamber conditions, samples were loaded via a load lock. A standard oxygen clean and Ar conditioning plasma in between each experiment ensured that chamber conditions were as consistent as possible.

Film thicknesses were monitored in real-time by *in-situ* ellipsometry[22] (λ = 632.8 nm) operating in the polarizer-rotating compensator-sample-analyzer configuration. The angle of incidence is ≈72°. Measurements are performed in Ψ-Δ-space, where Ψ and Δ correspond to changes in the phase and relative amplitude of the polarized laser light components. Optical multilayer modeling was used for interpretation of recorded data and to establish real-time thickness changes. After processing, samples were transferred under vacuum to a Vacuum Generators ESCALAB MK II surface analysis system for X-ray Photoelectron Spectroscopy (XPS). Narrow scan spectra of the Si 2p, Si 2s, C 1s, O 1s, Ge 3d and F 1s were obtained at 20 eV pass energy at an electron take-off angle of 20° with respect to the sample surface. Spectra were fitted and decomposed using least-square-fitting after Shirley background subtraction.[23, 24] The spectral decomposition was adjusted slightly for Si and SiGe substrates. For Si substrates, Si 2p spectra were fit with peaks corresponding to Si-Si, SiF, SiF_2, SiF_3, SiO_2, and fluorinated silicon oxide. C 1s spectra were fit with peaks corresponding to C-C, C-CF_x (x = 1, 2, and 3), CF, CF_2, and CF_3. O 1s spectra were fit with peaks corresponding to SiO_2 and fluorinated silicon oxide. F 1s spectra were fit with peaks corresponding to SiF_x (x = 1, 2, and 3), fluorinated silicon oxide, and CF. For SiGe substrates, the Si 2p spectra (97 to 107 eV) overlap with Ge Auger peaks (102 to 114 eV)**.** The Si 2s spectrum was therefore investigated instead. The spectra were decomposed into elemental and reacted Si. C 1s spectra were decomposed in an identical fashion as for Si substrates. Since the C 1s spectra for

processes on SiGe substrates did not show any significant amounts of CF_x species, they are not considered in the F 1s spectra. An additional peak at 685.5 eV related to GeF species is observed in the F 1s spectrum. The O 1s spectra show an additional peak related to GeO species at 531.6 eV. Ge 3d spectra were fit with peaks corresponding to Ge-Ge, GeF, and GeO_2. For a particular sample, all fits were required to be consistent across all individual spectra, i.e. the chemical information gained from Si 2s, Si 2p, C 1s, O 1s, F 1s, and Ge 3d was internally consistent. Additional information about this analysis method can be found in previous publications.[24, 32, 69-72, 81, 98]

8.3 Results and Discussion

8.3.1 Ar Sputtering.

To study the removal of a thin oxide film from a Si surface, bulk Si wafers with native oxide of ≈20 Å thickness were studied. Plasma based Ar sputtering served as a baseline and reference for the surface cleaning. Figure 8.1 shows the relative thickness change of the native SiO_2 layer when exposed to Ar plasma. In the case of an unbiased plasma, with a maximum ion energy of ≈15 eV, initial etching of the oxide was observed before net surface oxidation takes place after 30 s of plasma exposure. Surface analysis confirms higher levels of oxide on the surface after Ar sputtering. Enhanced ion bombardment, achieved through an applied bias potential increasing the ion energy to ≈30 eV and accelerated the reoxidation process significantly.[23] Ion enhanced reoxidation of surface can take place even with very low levels of oxygen present.[83] Several previous studies suggest erosion of the quartz coupling window as a possible source of oxygen.[18, 23, 86, 87] This result suggests that a potential cleaning process needs to be kept short while minimizing ion bombardment in order to prevent plasma based oxidation. Additionally,

any source of potential oxygen contamination should be minimized. It also shows that the ion energies used will not induce significant physical sputtering of the SiO_2 formed (the physical sputtering threshold for SiO_2 is on the order of 50 eV[9, 130]). This indicates that a chemical reactant is required for oxide removal.

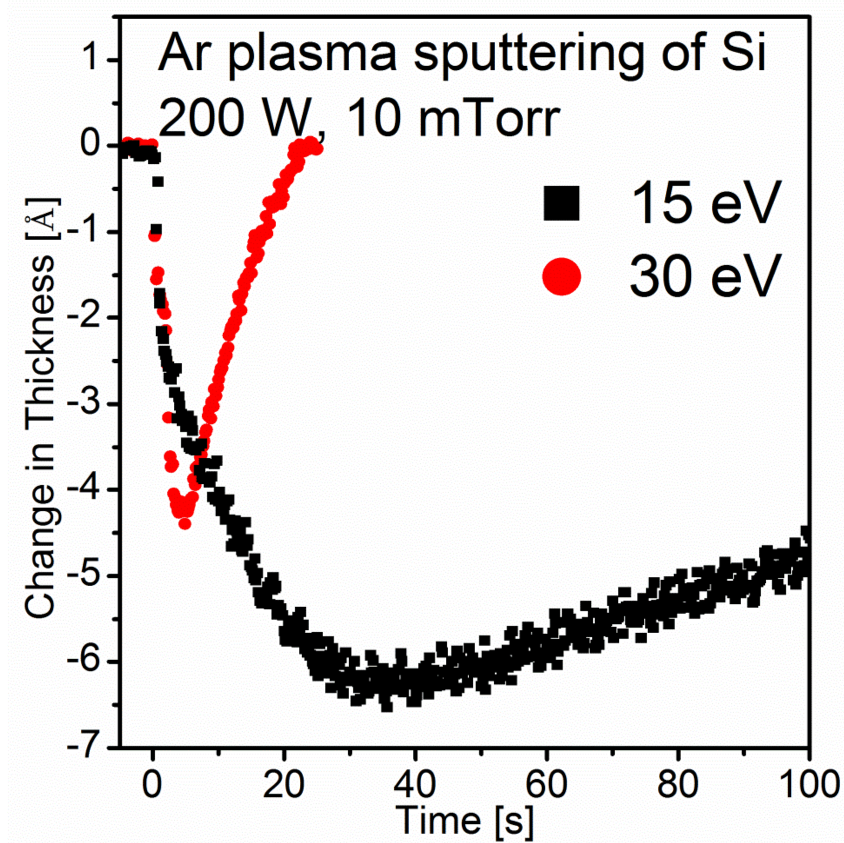

Fig. 8.1: Relative thickness change of Si native oxides exposed to Ar plasma with 15 eV (black) and 30 eV (red) ion energy.

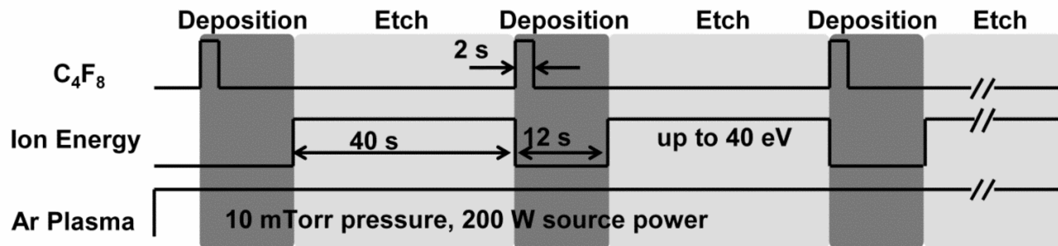

Fig. 8.2: Schematic of the cyclic ALE process used for SiO_2 etching. A FC film deposition step is followed by a subsequent etch step with low energy Ar^+ ion bombardment.

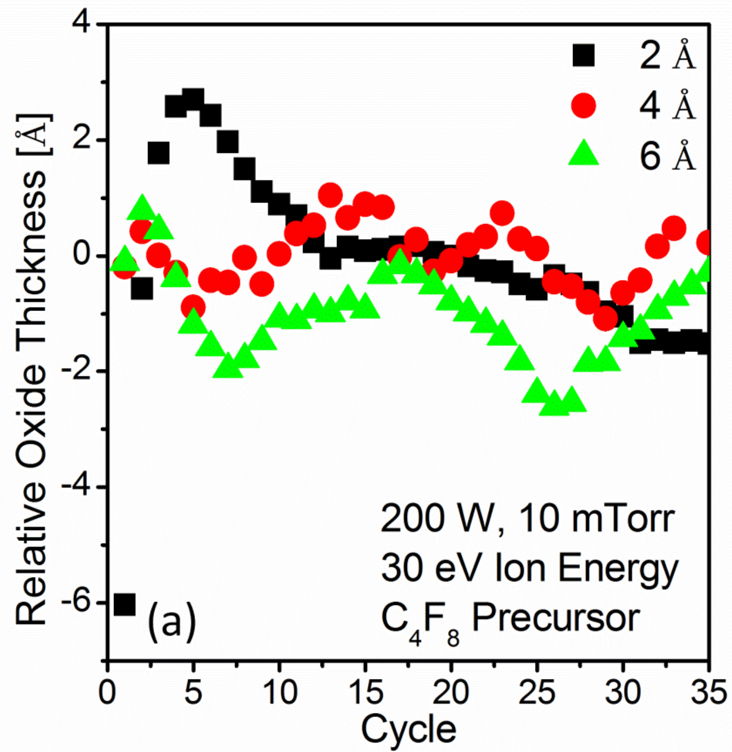

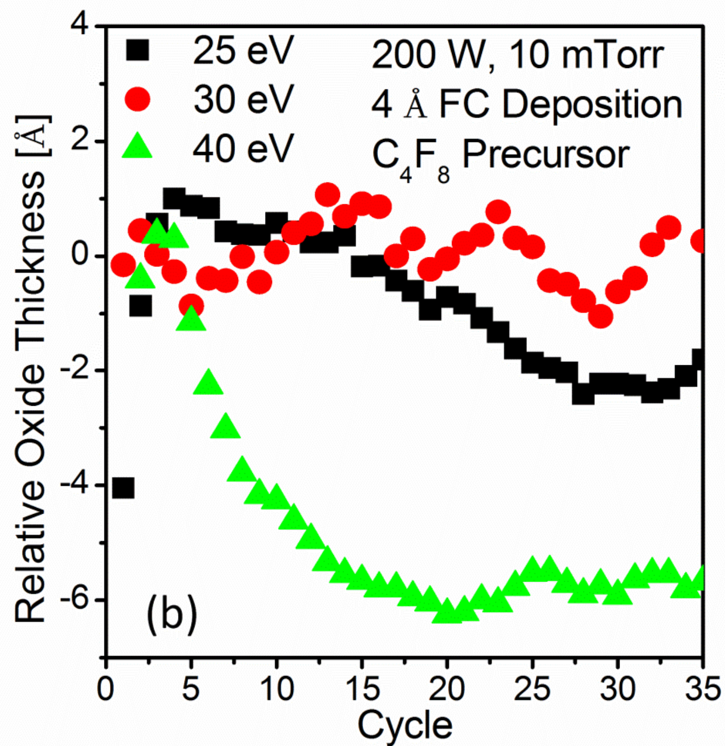

Fig. 8.3: Relative oxide thickness compared to pristine thickness of ~20 Å for each cycle at various (a) FC thicknesses deposited per cycle and (b) ion energies using the cyclic ALE process on Si with native oxide.

8.3.2 Removal of Thin, Native SiO_2 from Silicon Surfaces

8.3.2.1 Cyclic ALE Process

Initial cleaning studies were performed utilizing a process developed for ALE of SiO_2.[73] Periodic, precursor injection was coupled with a synchronized low energy Ar^+ ion bombardment. The cyclic process is schematically shown in Fig. 8.2, consisting of a deposition step and sequential etch step. During the deposition step, a precise precursor injection deposits a FC film on the order of several Ångstrom thin. Subsequent low energy (up to 40 eV) plasma-based Ar^+ ion bombardment has been shown to remove the FC film together with an Ångstrom thin layer of reacted SiO_2.[73] This process was applied to bulk, crystalline Si aiming to remove the native oxide layer. *In situ* ellipsometry showed limited thickness reduction, as seen in Fig. 8.3. Neither the FC layer thickness deposited per cycle, nor the ion energy during the etch step, have a significant impact on the oxide thickness evolution. When reducing the etch step length from 40 s to 20 s to potentially reduce oxidation during a reactant starved phase at the end of each etch step, no significant impact on the oxide thickness evolution was seen. Additionally, the impact of the precursor has been explored by comparing C_4F_8 and CF_4 as examples for a deposition precursor and an etching gas. The overall results using this cyclic ALE approach are similar for all conditions explored with both precursors in terms of thickness evolution as measured by *in situ* ellipsometry and surface chemistry as measured by XPS. All of these parameters (i.e. FC film thickness deposited per cycle, ion energy, etch step length, and precursor) have shown, however, a significant impact on etch depth per cycle during ALE of SiO_2 and Si in other work.[73, 98]

Surface chemistry analysis after the cyclic ALE process showed significant amounts of oxygen and low amounts of carbon on the surface for all conditions explored

here. Therefore, the film thickness measured by ellipsometry is remaining oxide and not residual FC from the deposition. Independent of each process parameter, there is a lack of full oxygen removal. Additionally, the cyclic ALE approach fluorinates the oxide.

This means that while the cyclic ALE process allows for controlled etching of SiO_2 and Si, its usefulness for Si surface cleaning is limited. Extensive work on ALE of Si showed that a fluorinated oxide layer persists during the etching of Si substrates.[98] One of the limitations for cleaning of Si surfaces using this cyclic ALE approach is reoxidation of the Si surface during reactant starved ion bombardment, similar to that seen in Fig. 8.1.[18, 23, 86, 87] Towards the end of each etch step the system becomes fluorine starved. Low energy Ar^+ ions are still striking the reactive Si surface during this time and can induce reoxidation of the surface in the presence of very low levels of oxygen impurities, e.g. introduced by bombardment of the quartz coupling window.

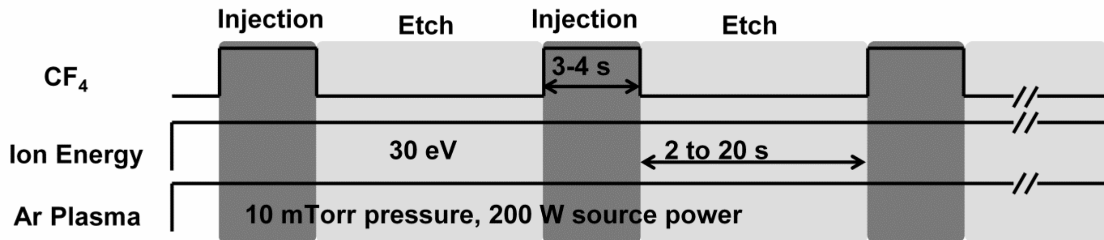

Fig. 8.4: Schematic of the continuously biased cleaning process. This process utilizes precise, periodic CF_4 injections into a continuously biased Ar plasma.

8.3.2.2 Continuous Bias Process

Since the cyclic ALE approach did not produce sufficiently clean surfaces, process changes were implemented. Firstly, reoxidation was prevented, and the extent of the fluorinated, mixed interface layer between the FC film and the substrate was minimized. The cleaning process was modified to a continuously biased cleaning

approach, i.e. a continuously biased Ar plasma with periodic precursor injection. Figure 8.4 shows a schematic of the process. A continuously biased Ar plasma provides low energy Ar^+ ion bombardment while periodic CF_4 precursor injections was used to provide periodic supply of chemical etchant to increase oxide etching while at the same time limiting FC film deposition. In addition, CF_4 injection rather than C_4F_8 was used, to improve FC deposition control based on a lower deposition yield for CF_4.

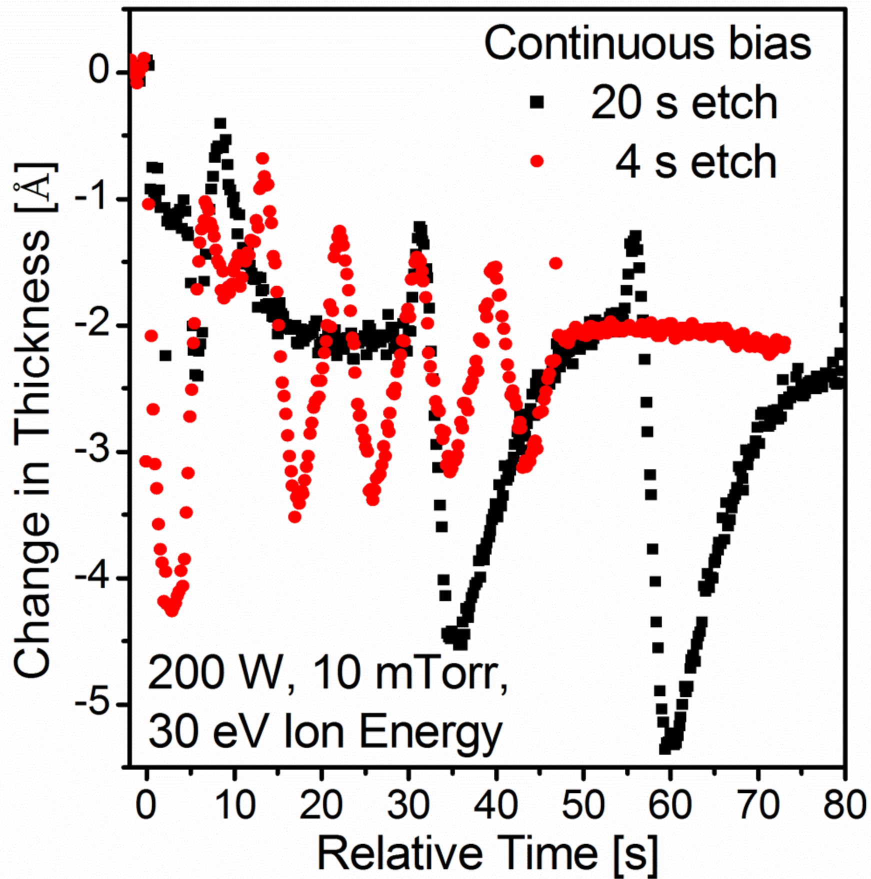

Fig. 8.5: Relative changes in oxide layer thickness as measured by *in situ* ellipsometry for a continuously biased cleaning process with a 4 s CF_4 injection.

Real time ellipsometry, shown in Fig. 8.5, displays the importance of the chemical etchant. In the case of 20 s of etching in between each precursor injection, a small thickness increase can be seen upon CF_4 injection, followed by a strong etch. Once the

etchant is depleted, etching stops and a net thickness increase is observed. This thickness increase is the main obstacle in successful oxide layer removal and based on surface reoxidation. Surface chemistry analysis shows comparable levels of oxide and little residual carbon.

Reducing the etch time in between injections from 20 s to 4 s, with the goal of minimizing the thickness increase after the etch stops, led to several strong changes in the thickness trajectory and surface chemistry. While the thickness increase in between injections is reduced, the etched thickness per cycle is also reduced. This suggests that the layer deposited in between injections is volatile and easily removed again during the subsequent cycle. The two effects essentially cancel each other, leading to a similar overall small net total thickness reduction. Surface chemistry analysis showed, however, that the shorter etches treatment lead to significant oxygen removal while leaving a residual carbon film. This essentially transforms the problem at hand from removing oxide to removing carbon films. The continuously biased cleaning process successfully removes oxygen from the surface, but leaves residual carbon and fluorine due to a potentially highly reactive Si surface produced by ion bombardment.

This cleaning process consumes a fairly high amount of substrate material for process conditions examined. Roughly 34 Å of Si are consumed during five cycles of cleaning. The substrate thickness removed per cycle increases during the first two cycles and is constant at ≈8 Å per cycle during the last three cycles.

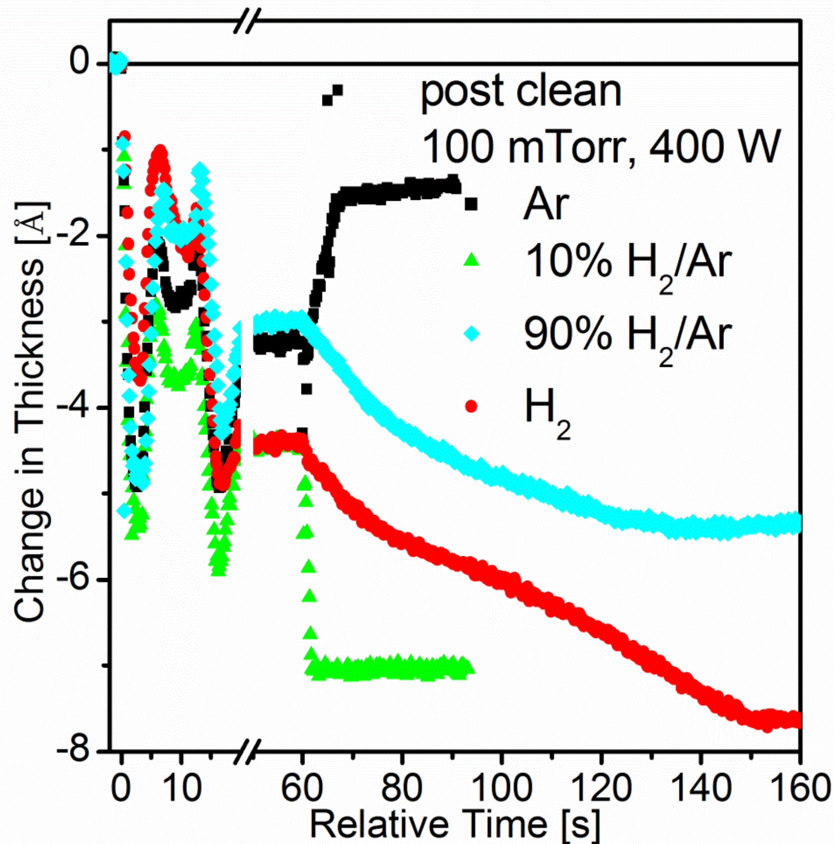

Fig.8.6: Relative changes in top layer thicknesses for post cleaning H_2/Ar plasma with 0, 10, 90, and 100 % H_2 admixture after a continuously biased clean.

8.3.2.3 Post Cleaning H_2/Ar Treatment

It has been shown that SiO_2 etch rates vanish, even with fluorine still present in a reacted surface layer.[17, 73] This suggests that a cleaning process using a fluorine chemistry, will always show at least some fluorinated silicon. As discussed above, the cleaning procedure left a reactive Si surface with a residual carbon layer and residual fluorine. An additional process is needed to remove these residues. Hydrogen-based cleaning procedures have been explored in the past, e.g. see Refs. [131-134]. It has been shown that hydrocarbons can be removed using an H_2 plasma.[135] Additionally, Si surfaces can be passivated by hydrogen exposure.[136-138] Therefore, an additional process step to remove residual carbon and fluorine left on the surface after a continuously biased

cleaning step, as well as to terminate the surface to prevent reoxidation, was explored. An H_2/Ar plasma treatment performed at 100 mTorr pressure and 400 W source power is promising in this respect. A higher processing pressure was chosen to minimize ion bombardment of the surface. H_2 admixtures of 0%, 10%, 90%, and 100% H_2 in Ar were explored, allowing for a H_2 rich and Ar rich plasma. *In situ* ellipsometry showed etching of ≈3 Å for all H_2 containing post cleaning plasma (see Fig. 8.6). The etch rate was significantly higher for Ar rich plasma, consistent with the impact of Ar^+ ions.

The surface chemistries after the continuously biased cleaning process, as well as with a subsequent 10% H_2/Ar and 90% H_2/Ar plasma, are shown in Fig. 8.7 and compared with a Si surface as received. A strong reduction of oxygen, fluorine, and carbon impurities is seen after the 90% H_2/Ar process. Ar rich post clean plasma show reoxidation of the Si surface, while H_2 rich plasma do not. This further supports the idea of ion driven reoxidation. In addition to carbon removal, H_2 rich plasma also show a significant reduction in the F 1s signal. The pure H_2 and pure Ar post clean treatment fail to remove the residual carbon film.

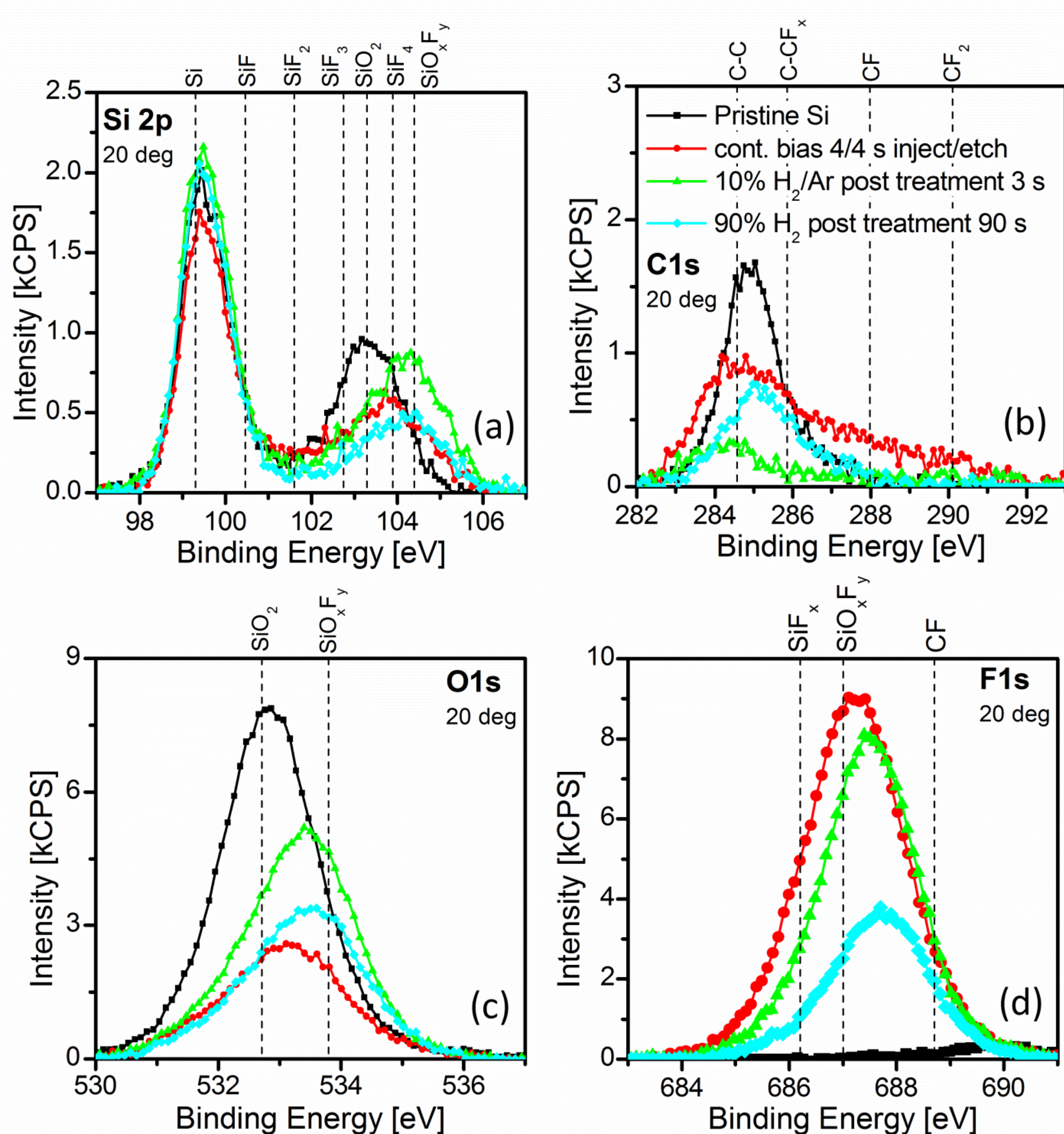

Fig. 8.7: XPS spectra of the (a) Si 2p, (b) C 1s, (c) O 1s, and (d) F 1s measured for a pristine Si sample (black squares), after continuous bias cleaning (red circles), after a post cleaning 10% H_2/Ar plasma (green triangles), and after a post cleaning 90% H_2/Ar plasma (cyan diamonds).

This combined treatment of continuously biased cleaning and subsequent 90% H_2/Ar plasma successfully removes native oxide and cleans Si surfaces. Figure 8.8 shows the relative intensity of Si, O, and C compared to an untreated surface, and the relative intensity of F compared to a continuously biased cleaning process. The as received

surface is compared to the three main processes, i.e. Ar sputtering, continuously biased cleaning with 4 s etches, and a continuously biased clean combined with a 90% H_2/Ar post clean treatment. It can be seen that the Ar plasma sputtering causes surface oxidation, as described above. The continuously biased cleaning process transforms the problem from removing oxygen to removing fluorine and carbon. The post clean treatment successfully removed more than half of the residual fluorine and carbon left after the continuously biased cleaning, leading to overall cleaner surfaces. The combined process reduces oxygen and carbon levels to ≈50 % compared to as received levels as can be seen in Fig. 8.8. The elemental Si signal is 10 % higher while the reacted Si signal is strongly reduced to 33 % after the cleaning process.

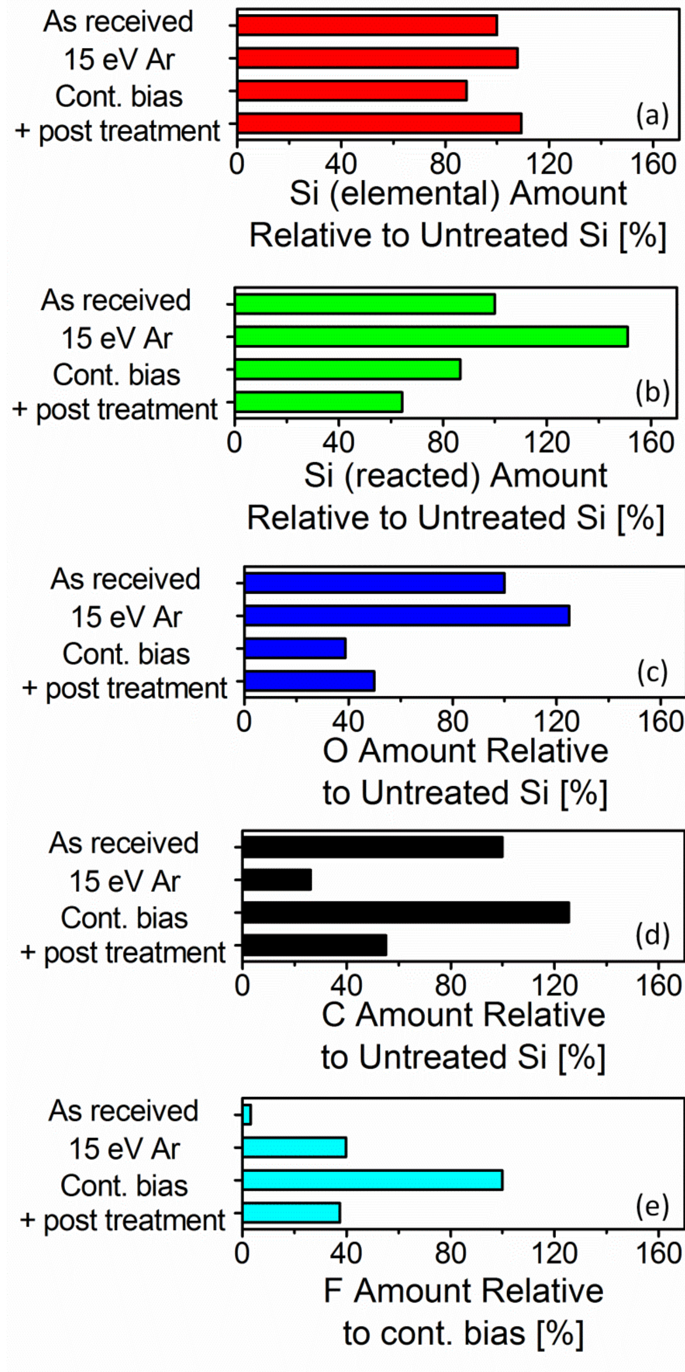

Fig.8.8: Summary of elemental intensities of (a) elemental and (b) reacted Si, (c) oxygen, and (d) carbon for cleaning processes of Si substrates relative to a Si substrate as received. (e) The fluorine intensity is taken relative to the continuously biased process. The treatments shown are Ar plasma sputtering at 15 eV, a continuously biased cleaning process, and a continuously biased cleaning process with a subsequent 90% H_2/Ar post treatment.

8.3.3 Removal of Thin, Native Oxide from SiGe Surfaces

The final cleaning process investigated for Si, i.e. the continuously biased cleaning process with short etches in between precursor injection and a subsequent 90% H_2/Ar post clean treatment, was subsequently applied to native oxide removal from SiGe substrates. Similar to Si surfaces, SiGe surface are typically very reactive and ion enhanced reoxidation can take place. Ge has been shown to act as catalyst for oxidation, i.e. Ge enhances the oxidation rate, while not being incorporated into the oxide itself.[139, 140] SiGe substrates have a native oxide layer on the surface. The thickness of this native oxide layer is about 25 Å, as measured by ellipsometry and angle resolved XPS. The chemical composition of this oxide layer has been investigated by XPS, showing a combination of GeO_2 and SiO_2. Dilute HF treatment, which etches surface oxide, increased the atomic concentration of Ge by 32% and decreased O by 31%, while Si percentages stayed constant. This indicates that the native oxide layer is composed dominantly of SiO_2 over GeO_2.

Ar plasma sputtering of native oxide on SiGe substrates is shown in Fig. 8.9. Overall, Si and SiGe surfaces exhibit a similar behavior when exposed to Ar plasma at low ion energies with one exception. The initial thickness removal seen for unbiased Ar (15 eV ion energy) plasma is slower for SiGe surfaces. The minimal thickness seen is similar to Si, and achieved after ≈60 s instead of ≈30 s for Si.

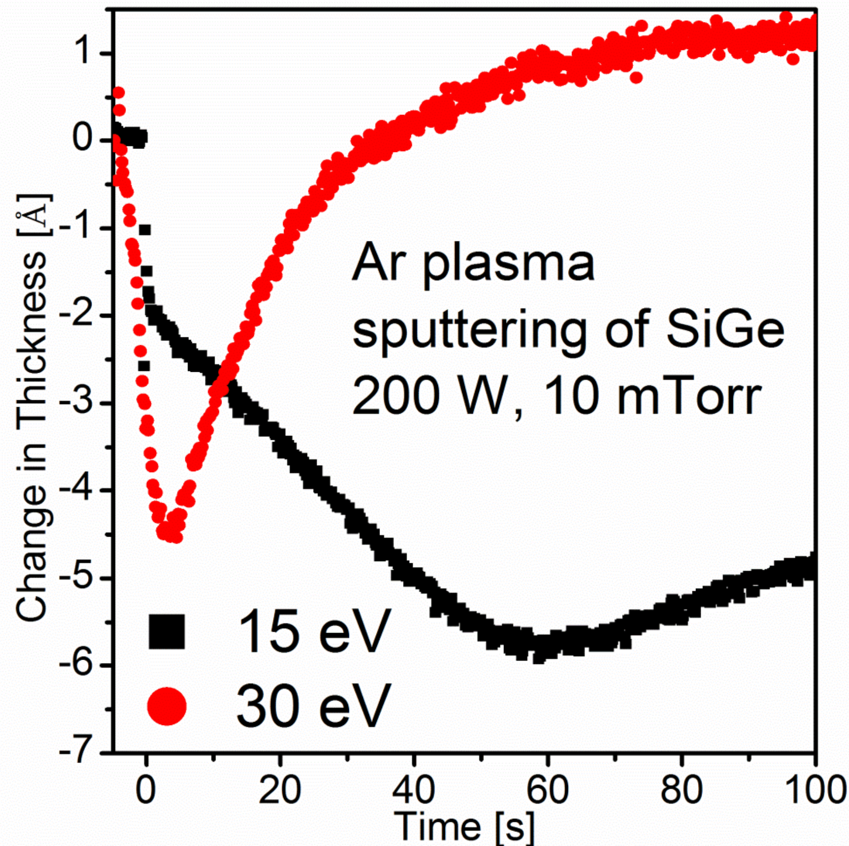

Fig. 8.9: Relative thickness change of SiGe native oxides exposed to Ar plasma with 15 eV (black) and 30 eV (red) ion energy.

The continuously biased cleaning process has been applied to SiGe and the resulting surface chemistry is shown in Fig. 8.10. Similar to Si, the continuously biased cleaning process shows a significant oxygen removal while pure Ar plasma sputtering introduces more oxygen on the surface. A significant reacted Ge peak at a binding energy of 32 eV was observed when the cleaning process was applied. This is indicative of fluorinated Ge or a lower degree of oxidization of Ge.[141] The F 1s spectra confirmed a relatively higher amount of GeF after cleaning. The FC based cleaning process introduces fluorine in the SiGe substrate. Etch rates are typically higher for SiGe compared to Si.[142-144] The continuously biased clean shows a significant substrate consumption of SiGe until a sufficient level of oxygen removal is observed. The SiGe removal is stronger during the

first cycle, and leads to a loss of 18 Å of material. A removal of ≈9 Å per cycle after the first cycle leads to a total consumption of 55 Å after five cycles. A 90% H_2/Ar post clean treatment has proven promising for Si and was also applied after SiGe cleaning. The surface chemistry is shown in Fig. 8.10. A slight increase in the O 1s intensity was seen, indicating little reoxidation. The F 1s spectrum as well as the GeF peak at 32 eV in the Ge 3d spectrum were significantly reduced. This shows the successful removal of GeF and SiF from the surface. The SiGe consumption is minimal during this post clean treatment. Overall, the post clean treatment shows similar effects on SiGe and Si substrates, i.e. removing residual fluorine without significant reoxidation of the surface.

In order to represent the degree of cleanliness of the SiGe surface, the relative amounts of Ge, Si, O, and C compared to an untreated SiGe surface are shown in Fig. 8.11. The F intensity is compared to a continuously biased cleaning process. It can be seen that the continuously biased cleaning process mostly removes SiO_2 from the surface. The amount of elemental and reacted Ge is higher compared to a sample as received. The strong GeF peak observed upon applying the cleaning procedure leads to an increase in the amount of reacted Ge. The 90% H_2/Ar post clean treatment is seen to remove GeF and SiF. The F level drops by ≈25 % during the post clean treatment. A significant improvement over SiGe substrates as received is observed. The oxygen and carbon levels are reduced to ≈70 % after the combined cleaning process. Elemental Si and elemental Ge signals increase by ≈60 % and ≈130 %, respectively. This also shows that the surface is relatively richer in Ge after the cleaning process as compared to surfaces as received. It is noteworthy that the C 1s signal was low for all processes applied to SiGe substrates and discussed here, i.e. carbon residues were minimal.

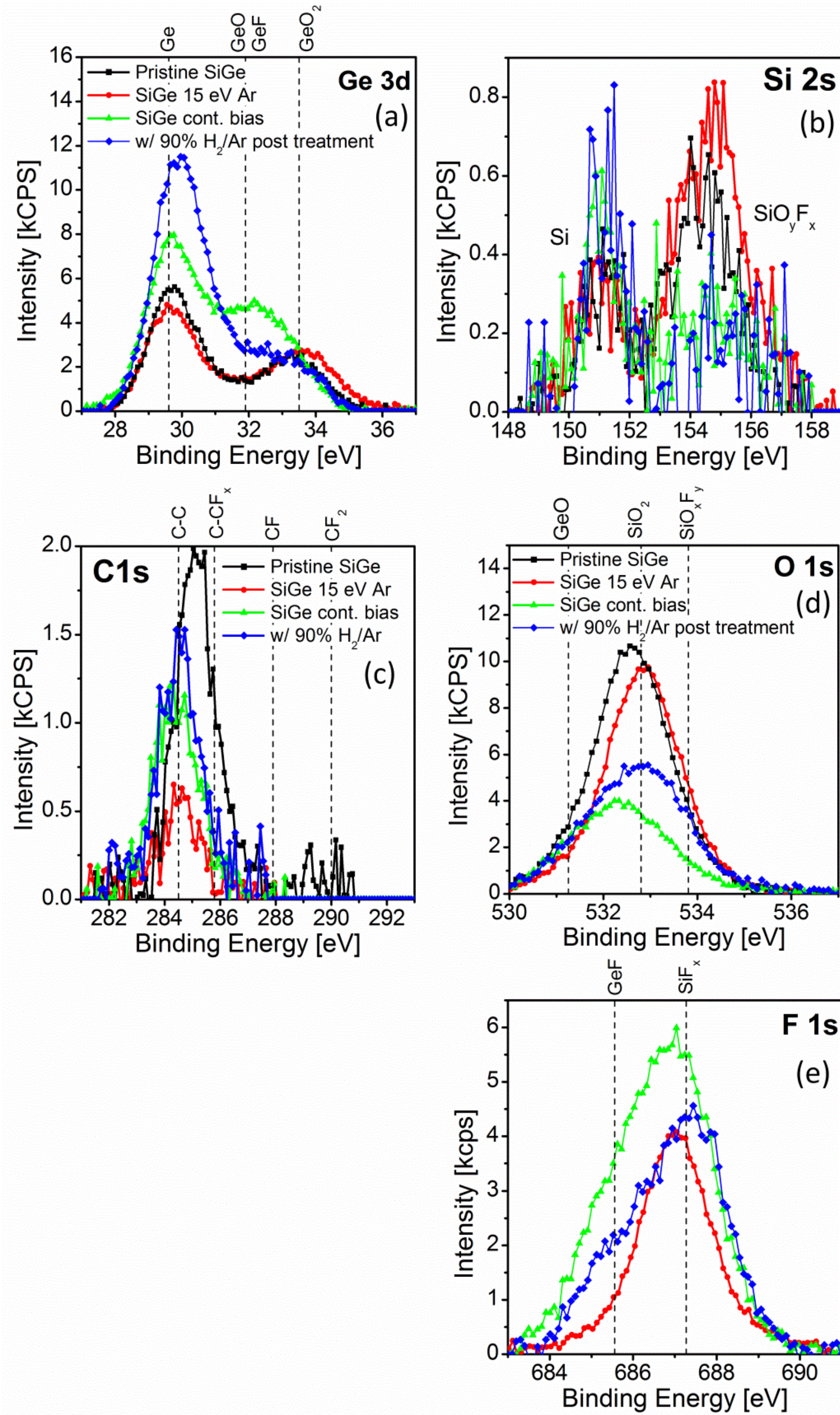

Fig.8.10: Surface chemistry of pristine SiGe with a native oxide layer (black squares), after Ar plasma exposure (red circles), after continuous bias cleaning (green triangles), and after continuous bias cleaning with a 90% H_2/Ar post clean treatment (blue diamonds).

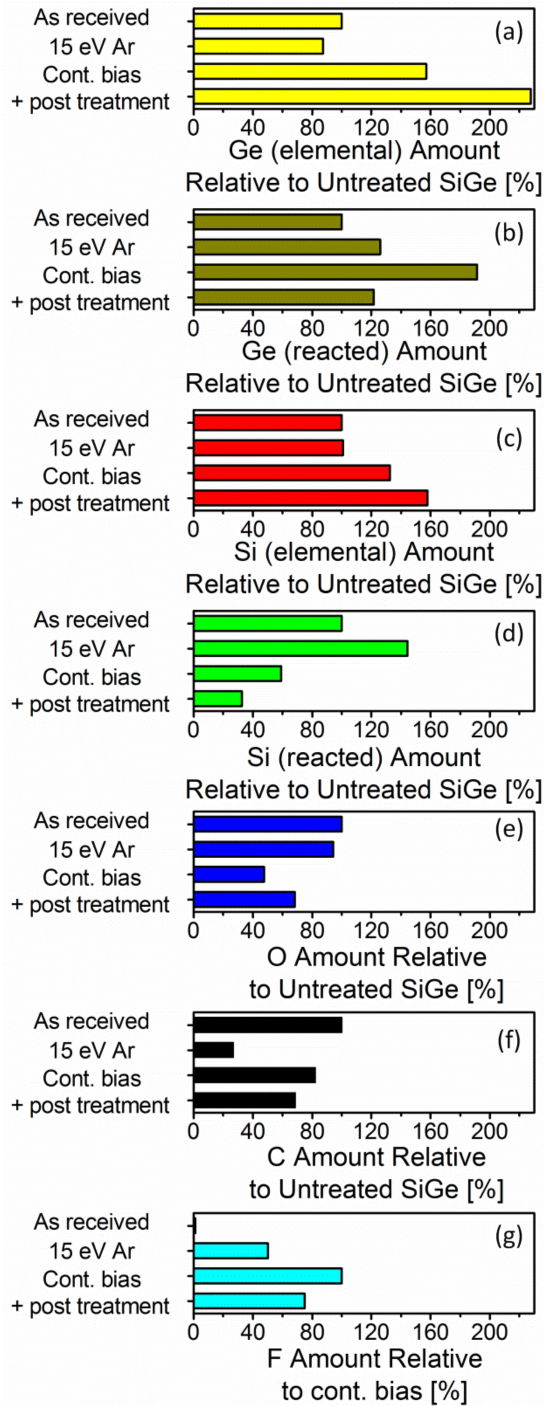

Fig. 8.11: Summary of elemental intensities of (a) elemental and (b) reacted Ge, (c) elemental and (d) reacted Si, (e) oxygen, and (f) carbon for cleaning processes of SiGe substrates relative to a SiGe substrate as received. (g) The fluorine intensity is taken relative to the continuously biased process. The treatments shown are Ar plasma sputtering at 15 eV, a continuously biased cleaning process, and a continuously biased cleaning process with a subsequent 90% H_2/Ar post treatment.

8.4 Conclusions and Summary

Ar sputtering mainly leads to oxidation of the Si surface at the low ion energies explored. The cyclic ALE process is leaving a residual fluorinated oxide layer on the surface after etching, independent of the process parameters explored here. Optimizing the cleaning process has led to a significant improvement over the initial cyclic ALE process for Si and SiGe substrates. For a continuously biased cleaning process, 20 s of ion bombardment in between injections causes too much surface oxidation, thus preventing actual oxide removal. Shortening the ion bombardment to 4 s successfully removes oxygen from the Si surface, but leaves a residual carbon film, essentially transforming the problem. A H_2/Ar plasma can be used after the continuously biased cleaning process to further remove residual carbon and fluorine as well as to terminate the surface. However, if this plasma is Ar rich, the ion bombardment will lead to reoxidation of the Si surface. The combined cleaning process reduces the oxygen level at the surface to ≈50 % while removing ≈37 Å of Si material.

Cleaning of SiGe substrates showed overall fairly similar trends to Si substrates. A continuously biased clean successfully removes oxygen from the surface, but introduces fluorine into the substrate. A subsequent 90% H_2/Ar post clean treatment removes fluorine (SiF and GeF) from the surface without significant reoxidation. Pairing a continuously biased cleaning process with a subsequent 90% H_2/Ar plasma exposure leaves minimal surface residues on Si and SiGe. Oxygen levels are reduced to ≈70 % compared to as received surfaces while the elemental Ge signal increases to ≈230 %. The cleaning process removes predominately SiO_2, leading to a Ge richer surface.

Additionally, small amounts of carbon residue have been seen at essentially every point during this work. For Si and SiGe substrates the carbon level was reduced to ≈50 % and ≈70 % of as received levels, respectively, using the combined cleaning treatment.

We conclude that the Ar/FC followed by hydrogen plasma surface cleaning process studied here has the potential to reduce oxygen levels for Si and SiGe substrates, albeit at the cost of introducing low levels of carbon and fluorine at the surfaces. A key issue is the substantial Si and SiGe substrate material loss that accompanies the cleaning process.

Acknowledgements:

We thank Andrew Knoll, Adam Pranda, Pingshan Luan, and Elliot Bartis for collaboration and helpful insights and discussion on this project. We thank Drs. Eric Joseph, Sebastian Engelmann, and Robert Bruce from the IBM T.J. Watson Research Center for helpful discussions. We gratefully acknowledge financial support of this work by the National Science Foundation (CBET-1134273), US Department of Energy (DE-SC0001939) and Lam Research Foundation.

Chapter 9: Conclusions and Future Work

The major contribution of this work is the first experimental demonstration of fluorocarbon-based (FC) atomic layer etching (ALE) of SiO_2 using an approach that had first been theoretically examined. The work is in excellent agreement with computational predictions, demonstrating the power of coupling computational simulations and experiments. This process is further characterized in terms of plasma and process parameters. Fundamental aspects of ALE of SiO_2 and Si, in particular surface mechanisms, have been explored. Key mechanisms are characterized in order to enable a highly selective process design. This ALE approach is a very sensitive process. The FC deposition thickness per cycle is of the order of a few Ångstrom, and maximum ion energies range from 20 to 30 eV. Despite these relatively small changes in processing parameters, a significant impact on the etch behavior can be seen. During this study it has become clear that highly controlled process parameters and chamber conditions are essential to maintaining high precision and etch control for ALE.

In chapter 2, the He PPT developed for roughness reduction of 193nm PR was applied to other common organic masking materials. The polymers studied in addition to 193nm PR were an anti-reflection coating (AR), a hard mask (HM), near frictionless carbon (NFC), and an extreme ultraviolet resist (EUV). First, it was shown that the approach is generic for 193nm PR polymers and did not depend on the specific type used. However, the other materials, with a different polymer structure, showed an overall lower UV/VUV sensitivity, and the He PPT approach was not effective in stabilizing these materials. The surface roughness was not affected for HM, while AR, NFC, and EUV showed a small increase in surface roughness.

During the investigation of the He PPT, an interesting delamination phenomenon was observed. This was discussed in chapter 3. Extended He PPT exposures of 193nm PR can lead to delamination of the ion-induced DAC layer during the subsequent PE. This delamination was only observed for the PMMA-based 193nm PR polymer with adamantyl side groups. Only the combination of He PPT and PE causes the DAC layer to delaminate from the surface. Neither process by itself causes a loss of adhesion. The delaminated layer is only several nanometers thick and composed of amorphous carbon. This phenomenon is believed to be based on the UV/VUV sensitivity of PMMA-based polymers. A large photon flux during the He PPT produces volatile scission products in the polymer. The subsequent ion bombardment during the PE causes the formation of an impermeable DAC layer, trapping these scission products underneath.

In chapter 4, a cyclic FC-based ALE approach was established for precise removal of SiO_2. The cyclic approach consists of a deposition step and subsequent etch step. During the deposition step, precise precursor injection allows for controlled FC film deposition on the order of several Ångstrom. After completion of the FC film deposition, a small bias potential is applied during the etch step. Low energy Ar^+ ion bombardment induces mixing of F with the SiO_2 substrate and removal of the FC film together with mixed, reacted substrate material. Once the chemical etchant is depleted, the etch rates decrease and self-limited material removal is observed. The thickness of the deposited FC film and ion energy can be used to precisely control the substrate removal per cycle. The results are consistent with simulations by Rauf *et al.* and Agarwal and Kushner.[4, 17]

The cyclic ALE process established in chapter 4 was expanded to etching of Si substrates in Chapter 5. The instantaneous etch rate during each cycle changed only

slightly for Si, whereas a strong time-dependence was observed for SiO_2. Si substrates exhibit a lower physical sputtering energy threshold as compared to SiO_2. A fluorinated, oxidized surface layer was present during ALE of Si. The Si etching occurs through this top layer, which strongly influences the Si etching behavior. Process conditions providing a FC film build-up on Si substrates while etching SiO_2 substrates were established. This allowed SiO_2 over Si etching selectivity. To further characterize the process, plasma properties were measured in real-time during cyclic ALE. The precursor injection was shown to have a strong, but short impact on electron temperature, electron density, and plasma potential, consistent with continuous precursor admixtures.

Chapter 6 further explored and characterized ALE of Si and SiO_2, especially with regard to etching selectivity. The main process parameters investigated were the FC film thickness deposited per cycle, the maximum ion energy, and the etch step length. The FC film thickness deposited per cycle does yield a strong control over etch depth per cycle, but not material etching selectivity. The ion energy and etch step length, however, proved to impact material etching selectivity significantly. Higher ion energies and longer etch steps provide SiO_2 over Si selectivity, while lower ion energies and shorter etch steps provide Si over SiO_2 selectivity. These selectivity considerations are independent of FC film build-up conditions, which need to be considered separately. Additionally, C_4F_8 and CHF_3 were used as precursors. The etching behavior of C_4F_8 and CHF_3 is generally similar. However, CHF_3 was shown to have a lower deposition yield than C_4F_8 and a dependence on substrate material. The FC film thickness deposited is higher on a Si substrate compared to SiO_2. An interesting reaction was observed during the deposition step. *In situ* ellipsometry showed a loss in elemental Si thickness upon precursor

injection. This reaction is stronger for CHF_3 and F richer conditions, e.g. thicker FC film deposition per cycle or shorter etch step lengths. The loss observed is based on a reaction of the fluorinated Si substrate with the precursor. The etch step conditions were shown to impact this reaction during the deposition step, despite the temporal separation.

In chapter 7, the cyclic ALE approach, successfully developed at UMD, was transferred to an industrial environment. Instead of the highly sophisticated ICP reactor at the Laboratory for Plasma Processing of Materials, a manufacturing scale reactor at the IBM T.J. Watson Research Center was used for device patterning. ALE typically offers a large parameter space. This allows for great adaptability but also raises the requirement for a good characterization. Low substrate temperatures lead to lower etch rates and a higher material selectivity, but worse pattern fidelity. Etch step length, source power, and bias power impact material removal per cycle and pattern fidelity. Despite non-optimized process conditions, improvements over a typical continuous etch process in terms of wafer uniformity and pattern fidelity were observed.

Chapter 8 discussed the application of cyclic ALE processes for surface cleaning of Si and SiGe. The process developed for precise etching of SiO_2 and Si in chapters 4 through 6 is not suitable for removing native oxide from Si surfaces. A fluorinated, oxidized surface layer is present at all times during the etching of Si. Therefore, the process was modified for better surface cleaning. Continuously biased Ar plasma with periodic CF_4 injections successfully removed O from the Si surface, leaving a residual C film. Subsequent 90% H_2/Ar plasma was used to remove the residual carbon film and passivate the surface. This combined cleaning procedure also successfully removed oxide from SiGe surfaces.

In this work we have been able to demonstrate a novel approach to ALE, with high etching precision and selectivity. The understanding obtained will impact micro- and nanostructure fabrication in general, and thus impact other disciplines which utilize the results of these fabrication methods. Challenges and obstacles encountered during this work help clarify how to approach and solve these issues for scientific work at the nanometer scale. This work has found wide-spread interest in many other research groups and several companies already.

The understanding of the mechanisms of ALE of SiO_2 and Si gained in this work can be used to optimize ALE of SiO_2 and Si for a variety of potential applications. Selective etching of SiO_2 over Si, directionality, and etch control should be maximized for any application. Several process parameters (e.g. ion energy, surface fluorination, and etch step length) greatly influence the etch performance. We have established a fundamental understanding of these impacts and involved mechanisms.

This work has shown that the chemistry employed during ALE has a strong impact on etching mechanisms. A reaction of the Si substrate with the injected precursor was described in chapter 6. Additionally, ALE of Si did not show a true self-limitation. This reaction and lack of true self-limitation poses limits to the application of FC-based ALE and stands in contrast to typical ALD methods. C_4F_8 and CHF_3 have been explored as two example precursors and have shown differences, especially in their deposition behavior and reaction with Si substrates. However, in order to clearly distinguish the impact of H, additional studies are necessary. H_2 admixture to C_4F_8 injections can be studied to show the impact of H radicals and ions on the etch behavior. Several other studies have been performed on H_2 addition to continuous etching.[81, 83, 106-108] It remains

to be seen, however, if ALE shows similar trends. Additionally, other chemistries are of great interest. A wide variety of FC precursors are commonly employed in industry, e.g. CF_4, C_2F_6, C_3F_6, or C_4F_6. Each precursor shows different dissociation, deposition yield, and deposited FC film characteristics. Addition of oxygen, in the form of O_2 admixture or directly in the precursor molecule (e.g. $C_5F_{10}O$) can yield potentially interesting results. It has been seen that ion assisted reoxidation interacts strongly with ALE of Si substrates. Precise oxygen addition could allow for control over the reoxidized surface layer.

Next to varying the precursor injection, the carrier gas chemistry can be explored, too. Ion bombardment plays an essential role in this ALE approach. For the current work, low energy Ar^+ ions are employed. Other typically employed carrier gases include He and N_2. The ion mass varies significantly between these three chemistries. Furthermore, H has been shown to passivate Si surfaces.[136-138] H ions can penetrate significantly deeper into the substrate than Ar ions.[107, 108] Therefore in addition to H_2 addition to the precursor, H_2 addition to the carrier gas can also greatly impact the etch characteristics.

One of the limitations of ALE is slow processing rates and the resulting low wafer throughput. The current process consists of a FC film deposition and subsequent etch step. This separation allows great process control and dedicated characterization. In order to speed up processing, the possibility of eliminating a dedicated FC film deposition step can be explored. The process itself is based on similar principles. The Ar plasma would in this case be continuously biased. Periodic, precise precursor injections control and limit the amount of chemical reactant. Similar etch characteristics, e.g. time-dependent etch rates and self-limitation, are expected. Considering the current typical times of 15 s

for a deposition step and 40 s for an etch step, cycle times could potentially be reduced by ≈20%.

Directionality is of key interest in the application of ALE. In contrast to atomic layer deposition, a well-developed isotropic technique,[3, 78-80] ALE ideally provides an anisotropic etch behavior. Directionality is usually based on energetic ion bombardment. The low ion energies needed for successful ALE may suffer from reduced directionality.[145] Most of this work has been performed with blanket samples for a better characterization and analysis. Blanket samples allow *in situ* real time ellipsometry thickness monitoring and surface chemistry characterization by XPS. However, for industrial purposes the application of ALE to 3D structures is of utmost importance. For example, plasma etching can show significantly tapered structures.[67, 146-148] The characterization of ALE of structures has been started at IBM Research and showed first promising results.[89] The effect of process parameters for cyclic etching on 3D structures is, however, not yet clear and can greatly differ from continuous etching. Further characterization, e.g. of tight pitch features and etch uniformity, is important for the potential implementation of ALE in manufacturing. A uniform deposition is necessary for a uniform etch. Feature size and aspect ratio can greatly influence FC sidewall deposition based on the line of sight of reactive species.[149, 150] This effect can lead to preferred deposition at the top of small features and ultimately to occlusion of these features. The uniformity of the cyclic deposition is of particular interest since it will greatly affect the subsequent etching.

The semiconductor processing industry is moving towards manipulating single layers of atoms. Critical dimensions have been shrinking, following Moore's Law, for

decades.[5] Continuing the current trend will eventually lead to critical dimensions on the order of only several atoms or molecules, therefore setting a hard limit to scaling.[151] In addition to this limit, heat dissipation becomes an increasing challenge in modern day processors. One possible solution is the move to other materials, e.g. graphene-like compounds. We believe that the understanding and knowledge gained with this work will help future studies on engineering at the Ångstrom scale.

References

1. F. Weilnboeck, D. Metzler, N. Kumar, G. S. Oehrlein, R. L. Bruce, S. Engelmann and N. Fuller, Appl Phys Lett **99** (26), 261501 (2011).
2. N. Marchack and J. P. Chang, J Phys D Appl Phys **44** (17), 174011 (2011).
3. M. Leskelä and M. Ritala, Angew. Chem. Int. Edit. **42** (45), 5548-5554 (2003).
4. A. Agarwal and M. J. Kushner, J. Vac. Sci. Technol. A **27** (1), 37-50 (2009).
5. G. E. Moore, Proc. IEEE **86** (1), 82-85 (1998).
6. R. H. Dennard, F. H. Gaensslen, H. N. Yu, V. L. Rideout, E. Bassous and A. R. Leblanc, Proc. IEEE **87** (4), 668-678 (1999).
7. C. G. N. Lee, K. J. Kanarik and R. A. Gottscho, J Phys D Appl Phys **47** (27), 273001 (2014).
8. V. M. Donnelly and A. Kornblit, J. Vac. Sci. Technol. A **31** (5), 050825 (2013).
9. G. S. Oehrlein, D. Metzler and C. Li, ECS J. Solid State Sc. **4** (6), N5041-N5053 (2015).
10. K. J. Kanarik, T. Lill, E. A. Hudson, S. Sriraman, S. Tan, J. Marks, V. Vahedi and R. A. Gottscho, J. Vac. Sci. Technol. A **33** (2), 020802 (2015).
11. K. J. Kanarik, S. Tan, J. Holland, A. Eppler, V. Vahedi, J. Marks and R. A. Gottscho, Solid State Technol. **56** (8), 14-17 (2013).
12. T. Meguro, M. Hamagaki, S. Modaressi, T. Hara, Y. Aoyagi, M. Ishii and Y. Yamamoto, Appl Phys Lett **56** (16), 1552-1554 (1990).
13. W. T. Tsang, T. H. Chiu and R. M. Kapre, Appl Phys Lett **63** (25), 3500-3502 (1993).
14. C. T. Carver, J. J. Plombon, P. E. Romero, S. Suri, T. A. Tronic and R. B. Turkot, ECS J. Solid State Sc. **4** (6), N5005-N5009 (2015).
15. K. Eriguchi and K. Ono, J Phys D Appl Phys **41** (2), 024002 (2008).
16. C. Cismaru, J. L. Shohet and J. P. McVittie, Appl Phys Lett **76** (16), 2191-2193 (2000).
17. S. Rauf, T. Sparks, P. L. G. Ventzek, V. V. Smirnov, A. V. Stengach, K. G. Gaynullin and V. A. Pavlovsky, J. Appl. Phys. **101** (3), 033308 (2007).
18. N. R. Rueger, M. F. Doemling, M. Schaepkens, J. J. Beulens, T. E. F. M. Standaert and G. S. Oehrlein, J. Vac. Sci. Technol. A **17** (5), 2492-2502 (1999).
19. S. Engelmann, R. L. Bruce, T. Kwon, R. Phaneuf, G. S. Oehrlein, Y. C. Bae, C. Andes, D. Graves, D. Nest, E. A. Hudson, P. Lazzeri, E. Lacob and M. Anderle, J. Vac. Sci. Technol. B **25** (4), 1353-1364 (2007).
20. T. E. F. M. Standaert, P. J. Matsuo, S. D. Allen, G. S. Oehrlein and T. J. Dalton, J. Vac. Sci. Technol. A **17** (3), 741-748 (1999).
21. X. F. Hua, X. Wang, D. Fuentevilla, G. S. Oehrlein, F. G. Celii and K. H. R. Kirmse, J. Vac. Sci. Technol. A **21** (5), 1708-1716 (2003).
22. H. G. Tompkins, *A User's Guide To Ellipsometry* (Dover Publications Inc., Mineola, 1993).
23. T. E. F. M. Standaert, M. Schaepkens, N. R. Rueger, P. G. M. Sebel, G. S. Oehrlein and J. M. Cook, J. Vac. Sci. Technol. A **16** (1), 239-249 (1998).
24. S. W. Robey and G. S. Oehrlein, Surf Sci **210** (3), 429-448 (1989).
25. G. S. Oehrlein, R. J. Phaneuf and D. B. Graves, J. Vac. Sci. Technol. B **29** (1), 010801 (2011).
26. T. Y. Chung, D. B. Graves, F. Weilnboeck, R. L. Bruce, G. S. Oehrlein, M. Q. Li and E. A. Hudson, Plasma Process Polym **8** (11), 1068-1079 (2011).
27. R. L. Bruce, F. Weilnboeck, T. Lin, R. J. Phaneuf, G. S. Oehrlein, B. K. Long, C. G. Willson, J. J. Vegh, D. Nest and D. B. Graves, J. Appl. Phys. **107** (8), 084310 (2010).
28. T. E. F. M. Standaert, P. J. Matsuo, S. D. Allen, G. S. Oehrlein and T. J. Dalton, J. Vac. Sci. Technol. A **17** (3), 741-748 (1999).

29. S. Engelmann, R. L. Bruce, T. Kwon, R. Phaneuf, G. S. Oehrlein, Y. C. Bae, C. Andes, D. Graves, D. Nest, E. A. Hudson, P. Lazzeri, E. Lacob and M. Anderle, J. Vac. Sci. Technol. B **25** (4), 1353-1364 (2007).
30. Yu. Ralchenko, A.E. Kramida, J. Reader and NIST ASD Team, NIST Atomic Spectra Database (ver. 4.1.0) (2011).
31. M. J. Titus, D. Nest and D. B. Graves, Appl. Phys. Lett. **94** (17), 171501 (2009).
32. F. Weilnboeck, R. L. Bruce, S. Engelmann, G. S. Oehrlein, D. Nest, T. Y. Chung, D. Graves, M. Li, D. Wang, C. Andes and E. A. Hudson, J. Vac. Sci. Technol. B **28** (5), 993-1004 (2010).
33. F. E. Truica-Marasescu and M. R. Wertheimer, Macromol Chem Phys **206** (7), 744-757 (2005).
34. S. Engelmann, R. L. Bruce, F. Weilnboeck, G. S. Oehrlein, D. Nest, D. B. Graves, C. Andes and E. A. Hudson, Plasma Process Polym **6** (8), 484-489 (2009).
35. J. J. Vegh, D. Nest, D. B. Graves, R. Bruce, S. Engelmann, T. Kwon, R. J. Phaneuf, G. S. Oehrlein, B. K. Long and C. G. Willson, Appl Phys Lett **91** (23), 233113 (2007).
36. N. Fourches and G. Turban, Thin Solid Films **240** (1-2), 28-38 (1994).
37. T. Schwarz-Selinger, A. von Keudell and W. Jacob, J. Appl. Phys. **86** (7), 3988-3996 (1999).
38. D. Sunil, V. D. Vankar and K. L. Chopra, J. Appl. Phys. **69** (6), 3719-3722 (1991).
39. V. A. Tolmachiev and E. A. Konshina, Diam Relat Mater **5** (12), 1397-1401 (1996).
40. X. Wang, P. J. Martin and T. J. Kinder, Thin Solid Films **256** (1-2), 148-154 (1995).
41. D. P. Dowling, K. Donnelly, M. Monclus and M. McGuinness, Diam Relat Mater **7** (2-5), 432-434 (1998).
42. G. Socrates, Infrared Characteristic Group Frequencies (Wiley, Chichester, 1980).
43. F. Weilnboeck, N. Kumar, G. S. Oehrlein, T. Y. Chung, D. Graves, M. Li, E. A. Hudson and E. C. Benck, J. Vac. Sci. Technol. B **30** (3), 031807 (2012).
44. B. Q. Wua and A. Kumar, J. Vac. Sci. Technol. B **25** (6), 1743-1761 (2007).
45. C.-T. Lee, M. Wang, N. D. Jarnagin, K. E. Gonsalves, J. M. Roberts, W. Yueh and C. L. Henderson, Proc. SPIE **6519** (doi:10.1117/12.713369) (2007).
46. D. L. Goldfarb, A. P. Mahorowala, G. M. Gallatin, K. E. Petrillo, K. Temple, M. Angelopoulos, S. Rasgon, H. H. Sawin, S. D. Allen, M. C. Lawson and R. W. Kwong, J. Vac. Sci. Technol. B **22** (2), 647-653 (2004).
47. A. P. Mahorowala, D. L. Goldfarb, K. Temple, K. E. Petrillo, D. Pfeiffer, K. Babich, M. Angelopoulos, G. Gallatin, S. Rasgon, H. H. Sawin, S. D. Allen, R. N. Lang, M. C. Lawson, R. W. Kwong, K. J. Chen, W. J. Li, P. R. Varanasi, M. I. Sanchez, H. Ito, G. M. Wallraff and R. D. Allen, P Soc Photo-Opt Ins **5039**, 213-224 (2003).
48. D. Nest, D. B. Graves, S. Engelmann, R. L. Bruce, F. Weilnboeck, G. S. Oehrlein, C. Andes and E. A. Hudson, Appl Phys Lett **92** (15), 153113 (2008).
49. T. C. Lin, R. L. Bruce, G. S. Oehrlein, R. J. Phaneuf and H. C. Kan, Appl Phys Lett **100** (23), 233113 (2012).
50. D. Nest, T. Y. Chung, D. B. Graves, S. Engelmann, R. L. Bruce, F. Weilnboeck, G. S. Oehrlein, D. Y. Wang, C. Andes and E. A. Hudson, Plasma Process Polym **6** (10), 649-657 (2009).
51. J. J. Vegh, D. Nest, D. B. Graves, R. Bruce, S. Engelmann, T. Kwon, R. J. Phaneuf, G. S. Oehrlein, B. K. Long and C. G. Willson, J. Appl. Phys. **104** (3), 034308 (2008).
52. K. J. Orvek and C. Huffman, Nucl Instrum Meth B **7-8** (Mar), 501-506 (1985).
53. Y. Koval, J. Vac. Sci. Technol. B **22** (2), 843-851 (2004).
54. J. Zekonyte, J. Erichsen, V. Zaporojtchenko and F. Faupel, Surf Sci **532**, 1040-1044 (2003).
55. M. C. Coen, R. Lehmann, P. Groening and L. Schlapbach, Appl Surf Sci **207** (1-4), 276-286 (2003).

56. T. Y. Chung, D. Nest, D. B. Graves, F. Weilnboeck, R. L. Bruce, G. S. Oehrlein, D. Wang, M. Li and E. A. Hudson, J Phys D Appl Phys **43** (27), 272001 (2010).
57. N. Fox-Lyon, G. S. Oehrlein, N. Ning and D. B. Graves, J. Appl. Phys. **110** (10), 104314 (2011).
58. M. W. Moon, J. W. Chung, K. R. Lee, K. H. Oh, R. Wang and A. G. Evans, Acta Materialia **50** (5), 1219-1227 (2002).
59. R. F. Egerton, *Electron energy-loss spectroscopy in the electron microscope*, 2nd ed. (Plenum Press, New York, 1996).
60. C. C. Ahn, *Transmission electron energy loss spectrometry in materials science and the EELS atlas*, 2nd ed. (Wiley, Weinheim, Germany, 2004).
61. F. Schrempel, Y. S. Kim and W. Witthuhn, Appl Surf Sci **189** (1-2), 102-112 (2002).
62. S. Unai, N. Puttaraksa, N. Pussadee, K. Singkarat, M. W. Rhodes, H. J. Whitlow and S. Singkarat, Maejo Int J Sci Tech **6** (1), 70-76 (2012).
63. S. Unai, N. Puttaraksa, N. Pussadee, K. Singkarat, M. W. Rhodes, H. J. Whitlow and S. Singkarat, Microelectron Eng **102**, 18-21 (2013).
64. M. J. Titus, D. Nest and D. B. Graves, Appl Phys Lett **94** (17) (2009).
65. H. Hiraoka, Ibm J Res Dev **21** (2), 121-130 (1977).
66. M. W. Moon, K. R. Lee, K. H. Oh and J. W. Hutchinson, Acta Materialia **52** (10), 3151-3159 (2004).
67. H. Shin, W. Zhu, V. M. Donnelly and D. J. Economou, J. Vac. Sci. Technol. A **30** (2), 021306 (2012).
68. G. V. Jorgenson and G. K. Wehner, J. Appl. Phys. **36** (9), 2672 (1965).
69. T. E. F. M. Standaert, C. Hedlund, E. A. Joseph, G. S. Oehrlein and T. J. Dalton, J. Vac. Sci. Technol. A **22** (1), 53-60 (2004).
70. D. Briggs, *Surface Analysis of Polymers by XPS and Static SIMS* (Cambridge University Press, Cambridge, 1998).
71. E. A. J. Bartis, D. B. Graves, J. Seog and G. S. Oehrlein, J Phys D Appl Phys **46** (31), 312002 (2013).
72. R. L. Bruce, F. Weilnboeck, T. Lin, R. J. Phaneuf, G. S. Oehrlein, B. K. Long, C. G. Willson and A. Alizadeh, J. Vac. Sci. Technol. B **29** (4), 041604 (2011).
73. D. Metzler, R. Bruce, S. Engelmann, E. A. Joseph and G. S. Oehrlein, J. Vac. Sci. Technol. A **32** (2), 020603 (2014).
74. K. J. Kanarik, G. Kamarthy and R. A. Gottscho, Solid State Technol. **55** (3), 15-28 (2012).
75. M. Guillorn, J. Chang, A. Pyzyna, S. Engelmann, E. Joseph, B. Fletcher, C. Cabral, C. H. Lin, A. Bryant, M. Damon, J. Ott, C. Lavoie, M. Frank, L. Gignac, J. Newbury, C. Wang, D. Klaus, E. Kratschmer, J. Bucchignano, B. To, W. Graham, I. Lauer, E. Sikorski, S. Carter, V. Narayanan, N. Fuller, Y. Zhang and W. Haensch, Int El Devices Meeting, 626-628 (2009).
76. S. Bangsaruntip, G. M. Cohen, A. Majumdar, Y. Zhang, S. U. Engelmann, N. C. M. Fuller, L. M. Gignac, S. Mittal, J. S. Newbury, M. Guillorn, T. Barwicz, L. Sekaric, M. M. Frank and J. W. Sleight, Int El Devices Meeting, 272-275 (2009).
77. T. Suntola and J. Antson, US Pat. 4058430 A (1977).
78. S. M. George, Chem. Rev. **110** (1), 111-131 (2010).
79. R. L. Puurunen, J. Appl. Phys. **97** (12), 121301 (2005).
80. M. Leskelä and M. Ritala, Thin Solid Films **409** (1), 138-146 (2002).
81. M. Schaepkens, T. E. F. M. Standaert, N. R. Rueger, P. G. M. Sebel, G. S. Oehrlein and J. M. Cook, J. Vac. Sci. Technol. A **17** (1), 26-37 (1999).
82. D. Metzler, C. Li, S. Engelman, R. Bruce, E. A. Joseph and G. S. Oehrlein, to be published (expected 2015).

83. N. R. Rueger, J. J. Beulens, M. Schaepkens, M. F. Doemling, J. M. Mirza, T. E. F. M. Standaert and G. S. Oehrlein, J. Vac. Sci. Technol. A **15** (4), 1881-1889 (1997).
84. Y. Y. Tu, T. J. Chuang and H. F. Winters, Physical Review B **23** (2), 823-835 (1981).
85. J. W. Butterbaugh, D. C. Gray and H. H. Sawin, J. Vac. Sci. Technol. B **9** (3), 1461-1470 (1991).
86. G. S. Oehrlein, Y. Zhang, D. Vender and M. Haverlag, J. Vac. Sci. Technol. A **12** (2), 323-332 (1994).
87. Y. Hikosaka, M. Nakamura and H. Sugai, Jpn J Appl Phys 1 **33** (4B), 2157-2163 (1994).
88. C. J. Mogab, A. C. Adams and D. L. Flamm, J. Appl. Phys. **49** (7), 3796-3803 (1978).
89. D. Metzler, K. Uppireddi, R. L. Bruce, H. Miyazoe, Y. Zhu, W. Price, E. S. Sikorski, L. Chen, S. Engelmann, E. A. Joseph and G. S. Oehrlein, J. Vac. Sci. Technol. A **34** (1), 01B102 (2016).
90. R. A. Gottscho, C. W. Jurgensen and D. J. Vitkavage, J. Vac. Sci. Technol. B **10** (5), 2133-2147 (1992).
91. X. Hua, S. Engelmann, G. S. Oehrlein, P. Jiang, P. Lazzeri, E. Iacob and M. Anderle, J. Vac. Sci. Technol. B **24** (4), 1850-1858 (2006).
92. M. Schaepkens, R. C. M. Bosch, T. E. F. M. Standaert, G. S. Oehrlein and J. M. Cook, J. Vac. Sci. Technol. A **16** (4), 2099-2107 (1998).
93. E. A. Hudson, V. Vidyarthi, R. Bhowmick, R. Bise, H. Shin, G. Delgadino, B. Jariwala, D. Lambert and S. C. Deshmukh, AVS 61st International Symposium & Exhibition, http://www2.avs.org/symposium2014/Papers/Paper_PS2012+TF-ThM2012.html (2014).
94. E. A. Hudson, R. Bhowmick, R. Bise, H. Shin, A. Srivastava, G. Delgadino, B. Jariwala, D. Lambert, S. J. Cho and S. C. Deshmukh, 1st AVS ALE Workshop, http://www2.avs.org/conferences/ALD/2015/aleworkshop.html (2015).
95. S. U. Engelmann, R. L. Bruce, M. Nakamura, D. Metzler, S. G. Walton and E. A. Joseph, ECS J. Solid State Sc. **4** (6), N5054-N5060 (2015).
96. T. Faraz, F. Roozeboom, H. C. M. Knoops and W. M. M. Kessels, ECS J. Solid State Sc. **4** (6), N5023-N5032 (2015).
97. F. Roozeboom, F. van den Bruele, Y. Creyghton, P. Poodt and W. M. M. Kessels, ECS J. Solid State Sc. **4** (6), N5067-N5076 (2015).
98. D. Metzler, C. Li, S. Engelmann, R. Bruce, E. Joseph and G. S. Oehrlein, J. Vac. Sci. Technol. A **34** (10.1116/1.4935462), 01B101 (2016).
99. D. Humbird and D. B. Graves, J. Appl. Phys. **96** (5), 2466 (2004).
100. S. Veprek, C. L. Wang and M. G. J. Veprek-Heijman, J. Vac. Sci. Technol. A **26** (3), 313-320 (2008).
101. M. J. Barela, H. M. Anderson and G. S. Oehrlein, J. Vac. Sci. Technol. A **23** (3), 408-416 (2005).
102. B. J. Kim, S. Chung and S. M. Cho, Appl Surf Sci **187** (1-2), 124-129 (2002).
103. Y. Aoyagi, K. Shinmura, K. Kawasaki, T. Tanaka, K. Gamo, S. Namba and I. Nakamoto, Appl Phys Lett **60** (8), 968 (1992).
104. S.-D. Park, K.-S. Min, B.-Y. Yoon, D.-H. Lee and G.-Y. Yeom, Japanese Journal of Applied Physics **44** (1A), 389-393 (2005).
105. T. Matsuura, J. Murota, Y. Sawada and T. Ohmi, Appl Phys Lett **63** (20), 2803-2805 (1993).
106. K. Takahashi and K. Ono, J. Vac. Sci. Technol. A **24** (3), 437-443 (2006).
107. M. Fukasawa, Y. Nakakubo, A. Matsuda, Y. Takao, K. Eriguchi, K. Ono, M. Minami, F. Uesawa and T. Tatsumi, J. Vac. Sci. Technol. A **29** (4), 041301 (2011).
108. N. Kuboi, T. Tatsumi, T. Kinoshita, T. Shigetoshi, M. Fukasawa, J. Komachi and H. Ansai, J. Vac. Sci. Technol. A **33** (6), 061308 (2015).

109. H. F. Winters and J. W. Coburn, Surf Sci Rep **14** (4-6), 161-269 (1992).
110. J. W. Coburn and H. F. Winters, Appl Surf Sc **22-3** (May), 63-71 (1985).
111. H. F. Winters and J. W. Coburn, J. Vac. Sci. Technol. B **3** (5), 1376-1383 (1985).
112. H. F. Winters and I. C. Plumb, J. Vac. Sci. Technol. B **9** (2), 197-207 (1991).
113. C. Cardinaud and G. Turban, Appl Surf Sci **45** (2), 109-120 (1990).
114. G. S. Oehrlein and H. L. Williams, J. Appl. Phys. **62** (2), 662-672 (1987).
115. G. S. Oehrlein, Y. Zhang, D. Vender and O. Joubert, J Vac Sci Technol A **12** (2), 333-344 (1994).
116. J. P. Simko and G. S. Oehrlein, J Electrochem Soc **138** (9), 2748-2752 (1991).
117. C. F. Abrams and D. B. Graves, J. Appl. Phys. **86** (11), 5938 (1999).
118. D. C. Gray, H. H. Sawin and J. W. Butterbaugh, J Vac Sci Technol A **9** (3), 779-785 (1991).
119. M. E. Barone and D. B. Graves, J. Appl. Phys. **77** (3), 1263-1274 (1995).
120. M. Kawakami, D. Metzler, C. Li and G. S. Oehrlein, J. Vac. Sci. Technol. A, accepted for publication (2016).
121. T. C. Wei and C. H. Liu, Surf. Coat. Tech. **200** (7), 2214-2222 (2005).
122. T. Ohiwa, K. Horioka, T. Arikado, I. Hasegawa and H. Okano, Jpn J Appl Phys 1 **31** (2A), 405-410 (1992).
123. J. H. Min, S. W. Hwang, G. R. Lee and S. H. Moon, J. Vac. Sci. Technol. B **21** (5), 2198-2204 (2003).
124. S. M. Irving, Solid State Technol. **14** (6), 47 (1971).
125. D. Hess, Handbook of Silicon Wafer Cleaning Technology, 2nd Edition, Xxi-Xxii (2008).
126. K. Choi, S. Ghosh, J. Lim and C. M. Lee, Appl Surf Sci **206** (1-4), 355-364 (2003).
127. C. Petit-Etienne, M. Darnon, L. Vallier, E. Pargon, G. Cunge, F. Boulard, O. Joubert, S. Banna and T. Lill, J. Vac. Sci. Technol. B **28** (5), 926-934 (2010).
128. J. K. Kim, S. I. Cho, S. H. Lee, C. K. Kim, K. S. Min, S. H. Kang and G. Y. Yeom, J. Vac. Sci. Technol. A **31** (6), 061310 (2013).
129. J. K. Kim, S. I. Cho, S. H. Lee, C. K. Kim, K. S. Min and G. Y. Yeom, J. Vac. Sci. Technol. A **31** (6), 061302 (2013).
130. V. V. Smirnov, A. V. Stengach, K. G. Gaynullin, V. A. Pavlovsky, S. Rauf, P. J. Stout and P. L. G. Ventzek, J. Appl. Phys. **97** (9), 093302 (2005).
131. T. R. Yew and R. Reif, J. Appl. Phys. **68** (9), 4681-4693 (1990).
132. L. M. Garverick, J. H. Comfort, T. R. Yew, R. Reif, F. A. Baiocchi and H. S. Luftman, J. Appl. Phys. **62** (8), 3398-3404 (1987).
133. R. K. Chanana, R. Dwivedi and S. K. Srivastava, Solid State Electron **35** (10), 1417-1421 (1992).
134. H. S. Tae, S. J. Park, S. H. Hwang, K. H. Hwang, E. Yoon, K. W. Whang and S. A. Song, J. Vac. Sci. Technol. B **13** (3), 908-913 (1995).
135. R. E. Thomas, M. J. Mantini, R. A. Rudder, D. P. Malta, S. V. Hattangady and R. J. Markunas, J Vac Sci Technol A **10** (4), 817-828 (1992).
136. S. Q. Xiao, S. Xu and K. Ostrikov, Mat Sci Eng R **78**, 1-29 (2014).
137. A. Descoeudres, L. Barraud, S. De Wolf, B. Strahm, D. Lachenal, C. Guerin, Z. C. Holman, F. Zicarelli, B. Demaurex, J. Seif, J. Holovsky and C. Ballif, Appl Phys Lett **99** (12), 123506 (2011).
138. M. Mews, T. F. Schulze, N. Mingirulli and L. Korte, Appl Phys Lett **102** (12), 122106 (2013).
139. O. W. Holland, C. W. White and D. Fathy, Appl Phys Lett **51** (7), 520-522 (1987).
140. F. K. Legoues, R. Rosenberg, T. Nguyen, F. Himpsel and B. S. Meyerson, J. Appl. Phys. **65** (4), 1724-1728 (1989).
141. K. Prabhakaran and T. Ogino, Surf Sci **325** (3), 263-271 (1995).

142. M. C. Peignon, C. Cardinaud, G. Turban, C. Charles and R. W. Boswell, J Vac Sci Technol A **14** (1), 156-164 (1996).
143. J. G. Couillard and H. G. Craighead, J. Vac. Sci. Technol. B **11** (3), 717-719 (1993).
144. G. S. Oehrlein, G. M. W. Kroesen, E. Defresart, Y. Zhang and T. D. Bestwick, J Vac Sci Technol A **9** (3), 768-774 (1991).
145. A. M. Mohs, M. C. Mancini, S. Singhal, J. M. Provenzale, B. Leyland-Jones, M. D. Wang and S. M. Nie, Anal Chem **82** (21), 9058-9065 (2010).
146. M. Schaepkens and G. S. Oehrlein, J Electrochem Soc **148** (3), C211-C221 (2001).
147. G. S. Oehrlein and Y. Kurogi, Mat Sci Eng R **24** (4), 153-183 (1998).
148. G. S. Oehrlein and J. F. Rembetski, Ibm J Res Dev **36** (2), 140-157 (1992).
149. S. Noda, N. Ozawa, T. Kinoshita, H. Tsuboi, K. Kawashima, Y. Hikosaka, K. Kinoshita and M. Sekine, Thin Solid Films **374** (2), 181-189 (2000).
150. N. Fox-Lyon, D. Metzler, G. S. Oehrlein, D. Farber and T. Lii, Plasma Process Polym **11** (7), 714-720 (2014).
151. M. M. Waldrop, http://www.nature.com/news/the-chips-are-down-for-moore-s-law-1.19338 (09 February 2016).